Universidade do Porto

Faculdade de Engenharia

FEUP

A new approach for RIM: from RIMCop technology to process design

Ph.D. Dissertation
in
Mechanical Engineering
by

Nuno Miguel de Oliveira Gomes

Supervisors

José Carlos Brito Lopes

Ricardo Jorge Nogueira dos Santos

Paulo Jorge da Silva Bártolo

Laboratory of Separation and Reaction Engineering - LSRE
Laboratório Associado LSRE/LCM
Departamento de Engenharia Química
Faculdade de Engenharia
Universidade do Porto

January 2014

Acknowledgments

I wish to express my gratitude to all whose contribution was fundamental in completion of this work:

- Prof José Carlos Lopes, my advisor, for his guidance, support during this course of the work and giving an opportunity to be part of this Mixing Group;
- Dr. Ricardo Santos, my co-advisor, for his guidance, support, patience, time and effort during this course of this work and being a friend;
- Prof Paulo Bártolo, my co-advisor, for support and the opportunity to start on research;
- Profª Madalena Dias for the review of my work during my work and for support and suggestions;
- Prof Artur Mateus, for the guidance and to introduced me on Reaction Injection Moulding;
- Prof Alírio Rodrigues, director of LSRE, where part of this work was carried out;
- Susana Cruz, for her administrative support at LSRE;
- Dr Carlos Sá and Dra Daniela Silva, both from CEMUP, for SEM analysis and help;
- Profª Fátima Barreiros, Prof Pedro Martinho, former directors of Departamento de Eng Mecânica of Instituto Politécnico de Leiria, where part of the work was carried out, Prof. Joel Vasco, responsible of Lab. de Tecnologias Mecânicas and Prof Mário Pereira, responsible of Lab de Materiais;
- My coworkers in the Lab de Tecnologias Mecânicas, Tiago Nunes, Carlos Mota, Dinarte Abreu, Eduardo Farinha, and specially to my friend Carlos Dias, for the all support and discussion;
- My coworkers in LSRE, Carlos Fonte, Anna Maria Karpsinka, Nuno Gomes, Marina V. Torres, Kateryne Kruppa, Angela Novais and Enis Leblebici, for their help, friendship and specially to Cláudio Fonte for value discussions and patient;
- My friends, for weekend breaks in Leiria, Ana Rita, Andreia, André, Pedro, Joana and Hugo Carriço, and for week breaks in Porto, Ashar, Julio and Rui;
- Francisco Gomes, for his support in all kinds of machining and ideas;
- José Gomes for his help and guidance;
- Maria Isabel and Sara, for their support and valuable ideas for work and the thesis;
- Rita, for her love, support and patience;

- Finally, to Portuguese Foundation for Science and Technology, for supporting this research work and the result dissemination activities under the grant SFRH/BD/45621/2008;

aos meus pais e irmã

ad majorem Dei gloriam

Abstract

The present work concerns the study of RIMCop technology and Reaction Injection Moulding (RIM) process design. RIMCop is a patented technology to improve the mixing in the RIM process. The process design consisted in the setting of RIMcop machine parameters and of the mould filling.

Computational Fluid Dynamics (CFD) tools were used to compare five different commercial types of RIM mixing chambers that were assessed from dimensionless maps of vorticity, pathlines and strain rate. Also an energy balance and the Residence Time Distribution (RTD) were measured. The results showed that the simplest T-jet configurations are more suitable as far as RIM mixing is regarded. A new project for new industrial prototype equipment was introduced.

Experimental study on poluyrethane mixing using a T-jet configuration, showed a dependency of the material properties on the pressure difference at the mixing head, ΔP^*, and it was also found that the pressure signal oscillates with typical frequencies. Based on these results, an impingement point position model was introduced. RIMCop technology proposes a unitary kinetic energy ratio between jets, $KE_r = 1$, for best mixing performance. Experimental results showed that KE_r influences the adiabatic temperature rise, and reaction kinetics. Physical and mechanical properties, such as density, deflection temperature, glass temperature, tensile, compressive and flexural properties clearly showed the influence of KE_r.

The RIM mould filling process was modeled with CFD using 2D and 3D models and Volume of Fluid model. The obtained results were in good agreement with available literature. This model was used for contracting and expanding flows. Four main phenomena were identified on RIM mould filling: stable front, air entrapment at salient corner, air entrapment and engulfment and air boundary layer; and were studied considering the effect of the gravitational, viscous, inertial and surface forces. From the CFD results were obtained maps with the occurrence of each particular phenomenon as function of some dimensionless numbers, aiming the selection of processing conditions. Also some considerations for calculating the thickness of mould plates, gate location and venting zone dimension were introduced.

Resumo

A presente dissertação dedica-se ao estudo da tecnologia RIMCop e ao projeto do processo de RIM. O RIMCop é uma tecnologia patenteada para melhorar a mistura durante o processo RIM. O projeto do processo consistiu na definição dos parâmetros de funcionamento duma máquina RIM com a tecnologia RIMCop e do enchimento do moulde.

Usando ferramentas de Computação de Fluídos Dinâmicos (CFD), cinco câmaras de mistura comerciais foram comparadas, e analisadas de acordo com os seus mapas adimensionais de vorticidade, linhas de fluxo e taxa de deformação. Também foi feita uma analise do balanço energético, e da distribuição dos tempos de residência. Os resultados mostram que as câmaras de mistura em T, são as mais adequadas para o RIM. Foi introduzido um novo projeto para um equipamento protótipo a nível industrial.

Estudos experimentais na produção de poliuretano, usando uma câmara de mistura em T, mostram a dependência das propriedades do material da diferença de pressão na cabeça de mistura, ΔP^*, bem como a existência de valores típicos de frequência nas oscilações do valor da pressão diferencial. Um modelo para a posição do ponto de impacto foi introduzido com base nos resultados. A tecnologia RIMCop propõe que a razão da energia cinética dos jactos deverá ser igual a um, $KE_r = 1$, de modo a melhorar a mistura. Resultados experimentais mostram que KE_r influencia a subida de temperatura adiabática, e a cinética da reação. Propriedades físicas e mecânicas, como a densidade, temperatura de defleção, temperatura vítrea, propriedades de extensão, compressão e flexão, mostram uma clara influência de KE_r .

O processo de enchimento de moldes em RIM foi simulado em 2D e 3D com ferramentas de CFD. Os resultados obtidos estão de acordo com os encontrados na literatura. Este modelo foi aplicado ao estudo do escoamento em contracções e expansões 2D. Quatro principais fenómenos foram identificados, e descritos: frente de escoamento estável, aprisionamento de ar no canto saliente, aprisionamento de ar no seio do escoamento e uma camada-limite de ar; sendo estudados de acordo com as forcas gravitacionais, viscosas, inerciais e de superfície. Os resultados obtidos permitiram a construção de mapas de ocorrência de cada fenómeno, em função de alguns números adimensionais, de modo a ajudar na selecção das condições de processamento. Foram apresentadas, ainda, algumas considerações para o cálculo da espessura das chapas dos moldes, localização dos pontos de injeção e zonas de ventilação.

Table of Contents

Page

Table of Figures

Page

Table of Tables

Page

Notation

$[NCO]$	NCO concentration
A	Area $[\mathrm{m}^2]$
A_v	Air entrapped area $[\mathrm{m}^2]$
$\mathbf{B}$	Body forces tensor $[\mathrm{N}]$
b	Width $[\mathrm{m}]$
c	Distance to the neutral plane $[\mathrm{m}]$
Ca	Capillary number
c_p	Specific heat capacity $[\mathrm{Jkg^{-1}K^{-1}}]$
d	Injector diameter $[\mathrm{m}]$
d_c	Cell diameter $[\mathrm{m}]$
D	Mixing chamber diameter $[\mathrm{m}]$
$\mathbf{D}$	Deformation tensor
D_1	Inlet thickness $[\mathrm{m}]$
D_2	Outlet thickness $[\mathrm{m}]$
$\mathbf{dA}$	Area's normal vector $[\mathrm{m}^2]$
E	Total Energy $[\mathrm{J}]$
e	Total energy per mass $[\mathrm{Jkg^{-1}}]$
$E^{'}$	Storage modulus $[\mathrm{Pa}]$
$E^{"}$	Loss modulus $[\mathrm{Pa}]$
E_a	Activation energy $[\mathrm{Jmol^{-1}}]$
E_C	Compressive modulus $[\mathrm{Pa}]$
E_f	Total work of friction $[\mathrm{J}]$
E_i	Young Modulus $[\mathrm{Pa}]$
$E(t_r)$	Residence Time Distribution
F	Free energy $[\mathrm{J}]$
F_{inj}	Injection force $[\mathrm{N}]$
f	Admissible displacement $[\mathrm{m}]$
f_{bd}	Bending displacement $[\mathrm{m}]$
f_{sh}	Shear displacement $[\mathrm{m}]$
$F(t_r)$	Tracer output
F_m	Mass flux
F^n	Cumulative distribution function
f_n	Natural frequency $[\mathrm{Hz}]$
f^n	Density distribution function
F_r	Flow rate ratio
Fr	Froude number

F_{ST} Force at interfacial surface $[\mathrm{N}]$
g Gravity $[\mathrm{ms}^{-2}]$
$\mathbf{g}$ Gravitational acceleration vector $[\mathrm{ms}^{-2}]$
G_{xx} Power spectra
H Mixing chamber length $[\mathrm{m}]$
h Specific enthalpy $[\mathrm{kJkg}^{-1}]$
h_i Convective heat transfer coefficient of fluid i $[\mathrm{Wm}^{-2}\mathrm{K}^{-1}]$
H_m Mould height $[\mathrm{m}]$
H_s Initial specimen height $[\mathrm{m}]$
H_r Heat released $[\mathrm{J}]$
I Cross-sectional beam moment of inertia $[\mathrm{m}^4]$
$\mathbf{I}$ Identity tensor
$\mathbf{J}$ Diffusion flux vector
j Position along inlet surface $[\mathrm{m}]$
k Specific velocity of reaction $[\mathrm{Jmole}^{-1}\mathrm{K}^{-1}]$
also, thermal conductivity $[\mathrm{Wm}^{-1}\mathrm{K}^{-1}]$
K_i Thougness $[\mathrm{Jm}^{-3}]$
K_D PID derivative term
KE Kinetic energy $[\mathrm{W}]$
KE_r Kinetic energy ratio
K_I PID integral term
K_p PID proportional term
k_{steel} Steel thermal conductivity $[\mathrm{Wm}^{-2}\mathrm{K}^{-1}]$
k_{sc} surface curvature radius
l Impingement point position $[\mathrm{m}]$
l^* Non dimensional Impingement point
L Length $[\mathrm{m}]$
m Mass $[\mathrm{kg}]$
$\dot{m}$ Mass flow rate $[\mathrm{kgs}^{-1}]$
M Torque $[\mathrm{Nm}]$
M_r Momentum ratio
N Nozzle length $[\mathrm{m}]$
n Number of reactors
$\mathbf{n}$ Normal vector
N_p Power number
P Power $[\mathrm{W}]$
p Pressure $[\mathrm{Pa}]$
$\mathbf{p}$ Pressure tensor $[\mathrm{Pa}]$
p_{inj} Injection pressure $[\mathrm{Pa}]$
PE Pressure energy $[\mathrm{W}]$
q Volumetric flow rate $[\mathrm{m}^3\mathrm{s}^{-1}]$

$\mathbf{q}$	Heat flux $[\mathrm{Wm^{-2}}]$
Q	Heat $[\mathrm{J}]$
Q_t	Transferred heat $[\mathrm{J}]$
R	Part radius $[\mathrm{m}]$ also, square sum of deviation also, Universal Gas Constant $[\mathrm{Jk^{-1}mol^{-1}}]$
r	Injector radius $[\mathrm{m}]$
$\mathbf{r}$	Position $[\mathrm{m}]$
$R(r)$	Correlation of volume fraction
Re	Reynolds number
s	Striation thickness $[\mathrm{m}]$
St	Strouhal number
s_d	Standard deviation
S_l	Linear shrinkage
s_l	Scale of segregation
S_w	Thickness shrinkage
T	Temperature $[\mathrm{°C}]$
$\mathbf{T}$	Traction forces tensor $[\mathrm{N}]$
t	Time $[\mathrm{s}]$ also, Thickness $[\mathrm{m}]$
$t_{0.975}$	t-Student parameter 97.5%
t_{av}	Average residence time
t_{cure}	Cure time $[\mathrm{s}]$
t_d	Dark structure thickness $[\mathrm{m}]$
T_d	Deflection Temperature $[\mathrm{°C}]$
$t_{extraction}$	Extraction time $[\mathrm{s}]$
T_g	Glass transition temperature $[\mathrm{°C}]$
t_{gel}	Gel time $[\mathrm{s}]$
t_r	Normalize residence time
T_r	Thickness ratio
$\mathrm{Tan}\delta$	Damping factor
u	Internal energy $[\mathrm{J}]$ also, PID output
U	Overall heat transfer coefficient $[\mathrm{Wm^{-2}°C^{-1}}]$
$\mathbf{v}$	Velocity vector $[\mathrm{ms^{-2}}]$
$V_{\Delta p}$	PTD $[\mathrm{V}]$
V	Volume $[\mathrm{m^3}]$
W	Work $[\mathrm{J}]$
w	Deflection $[\mathrm{m}]$
We	Weber number
x	Space coordinate $[\mathrm{m}]$
x_f	Flow front position $[\mathrm{m}]$

X_g Glycerine fraction
y Space coordinate [m]
z Space coordinate [m]

Greek letters

α Fraction conversion
α_i Volumetric fraction of phase i
γ_{g-l} Surface tension between phase gas and liquid [Nm^{-1}]
$\dot{\gamma}_{inj}$ Strain rate at injector walls [s^{-1}]
ΔH_r Released heat [J]
Δp^* Normalized differential static pressure
Δp Differential static pressure [Pa]
Δt Time step [s]
ΔT_{ad} Adiabatic temperature rise [°C]
Δx Numerical grid element length [m]
δ Internal walls thickness [m]
ε Strain
ε_{fe} Friction energy dissipation [Jkg^{-1}]
ε_{se} Shear energy dissipation [Jkg^{-1}]
ε_{sd} Shear dissipation [Jkg^{-1}]
ε_t Total energy dissipation [Jkg^{-1}]
ε_{tot} Energy dissipation rate [W]
ζ Surface Equation
η_g Volumetric efficiency
$\dot{\Theta}$ Rate of energy production per unit mass [Wkg^{-1}]
θ Angle [rad]
κ Contraction coefficient
μ Viscosity [$Pa \cdot s$]
ν Kinematic viscosity [m^2s^{-1}]
ξ Non-dimensional rate of strain
ρ Density [kgm^{-3}]
$\boldsymbol{\sigma}$ Normal stress Tensor [Pa]
$\sigma^2_{t_r}$ non-dimensional variance of RTD
σ_B Break strength [Pa]
σ_f Flexural strength [Pa]
σ_M Maximum strength [Pa]
σ_y Yield strength [Pa]
τ Passage time [s]
also, Shear stress [Pa]
$\boldsymbol{\tau}$ Stress tensor [Pa]
υ Velocity [ms^{-1}]

ϕ	Induced frequency [Hz]
ϕ_r	Diameter ratio
ς	Empirical loss coefficient
ψ	Stream function $[\mathrm{m^2 s^{-1}}]$
$\boldsymbol{\omega}^*$	Non-dimension vorticity

Mathematical operators

$\frac{d(\cdot)}{dt}$	Time derivative
$\nabla(\cdot)$	Gradient operator
$\nabla\times(\cdot)$	Curl operator
$\nabla\cdot(\cdot)$	Divergence operator
$\frac{D}{Dt}(\cdot)$	substantial derivate
$\nabla^2(\cdot)$	Laplacian operator
$(\cdot)^T$	Transpose
$\overline{(\cdot)}$	Avarage
$\|(\cdot)\|$	norm

Subscripts

∞	Flow
0	Initial
1	Left injector
2	Right injector
3	Outlet
a	Air
A	Species A
b	Bottom of mixing chamber
bd	Bending
c	Compressive
cm	Center of mass
cr	Critical
CS	Control surface
cs	Cross-sectional
CV	Control Volume
d	Dry
ds	Downstream
e	Control surface
$ext-a$	Exterior-air
$ext-o$	Exterior-oil
g	Gas
f	Flexural
fl	Fluid
fr	Friction
fs	Flow section
i	Species index

in	Inlet
inj	At injector
int	Interior
iso	Isocyanate
k	Refer to surrounds
l	Lateral of mixing chamber
liq	Liquid
max	Maximum value
o	Oil
o_d	Dry part of oil
o_w	Wet part of oil
out	Outlet
pol	Polyol
r	Room
s	Shaft
sh	Shear
t	Tensile
top	Top of the mixing chamber
us	Upstream
w	Wall
we	Wet
x	x component of variable
y	y component of variable
z	z component of variable

Abreviation

1½D	One-dimensional and half
2½D	Two-dimensional and half
3D	Three-dimensional
ALE	Arbitrary Lagrangean-Eulerian
ASTM	Americam Society for Testing Materials
CAD	Computeded Aided Design
CDRsp	Centro para o Desenvolvimento Rápido e Sustentado do Produto
CFD	Computational Fluid Dynamics
CNC	Computational Numerical Command
CVFEM	Control Volume Finite Element Method
DMA	Dynamical Mechanical Analyzer
DPT	Differential Pressure Transducer
FDM	Finite Difference Method
FEM	Finite Element Method
FEUP	Faculdade de Engenharia da Universidade do Porto
FVM	Finite Volume Method
IPLeiria	Instituto Politécnico de Leiria
ISO	International Standard Organization
LDA	Laser Doppler Anonemetry
LIF	Laser Induced Fluorescence
LSRE	Laboratory of Separation and Reaction Engineering
MAC	Marker-And-Cell
PID	Proportional Integrate Derivative
PIV	Particle Image Velocimetry
PIT	Particle Image Thermometry
PTV	Particle Tracking Velocimetry

RIM	Reaction Injection Moulding
RIMcop®	Reaction Injection Moulding with Control of Oscillation and Pulsation
RRIM	Reinforced Reaction Injection Moulding
RTD	Residence Time Distribution
SEM	Scanning Electron Microscopy
SRIM	Structural Reaction Injection Moulding
TIM	Thermoplastic Injection Moulding
VOF	Volume of Fluid

1 Introduction

1.1 Reaction Injection Moulding

Reaction Injection Molding (RIM) is a molding process consisting in the mixture of two or more raw materials', generally a polyol and an isocyanate, originating a Polyurethane. The mixing occurs in a mixing chamber followed by the injection of the reacting mixture of the two monomers into a mold. The RIM processes takes place at low pressure and temperature, when compared with Thermoplastics Injection Molding (TIM), due to the low viscosity of the monomers and of the reacting mixture of the monomers that solidifies inside the mold, originating a polymer part (see Figure 1-1).

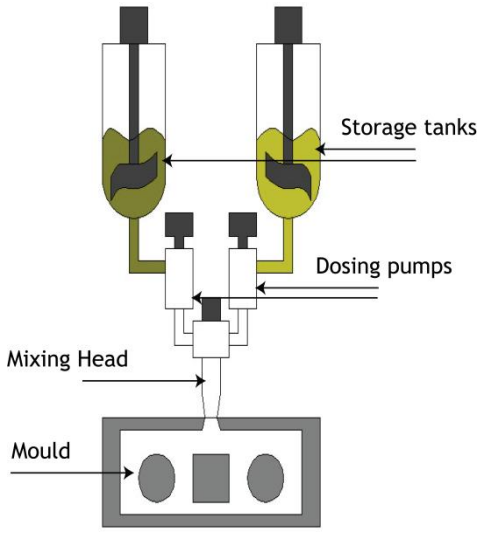

Figure 1-1 Reaction Injection Moulding scheme (Martinho et al., 2003)

Mixing in RIM can be promoted in two different ways: by stirring, using a static or dynamic mixer with several geometries and sizes – this is called low pressure RIM; or by impingement mixing, where two or more raw materials are mixed as opposed jets that impinge each other inside a mixing chamber at a high velocity, normally in the range between 10 to $100 ms^{-1}$ (Santos et al., 2005). The process with a stirrer is called low pressure RIM and the process with impinging jets is called high pressure RIM. The mixing chamber is, usually, cylindrical with 10mm diameter, with two or more nozzles, with 1 to $3mm$ of diameter. The mixing phase is the only difference between high pressure RIM or low pressure RIM.

After the mixing phase, the mixture is injected into a mold. Inside the mould cavity the reacting mixture flows at low pressure, temperature and viscosity. The polymerization, called cure reaction, occurs in the mold, where the material solidifies also at low pressure and temperature. This is an exothermic and a fast process, requiring less energy than injection of other types of polymeric materials (Teixeira, 2000).

It is possible to determine four or five distinct phases, depending on final part's quality requirements in the RIM process:

- the mixing of low viscosity monomers in the mixing chamber;
- the mold filling;
- the polymerization or cure reaction;
- the part extraction;
- eventually, post-cure operations to achieve better properties.

The mixing phase has a major impact on the final quality of the parts, since there is a relation between mixing and the extent of the polymerization reaction and as a consequence on the mechanical properties of the formed polymer properties. The mixing phase is short, and heavily relies on the hydrodynamics inside the RIM mixing chamber. After the mixing, the reacting mixture of monomers is injected into a mould, with a flow regime that should be as close to laminar regime as possible to avoid air bubbles entrapment and other parts defects. The mould should be totally filled before the viscosity increase due to the chemical reaction will cause a huge increase on the filling pressure. This viscosity increase rate is determined by the kinetics of the polymer curing. During the polymerization the mechanical properties, the transition temperature and the molecular weight of polymers increase. The cure reaction is exothermic, releasing a considerable amount of heat and promoting heat transfer between part and mould material. Due to this heat transfer and cure reaction, there are expansion and contraction phenomena, promoting residual tensions on the part. In order to avoid these residual tensions, the mould designers should project a proper cooling system. This phase and

phenomena are shown, over the moulding cycle, in Figure 1-2 (Bártolo and Mateus, 2003; Martinho et al., 2003).

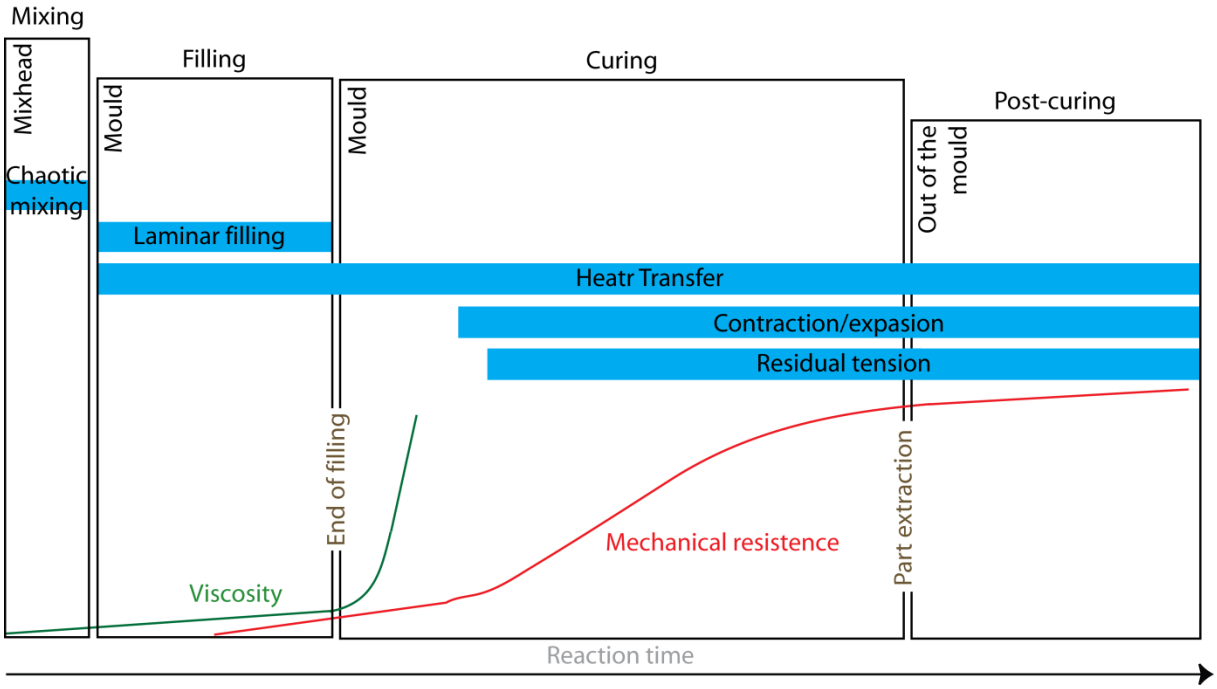

Figure 1-2 Phenomena associated to the different stages in RIM(Bártolo and Mateus, 2003)

In Figure 1-3 are shown the cycle times associated to the RIM process. From this figure is possible to concluded that most of the cycle time is spent in the cure reaction inside the mould (60% of total time). Post-moulding operations uses 20%, and opening and closing the mould account for 10% of the cycle time. The filling time corresponds to 1% of the total cycle, although, this time depends on the chemical system used, the part thickness and on the mould and cooling system design (Bártolo and Mateus, 2003; Martinho et al., 2003).

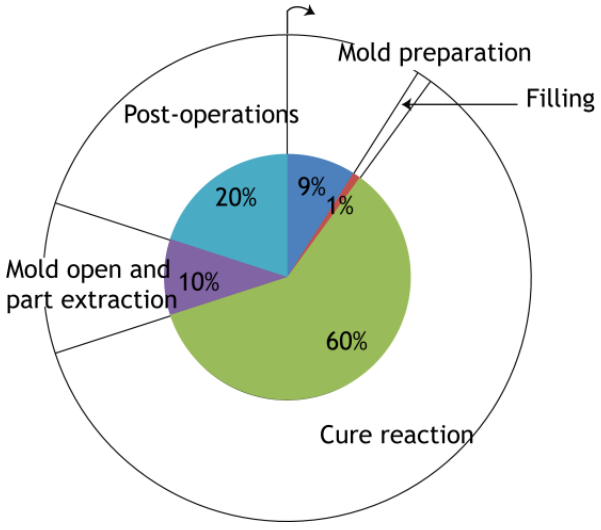

Figure 1-3 RIM cycle (Martinho et al., 2003)

The utilization of low viscosity materials (in the range of 10 a $1500 mPa \cdot s$), the low processing temperature and the low pressure required for filling (up to $30 bar$) are the the basis of the major advantages of RIM over other polymer injection processes, namely TIM. The low pressures and temperatures allow simpler and less resistant moulds, and thus construction materials other than steel can be employed, an in addition to this less usual fabrication technologies, such as Rapid Manufacturing techniques, can be used (Bártolo and Mateus, 2003). This lead to economic advantages, since the equipment price is lower and also the energy consumption is lower (Bártolo and Mateus, 2003). Another advantage is the injection of bigger parts (until $50 kg$), with high complexity and large thickness variation without affecting the final quality. RIM also enables the injection of parts with metallic inserts, thinner walls and A Class surfaces (Bártolo and Mateus, 2003; George, 2000). Besides, it is possible to inject a huge range of materials with RIM, some of them with similar properties to thermoplastics, such as polycarbonate and ABS. The RIM material show high chemical resistance, and the manufactured parts show good resistance to organic and inorganic acids and a higher resistance to ageing (Bártolo and Mateus, 2003; Martinho et al., 2003).

On the other hand, some RIMs characteristics that are related with the advantages, also present disadvantages in industrial projects: the low viscosity of materials causes difficulties in mould seals, the resin can adhere to mould surface and if the filling is too fast, can create air bubbles or other defects. The low mould filling pressure introduces difficulties on removing air bubbles, mainly in corners or over inserts. If the filling is slower than curing, which could occur due to the usage of highly reactive materials, this could originate a *short shot*, where the mould is not totally filled (Macosko, 1989).

Intrinsic characteristics of the RIM, enables the processing of a wide variety of materials, where some reinforcements can be placed. Macosko (1989) points that half of the materials processed in RIM have fillers. Several fillers can be used, being the most common ones the mineral fibers that could be milled, flakes or continuous fibers (Bártolo and Mateus, 2003). Depending on the type of fiber the process can be classified as Reinforced RIM (RRIM) or Structural RIM (SRIM). The RRIM consist in mixing the fiber, or another type of filler, in one of the raw materials. The reinforcement filler, normally has small dimensions (between 0.4 to $1.5 mm$), which enables the dosing and pumping directly inside the mould (Bártolo and Mateus, 2003). Relatively to SRIM, the fiber is placed inside the mould, and after the resin is injected into the moulds, a pre-formed layout of the fiber is impregnated with the resin (Bártolo and Mateus, 2003).

1.2 Relevance and Motivation

The Reaction Injection Moulding is a process for the production of parts with a wide range of applications and, until today, RIM has relevant utilization in low and medium size series. Despite the industrial relevance and advantages of the process, RIM is not so-well studied and so there is plenty of room to enhance this process and solve a number of operational issues, which is the main aim of this research work.

This thesis was framed within the scope of a joint project on RIM between LSRE-FEUP and CDRsp-IPLeiria, funded by Fundação da Ciência e Tecnologia: "*Reaction Injection Moulding (RIM): Controlled Mixing and Novel Design Concepts in a New Prototype Machine*", REF: PTDC/CTM/72595/2006. This project was the follow-up of other projects on RIM, either at LSRE, and CDRsp. This thesis covers the previous work that was done by these two distinct research groups, LSRE-FEUP and CDRsp-IPLeiria, in different but complementary fields of the RIM technology.

The first part of the work will focus on the new technology RIMcop. This technology was patented and it was based on knowledge gathered from previous studies on the hydrodynamics in the RIM machine mixing head, namely on the results from the PhD theses of Teixeira (2000) and Santos (2003).

Teixeira (2000) studied the flow field experimentally using a Laser Doppler Anemometry (LDA) technique, and Computational Fluid Dynamics (CFD). The computational work was done with a 2D model of the RIM mixing chamber, and was the first computational approach to the study of the flow dynamics in RIM.

Santos (2003) studied the dynamic behavior of flow field, its dependence on the operational and some design parameters of the mixing chamber, using both LDA and CFD tools. Furthermore, using Particle Image Velocimetry (PIV), Santos (2003) observed and proposed the flow structures formed inside the RIM Mixing Chamber.

In the second part of this work, the use of CFD tools on the definition of rules for the design of RIM moulds will be studied. The knowledge of the behavior of polymeric flowing materials inside the mould cavity is a powerful tool on the design of RIM moulds, which can reduce the part rejection rate due to poor mould design. Presently, the mould design for thermoplastics is widely studied by several groups, who introduced concepts and project rules (Knipp, 1998). On the other hand, for the reactive polymers, and particularly, for polyurethanes, the available literature is scarce, and the few available guidelines are from private companies and it mainly is based on empirical approaches (Torcato et al., 2011). Another major motivation behind the present work, is to contribute on the methodologies

for RIM moulds design, which could contribute to an increase of the RIM technology share in the plastics injection market.

1.3 Thesis Objectives and Layout

This work intends to study several steps of the RIM process from mixing to mould design. The main goals of this study were the design of a new mixing head based on the patented RIMCop technology (Lopes et al., 2005), assess the mixing quality of the RIMCop technology for a polyurethane system and set rules for the design of RIM moulds. CFD tools were used for comparison between commercial solutions for RIM mixing heads, and to study the mould filling in RIM for characteristic geometry features of moulds. The implementation of the RIMcop technology in industrial prototype equipment enabled a better insight into the effect of mixing in RIM on the mechanical properties of the processed material.

The thesis goals are addressed following this structure:

- Chapter 2 sets the state-of-art in RIM mixing chambers, from the first commercial mixing heads of Keuerleber and Pahl (1972) up to the RIMcop technology introduction (Lopes et al., 2005). This chapter also describes the different methods used for undirected mixing analysis in RIM. Chapter 2 also reviews the state-of-art of project rules for mould design in RIM.
- Chapter 3 focus on the project of machines with RIMCop technology. This chapter introduces the actual project of the RIMCop pilot machine built at LSRE-FEUP. In the first section, a comparative study of several mixing geometries, used at commercial equipment, is made. The second section presents the two pilot RIM machines used along this work at CDRsp-IPLeiria and LSRE-FEUP. The equipment at LSRE-FEUP introduces the novel mixing control technology denominated RIMCop. The last section introduces the calibration and preparation of the RIM equipment for proof of concept of the RIMcop technology.
- Chapter 4 provides details on the RIMCop technology usage. In this chapter, opposed mixing chamber RIM moulding and RIMCop technology were used to produce PU parts. In the first part of the chapter, the mechanical properties of RIM moulded part are assessed. The second part of Chapter 4 introduces the results from the application of RIMCop technology on the processing of the PU part, namely on the effect of the opposed kinetic energy ratio as a process control variable.

- Chapter 5 presents a 2D and 3D VOF model for mould filling simulation in Reaction Injection Moulding, which tracks the flow filling front. Using the model, several simulations were run to identify the phenomena that occur during the RIM mould filling flow, and the effect of several fluid mechanics parameters. From this study, a flow map was created to help the decision based on inertial, viscous, gravitical and superficial forces. The last part of the chapter, introduces some rules for RIM moulds design, covering the project, filling and extraction operations.
- Finally, the last chapter condenses the results and knowledge developed in course of the present work. Future steps, related with present work, are suggested.

1.4 References

Bártolo, P., Mateus, A., 2003. Moldação por Reacção a Baixa Pressão (RIM - Reaction Injection Moulding). Molde 57, 32-37.

George, H., 2000. Reaction Injection Molding(RIM) Technology - New Horizons. Tucson, Fall Meeting of Polyurethane Manufacturing Association.

Keuerleber, R., Pahl, F., 1972. Devide for feeding flowable material to a mold cavity. Patent US3706515.

Knipp, U., 1998. Molds for Polyurethanes Products, in: Stoeckhert, K., Menning, G. (Eds.), Mold-Making Handbook. Hanser Publishers, Munich, Germany.

Lopes, J.C.B., Santos, R.J., Teixeira, A.M., Costa, M.R.P.F.N., 2005. Production Process of Plastic Parts by Reaction Injection Moulding, and Related Head Device. Patent WO 2005/097477.

Macosko, C., 1989. RIM Fundamentals of Reaction Injection Molding. Hanser Publishers, Munich, Germany.

Martinho, P., Mateus, A., Bártolo, P., Bolrão, J., Gaspar, J., Ferreira, P., 2003. Utilização integrada de Técnicas Avançadas para Análise e Optimização do Processo RIM. O Molde 58, 43-49.

Santos, R.J., 2003. Mixing Mechanisms in Reaction Injection Moulding - RIM - An LDS/PIV Experimental Study and CFD Simulation, Ph.D. Thesis, Deparment of Chemical Engineering, Universidade do Porto, Porto.

Santos, R.J., Teixeira, A.M., Lopes, J.C.B., 2005. Study of mixing and chemical reaction in RIM. Chemical Engineering Science 60, 2381-2398.

Teixeira, A.M., 2000. Escoamento na Cabeça de Mistura de uma Máquina RIM, Ph.D. Thesis, Deparment of Chemical Engineering, University of Porto, Porto.

Torcato, R., Santos, R., Dias, M., Olivetti, E., Roth, R., 2011. Concurrent Development of RIM Parts, in: Frey, D.D., Fakuda, S., Rock, G. (Eds.), 18th ISPE International Conference on Concurrent Engineering. Springer-Verlag, Boston.

2 State of Art

2.1 Mixing Head

The key element in RIM equipment is a mixing head, which has several elements such as: mixing chamber, recirculation circuits, injectors and a cleaning piston. There are two types of mixing head: Low pressure mixing head, where mixing proceeds by mechanical stirring; High pressure mixing head, where mixing is done by the jets impact, as will be detailed later in this chapter. Over the last years, the high pressure mixing head has gained industrial importance, and today it is an economically viable technology for the production of parts with reactive materials, such as polyurethanes.

The High Pressure Mixing head, have the ability of (Macosko, 1989):

- Recirculating reactants between the mixing head and the storage tanks, to maintain the homogenization of monomers, the dispersion of solid content and temperature. This recirculation should be done at high pressure in order to eliminate transient effects that in the initial phase of component shot.
- Controlling the stoichiometry of reactants mixing from the very beginning of mixing through quick opening valves.
- Accelerating the reactants to high velocity jets through the inlet nozzles.
- Quickly and completely fill the mixing chamber, enabling proper mixing from the beginning.
- Flush all the remains of polymerized material at the end of filling, from mixing chamber by action of a cleaning piston.

Today, in High pressure RIM is possible to find two types of mixing heads: L mixing head and T mixing head. Usually, the L mixing head has two perpendicular chambers, one for jets impingement and another for discharge into the mold cavity. The T mixing head only has one mixing chamber. According to experimental results of Molnar Jr. and Lee (1989) the L mixing head provides a much more laminar flow at the outlet than the T mixing head, being more suitable for open mould operations as foam blowing process.
Another application for L mixing heads may be found in the structural RIM, since in this process a continuous fiber or woven mat is placed directly into the mold before the filling. In this process, the mixture is injected directly to the part, using a center gate design to minimize the flow path and to stabilize the mat against the pressure generated from mold filling. So, the incorporation of an aftermixer and runner system is impractical, giving an advantage for L mixing head over T mixing head (Molnar Jr. and Lee, 1989).
A review about these two types of mixing heads is introduced next, but a more detailed evaluation will be done on T mixing head since it is more commonly used in conventional RIM machines.

2.1.1 L Mixing Head

L mixing heads consist in two perpendicular chambers, the first one, where the jets impinge is called the mixing chamber, and the other one is the discharge chamber. In the mixing chamber, the jets impinge at high velocities. The nozzles are screw adjustable and allow different flow velocities. They also permit the reactants recirculation from mixing head to the storage tanks. After the mixing phase, the mixture is forced to flow from the first to the second chamber through a right angle elbow, before filling the mould, see Figure 2-1. This angle creates a vortex near the corner when the fluid changes direction (Molnar Jr. and Lee, 1989). This allows a back pressure in impingement point and a laminar flow in the second chamber. The second chamber is longer than the first one, enabling a more efficient flow transition from “turbulent mixing” to laminar flow. At the end of the shot, when the mould cavity is filled, the cleaning piston of the mixing chamber moves forward flushing the inner content of the chamber setting a surface wall for the second chamber. Then, the discharge chamber cleaning piston moves forward flushing the remaining of the system (Molnar Jr. and Lee, 1989).

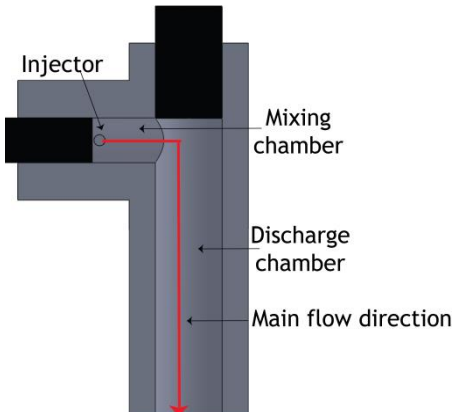

Figure 2-1 L Mixing chamber (Schluter, 1976)

The first L mixing head was patented by Schluter (1976). With similar design, but without affecting the hydrodynamics patterns, several authors, such as Muhle (1978a), Schneider (1979), Fiorentini (1982), Johnson and Moser (1987), Ridenour (1991), Bauer and Mertens (1994), Jeong (2004) and Breuker and Robinson (2006), proposed changes in the recirculation and nozzles work schemes.

Based on previous design and with analogous work some authors have introduced variations in the geometry of the mixing chamber, for example Tenhagen (1986) proposed several geometries for the discharge chamber that are shown in Figure 2-2.

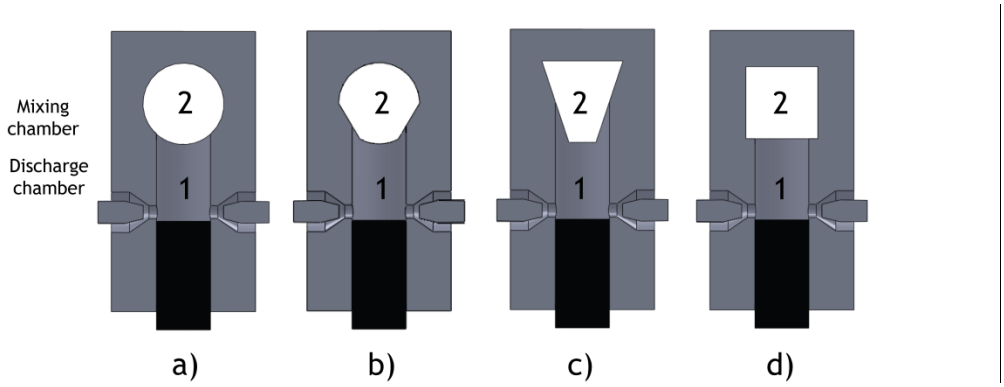

Figure 2-2 Several mixing chamber geometries: a) circular b) balloon c) triangular d) rectangular (Tenhagen, 1986)

For a rapid transition between the two different flow regimes in the two chambers, Schmitz and Krompass (1984) suggest that the second chamber's cleaning piston should be positioned in the impingement plane, i.e. blocking half the mixing chamber outlet, as shown Figure 2-3.

Because the "spray" effect that could occur at the exit of discharge chamber, Schneider (1991) propose a similar mixing head to the one from Schmitz and Krompass (1984), with a 45^{o} angle between the two chamber's axis (cf. Figure 2-4). This enables a better laminar flow field, removing air bubbles trapped in the mixture.

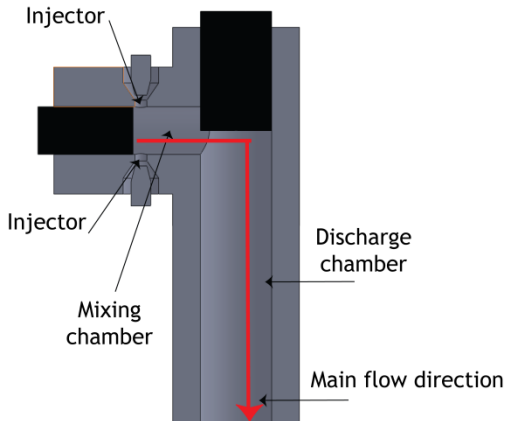

Figure 2-3 L Mixing head of Schmitz and Krompass (1984)

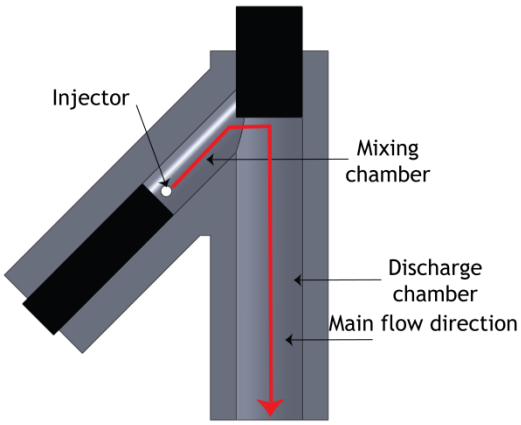

Figure 2-4 L Mixing head of Schneider (1991)

Another idea for enhancing the mixing quality is adding a third chamber called aftermixer, in front of the mixing chamber. This was first introduced by Schneider (1984a). This aftermixing chamber has a larger diameter than the mixing chamber, but smaller than the discharge chamber. Both mixing and aftermixing chambers have screw adjustable nozzles, and the mixing head has two impingement points. The lower faces of mixing and aftermixing chambers share a tangential plane, perpendicular to the discharge chamber, see Figure 2-5. The different diameters of the mixing and aftermixing chambers enable flow velocities differences and pressure drops, originating a fluid movement at high speed between both chambers. Since the flow “has some difficulties” to move out, the flow repeats this movement several times before discharge. The right angle deflection creates a “turbulence” pattern to maximize the mixing efficiency. Regarding the work procedure for this mixing head, this is similar to the case of Schluter (1976) with one more movement, when the aftermixer plunger moves forward before the discharge plunger movement.

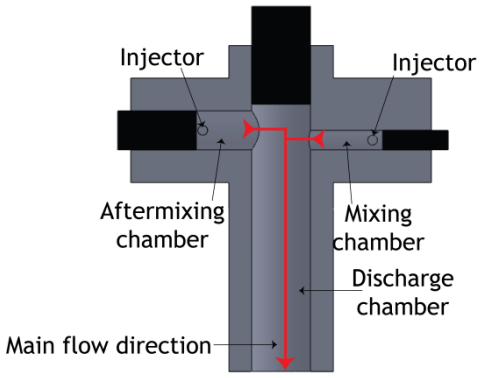

Figure 2-5 L Mixing head with aftermixing (Schneider, 1984a)

Fiorentini (1989) proposed a mixing head with an aftermixing chamber, see Figure 2-6, which is similar to the previous mixing head of Schneider (1984a), but with only one impingement point in the mixing chamber. The aftermixing plunger also delimitates the top of the discharge chamber and downstream the cross section of the mixing chamber, reducing the passage area from the mixing chamber to the discharge chamber. The work procedure is more complex than the one for Schneider (1984a), since, before the basic movements from top discharger plunger and top mixing chamber plunger, the aftermixing plunger, first moves forward to the mixing chamber and after moves backward until the discharger chamber is free to the top discharger plunger moves downward to clean the chamber.

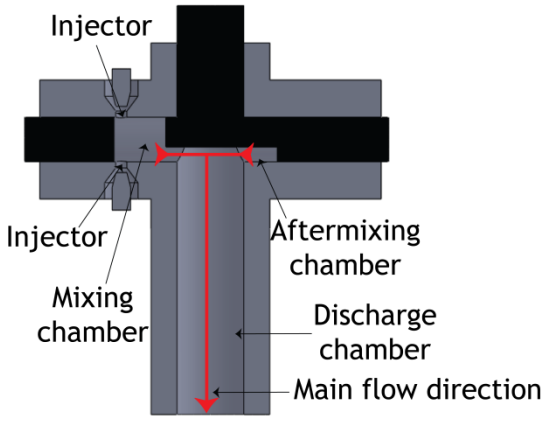

Figure 2-6 Moveable mixing chamber, at a L mixing head (Fiorentini, 1989)

2.1.2 T Mixing Head

The first type of mixing heads have a simple T design of the mixing chamber, where two jets impinge into each other near the top of mixing chamber. This type of mixing head was patented by Keuerleber and Pahl (1972) and had two nozzles, one cleaning piston and one mixing chamber. This was one of the first mixing heads to appear in the market.

This mixing head can make the recirculation of the material between the mixing chamber and the storage tanks, through lateral grooves in the piston that connect the nozzles with the recirculation circuits when the piston is blocking the mixing chamber. This mixing chamber has a simple operation. At the beginning of each shot the cleaning piston is retracted, enabling the reactants to flow into the mixing chamber. At the end of the shot, when the mould is filled, the cleaning piston moves forward flushing the mixing chamber. This can be seen in Figure 2-7, that shows the two main positions of the piston. The injection velocity is controlled through opening or closing of the nozzle located in the injector, done by a screwattached to a spear as shown in Figure 2-7. This design is very common in RIM mixing heads, and some commercial companies still use it.

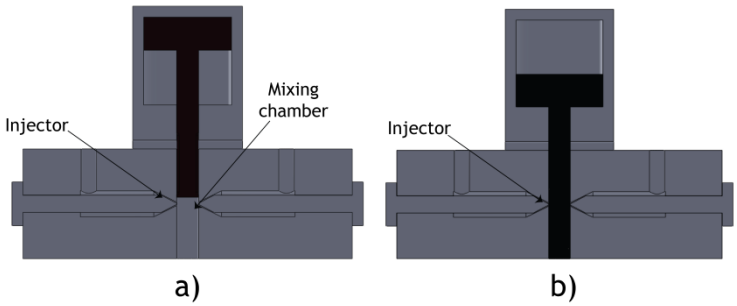

Figure 2-7 T mixing head with two pistons positions: a) injection position b) recirculation position (Keuerleber and Pahl, 1972)

Based on the original design of the T mixing head, some authors/inventors have introduced several inovations. For example, Laurent and Feltan (1978), from Secmer, introduced a mixing head, where the recirculation was done inside the injector. Another interesting aspect from this mixing head is the fact that the injector orifice is controlled by a spring system. The advantage of this mixing head is that the injectors are auto-controlled, which means the work is more auto-mated and less hindered by the need of tunning the machine. Nevertheless, when the material stoichiometry is different from one, the spring system control has to be operated on manual mode and separately. There are other changes proposed to these mixing heads, details can been seen at Schlieckmann (1978), Wingard and Leidal (1978), Leidal (1978), Muhle (1978b), Boden et al. (1983), Schneider (1984b), Scrivo (1986), Stuper (1992), Reisinger (1994) and Decker (1993a).

More recently, Lopes et al. (2005), patented a new mixing concept based on a T mixing head, see Figure 2-8. The main advantage of this new concept is the fact that this mixing head introduces a real-time control of mixing, through the acquisition of differential pressure between the injectors (Lopes et al., 2005). When deviations from the set point associated with better mixing are detected, the system is controlled by changing the

pumps flow rate. This new RIM process eliminates the need for mixing head tuning. The concept proofing of this process is the main goal of this thesis.

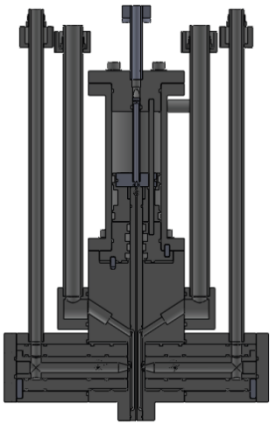

Figure 2-8 RIMCop mixing head (Lopes et al., 2005)

A previous review on mixing head geometries was done by Bolde and Schulte (1994), who detailed some of the industrial mixing heads. In this review two interesting schemes for the raw material recirculation, using valves, were shown. First scheme, is from Hennecke (Bolde and Schulte, 1994), where a piston actuates one slide valve with two positions – recirculation and mixing, as shown in Figure 2-9. The raw material flow rate to the mixing in the chamber was controlled by the position of the slide valve.

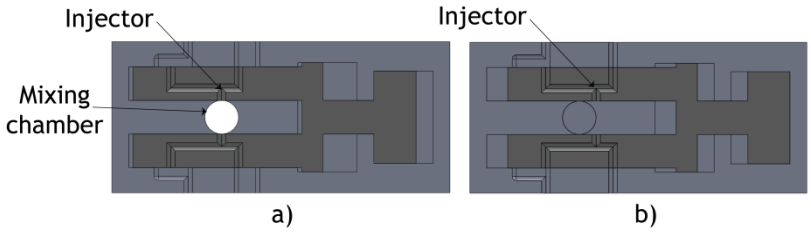

Figure 2-9 Slide valve mixing head: a) mixing position b) recirculation position (Bolde and Schulte, 1994)

Cannon (Bolde and Schulte, 1994) has introduced the second scheme using a valve, where the recirculation was controlled by a rotary valve, see Figure 2-10. In this case, rack and pinions are engage to a cleaning piston, and with moving forward or back, the mixing was controlled, and consequently the reactants recirculation, but this is a more complex scheme.

Another mixing head where the recirculation was controlled through a valve, in this case an external valve, was introduced by Wisbey (1977). In mixing position, the external valve contacts two jets of each reactant with two jets of the other reactant, but when in recirculation mode each of the reactant channels is used for the recirculation (cf. Figure 2-11). The injector size is controlled by a screw in the cylinder of the cleaning piston.

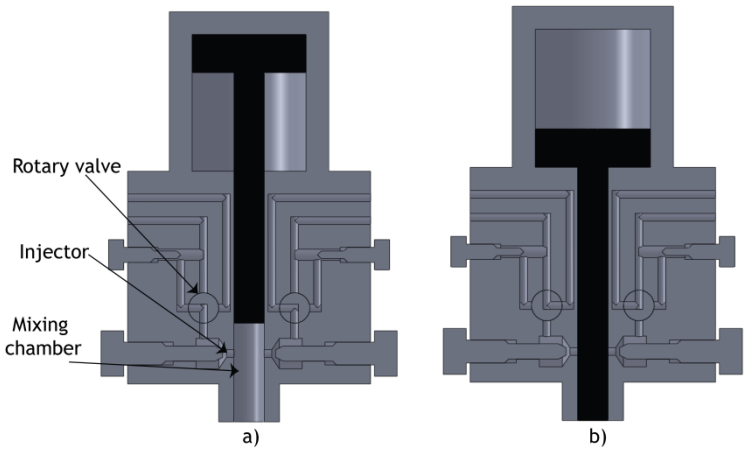

Figure 2-10 Rotary valve mixing head, from Cannon: a) mixing position b) recirculation position (Bolde and Schulte, 1994)

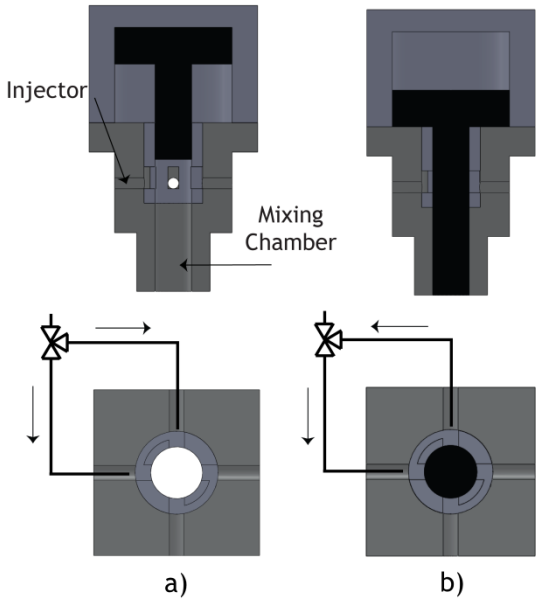

Figure 2-11 Wisbay mix –head: a) mixing position b) recirculation position (Wisbey, 1977)

The previous versions of T mixing heads were based on the original idea of Keuerleber and Pahl (1972), where mixing was done by the jets directly impinging into each other, without any chamber restriction or modification. But, over the years, others have proposed some modifications in order to achieve a proper mixing degree (Ranz, 1986) in a process that up to Lopes et al. (2005) had no means of control and was often hindered by mixing problems.

Some authors proposed a different geometrical position of the injectors. Macosko and McIntyre (1984) suggest the collocation of injectors with an angle of 45^{o} to 60^{o} between injector's axis and central axis of mix chamber, see Figure 2-12. Another feature of this mixing head is that the recirculation grooves has the same axis with the nozzle and has a bypass channel in the cleaning piston. This avoids greater pressure drop and prevent

excessive wear in the piston. The flow rate is possible to control by a lateral screw as shown in Figure 2-13. More recently, Decker (1993b) and Nennecker (1996) also suggest mixing chambers with angled jets.

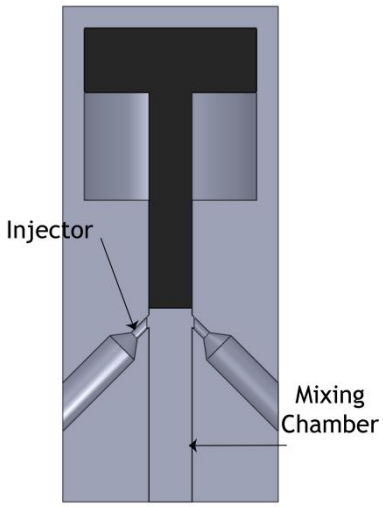

Figure 2-12 Vertically angled mixing head (Macosko and McIntyre, 1984)

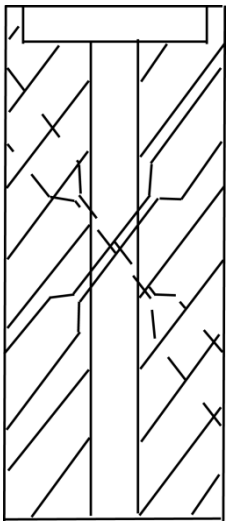

Figure 2-13 Recirculation Grooves (Macosko and McIntyre, 1984)

A horizontally angled mixing head adopts non-concentrical nozzles, but in this case, the impingement plane is perpendicular to the mixing chamber and the injectors have an angle of 100^{o} between them as shown in Figure 2-14 (Sweeney, 1987). This maximizes the offset process of kinetic energy for high viscosity raw materials, without compromise a soft laminar flow at the outlet pipe.

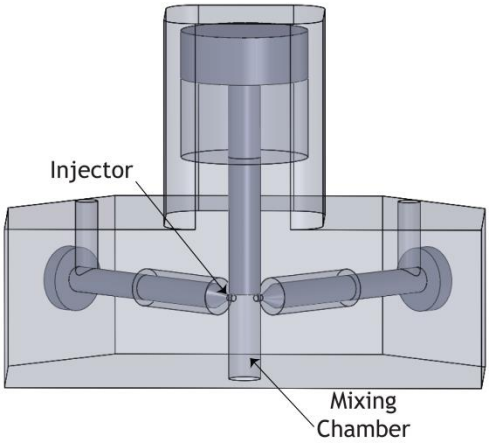

Figure 2-14 Horizontal angled mixing head (Sweeney, 1987)

The main concept on the basis of the angle jets mixing chambers is on one side to create recirculation patterns that could promote mixing even at low Reynolds numbers. However, the main problem this mixing geometries tried to overcome was the lack of control of the opposed jets impingement point, which for small deviations from isokinetic conditions between the jets leads them to impinge too close to one of the nozzles causing material formation inside the said nozzle and clogging (Fonte, 2012). The mixing head proposed by Lopes et al. (2005) solved this issue by monitoring the pressure difference in the injectors.

One idea that has been applied on several mixers is the collocation of turbulence bars in the mixing chamber, which in the case of RIM mixing heads are retractable bars to allow flushing the chamber with the cleaning piston. This idea was patented by Taubenmann (1986) and Wallner (1988). The retractable turbulence bars promote better mixing inside the mixing chamber (cf. Figure 2-15). These pins assure a back pressure near the impingement point, maximizing the mixing efficiency. The work process is very simple, and similar to the one in the Keuerleber and Pahl (1972) mixing head. The only exception is that the retractable turbulence bars are hydraulically actuated, adding one more movement, and weight.

Based on that idea, the Elastogran (Bolde and Schulte, 1994) added a rectangular mixing chamber, where the lower mixing chamber is equipped with a retractable turbulence bar. This configuration produces a division and a backflow, and the retractable turbulence bar will provide an increase of the back pressure. This will raise the mixing intensity at impingement point, providing more turbulence and a better mixing.

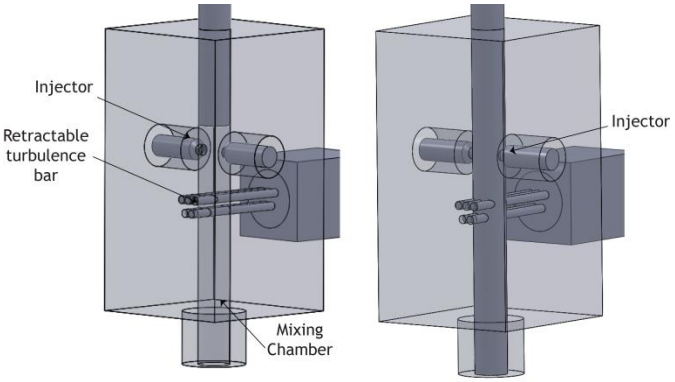

Figure 2-15 Delivery system with retractable turbulence bar: a) mixing position b) recirculation position (Taubenmann, 1986)

Another approach based on T mixing head is to introduce complex chamber movements and geometries in order to produce the necessary turbulence. One example is Schlueter (1984) mixing head, see Figure 2-16, where the nozzles were moveable tubes. The injectors enter in the mixing chamber and the material is injected into the mixing chamber by angled injectors directed toward the top of the mixing chamber. In this configuration, the impingement point is near the top of the mixing chamber. Another key aspect is that the nozzles will squeeze part of the mixing chamber, forcing the mixture to accelerate and originating back pressure that promotes mixing. The work procedure of this mixing chamber is complex, since to start mixing it is needed to move both nozzles in opposite directions. This is done using a hydraulic cylinder. When the mould is filled, mixing is stoped, by first moving back the nozzles, and then moving forward the cleaning piston.

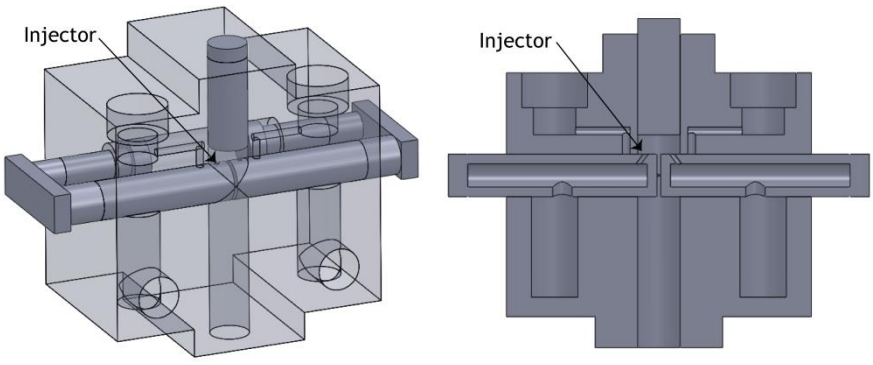

Figure 2-16 Schlueter mixing head in mixing position (Schlueter, 1984)

A new complex mixing head was proposed by Bauer (1985), that considers a pre-chamber for the initial mixing stages. In this hydraulic controlled pre-chamber, the opposed jets impinge, and mixture flows through a complex pattern around the injectors, since the passage to the lower part of mixing chamber is done by sideways. This chamber promotes more efficient mixing for materials that are harder to mix, such as high viscosity materials. This pre-chamber shape is done using two sliding parts (cf. Figure 2-17).

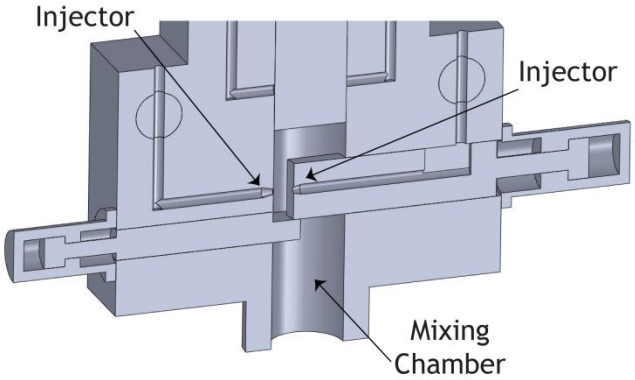

Figure 2-17 Bauer mixing head in mixing position (Bauer, 1985)

A similar mixing head was patented by Toda and Hori (1989), where the mixing chamber has several obstacles, which can be better seen in Figure 2-18. Those obstacles are hydraulically moved. This maximizes the mixing. The main disadvantage of this mixing is the complexity of movements of the mechanical parts. This mixing head also permits the recirculation of materials through a valve, but does not allow a proper acceleration mechanism for the reactants entering the mixing chamber.

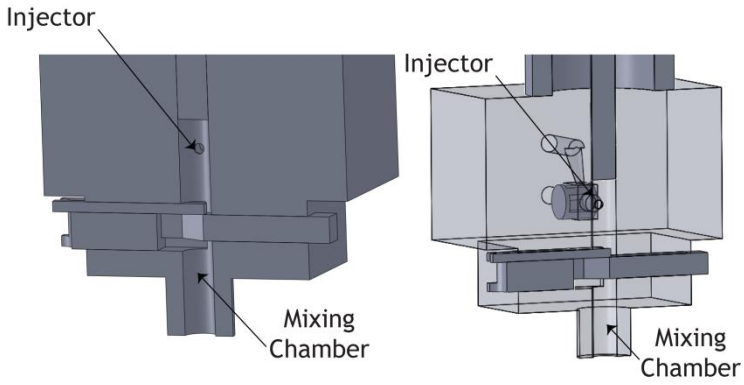

Figure 2-18 Toda and Hori mixing head in mixing position (Toda and Hori, 1989)

2.1.3 Geometric Studies

Some studies have been made on the geometry of the RIM mixing chamber, particularly on the effect of the design parameters of the mixing chamber on mixing. One of the first works was done by Sebastian and Boukobbal (1986), who reviewed previous works and tried to establish one critical parameter that relates the reaction extension, the geometry of mixing-head and flow parameters. Sebastian and Boukobbal (1986) also performed experimental work testing on different parameters that are shown in Table 2-1, and where d era the injector diameter and D the mixing chamber diameter, as shown in Figure 2-19. The main conclusion from this work is that the impact point of the opposed jets, should be as close as possible to the axis of the mixing chamber, avoiding the wall effect.

This effect is important to the mixing dynamics. Other conclusion is that the ratio between the nozzle diameters and mixing chamber is a critical factor, where one of the nozzles should have an equal diameter to the mixing chamber, and the other one is adjustable from momentum ratio balance.

Table 2-1 Geometric parameters from experimental Work done by Sebastian and Boukobbal (1986)

Exp.	d_{pol}[mm]	d_{iso}[mm]	d_{iso}/D	M_r
1	1.270	0.889	0.313	1.18
2	0.899	0.889	0.224	2.42
3	0.711	0.535	0.179	1.36
4	0.635	0.406	0.160	0.99

Wood et al. (1991) studied the flow inside a mixing head, through velocity measurements with Laser Doppler Anenometry (LDA) and numerical analysis. In their work, Wood et al. (1991) proposed different values for the space of the mixing chamber above the jets, the headspace that was studied numerically from Computational Fluid Dynamics (CFD) simulations. Nevertheless the main focus of this work was on influence of the jets Reynolds number in the flow dynamics.

Later, the same team (Johnson et al., 1996), studied the influence of the following geometrical parameters(cf. Figure 2-19):

- Mixing chamber diameter, D – 10 and 21.5mm;
- Ratio between the distance of the top of mixing chamber to the nozzle center and the nozzle diameter, H/d – 0.5; 2.5 and 5.375;
- Nozzle length, N - 1 and 3mm;
- Ratio between mixing chamber diameter and nozzle diameter D/d – 5 and 10.75;
- Ratio between mixing chamber diameter and the distance from center of nozzle to the bottom of mixing chamber, D/H – 6.25 and 10.5;

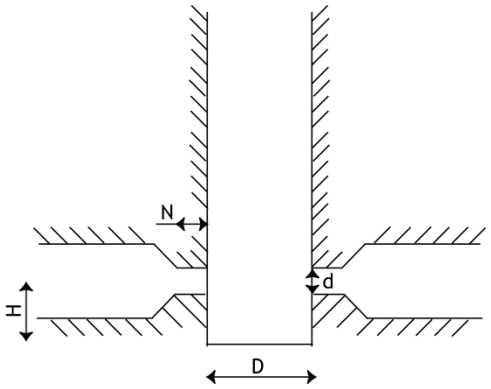

Figure 2-19 Mixing head adopted from Johnson et al. (1996)

One main conclusion of Johnson et al. (1996) is that the mixing region should be as small as possible, in order to form a uniform flow field to improve the mixture. Based on this principle, this studied reveals that the best mixing was for the lowest values of the relations:

- $H/d = 0.5$;
- $N = 1\text{mm}$;
- $D/d = 5$.

Trautmann and Piesche (2001) studied a bigger range of geometrical parameters. One new parameter was the α angle. This is the angle between the nozzle with the perpendicular line to the axis of mixing chamber, as shown in Figure 2-20.

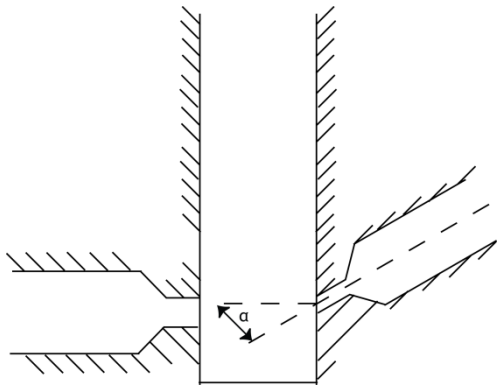

Figure 2-20Mixing head Parameters adopted from Bierdel and Piesche (2001)

Trautmann and Piesche (2001) reported that the geometrical parameters with more influence in mixing quality are the nozzle diameter and mixing chamber diameter. They concluded that reactants with higher viscosity are more difficult to mix.

More recently, Teixeira (2000) proposed a mixing chamber with the dimensions shown in Figure 2-21. Teixeira (2000) studiedy the influence of several flow parameters, through numerical analysis and experimentally with LDA. This work was the first Ph.D. thesis on mixing in RIM at the Laboratory of Separation and Reaction Engineering. From the work of Teixeira (2000) it was validated numerically and from LDA data a 2D model for the study of mixing in the RIM mixing chamber (Teixeira et al., 2005).

A second thesis on RIM capitalizing on the findings of Teixeira (2000) from Santos (2003) used the 2D model to study the impact of mixing chamber geometry on the flow dynamics. The flow dynamics is key for mixing in RIM as shown by Santos et al. (2005) . Santos et al. (2005) and Santos et al. (2010) showed that the injectors location has a critical role om mixing in RIM. Four different positions were proposed for the injectors: at the top of the mixing chamber, 2.5, 5 and 7.5mm. The injectors placed at the top of the chamber

seriously compromise mixing, due to the fact that the top wall hinders the jets auto-oscillation, which is an important mixing mechanism in RIM (Santos et al., 2008; Santos et al., 2005). For the geometries with the injectors placed at 2.5, 5 and $7.5\mathrm{mm}$ the jets impingement point engages on an oscillatory motion that is associated with intense dynamics of mixing between the two fluids issuing into the mixing chamber.

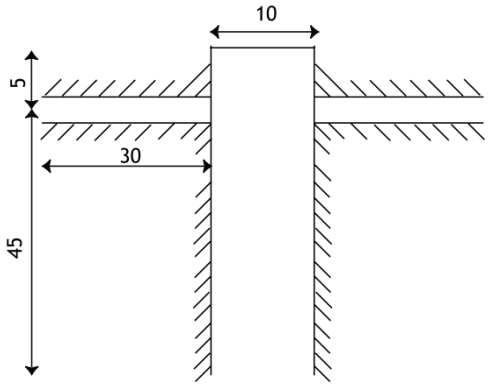

Figure 2-21 Mixing head used adopted from Teixeira (2000)

Santos et al. (2002) also proposed a relation for the injectors diameter based on results from the 2D CFD model of the mixing chamber. This model proposed a change on the opposed injectors diameter that balanced the momentum ratio of the jets ensuring a high dynamics of mixing when the flow rates in each jet were different. This model was later extended by Fonte et al. (2012) , another PhD thesis made at the LSRE. Fonte et al. (2012) found a more complete relation for the design of the opposed injectors that accounts for the impact of viscosity differences in addition to the balance of the jets kinetic energies.

2.2 Mixing Analysis Method

In RIM, mixing can be done by stirring or using a static mixer with obstacles, such as the Kenics® static mixer, or by impingement of two opposed monomer streams against each other. On the opposed jets mixing, the kinetic energy plays a key role, since there is a shock between the jets. Several authors (Fruzzetti et al., 1977; Lawler, 1976; Manas-Zloczower and Macosko, 1988; Vespoli, 1984) tried to understand the mixing mechanism associated to this type of mixer, in order to optimize the mixing quality. It was observed that when the temperature increases, mixing also increases due to a decrease of the viscosity. Also when the flowrate increases, the final quality of the parts is better due to the increase of kinetic energy dissipation in the mixing chamber. Both the viscosity decrease and flow rate increase go on the same direction of increasing the operation Reynolds number, which is a critical operation parameter in RIM machines.

Although the kinetic energy plays a key role, several studies (Baldyga and Bourne, 1983; Nguyen and Suh, 1985; Tucker and Suh, 1980b) show that the impingement between two or more jets is not sufficient to mix the fluid of the jets, and only above a critical Reynolds number, Re_{cr}, it is possible to get striation thickening at a rate that enables small enough scales for the chemical and molecular diffusion to promote the complete mixing of the monomers at the molecular level (Ranz, 1979). The Reynolds number is a ratio between inertial and viscous forces, and for RIM mixing was defined by by Malguernera and Suh (1977) as

$$Re = \frac{\rho \upsilon_{inj} d_{inj}}{\mu} \qquad 2.1$$

where ρ is the density, υ_{inj} is the injector velocity, d_{inj} is the injector diameter and μ the viscosity.

Ranz (1979) suggested that the molecular interface between the monomers can be instable during the mixing due the density changes. Nguyen and Suh (1985) studied a Re range until 4000, to create an interpenetrating network between the polymers. Although, for these high Re values, it was observed striations with only a $30\mu m$, far from the $1\mu m$ that Macosko (1989) suggested as necessary for the molecular diffusion to enable the polymerization reaction. Several authors (Fields et al., 1986; Machuga et al., 1988; Wickert and Macosko, 1987) observed that the activity at the interface zone between the jets can lead to dilution of the steep transitions between laminas formed downstream the jets impingement zone, leading to better polymerization.

The model proposed by Macosko (1989) suggests that the segregation scale is reduced from the injectors diameter until a scale of the order of $100\mu m$ through the kinetic energy dissipation in the impingement mixing. This reduction doesn't have a big dependency on the mixing chamber design. Post scale reduction after the jets impingement region relies on several shearing mechanics on the reacting mixture while it flows through the moulds channels and moulds cavity, and also due to chemical and physical effects at interface between the monomers. The existent pressure in the interface, forces one of the monomers to penetrate in the other, in a tubular form. The size and the penetration of the tubes depend on the reaction velocity and on the monomers properties. Figure 2-22 shows an interfacial phenomenon, molecular contact and diffusion between two reacting monomers with a tubular spontaneous growth, after the contact of the reactants, in this case amine terminated polypropylene oxide with uretonemine modified MID at 25^0C. Figure

2-22 shows an interfacial phenomena molecular contact and diffusion, finishing the reaction.

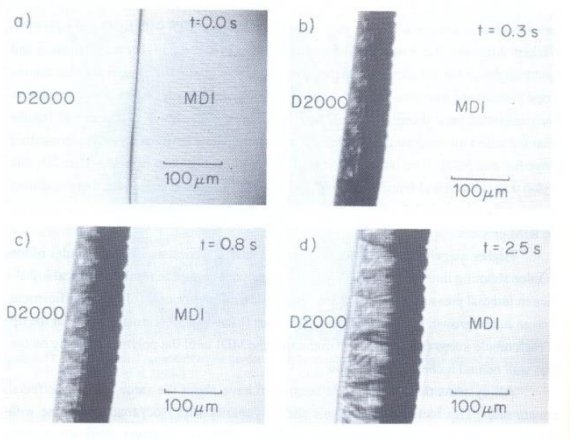

Figure 2-22- Spontaneous growth between the two interfaces of mixing phases (Macosko, 1989)

To study the mixing mechanics, introduced before, several techniques could be used. Besides the few works done in liquid-liquid mixing (Santos, 2003),there are several approaches that could be used, which were classified by Santos (2003) as follows:

- Visualization experiments;
- Hydrodynamics studies;
- Modelling and numeric simulations;
- Mixing and Reaction Studies.

The visualization experiments show what is happening inside the mixing chamber, using the imaging of flow field. One of the simplest techniques consists in adding a color tracer to one of the monomers, and capturing images of both fluids interaction and patterns (Bierdel and Piesche, 2001; Lee et al., 1980; Tucker and Suh, 1980b). A similar but more elaborated method uses a dye that fades with mixing to get a clear view of the mixing patterns (Sandell et al., 1985). Using the particles' paths for seeding the flow it is also possible to visualize the mixing patterns (Wood et al., 1991). More advanced techniques, such as the Laser Induced Fluorescence (LIF), enable the visualization of mixing patterns in planes inside the mixing chamber, highlighting the pattern promoted by the jets interaction, where one of the jets contain a fluorescent tracer (Fonte, 2012; Johnson et al., 1996; Unger et al., 1998).

For a study about hydrodynamic variables, the visualization studies lack on the actual quantification of the flow variables. This quantification is important to assess the effect of several parameters, as for example, the *Reynolds number*, on the hydrodynamics and thus mixing in the mixing chamber. The following techniques have been applied to the

characterization of the flow field in the RIM mixing chamber: LDA (Johnson, 2000a; Johnson and Wood, 2000; Johnson et al., 1996; Santos, 2003; Santos et al., 2002; Teixeira, 2000; Teixeira et al., 1998; Teixeira et al., 2005; Wood et al., 1991), Particle Tracking Velocimetry (PTV) (Zhao and Brodkey, 1998a, b) and PIV (Santos, 2003; Santos et al., 2008; Santos et al., 2002; Unger et al., 1998).

Another useful tool is modelling and numeric simulation, that allows a deeper insight of the mixing mechanism, since all the hydrodynamics variables are known at every instant and point in the physical domain. The first studies on modelling and numeric simulations in RIM mixing chambers are from the late seventies and early eighties. The computational resources at that time, did not allow a simulation of the flow field. Due to this limitation, the first modelling approaches were based on mixing models to calculate the striation thickness (Lee et al., 1980; Tucker and Suh, 1980b) and a lamellar model applied to an impingement reaction (Kusch et al., 1989). CFD studies have been performed from the nineties for steady (Unger et al., 1998; Zhao and Brodkey, 1998b) and unsteady flow regimes (Bierdel and Piesche, 2001; Erkoc et al., 2007; Fonte et al., 2011; Fonte et al., 2010; Johnson, 2000a, b; Li et al., 2007; Santos, 2003; Santos et al., 2009; Santos et al., 2002; Santos et al., 2005; Teixeira et al., 1998; Wood et al., 1991).

The last group of techniques to assess the RIM process are the Mixing and Reaction Studies, where several techniques can be used, such as tracer studies, Adiabatic temperature rise, physical characteristics of the final polymer and product distributions from test reactions. Although these techniques are indirect, they enable the study of the industrial RIM machines mixing chambers.

The aim of this work, is the study of industrial mixing chambers. So, the following sections will review the previous work using these techniques.

2.2.1 Mixing and Reaction Studies

2.2.1.1 Product Distribution from Test Reactions

Test reactions are reactions having consecutive competitive reaction steps, where the final product distribution depends on micromixing. The test reaction by Bourne (1982) was applied to a mixing chamber by Kusch et al. (1989). It was observed that the mixing efficiency increases until $Re = 300$ and for larger Reynolds numbers there is no observable increase on mixing efficiency. For the range of Reynolds numbers between 100 and 200, the mixing efficiency increased very steeply, and above this range there was a only slight increase up to $Re = 300$. The experimental data of Kusch et al. (1989) were affected by

large standard deviations that could be caused by the use of water as working fluid, which makes the testing flow rates very low and hinders the basic mechanism of mixing in T mixing heads, the impingement of two high speed jets. Using a working fluid with a viscosity of $20\text{mPa}\cdot\text{s}$, Nunes (2007) identified a transition regime between $100 < Re < 125$ where the flow field passes from segregated to mixing state, identifying a narrow range for the critical Reynolds number, Re_{cr}, which operated ranges for industrial machines should be above this value.

2.2.1.2 Tracer Studies

One of the simplest ways, and also one of the first methods used to characterize mixing in a reactor, is by means of a passive a tracer (Danckwerts, 1952). Malguernera and Suh (1977) applied the method to a mixing chamber and made a dimensional analysis of what parameters could influence the mixing mechanism. It was used glycerin as the working fluid and an acetic acid solution as tracer in one of the streams. At outlet, the concentration deviation was determined. This work defined for the first time the jets Reynolds number as a critical parameter for the operation in a RIM mixing chamber. It was pointed a critical value of 50 for Re, above which the advective mixing occurs associated to a dramatic change in flow and mixing mechanisms over a short range of Re values. It was observed that at a range between $400 < Re < 500$, the quality of mixing remains the same. Several important conclusions were achieved:

- The injectors length has not a measurable effect in mixing quality;
- The mixing chamber diameter has no influence in mixing quality, however the impact volume has some operational effects, since bigger mixing chamber can have more air entrapment and smaller chambers require a more tight control of the flow feeding;
- The distance to the top, don't have any significant impact in mixing quality.

Another critical parameter, momentum ratio between the jets, was defined in this work and is expressed by equation

$$M_r = \frac{\rho_1 \upsilon_{inj1}^2 d_1^2}{\rho_2 \upsilon_{inj2}^2 d_2^2} \qquad 2.2$$

where the indices inj refers to injection, the 1 and 2 refers to each jet.

Tucker and Suh (1980a) observed that the spatial variance of concentration decreases with the Re increase. Also the momentum ratio was studied for a constant Re of 170. It was

observed that until a $M_r = 2.5$ the mixing efficiency did not change with the momentum ration, a result in opposition with the findings of Malguernera and Suh (1977).

2.2.1.3 Physical Characteristics of the Final Polymer

One way to assess and quantify the mixing degree is analyzing the physical characteristics of the final polymer (Ranz, 1979). Kolodziej et al. (1982) measured the striation thickness in final polymer, adding a carbon black tracer to one of the streams of monomer. This technique was used with polymerization reactions less sensitive to the adiabatic temperature rise. It was studied a Re range between 80 and 450. It was observed that the striation thickness decreases until $Re = 200$ and after the thickness remains constant. This decrease is a clear indication of an increase on the dynamics of mixing with the Reynolds number up to a critical value. Another approach used by Kolodziej et al. (1986) was the quantification of the molecular weight distribution of the formed polymer, produced over a Re range of 80 to 210. In this work, it was observed that for high Re, the molecular weight distribution is also higher. This is associated with better mixing that enables a better contacting between the monomers promoting larger grows of the polymer macromolecule.

Nguyen and Suh (1985) studied the size of gaps (or holes) produced in the final material by increasing the processing Re, in a range between 311 to 4534. A less common geometry for industrial equipment was used, since the mixing chamber had three nozzles with a 120° apart each other. It was used Isocyanate, Polyol and a third jet with an inert material. After the injection of the jets streams, the inert material was removed to measure the gaps in final polymer. It was observed that the gaps size decrease was related to Re.

2.2.1.4 Adiabatic Temperature Rise

The adiabatic temperature rise is used to quantify the mixing in experiments with exothermic reaction, i.e. the more intense the mixing the faster the reaction proceeds and so the higher will raise the adiabatic temperature. The first approach of this method to a mixing chamber was performed by Ritcher and Macosko (1978), who measured the heat released by the reaction. It was observed that there is an increase in reaction velocity and temperature until a critical Re value. Ranz (1979) and Chella and Ottino (1983) related that temperature increase with the formation of a lamellar structure of both monomers. The lamellar structure is formed due to the mixing patterns in the RIM machine mixing chamber (Fonte et al., 2011). A thinner striation reduces the time needed by diffusion to contact the monomers molecules, and is thus related with better micromixing. Although, if

the strias are thicker, the monomers get stuck between layers of reacted polymers, originating an unbalanced stoichiometry and, consequently, decreasing the reaction velocity and temperature. In addition, clumps of unreacted monomers originate wet spots which are a major cause for part rejection in RIM.

Lee et al. (1980) used the adiabatic temperature rise to study the influence of injectors diameter ratio, alignment and direction of a mixing chamber on mixing quality. It was found that above a critical Re of 200, the geometric parameters did not affect the quantity of heat released. Below this value, significant changes occurred in a Re range between 100 and 160. This study was of particular practical interest, since it was performed with a mixing chamber design common in industrial equipment. Later, Harris et al. (1992), observed the same critical Re with a similar technique.

The momentum ratio between the jets was studied by Sebastian and Boukobbal (1986), using different nozzles diameters but keeping the flow rate ratio according to the reaction stoichiometry. It was observed that the maximum adiabatic temperature rise was for a $M_r = 1$ and a $Re_{cr} = 200$.

2.3 Numerical Simulation of RIM Process

The first studies in modeling the RIM process were done by Broyer and Macosko (1976) and Lee and Macosko (1980), where heat transfer and curing were analysed considering that both stages are not linked to the filling's flow phase.

Later, several authors used a 1½D approximation, considering the fountain flow (Castro and Macosko, 1982; Domine and Gogos, 1980; Kamal and Ryan, 1987; Lack and Silebi, 1988; Lekakou and Richardson, 1986; Manas-Zloczower et al., 1987). Although these works did not study the key aspects of the process, e.g. large pressure variation during mould filling, the models proposed found some applications, namely on the work of Castro and Macosko (1982) that precisely defined several dimensionless quantities with an important role in filling and curing, and it was used as a reference for later works. Castro and Macosko (1982) obtained numerical results with the finite difference method and compared those with experimental dada. A good prediction of pressure rise, extent of reaction and temperature profiles in a rectangular thin-mold, during the filling and curing, were obtained. It was also reported that the flow front should not be neglected otherwise the pressure rise would be poorly predicted.

Due to its importance, the fountain flow was the study field of several authors. One of the proposed models for fountain flow by Garcia et al. (1991), used a 2½D model applied to finite element method (FEM) and was applied over a thermo-activate resin and used to study the conversion degree. Later, Perrett et al. (1993) proposed the application of Patankar (1980) SIMPLE model to the RIM. Using a Petrov-Galerkin FEM, Anturkar (1994) obtained identical results from experiments and simulations. Using a 2½D FEM model, Haagh et al. (1996), studied experimental and numerically, the filling of an industrial and complex piece, produced in a thermoset resin. Good agreement between experimental and numerical results was found, however, major problems related with material characterization were observed, since the viscosity rise plays a major role in the flow during the part filling. Further improvements should be done concerning a proper definition of the initial and boundary conditions in the RIM moulds.

Using a Control Volume Finite Element Method (CVFEM), Young (1994) sucessfull developed a model to simulate complex 3D geometries, modelling the filling and curing. More recently, Mitani and Hamada (2003) also used a CVFEM, coupled with Hele-Shaw , or Stokes formulation for the flow field of tri-dimensional cases, and Volume of Fluid (VOF) for tracking the flow front. Their results agreed very closely with experimental data, particularly for the Stokes formulation, in predicting the edge effect, in which the flow slows down at the edge, resulting in a suitable model to predict the pouring position, volume of the mixture, and the air vent location. Also Foudrinier et al. (2008) used a 3D FEM, although there was some discrepancy in temperature profile when compared to the experimental data. This work was incorporated in commercial software denominated Rem3D.

The previous work was done, initially, using a finite difference method, and afterwards using FEM, or hybrid methods between both. More recently, some works have been using Finite Volume method that is widely used by the fluid mechanics community.

Using FVM, Seo et al. (2003) successful developed an algorithm based on SIMPLE method for bi-dimensional problems, neglecting the curing. In the same model was incorporated experimental data, as reaction kinetics, foam rheology and bubble growth, and was applied to 3D cases(Seo and Youn, 2005).

With the development of powerful commercial software related to the fluid mechanics simulation, a few works, using it and applied to the RIM, have been done. Using Fluent, Michalek and Kowaleski (2003) study the filling of a cavity with VOF, as shown in Figure 2-23. The numerical results were compared with experimental data obtained, using a PIV

and Particle Image Thermometry (PIT). Although in this work, the results showed good agreement between numerical and experimental data for the tracking of a flow front, some discrepancies were noticed in the flow field. Also using Fluent and VOF, Sekula et al. (2003), developed a new approach for 3D simulation of reactive process, modeling the fluid dynamics and heat transfer during the filling and curing. The model was applied to a simple case and yields a good agreement with experimental data. Also an industrial case was successfully studied. The results obtained are promising, since they provide an insight of physical phenomena inside the mould, and could include engineering tools for virtual process trials, saving time and costs.

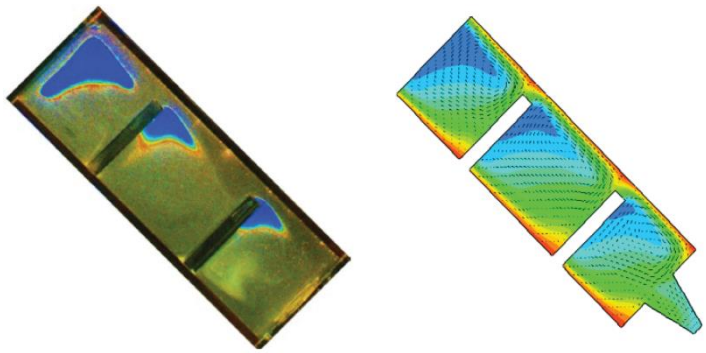

Figure 2-23 Cavity Filling from Michalek and Kowaleski (2003): a) Temperature Profile from PIT b) Temperature Profile from Fluent

Recently, Igreja (2007) used Ansys CFX and the homogeneous and in-homogeneous model (an extension of multiphasic Euler-Euler Model for free surface), and applied to the RIM, as shown in Figure 2-24. Igreja (2007) used reference work of Castro and Macosko (1982), and show the ability of CFX to simulate with accuracy the complexity of the process mould filling and polymer curing in a 3D geometry. The main disadvantage of the used model is the need for small meshes, resulting in high computational times.

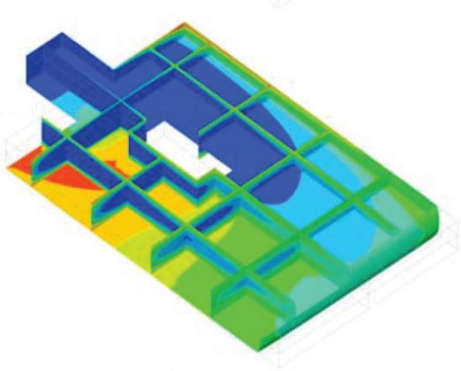

Figure 2-24 – Cure degree (Igreja 2007)

2.4 Project Rules for RIM's Moulds

The final stages of the RIM process are the filling of a cavity inside a tool denominated mould and the curing of the reacting mixture of monomers in said cavity. The moulds project should be carefully made, in order to assure a good quality of final parts, with few flaws and the best homogeneity of the part materials. To achieve these goals, the RIM Mould project, should take into consideration several aspects, mainly the following ones (Bartolo and Mateus, 2003):

- Be able to cope with the injection pressure;
- High superficial quality;
- High superficial resistance;
- High abrasive resistance;
- Allow a good ventilation;
- Assure the proper material flow inside the mould cavity;
- Had an adequate injection and extraction system;
- Characterize the temperature distribution;
- Where is the parting line (the parting line is the plane that divides the mould into two parts, cavity and core) location.

Nevertheless, there are only few scientific studies on moulds for RIM. The most important reference works are from Müller et al. (1985a); Müller et al. (1985b) and Silva (2007). Müller et al. (1985a); Müller et al. (1985b) analyzed the relation between mixing and injection and their effect on the quality of the part. Two causes were identified for bad part quality: air bubbles formation and entrapment. The bubbles formation can appear due to unfavorable flow somewhere between the tanks and the mould. The bubbles entrapment is due to phenomena on the flow front interphase with air or the wrong positioning or lack of gas escape points (Müller et al., 1985a).

During the injection and in the mixing head, the raw materials flow into a space occupied by air, and the bubbles can be incorporated in the reacting mixing by the complex flow patterns inside the mixing head (Müller et al., 1985a). This bubble incorporation, when it occurs in foam will create defects that can be neglected. However, if the part is made of a rigid material, the bubbles will cause empty zones, affecting quality and leading to part rejection. These empty zones can, also, be due to the existence of static bubbles (Müller et al., 1985a).

To avoid the air entrapment problems, between the cavity and the mixing head the flow, should be decelerated making it as laminar as possible (Müller et al., 1985a). Furthermore,

unequal sections and large variations of thickness in the mould should be avoided. Also economic considerations should be present on the mould design, as so the geometries should be simple and easy to fabricate (Müller et al., 1985a). Placing an flow restriction before the mixing chamber will increase the velocity, and consequently the mixing efficiency (Müller et al., 1985a). However, downwards, the flow must decelerate to ensure the ideal conditions to fill the cavity, i.e., a laminar flow. For this purpose, it is common to employ a local restriction, at the outlet of the mixing head or in the mould entry, being the last one largely used (Müller et al., 1985a). Nevertheless, local restrictions obeyed to specific rules design, since the simple fact of restricting the flow can promote flow separation downstream and upstream the restriction, and that can lead to the entrapment of air bubbles, see Figure 2-25.

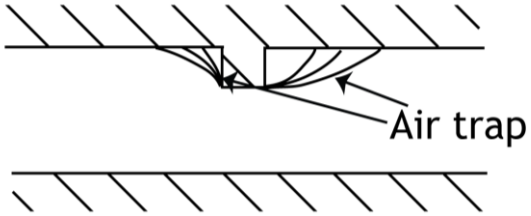

Figure 2-25 – Flow around a restriction, where the streamlines represent the flow along time (Müller et al., 1985a)

Figure 2-25 shows that downward the restriction, the gas entrapment will decrease, however some gas remains in that zone. If no vent is placed around, the gas accumulated will be incorporated in the materials, which can originate part defects (Müller et al., 1985a).

Another problem related with the restrictions, is that the flow will accelerate until a limit where it will be difficult to decrease the velocity to the desirable flow to fill the cavity. So, different approaches must be used to decelerate the flow. The common procedure is to use a fir-tree mixer or after-mixer, as shown in Figure 2-26 (Müller et al., 1985a). The aftermixer is placed between the mixing-head outlet and gate, in the parting line plane.

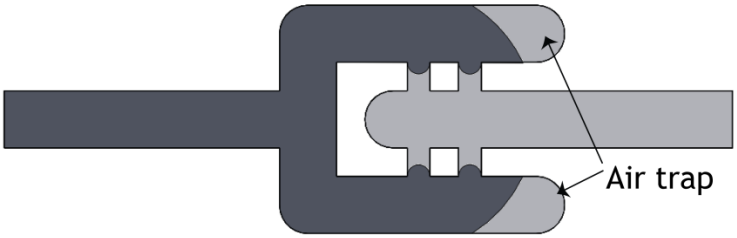

Figure 2-26 Flow inside an aftermixer (Müller et al., 1985a)

Several configurations for the after-mixer can be used, as shown in Figure 2-27. However, these kind of elements have big stagnation zones, as shown in Figure 2-26, which is critical for RIM due to air entrapment, besides the obvious material losses (Müller et al., 1985a).

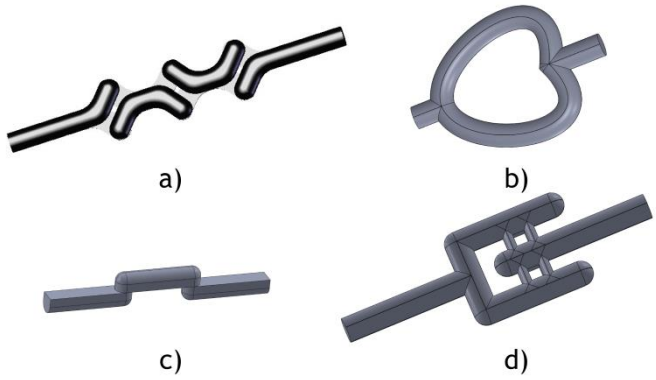

Figure 2-27 Aftermixers: a) peanut b) heart c) dipper and d) harp

Downstream the after-mixers the material is injected into the mould cavity through a gate. The gate design should be careful, since the flow cannot enter freely, and must produce a certain amount of controlled resistance on the flow to the cavity, using a progressive cross section reduction (Silva, 2007). The gate should be located in a lower zone of the mold, and should avoid long flows, filling against a wall. Preferably the gate should be located close to the parting line, in a less visible local of the part and close to complex details. If the part has ribs, the gate should be located parallel to them. The gate thickness should be approximately close to the part thickness (Silva, 2007). The thickness difference between part and gate is critical, and should not be larger than $2.5\times10^{-2}\,\mathrm{mm}$, otherwise the flow transition can promote the flow separation and air entrapment, compromising the quality of the parts (Silva, 2007).

The simplest gate is the direct gate, shown in Figure 2-28, that consists in fitting the mixing head into the part face (Oertel, 1989). The advantages of the direct gate are the minimal material loss and constant cross section (Müller et al., 1985a). However, for thicker parts, there is a higher probability that the flow front creates some vortices and entraps air bubbles. Beside, since the mixing head is directly fitted to the part, this configuration does not allow for any after-mixer system, the reacting mixture issuing from the mixing head should be as laminar as possible in order that the part quality is not hindered (Müller et al., 1985a).

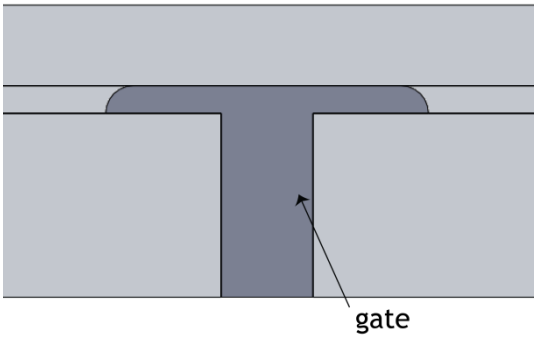

Figure 2-28 Direct gate

According to Müller et al. (1985b) the film gate is also common in RIM, and can be designed in two different ways: fan gate and sprue gate. These types of gate geometries, aim to convert the circular flow issuing from the mixing head, into a rectangular flow, with constant cross-section, maintaining a constant flow rate.

Regarding the fan gates, see Figure 2-29, the gate design consists in a circular part and ends in a rectangular cross-section, having a $90°$ bend in the end of the gate. The rectangular width should be similar to the part width. One of the advantages of this gate is that it maintains a constant flow velocity entering in the cavity. One disadvantage of this gate is the fact that it cannot be used in long moulds, since a maximum angle of $20°$ for the gate expansion should be set to prevent discontinuities in the flow and vortices formation (Müller et al., 1985a). For processing an elastomeric material, the gate thickness should be close to the gate thickness, with maximum velocity values of $8 \mathrm{ms}^{-1}$ as recommended by Silva (2007).

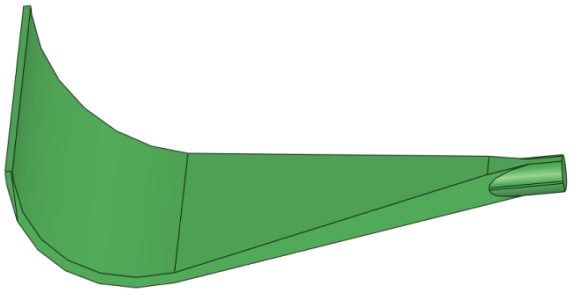

Figure 2-29 Fan gate

Müller et al. (1985b) proposed a fan gate, composed by an elliptical manifold and a split similar to the original fan gate, shown in Figure 2-30. This gate injects the filling material across all the part width. The Müller et al. (1985b) version is designed to maintain a constant pressure along the manifold. The “island” position (Figure 2-30), is defined in the flow direction and regarding to the end of the gate according to

$$y = \frac{h^3}{3\pi R_0^4}\left(L_0^2 - l^2\right) \qquad 2.3$$

where h is the rectangular cross-section thickness, R_0 is the initial radius, L_0 is the part width and l is the position perpendicular to the flow direction.

The Müller et al. (1985b) version of the gate has a more homogenous flow distribution over the all width, promoting a simultaneous filling with an uniform flow velocity profile and avoiding the air entrapment in the cavity. The bigger disadvantage is the fact that this gate is difficult to fabricate, in addition it causes large waste of material (Müller et al., 1985b).

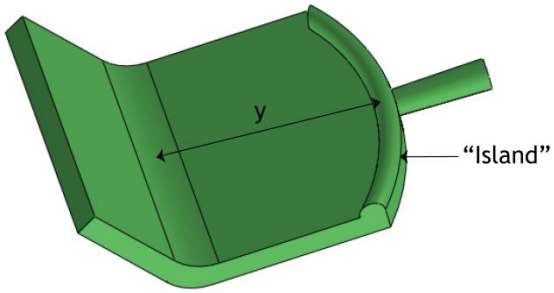

Figure 2-30 IKV version of fan gate

The sprue gates are composed by a manifold, parallel to the cavity, followed by a slip, as shown by Figure 2-31. The sprue gate can be designed in two distinct forms, one where the material inlet is in the flow direction, see Figure 2-31a, and another perpendicular to the flow direction, see Figure 2-31b (Müller et al., 1985b). From the two versions, the less critical is with the perpendicular inlet, since it does not promote the flow separation. However, the perpendicular inlet can cause some vorticity and air entrapment (Müller et al., 1985b). Regarding the flow direction inlet gate, the flow entries are split in two zones, as shown in Figure 2-31a, permitting air entrapment into the flow and vorticity that decreases the part quality (Müller et al., 1985b).

Another gate design used in RIM is the dam. It is very similar to the film gates, with a manifold and a triangular configuration, as shown in Figure 2-32. In this gate, the manifold divides the flow into two streams distributed uniformly through the slit. To guarantee a laminar flow throughout the whole cavity, the inlet velocity in the gate should be limited to 1.5ms^{-1} (Silva, 2007).

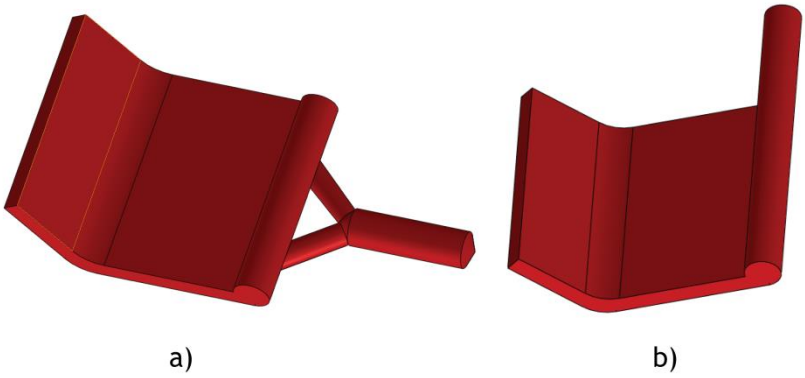

Figure 2-31 Sprue gate with a) frontal inlet b) lateral inlet

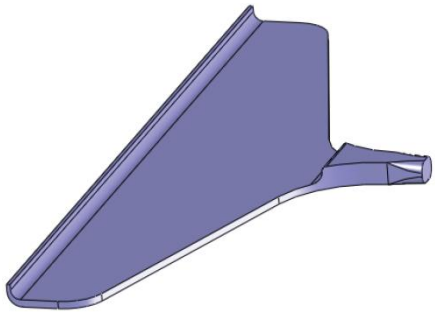

Figure 2-32 Dam gate

As far as the flow inside the mould cavity is regarded, it is important to know the filling pattern inside, since this is a critical step of the RIM cycle. The identification of the critical zones for fillling is an added value for the mould design concerning the gate position, part thickness and venting elements or even the correction of the initial project in earlier project development phases (Knipp, 1998). Careful attention should be endorsed to the flow direction inside the cavity, since it can left visual marks as sink or meld lines that can also compromise the mechanical properties on that zones (Silva, 2007).

Also the parting line must be careful selected. The parting line must be located in a zone where the material losses are minimal or null (Silva, 2007), and with an easy extraction without the need for complex movements or with negative flow regions in the moulds (negative parts are zones where, a priori, it is impossible to extract).

The air vents should be placed in the highest zone of the mould cavity (Silva, 2007), and preferably in the parting line (Knipp, 1998). For low density foams, due to the low viscosity the fluid can fill venting zones with a minimal size of 10^{-1}mm (Knipp, 1998). In literature the suggestions for venting zones are with rectangular cross section with 25mm length and and $2.5\times10^{-1}\text{mm}$ thickness, at an adequate number to promote the part filling without any flaws, and with a distance between vents from 76 to 101mm (Silva, 2007).

Concerning the integral skin, the venting zones are composed by vent orifices connected to an exterior cavity, as shown in Figure 2-33. The venting orifices are suggested to have 10mm length and $5\times10^{-2}\text{mm}$ thickness, and the cavity has 8mm width and 4mm depth.

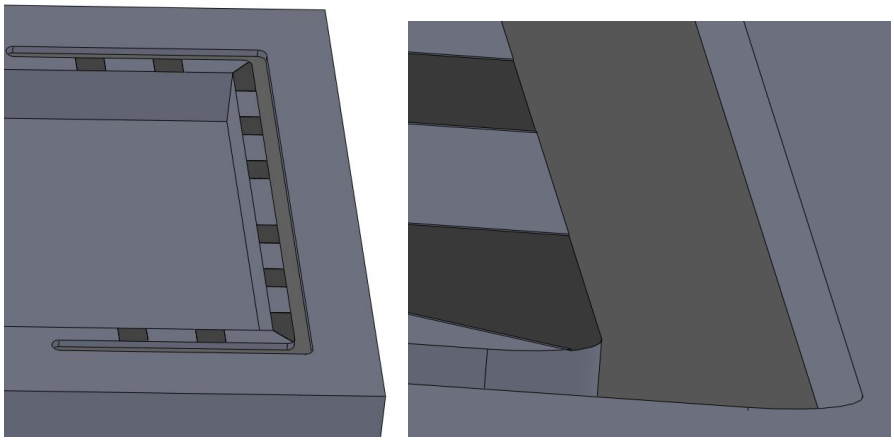

Figure 2-33 Air or gas venting – at black the venting holes, and at grey the cavity

Similarly to TIM, the RIM process can be injected into multiple cavities, allowing a flexible capacity of production (Silva, 2007). When injecting multiple cavities, the material should flow and fill the different parts simultaneously. This is only achieved when a balanced project between the multiple cavities is done. One of the simplest ways for a balanced project, is to have different cross sections on flow distributors, proportional to the ratio between the cavity volume and total injected volume (Silva, 2007). For structural foams, the balanced project is more difficult to design, since the amount of material injected into the mould is small when compared to the volume of the mould cavity. Further, the foam expansion will distribute and fill the material over the different cavities. For the distribution of material between the cavities, the material must be divided and is distributed by flow distributors, as shown in Figure 2-34. To avoid any disturbance in the flow and enable a smooth flow separation, the flow distributors should be in "Y", as shown in Figure 2-34a, and the design shown in Figure 2-34b should be avoided (Silva, 2007).

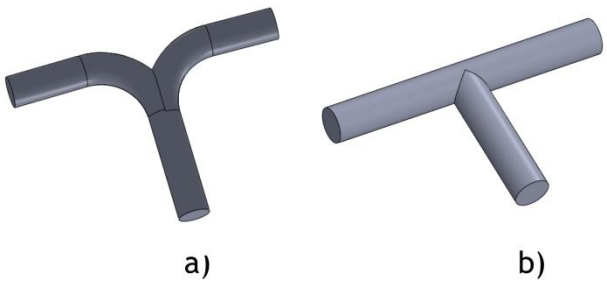

Figure 2-34 Flow distributor for RIM cavities: a) correct design b) incorrect design

Another important system that can influence the part quality is the cooling system. Since during the curing process heat is released from the reaction, it is important to maintain a constant temperature over the part, to avoid the occurrence of temperature gradients. The gradients will affect a uniform cure process and can affect the final mechanical properties. Heating channels should be placed in such a way that the part surface has a uniform temperature, as shown in Figure 2-35 (BayerCorporation, 2008). Also, the heating channels project must be balanced (Silva, 2007). From Figure 2-35, it is possible to observe a balanced (Figure 2-35a) and unbalanced (Figure 2-35b) heating system project.

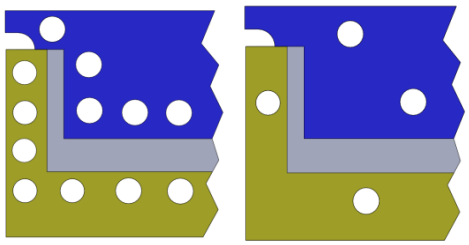

Figure 2-35 Heating channels: a) thermal balanced b) thermal unbalanced

Some dimensions are suggested by BayerCorporation (2008) for the channels size and for the distance between the different channels, and are shown in Figure 2-36 and Table 2-2.

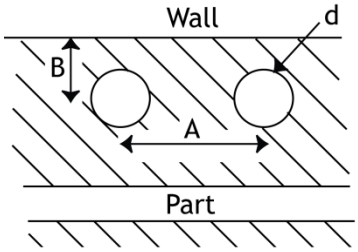

Figure 2-36 Main dimensions of the heating channels

Table 2-2 heating system dimensions, regarding Figure 2-36

$d[\mathrm{mm}]$	9.5 to 12.5
$B[\mathrm{mm}]$	19
$A[\mathrm{mm}]$	50

The cooling system configurations should enable higher heat exchange rates between the refrigerant flow and the filling material (Silva, 2007). Two simple configurations can be employed: manifold (see Figure 2-37a) and single pass (see Figure 2-37b). heating circuits similar to manifold configuration are not advisable, since in the end of the circuit the fluid is already hot and this hinders the heating of the material in those regions (Silva, 2007). A careful choice of refrigerant fluid must be done. The most common refrigerant fluid is water (Silva, 2007).

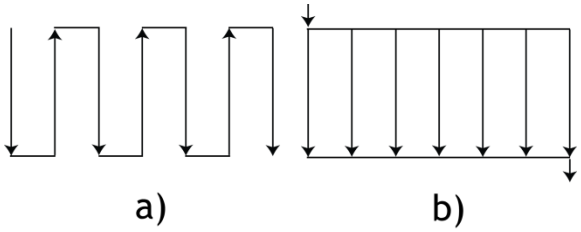

Figure 2-37 Heating circuits configuration: a) manifold b) single pass

The mould should be designed according to the contraction ratios, with values of 1.5% for polyurethane foams and 0.5% for rigid polyurethanes, according to the material supplier specifications (Knipp, 1998). The addition of fillers can change these values.

For an easy extraction, the mould should be projected with a draft angle (Knipp, 1998). Some reference values are 0.5^{o} for parts up to 25.4mm height, and additional 0.25^{o} for additional 25.4mm height (BayerCorporation, 2008).

Regarding the mould material, due to the low pressures during the mould filling a wide range of materials can be used for RIM moulds, such as silicone, epoxy resins, spray metal, etc. The materials choice depends on the series size, the superficial quality of the part, the production times, and tolerances, to name a few. More details about mould material selection can be found at Mateus (2011); Mateus et al. (2008); Silva (2007); Silva et al. (2007).

For the mould fabrication, the usual process is the milling or machining of a block of solid material. Alternative processes can be employed in the mould manufacturing, for example rapid prototyping techniques. The selection of the manufacturing process depends on the production volume, if the part needs some inserts, finishing quality and complexity of the part (Silva, 2007). Also the works of Silva (2007) and Mateus (2011) reviewed and study with detail some alternative techniques. For the designers, the knowledge of the available fabrication techniques is important, because this has a huge impact on the price of the tool, which at the end could be the deciding factor determining the part production.

2.5 Conclusions

Present work covered over forty years of RIM mixing chamber design, from the T mixing head proposed by Keuerleber and Pahl (1972) until more recent patent from Lopes et al. (2005). From the state of the art, it is possible to understand that the mixing head was projected over the years, based in experience and not in scientific studies, a fact that was previously observed by Knipp (1998). An adapted strategy to enhance the mixing head design was increasing the complexity of the mixing chamber geometry, which promotes

more complex paths of the fluids and thus mixing. It was a common empirical believe that the increase on the flow complexity could improve the process reliability. Later, some studies were performed to study the influence of geometrical parameters of T mixing head in mixing quality.

Study of mixing in industrial prototypes is difficult particularly with visualization techniques, and several techniques were employed to assess the mixing quality on lab setups. Within the scope of present work, these techniques for mixing and reaction studies were reviewed. One of such techniques, relies on the product distribution from a test reaction to identify the operational parameters that favour mixing. From works with test chemical reaction it was observed that the increasing Re between 100 to 200, causes a steep increase on micromixing degree and that for Re higher than 300 micromixing remains constant. Tracer studies were also employed to assess the quality of mixing in RIM, which enable the identification of critical values for the operation Reynolds number. The mixing studies enabled the identification of other critical parameters for the RIM process, such as the momentum ratio between the jets, M_r. The physical characterization of the final polymer can also be used to evaluate mixing in the RIM process. Polymerization studies were made with the analyzes of the striation thickness and molecular weight distribution. From these studies it was noticed the relation of these parameters with the mixture quality and Re. Last, the adiabatic temperature rise was also employed in RIM corroborating the results of the other techniques on the identification of a transition on flow regime between $100 < Re < 160$.

This work deals with the demonstration of a new technology for mixing control in the RIM mixing chamber, the RIMcop®. This technology addressed some of the issues left to be solved from the state of the art of RIM technologies. Currently the flaws of the process are compensated by the addition of aftermixers.

Several numerical techniques have been developed to analyse the mould filling, and more concretely, the RIM mould filling. The trend has been the evolution to 3D multiphasic models: VOF has been employed by several authors.

There are very few studies on RIM mould filling, and the existing ones have, at least, fifteen years (Knipp, 1998; Müller et al., 1985a; Müller et al., 1985b). Some mould project rules were collected, mainly from the referred works, and from Silva (2007) and BayerCorporation (2008). The project rules, even the ones collected in Silva (2007) are, mostly, advises from material producers in order to potentiate the RIM process. One of the

key contributions the present thesis intends to have on RIM is the use of more advanced computational tools on the design of moulds for RIM.

2.6 References

Anturkar, N.R., 1994. A Model of Advancing Flow Front in RIM. Polymer Engineering and Science 34, 1450-1454.

Baldyga, J., Bourne, J.R., 1983. Distribution of Striation Thickness from Impingement Mixers in Reaction Injection Molding. Polymer Engineering and Science 23, 556-559.

Bartolo, P., Mateus, A., 2003. Moldação por Reacção a Baixa Pressão(RIM - Reaction Injection Moulding). Molde 57, 32-37.

Bauer, A., 1985. Mixing Head. Patent US4510120.

Bauer, A., Mertens, G., 1994. Apparatus for Mixing Reactive Synthetic-Resin Components. Patent US5277567.

BayerCorporation, 2008. Engineering Polyurethanes - RIM Part and Mold Design Guide. Bayer Material Science.

Bierdel, M., Piesche, M., 2001. CFD - Simulation and Experimental Investigation of Impingement Mixing in Reaction Injection Molding (RIM), 3rd European Congress of Chemical Engineering, Nuremberg, Germany.

Boden, H., Niggemann, J., Rentz, B., Raffel, R., Althausen, F., 1983. Devide for Producing a Solid-Forming or Foaming Flowable Reaction Mixture. Patent US4378335.

Bolde, H., Schulte, K., 1994. Polyurethane Processing, in: Oertel, G. (Ed.), Polyurethane Handbook. Carl Hanser Verlag, Munich, Germany, pp. 160-170.

Bourne, J.R., 1982. The Characterization of Micromixing Using Fast Multiple Reactions. Chemical Engineering Communications 16, 79-90.

Breuker, G.W., Robinson, M.D., 2006. The-Tilt Mixng Head. Patent US7093972 B3.

Broyer, E., Macosko, C.W., 1976. Heat transfer and curing in polymer reaction molding. AIChE Journal 22, 268-276.

Castro, J.M., Macosko, C.W., 1982. Studies of mold filling and curing in the reaction injection molding process. AIChE Journal 28, 250-260.

Chella, R., Ottino, J.M., 1983. Modelling of Rapidly -Mixed Fast-Crosslinking Exothermic Polymerizations. AIChE Journal 29, 373-382.

Danckwerts, P.V., 1952. The Definition and Measurement of Some Characteristics of Mixtures. Applied Science Research 3, 279-196.

Decker, H., 1993a. Reactive Fluid Mixing Head. Patent US5270013.

Decker, H.W., 1993b. Reactive Fluid Mixing Head. Patent US5270013.

Domine, J.D., Gogos, C.G., 1980. Simulation of reactive injection molding. Polymer Engineering & Science 20, 847-858.

Erkoc, E., Santos, R.J., Nunes, M.I., Dias, M.M., Lopes, J.C.B., 2007. Mixing dynamics control in RIM machines. Chemical Engineering Science 62, 5276-5281.

Fields, S.D., Thomas, E.L., Ottino, J.M., 1986. Visualization of interfacial urethane polymerizations by means of a new microstage reactor. Polymer 27, 1423-1432.

Fiorentini, C., 1982. Head for Mixing and Ejection Interacting Liquid Components, for Molding Plastic Materials. Patent US4332335.

Fiorentini, C., 1989. High Pressure Mixing Device. Patent US4802770.

Fonte, C., 2012. Mixing Studies with Impinging Jets - PIV/PLIF Experiments and CFD Simulation, Ph.D. Thesis, Deparment of Chemical Engineering, Universidade do Porto, Porto, Portugal.

Fonte, C., Santos, R., Dias, M., Lopes, J.C., 2011. Quantification of Mixing in RIM Using a Non-Diffusive Two-Phase Flow Numerical Model. Internation Journal of Chemical Reactor Engineering 9, A114.

Fonte, C.P., Santos, R.J., Dias, M.M., Lopes, J.C.B., 2010. Quantification of mixing in RIM using a non-diffusive two-phase flow numerical model, ECCE 7 - 7th European Congress of Chemical Engineering & CHISA 2010 - 19th International Congress of Chemical and Process Engineering. Process Engineerig Publisher, Prague, Prague, Czech Republic, pp. 871-872.

Fonte, C.P., Sultan, M.A., Santos, R.J., Dias, M.M., Lopes, J.C.B., 2012. Flow Field Characterization and Impinging Jets Stability Studies in RIM, 14th European Conferences on Mixing, Warsaw, Poland, pp. 113-115.

Foudrinier, E., Venet, C., Silva, L., 2008. 3D Computation of reactive moulding processes. International Journal of Material Forming 33, 735-738.

Fruzzetti, R., Hogan, K., Murray, F., White, J., 1977. Factors Affecting the Quality of Impingment Mixed RIM Urethanes. SAE Technical Paper.

Garcia, M.A., Macosko, C.W., Subbiah, S., Guçeri, S.I., 1991. Modelling of Reactive Filling in Complex Cavities. International Polymer Processing 1991, 73-82.

Haagh, G.A.A.V., Peters, G.W.M., Meijer, H.E.H., 1996. Reaction injection molding: Analyzing the filling stage of a complex product with a highly viscous thermoset. Polymer Engineering & Science 36, 2579-2588.

Harris, R.F., Anderson, R.M., Shannon, D.M., 1992. Speciality Polyurethane Soft Segments. II. Mixing Studies in Micro-RIM Using Polyether Diamine Oligomers Containing Backbone Urea Moieties. Journal of Applied Polymer Science 46, 1547-1560.

Igreja, R., 2007. Simulação Numérica das Fases de Enchimento e Cura em Reaction Injection Moulding, usando o CFX, Master Thesis, Mechanical Department, University of Aveiro, Aveiro, Portugal.

Jeong, Y.C., 2004. Mixing Head Assembly with Double-Angled Injection Nozzle. Patent WO 2004/004879 A1.

Johnson, D.A., 2000a. Experimental and Numerical Examination of Confined Laminar Opposed Jets. Part I Momentum Imbalance. International Communications in Heat and Mass Transfer 27, 443-454.

Johnson, D.A., 2000b. Experimental and Numerical Examination of Confined Laminar Opposed Jets. Part II Momentum Balancing. International Communications in Heat and Mass Transfer 27, 455-463.

Johnson, D.A., Wood, P., 2000. Self-Sustained Oscillations in Opposed Impinging Jets in an Enclosure. Canadian Journal of Chemical Engineering 78, 867-875.

Johnson, D.A., Wood, P., Hrymak, A.N., 1996. The Effect of Geometrical Parameters on the Flow Field of an Opposed Jet RIM Mix Head: Equal Flow and Matched Fluids. Canadian Journal of Chemical Engineering 74, 40-48.

Johnson, V.L., Moser, K., 1987. High-Pressure Mixing Head. Patent US4707339.

Kamal, K.M.R., Ryan, M.E., 1987. Thermoset Injection Molding, in: Isayev, A.I. (Ed.), Injection and Compression Moulding fundamentals. Marcel Dekker, New York.

Keuerleber, R., Pahl, F., 1972. Devide for feeding flowable material to a mold cavity. Patent US3706515.

Knipp, U., 1998. Molds for Polyurethanes Products, in: Stoeckhert, K., Menning, G. (Eds.), Mold-Making Handbook. Hanser Publishers, Munich, Germany.

Kolodziej, P., Macosko, C.W., Ranz, W.E., 1982. The Influence of Impingement Mixing on Striation Thickness Distribution and Properties in Fast Polyurethane Polymerisation. Polymer Engineering and Science 22, 388-392.

Kolodziej, P., Yang, W.P., Macosko, C.W., Wellinghoff, S.T., 1986. Impingement Mixing and its Effect on the Microstructure of RIM Polyurethanes. Journal of Polymer Science 25, 2359-2377.

Kusch, H.A., Ottino, J.M., Shannon, D.M., 1989. Analysis of Impingement Mixing-Reaction Data: Use of a Lamellar Model to Generate Fluid Mixing Information. Industrial & Engineering Chemistry Research 28, 302-315.

Lack, C.D., Silebi, C.A., 1988. Numerical simulation of reactive injection molding in a radial flow geometry. Polymer Engineering & Science 28, 434-443.

Laurent, D., Feltan, A., 1978. Head for Mixing and Discharging at Least Two Ingredients. Patent US3706515.

Lawler, L.F., 1976. personal communication, in: Corporation, U.C. (Ed.), Charleston, Wa, USA.

Lee, L.J., Macosko, C.W., 1980. Heat transfer in polymer reaction molding. International Journal of Heat and Mass Transfer 23, 1479-1492.

Lee, L.J., Ottino, J.M., Ranz, W.E., Macosko, C.W., 1980. Impingement Mixing in Reaction Injection Molding. Polymer Engineering and Science 20, 868-874.

Leidal, S.M., 1978. Stem Adjusment Seal for Reaction Injection Molding Machine. Patent US4099919.

Lekakou, C.N., Richardson, S.M., 1986. Simulation of reacting flow during filling in reaction injection molding (RIM). Polymer Engineering & Science 26, 1264-1275.

Li, X., Santos, R.J., Lopes, J.C.B., 2007. Modelling of self-induced oscillations in the mixing head of a rim machine. Canadian Journal of Chemical Engineering 85, 45-54.

Lopes, J.C.B., Santos, R.J., Teixeira, A.M., Costa, M.R.P.F.N., 2005. Production Process of Plastic Parts by Reaction Injection Moulding, and Related Head Device. Patent WO 2005/097477.

Machuga, S.C., Midje, H.L., Peanasky, J.S., Macosko, C.W., Ranz, W.E., 1988. Microdispersive Interfacial Mixing in Fast Polymerizations. AIChE Journal 34, 1057-1064.

Macosko, C., 1989. RIM Fundamentals of Reaction Injection Molding. Hanser Publishers, Munich, Germany.

Macosko, C.W., McIntyre, D.B., 1984. RIM Mixhed with High Pressure Recycle. Patent US4479531.

Malguernera, S., Suh, N., 1977. Liquid Injection Molding I. An Investigation of Impegiment Mixing. Polymer Engineering and Science 17, 111-115.

Manas-Zloczower, I., Blake, J.W., Macosko, C.W., 1987. Space-time distribution in filling a mold. Polymer Engineering & Science 27, 1229-1235.

Manas-Zloczower, I., Macosko, C.W., 1988. Moldability diagrams for the reaction injection molding of a polyurethane crosslinking system. Polymer Engineering & Science 28, 1219-1226.

Mateus, A., 2011. Modelling and optimising of reaction injection moulding, Ph.D. Thesis, Departament of Physics, University of Reading, Reading, UK.

Mateus, A., Bártolo, P., Mitchell, G., Silva, M., Pouzada, A., Pontes, A., 2008. The effect of thermal conductivity of RIM moulds in kinetics cure, in: Bártolo, P. (Ed.), Virtual and rapid Manufacturing. Taylor & Francis Groud, Leiria.

Michalek, T., Kowaleski, T.A., 2003. Experimental model of mould filling flow, in: Šarler, B., Gobin, D. (Eds.), Heat and Mass Transfer - In Solid-Liquid Phase Change Processes, Ljubljana, Slovenia.

Mitani, T., Hamada, H., 2003. Prediction of flow patterns in the polyurethane foaming process by numerical simulation considering foam expansion. Polymer Engineering & Science 43, 1603-1612.

Molnar Jr., J.A., Lee, L.J., 1989. Mixing Study of L-shape Mixheads in Reaction Injection Molding. Journal of Applied Polymer Science 37, 2295-2312.

Muhle, D., 1978a. Frothing Method and an Apparatus For Carrying out the Method. Patent US4115299.

Muhle, D., 1978b. High Pressure Mixing Head. Patent US4115066.

Müller, H., Küper, B., Maier, U., Pierkes, L., 1985a. The latest on molding of polyurethane. Advances in Polymer Technology 5, 257-304.

Müller, H., Mrotzek, W., Menges, G., 1985b. Mold Filling with Polyurethane, Reaction Injection Molding. American Chemical Society, pp. 237-258.

Nennecker, G.H., 1996. Mixing Head for Molding Machine. Patent US5498151.

Nguyen, L.T., Suh, N.P., 1985. Effect of High Reynolds Number on the Degree of Mixing in RIM Processing. Polymer Process Engineering 3, 37-56.

Nunes, M.I., 2007. Micromixing in Chemical Reactions - Test Reaction, Ph.D. Thesis, Deparment of Chemical Engineering, Univeristy of Porto, Porto, Portugal.

Oertel, G., 1989. Polyurethane Handbook. Hanser Publishers, Munich.

Patankar, S.V., 1980. Numerical Heat Transfer and Fluid Flow. Tayler&Frances, Philadelphia.

Perrett, F.J., Reible, D.D., McIlhenny, R.C., 1993. Modeling fountain flow and filling front shape in reaction injection molding. Polymer Engineering & Science 33, 716-720.

Ranz, W.E., 1979. Applications of a Stretch Model to Mixing Diffusion, and Reaction in Laminar and Turbulent Flows. AIChE Journal 25, 41-47.

Ranz, W.E., 1986. Analysis of Reaction Processes in Which Microscopic Heterogeneities Appear: Scale-Up and Scale-Down of Polymerization Reactions. Industrial & Engineering Chemistry Fundamentals 25, 561-565.

Reisinger, G., 1994. Mixing Apparatus for Processing Liquid Multi-Component Plastics in Particular Polyurethane. Patent US5295508.

Ridenour, H., 1991. Mixing Head with Sleeved Quieting Chamber. Patent WO 91/17878.

Ritcher, E.B., Macosko, C.W., 1978. Kinetics of Fast (RIM) Urethane Polymerization. Polymer Engineering and Science 18, 1012-1018.

Sandell, D.J., Macosko, C.W., Ranz, W.E., 1985. Visualization Technique for Studying Impingement Mixing at Representative Reynolds Numbers. Polymer Process Engineering 3, 57-70.

Santos, R.J., 2003. Mixing Mechanisms in Reaction Injection Moulding - RIM - An LDS/PIV Experimental Study and CFD Simulation, Ph.D. Thesis, Deparment of Chemical Engineering, Universidade do Porto, Porto.

Santos, R.J., Erkoc, E., Dias, M.M., Lopes, J.C., 2009. Dynamic Behavior of the Flow Field in a RIM Machine Mixing Chamber. AIChE Journal 55, 1338-1351.

Santos, R.J., Erkoc, E., Dias, M.M., Teixeira, A.M., Lopes, J.C.B., 2008. Hydrodynamics of the mixing chamber in RIM: PIV flow-field characterization. AIChE Journal 54, 1153-1163.

Santos, R.J., Teixeira, A.M., Costa, M.R., Lopes, J.C.B., 2002. Operational and design study of RIM machines. International Polymer Processing 17, 387–394.

Santos, R.J., Teixeira, A.M., Erkoç, E., Sultan, M.A., Karpinska, A., Dias, M.M., Lopes, J.C.B., 2010. Validation of a 2D CFD Model for Hydrodynamics' Studies in CIJ Mixers. International Journal of Chemical Reactor Engineering 8, A32.

Santos, R.J., Teixeira, A.M., Lopes, J.C.B., 2005. Study of mixing and chemical reaction in RIM. Chemical Engineering Science 60, 2381-2398.

Schlieckmann, A., 1978. High Pressure Mixing Head. Patent US4070008.

Schlueter, K., 1984. Apparatus for Producing a Preferably Chemically Reactive Mixture from Two or More Plastics Components. Patent US4490048.

Schluter, K., 1976. System for Filling a Mold with Reactive Synthetic-Resin Components. Patent US3975128.

Schmitz, H., Krompass, W., 1984. Mixing Head for Reactive Materials. Patent US4464056.

Schneider, F., 1984a. High Pressure Impingement Mixing Apparatus. Patent US4440500.

Schneider, F., 1991. Apparatus for Mixing At Least Two Reactive Plastics Materials. Patent US5063027.

Schneider, F.W., 1979. High Pressure Injection Mixing Head for Multi-Component Plastics, particularly Polyurethane. Patent US4175874.

Schneider, F.W., 1984b. High Velocity Mixing Method. Patent US4452919.

Scrivo, J.V., 1986. Impingement Mix-Head for RIM Process. Patent US4600312.

Sebastian, D.H., Boukobbal, S., 1986. Mixhead Parameters Governing Impingement Mixing Effectiveness for Polyurethane Reactive Injection Molding Processes. Polymer Process Engineering 4, 53-70.

Sekula, R., Saj, P., Nowak, T., Kaczmarek, K., Forsman, K., Rautiainen, A., Grindling, J., 2003. 3-D modeling reactive molding processes: From tool development to industrial application. Advances in Polymer Technology 22, 42-55.

Seo, D., Ryoun Youn, J., Tucker, C.L., 2003. Numerical simulation of mold filling in foam reaction injection molding. International Journal for Numerical Methods in Fluids 42, 1105-1134.

Seo, D., Youn, J.R., 2005. Numerical Analysis on Reaction Injection Molding of Polyurethane Foam by Using a Finite Volume Method. Polymer 46, 6482-6483.

Silva, M., 2007. Moldes protótipos para a produção de peças em RIM, Master Thesis, Polymer Departament, University of Minho.

Silva, M., Mateus, A., Bártolo, P., Pouzada, A., Pontes, A., 2007. Influência do material do molde em produtos obtidos pelo processo RIM. O Molde 75, 22-26.

Stuper, J., 1992. Mix Head for Mixing Reactive Chemicals. Patent US5082633.

Sweeney, F., 1987. Reaction Injection Molding Machinery and Processes. Marcel Dekker, New York, USA.

Taubenmann, P., 1986. Mixing Head for Producing a Preferably Chemically Reactive Mixture of Two or More Plastics Components. Patent US4592657.

Teixeira, A.M., 2000. Escoamento na Cabeça de Mistura de uma Máquina RIM, Ph.D. Thesis, Deparment of Chemical Engineering, University of Porto, Porto.

Teixeira, A.M., Santos, R.J., Lopes, J.C.B., 1998. Flow Field Characterisation in the Mixing Head of a RIM Machine, CHEMPOR' 98 - 7th International Chemical Engineering Conference, Lisboa, Portugal, pp. 135-142.

Teixeira, A.M., Santos, R.J., Rui, M., Costa, P.F.N., Lopes, J.C.B., 2005. Hydrodynamics of the mixing head in RIM: LDA flow-field characterization. AIChE Journal 51, 1608-1619.

Tenhagen, R.J., 1986. Equipment for Mixing Liquid Reactants. Patent US4595565.

Toda, K., Hori, T., 1989. Mixing Apparatus for Synthetic Resin with Multiple Resin Components. Patent US4876071.

Trautmann, P., Piesche, M., 2001. Experimental investigation on the mixing behaviour of impingement mixers for polyurethane production. Chemical Engineering and Technology 24, 1193-1197.

Tucker, C.L., Suh, N.P., 1980a. Mixing for reaction injection molding. I. Impingement mixing of fiber suspensions. Polymer Engineering & Science 20, 887-898.

Tucker, C.L., Suh, N.P., 1980b. Mixing for Reaction Injection Molding. I. Impingement Mixing of Liquids. Polymer Engineering and Science 20, 875-886.

Unger, D.R., Muzzio, F.J., Brodkey, R.S., 1998. Experimental and Numerical Characterization of Viscous Flow and Mixing in an Impinging Jet Contactor. The Canadian Journal of Chemical Engineering 76, 546-555.

Vespoli, N.P., 1984. in: Co, U. (Ed.), New Haven CT.

Wallner, J., 1988. Mixing Head for Producing a Preferably Chemically Reactive Mixture from Two or More Plastic Components. Patent US4773564.

Wickert, P.D., Macosko, W.E.R.C.W., 1987. Small Scale Mixing phenomena during Reaction Injection Moulding. Polymer 27, 1105-1110.

Wingard, R.D., Leidal, S.M., 1978. Mixing Head for a Reaction Injection Molding Machine. Patent US4773564.

Wisbey, J.D., 1977. Mixing Apparatus. Patent US4043486.

Wood, P., Hrymak, A.N., Yeo, R., Johnson, D.A., Tyagi, A., 1991. Experimental and Computational Studies of the Fluid Mechanics in an Opposed Jet Mixing Head. Physics of Fluids A 3, 1362-1368.

Young, W.-B., 1994. Three-dimensional nonisothermal mold filling simulations in resin transfer molding. Polymer Composites 15, 118-127.

Zhao, Y., Brodkey, R.S., 1998a. Averaged and Time-resolved Full-field (three-dimensional), Measurements of Unsteady Opposed Jets. The Canadian Journal of Chemical Engineering 76, 536-545.

Zhao, Y., Brodkey, R.S., 1998b. Particle Paths in Three-dimensional Flow Fields as a Means of Study: Opposing Jet Mixing System. Powder Technology 100, 161-165.

3 RIMCop technology project

3.1 Introduction

Mixing remains one of the biggest challenges to be solved in RIM. Up to this day the problem of assuring mixing in RIM has been tackled through the design of increasingly complex mixing chamber geometries, to force the flow to have complex patterns that promote striation mechanism. The striation reduces the scale of segregation of the monomers from the diameter of the inlet nozzles (1 to 2mm) to a scale where the thickness of the monomers is small enough for the polymerization to be chemically controlled, normally around $10\mu\text{m}$ (Ranz, 1986). Recent studies (Santos, 2003; Santos et al., 2005a; Santos et al., 2002), have been making a point that the failure to operate RIM at induced or self-sustainable chaotic flow regimes results in unusable RIM produced parts, for example due to the presence of wet spots in the final product.

Hydrodynamic studies showed that the main problem in most of the industrial RIM processes is the control of the balance between the monomer jets and the operation at a jets Reynolds number, Re, higher than 120 (Santos et al., 2002), the critical Reynolds number, Re_{cr}. Recently Fonte (2012) demonstrated that the kinetic energy of the two opposed jets must be balanced to ensure that the opposed jets impinge at the centre of the mixing chamber, promoting a chaotic flow pattern that reduces the initial segregation scales (Santos et al., 2002). On the other hand, the monomers have to be introduced in the mixing chamber at the proper stoichiometric balance for each formulation, and so the flow

rates of the opposed jets are often different. To handle with the jets flow rates difference, and with different monomers physical properties, Fonte (2012) introduced a new parameter, the kinetic energy rate ratio between the two jets, KE_r, defined as

$$KE_r = \frac{\rho_1 \upsilon_1^3 d_1^2}{\rho_2 \upsilon_2^3 d_2^2} \qquad 3.1$$

This chapter introduces a novel design of the injectors nozzles that balances the energy of the jets, $KE_r = 1$, for formulations with flow rates ratio different than one.

The assessment of flow regime inside the mixing chamber is also of the out-most importance for RIM control, even when design ensures high mixing efficiency it is necessary to monitor the system operation. The flow field of the reacting monomers inside the mixing chamber is not easily assessable, but since pressure field and velocity field are coupled the flow field regime can be monitored from static pressure measurements in the injectors' feeding lines. This is the basic concept for a recently patented control scheme for RIM (Lopes et al., 2005), with its respective commercial product RIMcop, and its technology development is the subject of the present chapter.

This chapter starts with a qualitative analysis of different RIM mixing chamber geometries. The opposed jets configuration is tested with three variations: simple, with restrictions and with an elbow of $90°$. After the opposed jets, angled jets, with vertically and horizontally angled jets was studied. From results of steady state hydrodynamic simulations, it was studied the energy dissipation rate, energy balance and macromixing for each geometry.

After comparing geometries, the RIMCop system is characterized with detail, comprising the main concepts of this technology, and the calibration and setup of an actual pilot RIMCop mahine.

3.2 Mixing-Chamber: Simple or Complex Geometries?

Mixing is still one of the biggest challenges in the RIM process. Nowadays, there are several available technical solutions some of them in commercial equipments, which address the issue of mixing in RIM. The increase in the complexity of the mixing chamber geometries has been one of the more common ways to force a complex flow pattern and promoting striation mechanics between the two monomer streams contacting in the mixing chamber (Gomes et al., 2009). This complex flow induces the reduction of segregation scale, from

the inlet diameter down to the final monomers thickness, which should become small enough to promote the lamella's formation and polymerization – normally to a thickness of less than $10\mu m$ (Ranz, 1979).

However, recent studies on the RIM mixing chamber hydrodynamics have proven that the simplest geometries can promote flow patterns that induce a very intense mixing of both monomer streams (Erkoc et al., 2007; Fonte et al., 2011; Gomes et al., 2010; Santos et al., 2002).

In this work, a comparative study between five mixing chambers used in commercial equipment, is done using CFD tools.

3.2.1 Model

3.2.1.1 Geometric Model

From the several configurations present in a large number of patents, and shown in Chapter 2, four are studied in addition to the geometry with oppose jets (Keuerleber and Pahl, 1972; Lopes et al., 2005). The four configurations are the most common ones that can be found in commercial equipments:

- Horizontally angled jets mixing chamber (Gomes et al., 2009);
- Opposed jets mixing chamber in L configuration (Schluter, 1976);
- Vertically angled jets mixing chamber (Macosko and McIntyre, 1984);
- Opposed jets mixing chamber with restrictions (Taubenmann, 1986).

The geometries were modelled in 3D, and are shown in Figure 3-1. Main dimensions are in Table 3-1. One of the mixing chambers is crossed by a set of five cylindrical rods that have 1.5mm of diameter, this geometry is referred to as the mixing chamber with restriction.

Several works have shown that mixing occurs for a Reynolds number higher than a critical value, Re_{cr}, (Fonte et al., 2011; Harris et al., 1992; Lee et al., 1980; Malguernera and Suh, 1977; Santos et al., 2008; Santos et al., 2002). In order to compare the different mixing chambers at different mixing state conditions, namely below and above Re_{cr}, each mixing chamber was studied at three different Re: 75, 150 and 300.

Table 3-1 Main Dimensions of the different mixing chamber's studied

Mixing Chamber	Opposed Jets	Opposed jets with restriction	L	Vertically angled	Horizontally angled
	a)	b)	c)	d)	e)
Diameter [mm]	10	10	10	10	10
Nozzle Diameter [mm]	1.5	1.5	1.5	1.5	1.5
Distance between top and nozzle centre [mm]	5	5	1		2
Angle between nozzle's axis in XY plane [°]	180	180	180	180	100
Angle between the nozzle's axis and the mixing chamber's axis (in z^+ direction) [°]	90	90	90	45	90

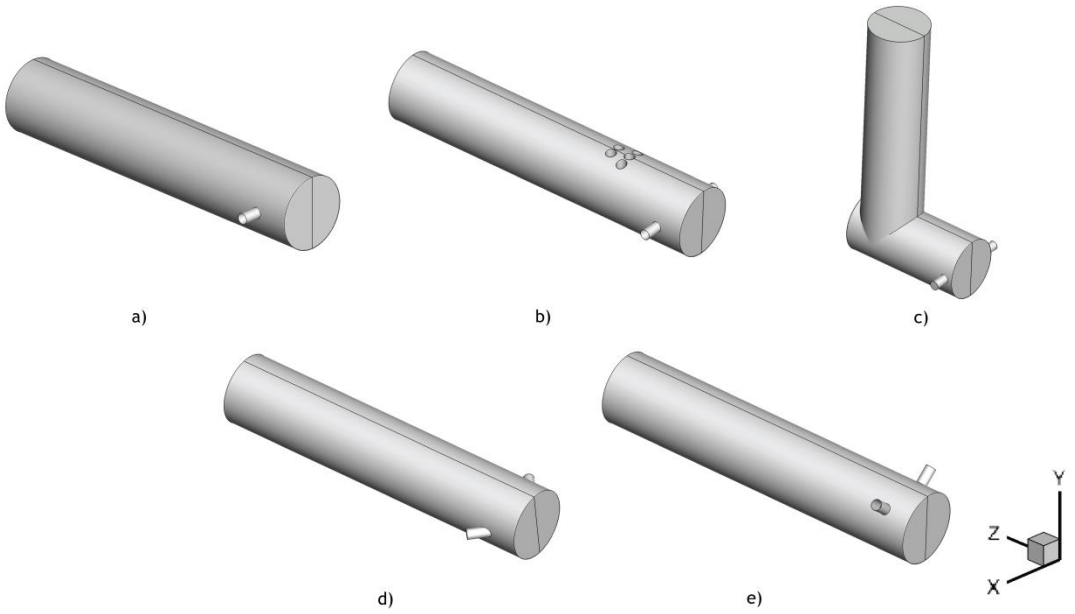

Figure 3-1 Studied Geometries: a) Opposed jets mixing chamber, b) **Opposed jets mixing chamber with restrictions**, c) **Opposed jets mixing chamber in L configuration**, d) **Vertically angled jets mixing chamber** e) **Horizontally angled jets mixing chamber**

3.2.1.2 Physical Model

For a Newtonian and incompressible fluid, the flow is governed by a set of equations that comprise the mass conservation

$$\nabla \cdot \mathbf{v} = 0 \qquad 3.2$$

where $\mathbf{v}$ is the velocity vector, and the conservation of momentum, described by the Navier-Stokes equation

$$\frac{D}{Dt}(\rho \mathbf{v}) = -\nabla p + \mu \nabla^2 \mathbf{v} - \rho \mathbf{g} \qquad 3.3$$

where t is the time, ρ the fluid density, p the pressure, μ the fluid viscosity and $\mathbf{g}$ is the gravitational acceleration vector.

3.2.1.3 Boundary Conditions

The inlet boundary condition in the nozzles is a parabolic velocity profile with normal direction to the inlet plane, defined by

$$\upsilon_x = 2\upsilon_{inj}\left(1 - \left(\frac{l}{d/2}\right)^2\right) \qquad 3.4$$

where υ_{inj} is the inlet injection velocity and l is the position along the inlet surface calculated by

$$l = \sqrt{y^2 + z^2} \qquad 3.5$$

where y and z are the Cartesian coordinates over the inlet surface, and the inlet centre as coordinates $(y, z) = (0, 0)$.

The velocities used for each Re are shown in Table 3-2. It was also considered a stoichiometry ratio of $1{:}1$, between the nozzles, so the υ_{inj} is the same on both sides.

Table 3-2 Inlet Velocities

Re	$\upsilon_{inj}\left[\mathrm{ms}^{-1}\right]$
75	1
150	2
300	4

At the walls were assumed no slip boundary conditions, i.e., the tangential components of velocity at the walls are null so as the normal components: $\upsilon = 0$. In order to get a symmetric steady state, a wall with no friction was assumed in the symmetry plane of the mixing chamber, i-e. the tangential stresses are equal to zero,

$$\tau_{ij} = 0 \qquad 3.6$$

This wall blocks the normal velocity components, i.e. does not allow convective mass transport between both sides of the wall,

$$\mathbf{v} \cdot \mathbf{n} = 0 \qquad 3.7$$

where $\mathbf{n}$ is the normal direction.

For calculating the Residence Time Distribution, the symmetry plane was set as interior, i.e the virtual wall was switched off for mass transfer. Nevertheless the flow field was kept frozen for tracer simulation, so this only had an impact on diffusional mass transport not on the flow field or on the convective mass transfer mechanisms. At the outlet was set an uniform pressure. For all cases it is assumed an atmospheric pressure.

3.2.1.4 Numerical Method and Discretization

Ansys Fluent™ software was used in the present study. The computational mesh consisted in quadrangular elements with $\Delta x = 1.5 \times 10^{-4}\,\mathrm{m}$, in order to have ten radial elements per each nozzle diameter, previously validated by Fonte (2012). A Coupled Scheme for pressure-velocity coupling was used. For pressure and momentum discretization was used MUSCL and PRESTO! schemes, respectively. The residuals were set to 10^{-4} for both continuity and momentum equations.

An inert and incompressible fluid was set for both inlets. The main properties are in Table 3-3.

Table 3-3 Fluid's properties

Property	Value
$\rho\left[\mathrm{kgm^{-3}}\right]$	1000
$\mu\left[10^{-3}\mathrm{Pas}\right]$	20

3.2.2 Results

3.2.2.1 Flow Maps

Although the flow on RIM is dynamic and mixing is strongly dependent on the flow dynamics, due to limitation on computational resources, here only 3D steady state simulations were made. From these simulations it is possible to study the overall flow patterns, for example the location and size of vortices, the way opposed jets contact or the distribution of shear inside the mixing chamber. Analysing a tridimensional flow is a complex task (Zhao and Brodkey, 1998a, b) and to simplify it, in this work the path lines,

dimensionless vorticity and strain rate are shown. These maps were set in several planes that are shown in Figure 3-2:

- Plane XY is in the normal direction to the mixing chamber axis and it contais the axis of the opposed jets, with exception of vertically angled jets mixing chamber;
- Plane XZ that is normal to the direction of the half angle of intersection of both jets axis and it contains the mixing chamber axis;
- Plane YZ that is perpendicular to the mixing chamber axis and it is aligned with the half angle of intersection of both jets axis.

In the case of vertically angled jets mixing chamber the nozzle plane was set at $5\times10^{-5}\,\mathrm{m}$ below the top, since the jets impinge in the closed top of the mixing chamber. Based on Plane XY is possible to divide the mixing chamber in two imaginary parts, above and below this plane, called upper and bottom part, respectively.

The dimensionless vorticity maps for $\mathrm{Re}=75$, 150 and 300 are shown in Figure 3-3 to Figure 3-8. The maps at impact plane, Plane XZ, are illustrated at left, whereas the maps at nozzle plane, Plane XY, are illustrated at right. The dimensionless vorticity vector is defined as

$$\boldsymbol{\omega}^{*}=\frac{d_{inj}}{\upsilon_{inj}}\left(\nabla\times\mathbf{v}\right) \qquad 3.8$$

The vorticity shows the recirculation patterns inside the mixing chamber. The occurrence of vortices capable of engulfing the two monomers and refreshing the contact area between monomer streams is the main mixing mechanism in RIM as proven by Santos et al. (2005b). The normal vorticity component to a plane is twice the value of angular velocity observed in that plane, and is here used to assess the overall patterns in the studied five geometries.

The opposed jets mixing chamber has the flow structure that is better known from previous works, most of these works are from the research group at LSRE/FEUP (Santos et al., 2009; Santos et al., 2008; Santos et al., 2010) but also from the works of Johnson and Wood (Johnson and Wood, 2000; Johnson et al., 1996; Wood et al., 1991) and Nakamura (Nakamura and Brodkey, 2000). In this mixing chamber the jets impinge each other and spread radially from the impingement point (Johnson and Wood, 2000) promoting an area of contact between the opposed jets approximately equal to the mixing chamber longitudinal section, $D\times H$, where D is the mixing chamber diameter an H is the mixing chamber height. This flow pattern is clear from the path lines at specific planes (Figure

3-3a to Figure 3-8a) and from the 3D visualization of the path lines in Figure 3-9a to Figure 3-11a. In each side of the contact area a vortex is formed that can engulf one of the fluids with fluid dragged from the opposite side of the chamber. Each vortex is partially a toroid that circulates around each inlet jet with an open part below the jet, as clearly seen from Figure 3-9a to Figure 3-11a. In the case of dynamic flow fields that are not simulated here, the symmetry of the flow field is broken by the onset of vortices street downstream the jets. These vortices detach from the impingement point having a diameter around $D/2$ and promote an intense engulfment of fluid from both sides of the mixing chamber. Vector maps and isovorticity 3D surface illustrating this flow regime adapted from Santos et al. (2009) are shown in Figure 3-12.

The addition of post-mixers in the opposed jets mixing chamber with restrictions breaks the long recirculation vortices that engulf fluid from both jets in the mixing chamber without obstacles. This is clear from the vorticity maps in the XZ plane of Figure 3-3b, Figure 3-5b and Figure 3-7b, where it is clear the restriction of the flow recirculation pattern inside the limit defined by the obstacles. The obstacles were introduced to create a region of vortex shedding that is only clear from dynamic simulations. The transition to a vortex flow regime after a cylinder is marked by a Reynolds number defined as (Berger and Wille, 1972)

$$Re = \frac{\rho \upsilon_{\infty} d_o}{\mu} \qquad 3.9$$

where d_o is the obstacle diameter and υ_{∞} the flow velocity. The transition Reynolds number is generally around $Re = 48$ (Nishioka and Sato, 1978), which corresponds to a jets Reynolds number also around $Re = 48$.

Mixing chambers where the runner has the shape of an elbow, named opposed jets mixing chamber in L configuration, were also introduced to enhance mixing in RIM, and are quite common in commercial machines. Although the elbow limits the recirculation zone where the two elongated vortices (Figures Figure 3-3c, Figure 3-5c, and Figure 3-7c) are formed, it creates additional rotation of the flow as seen from the vorticity maps in the YZ plane in Figure 3-4c, Figure 3-6c, and Figure 3-8c, which also contributes to enhance mixing.

Both the L shaped mixing chamber and the one with obstacles make the cleaning mechanism with a piston more complex.

Angled jets were introduced to enhance mixing while keeping the cleaning piston device as simple as possible. The flow in angled and directly opposite jets has many common features, namely the recirculation zones and the spreading of the fluids through an impinging plane where fluid from both jets contact, as show in Figure 3-3d, Figure 3-5d and Figure 3-7d and Figure 3-3e, Figure 3-5e and Figure 3-7e for horizontal angled mixing chamber, and vertical angled mixing chamber, respectively. Nevertheless there are some differences between the flows in angled jets and the directly opposed jets mixing chambers. The existence of an head space above the jets impingement point is known to be critical for mixing in RIM (Santos et al., 2002) and this is the reason this headspace is present in the commercial mixing chambers, even when the reason is not clear to the designer this headspace is set as a rule of thumb for the process to work. The configuration of the vertically angled mixing chamber with the jets pointing upwards compromises these recirculation vortices (Figure 3-9d to Figure 3-11d), which as proven by Santos (2003) do not have much impact on steady flow regime but seriously compromise the dynamics of mixing because the jets impingement point is not so "free" to oscillate. Although the angled jets mixing chambers seem to keep the same overall flow patterns they promote a placement of the jets impingement point close to the walls, which can compromise the dynamics of mixing in RIM that heavily relies on the ability of the jets impingement point to oscillate.

Regarding the Re effect, Figure 3-4, Figure 3-6 and Figure 3-8, for $Re=75$, $Re=150$ and $Re=300$, respectively, shown an increasing in vortex length with increasing Re for all the geometries, except for the L mixing chamber and opposed jets with obstacles, where for all Re range the path lines shown the same vortex shedding length, due the shorter top of the mixing chamber.

The same overall flow patterns are observed in all Re range studied. Although, the vortex size and volume change, increases as Re increases. Santos et al. (2005b) and Fonte et al. (2011), reported the existence of a critical Re, $Re=120$, above which intense advective mixing patterns are onset. In the impingement plane YZ, for opposed jets it is possible to see an increase in vorticity intensity in the upper part of mixing chamber for Re above the Re_{cr} as shown Figure 3-6a and Figure 3-6b for $Re=150$ and Figure 3-8a and Figure 3-8b for $Re=300$. Below the Re_{cr}, this intensity decreases, as shown Figure 3-4a and Figure 3-4b, for $Re=75$. For other mixing chamber configurations, since the upper part volume is negligible, it is not promoted the formation of any vorticity structure. For the bottom part, a similar behaviour, i.e., an increasing in vorticity intensity is found for all

the geometries, as shown Figure 3-4, Figure 3-6 and Figure 3-8. From plane XZ, presented in Figure 3-3, Figure 3-5 and Figure 3-7 and plane YZ for L configuration in Figure 3-4c, Figure 3-6c and Figure 3-8c is possible to see the existence of a recirculation point, that it is getting closer to the outlet of mixing chamber for increasing Re. The only exception is for horizontal angled mixing chamber, where these recirculation points stay more or less at the same position along the Re increasing.

Mixing in a RIM mixing chamber mainly occurs due to the stretching and folding of fluid laminas from the two jets. From strain rate fields it is not possible to assess the distribution of the striation between the two jets, however, the instantaneous strain rate maps can present an indication of the spatial distribution for the stretching potential in the flow, and can be used for comparison purposes between the different mixing chambers. Non-dimensional rate of strain, ζ, was defined as

$$\zeta = \frac{1}{2}\frac{\sqrt{(\mathbf{D}:\mathbf{D})}}{\dot{\gamma}_{inj}} \qquad 3.10$$

where $\mathbf{D}$ is the deformation tensor, and $1/2\sqrt{(\mathbf{D}:\mathbf{D})}$ is the norm of the rate strain tensor and $\dot{\gamma}_{inj}$ is the strain rate experienced by the fluid at injectors, and considered a Newtonian behaviour and that strain rate has a linear dependence on the radius of the tube and consequently, on Re can be defined as

$$\dot{\gamma}_{inj} = \frac{8\mu}{\rho d^2} Re \qquad 3.11$$

Figure 3-13 to Figure 3-18 show the non-dimensional rate of strain for different mixing-chambers in the three main planes (plane XY, plane XZ and plane YZ) for the range of Re considered. Since the strain rate distribution covers different orders of magnitude, a logarithmic scale was used for the maps. Regarding the spatial distribution of the rate of strain, it is possible to see that it decays several orders of magnitude in the outlet of the mixing chamber, for all geometries and for Re. Similar to what was reported by Fonte (2012), three ζ main regions where identified:

- $0.1 < \zeta < 1$ in the region where the jets impinge and the resulting impingement plane

- $0.01 < \zeta < 0.1$ in the remain of the top of the mixing chamber until a distance of $\sim D$ for $Re = 75$, to $\sim 2D$ for $Re = 300$ from the top
- $\zeta < 0.01$ in the regions further downstream in the mixing chamber, although close to the walls the values are higher

From the planes XZ, present at Figure 3-14 to Figure 3-18, it is possible to observe that most of the energy dissipation is in the impingement point. For opposed jets, we can see a radial pattern of the energy dissipation from the impingment point on, Figure 3-14a to Figure 3-18a and Figure 3-14c to Figure 3-18c. However on opposed jets mixing chamber with restriction, the existent restrictions divide the central zone of higher strain rate in three parts. This phenomenon causes a considerable loss of the energy that could be used for mixing, and it shortens the higher strain rate zones, whose length is reduced $-D/2$ for $Re = 75$ to $\sim D$ for $Re = 300$, when compared with simplest opposed jets mixing chamber. For the angled jets mixing chambers, there is considerable energy dissipation on the walls, as shown in Figure 3-13d to Figure 3-17d for the vertically angled mixing chamber, and Figure 3-13e to Figure 3-17e for the horizontal angled mixing chamber. Comparing with opposed jets, also a reduction of energy dissipation occurs when the mixing chamber is shorter, whether by reducing the top length of mixing chamber, whether by severe reduction of downstream length of mixing chamber, as an elbow geometry reduces. This phenomenon is found in mixing chamber geometries close to the L mixing chamber, and is shown in Figure 3-13c to Figure 3-17c.

The energy dissipation rate can be computed from the volume average integration of shear rate, according to

$$\varepsilon_{Tot} = \frac{1}{V}\int \nu\dot{\gamma} dV \qquad 3.12$$

where ν is the kinematic viscosity.

Table 3-4 shows the ε_{Tot} for each geometry, from where it is clear an expectable increasing in energy dissipation, ε_{Tot}, with an increase in Re due to the decrease of viscous forces in relation to the inertial forces. These values confirm the analysis made from non-dimensional strain rate figures, with the highest energy dissipation for the oppose jets with no restrictions. The lowest value is achieved when the impingement zone of the opposed jets in the mixing chamber is shorter. For example angled mixing chambers present lower values of energy dissipation when compared to the opposed jets

configuration, due to the fact that the region of jets contacting is closer to one of the walls which hinders its spreading in all directions. When comparing both angled mixing chamber geometries, it is possible to deduce that the vertical angled will loose more energy, due the impingement point being very close to the top wall.

Table 3-4 Energy dissipation for different geometries for different Re

Mixing Chamber	Re	$\varepsilon_{Tot}\left[10^{-1}\mathrm{m}^2\mathrm{s}^{-3}\right]$
Opposed jets	75	9.0
	150	24
	300	63
Opposed jets with restrictions	75	9.6
	150	24
	300	56
L	75	7.2
	150	22
	300	40
Vertically angled	75	8.8
	150	22
	300	58
Horizontally angled	75	8.5
	150	23
	300	60

The jet's radial distribution after impingement, creates a structure identical to a *pancake* (Wood et al., 1991). In order to compare the jet's radial structures for each mixing chamber geometry, it were computed the isosurfaces of a non-dimensional vorticity: $\omega_z^* = 2$. Figure 3-19 shows the *pancake* structure for each geometry, taken from Ansys CFD-Post for $Re = 300$. From this figure, it is shown that the pancake area is confined to the top of mixing chamber, however for the opposed jets, it is clear that the area for pancakes formed are bigger than from other geometries. To quantify it, the *pancake's* projected area onto impingement plane was computed using area calculator function, and the results are present in Table 3-5. Comparing both of opposed jets geometries, it is possible to see that the simplest geometry, i.e., for opposite jet's without any flow restriction, promotes the *pancake* with the biggest area. In order to understand the Re effect, is presented the area of the *pancake* for the Re range studied, for the simplest opposed jets geometry. Since this *pancake* was related with vorticity, increasing Re the area also increases from zero, for a $Re = 75$, to $13\times10^{-5} m^2$ for $Re = 300$. The steep increase on the *pancake* area coincides with the existence of a critical Re that is defined as the value where advective mixing mechanisms are onset (Fonte et al., 2011; Santos et al., 2005b). From Table 3-5 the Re_{cr} is in range between $75 < Re_{cr} < 150$, although from

PIV measurements of Santos et al. 2008, this value was set at $Re_{cr} = 120$, that is quite accepted in literature.

The ability to generate interfacial area between the fluids issuing from the opposed injectors is directly related to the geometries yielding larger values of the average shear rate. Since shear rate and interfacial area generation are the main mixing mechanisms in laminar flows, the simplest concept of impinging two jets directly into each other and allow them to expand radially, is the one that from steady flow simulations proofs to promote better mixing efficiency.

Table 3-5 "Pancake" area, for several geometries at $\omega^* = 2$

Mixing Chamber	Re	$A_{pancake}\left[10^{-5}\mathrm{m}^2\right]$
Opposed jets	75	0
	150	1.7
	300	13
Opposed jets with restrictions	300	13
L	300	8.6
Vertically angled	300	12
Horizontally angled	300	12

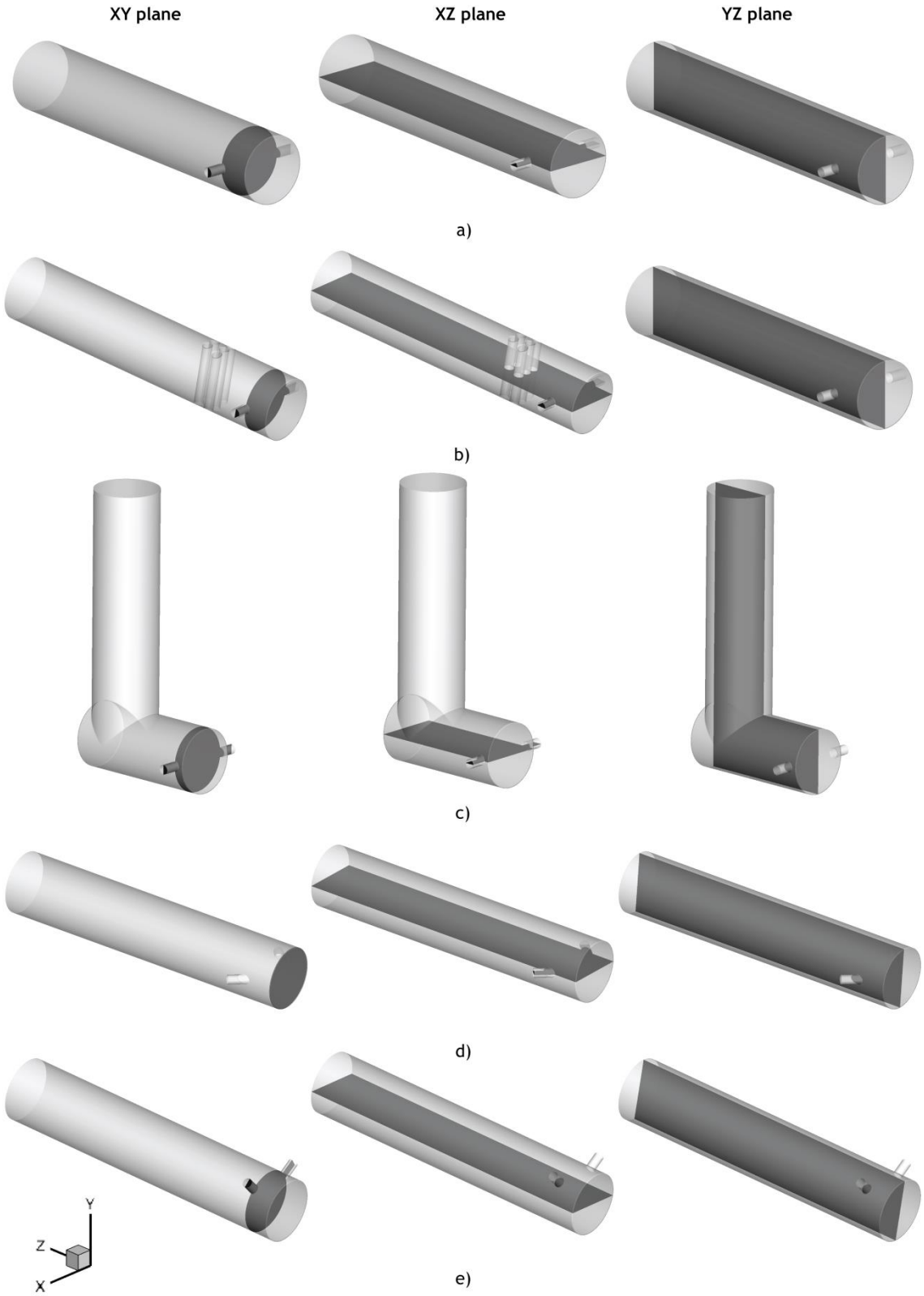

Figure 3-2 Studied planes from different geometries: a) Opposed jets mixing chamber, b) **Opposed jets mixing chamber with restrictions**, c) **Opposed jets mixing chamber in L configuration**, d) **Vertically angled jets mixing chamber** e) **Horizontally angled jets mixing chamber**

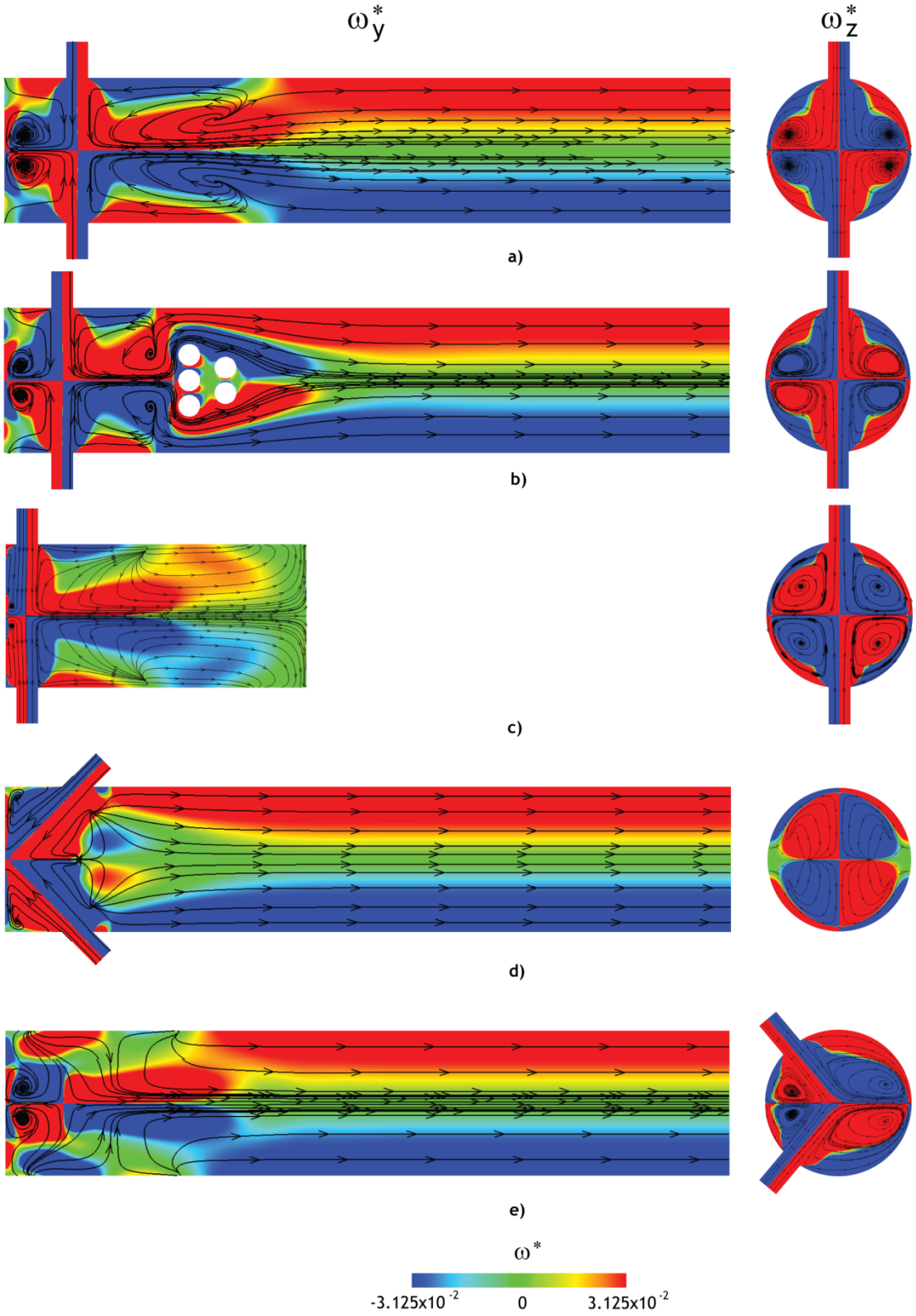

Figure 3-3 Non-dimensional Vorticity maps, with pathlines for a $Re = 75$, at planes XZ and XY a) Opposed jets mixing chamber, b) **Opposed jets mixing chamber with restrictions**, c) **Opposed jets mixing chamber in L configuration**, d) **Vertically angled jets mixing chamber** e) **Horizontally angled jets mixing chamber**

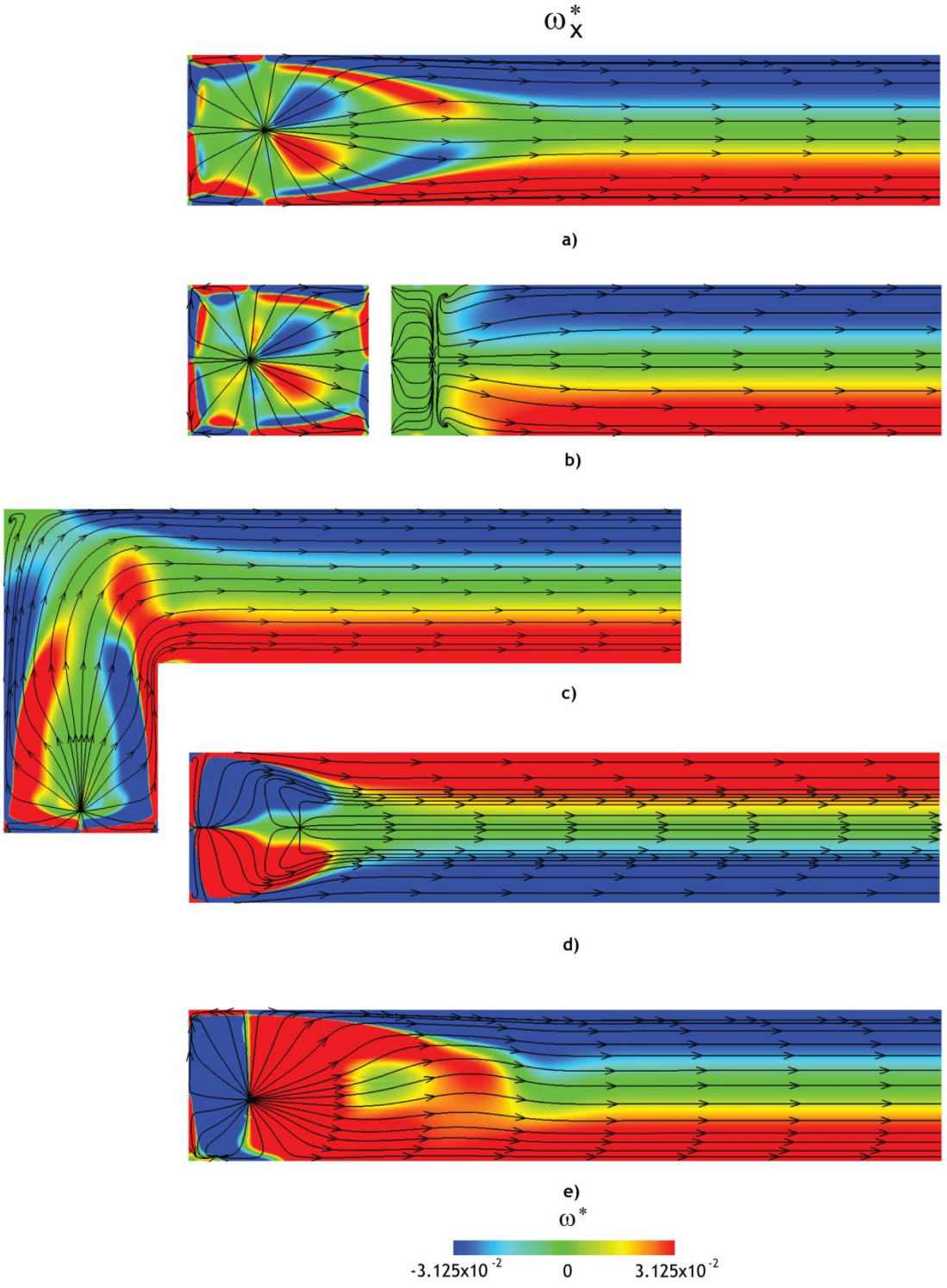

Figure 3-4 Non-dimensional Vorticity maps, with pathlines for a $Re = 75$, at plane YZ a) Opposed jets mixing chamber, b) **Opposed jets mixing chamber with restrictions**, c) **Opposed jets mixing chamber in L configuration**, d) **Vertically angled jets mixing chamber** e) **Horizontally angled jets mixing chamber**

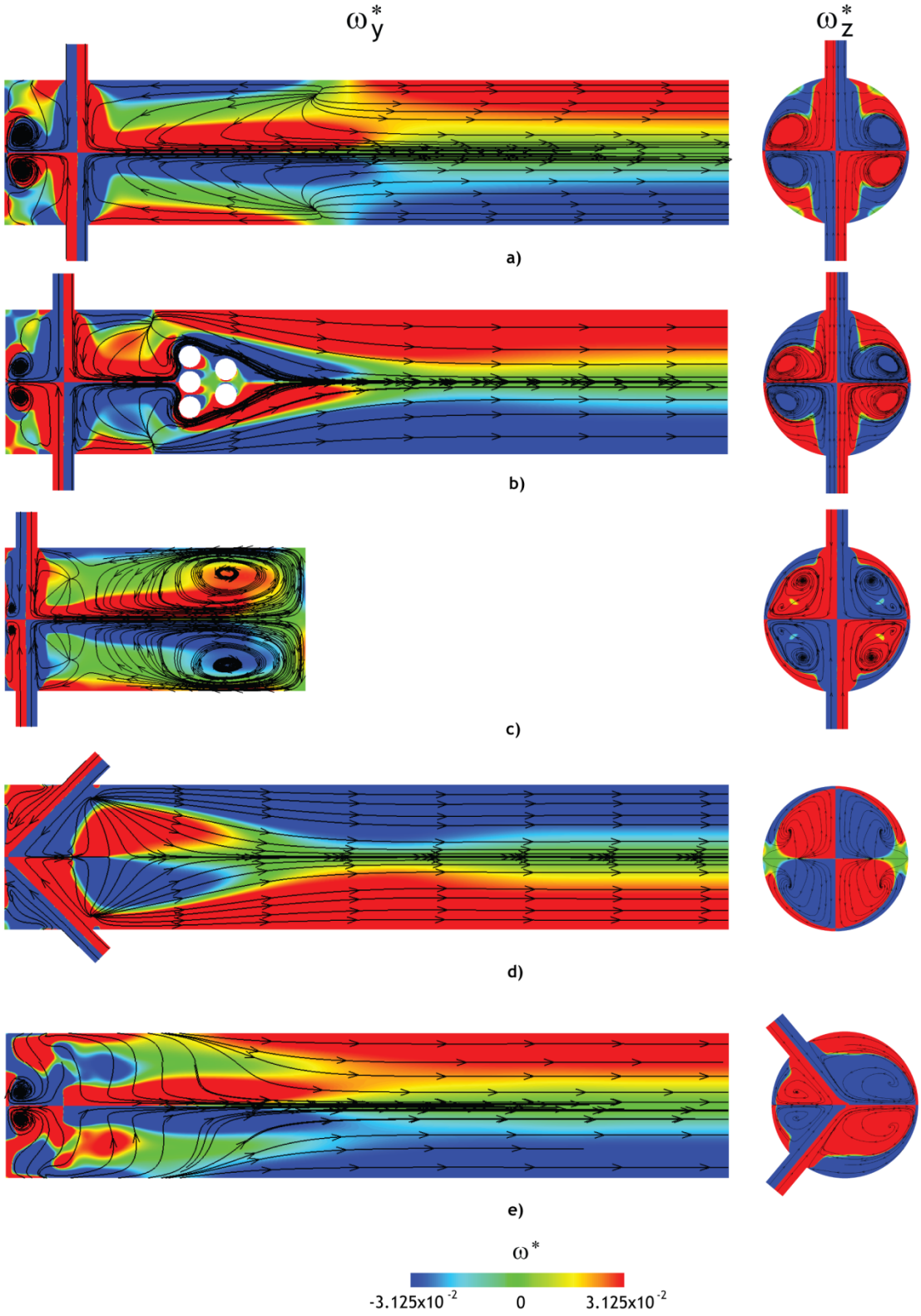

Figure 3-5 Non-dimensional Vorticity maps, with pathlines for a $Re = 150$, at planes XZ and XY a) Opposed jets mixing chamber, b) **Opposed jets mixing chamber with restrictions**, c) **Opposed jets mixing chamber in L configuration**, d) **Vertically angled jets mixing chamber** e) **Horizontally angled jets mixing chamber**

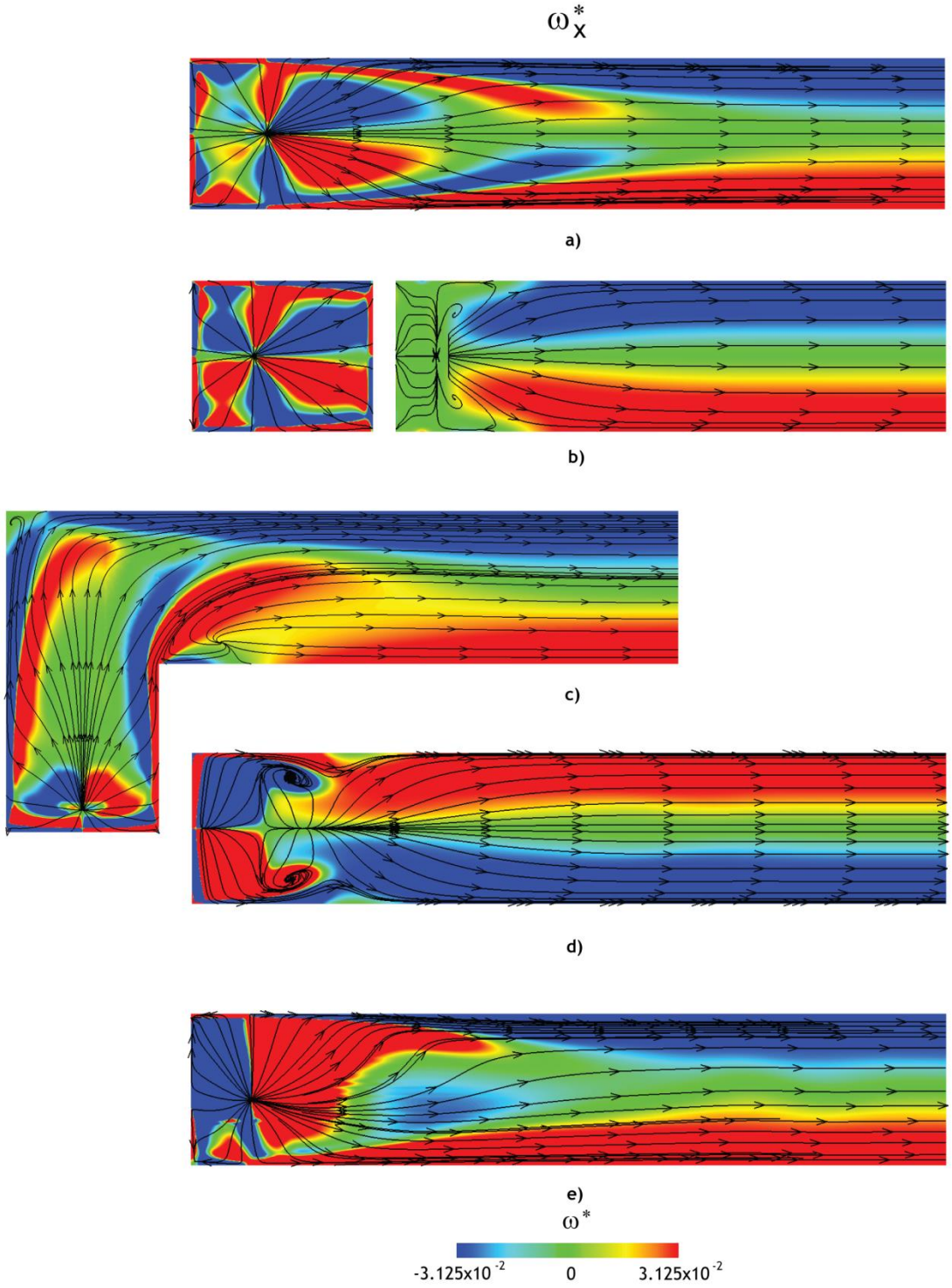

Figure 3-6 Non-dimensional Vorticity maps, with pathlines for a $Re = 150$, at plane YZ a) Opposed jets mixing chamber, b) **Opposed jets mixing chamber with restrictions**, c) **Opposed jets mixing chamber in L configuration**, d) **Vertically angled jets mixing chamber** e) **Horizontally angled jets mixing chamber**

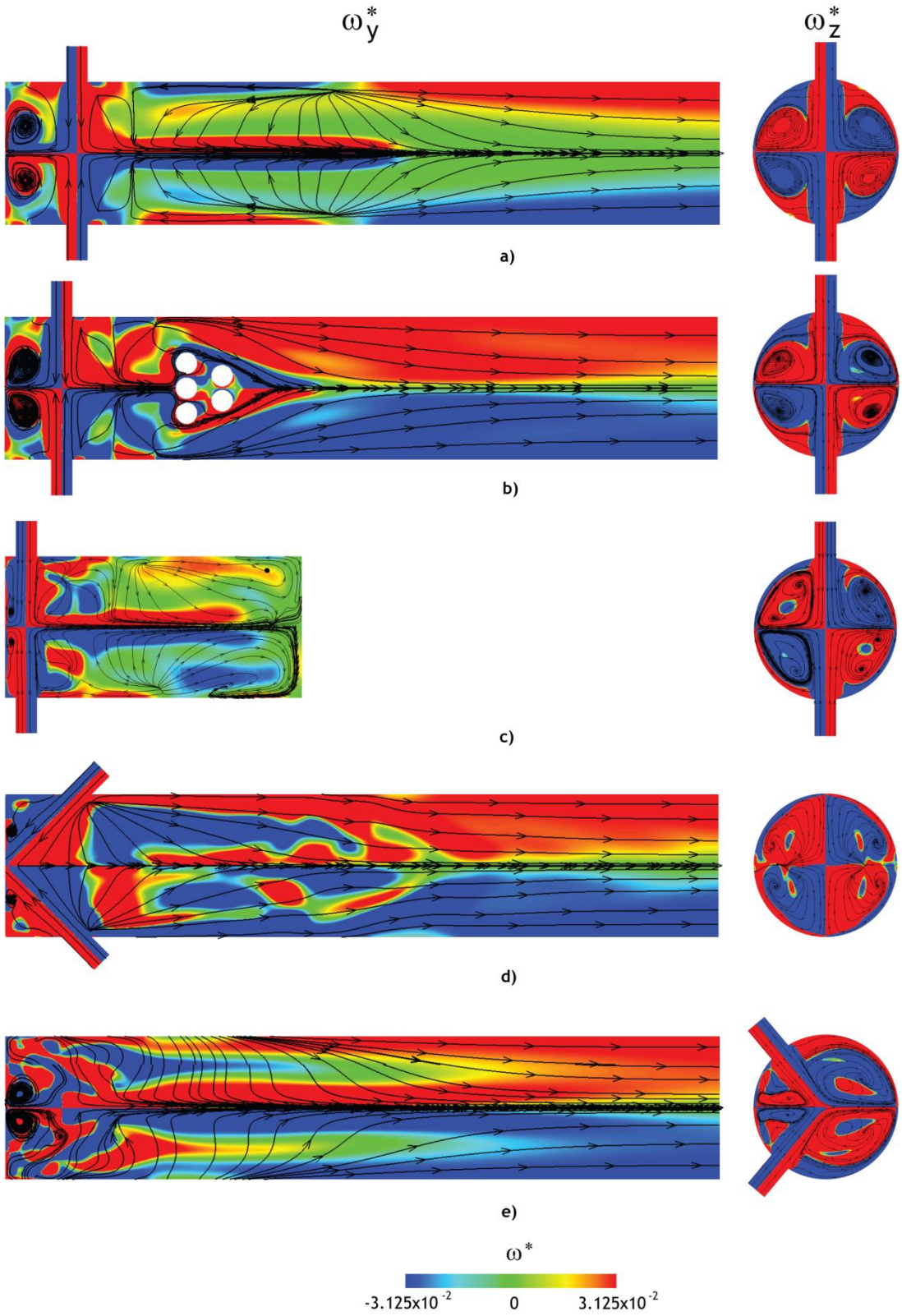

Figure 3-7 Non-dimensional Vorticity maps, with pathlines for a $Re = 300$, at planes XZ and XY a) Opposed jets mixing chamber, b) **Opposed jets mixing chamber with restrictions**, c) **Opposed jets mixing chamber in L configuration**, d) **Vertically angled jets mixing chamber** e) **Horizontally angled jets mixing chamber**

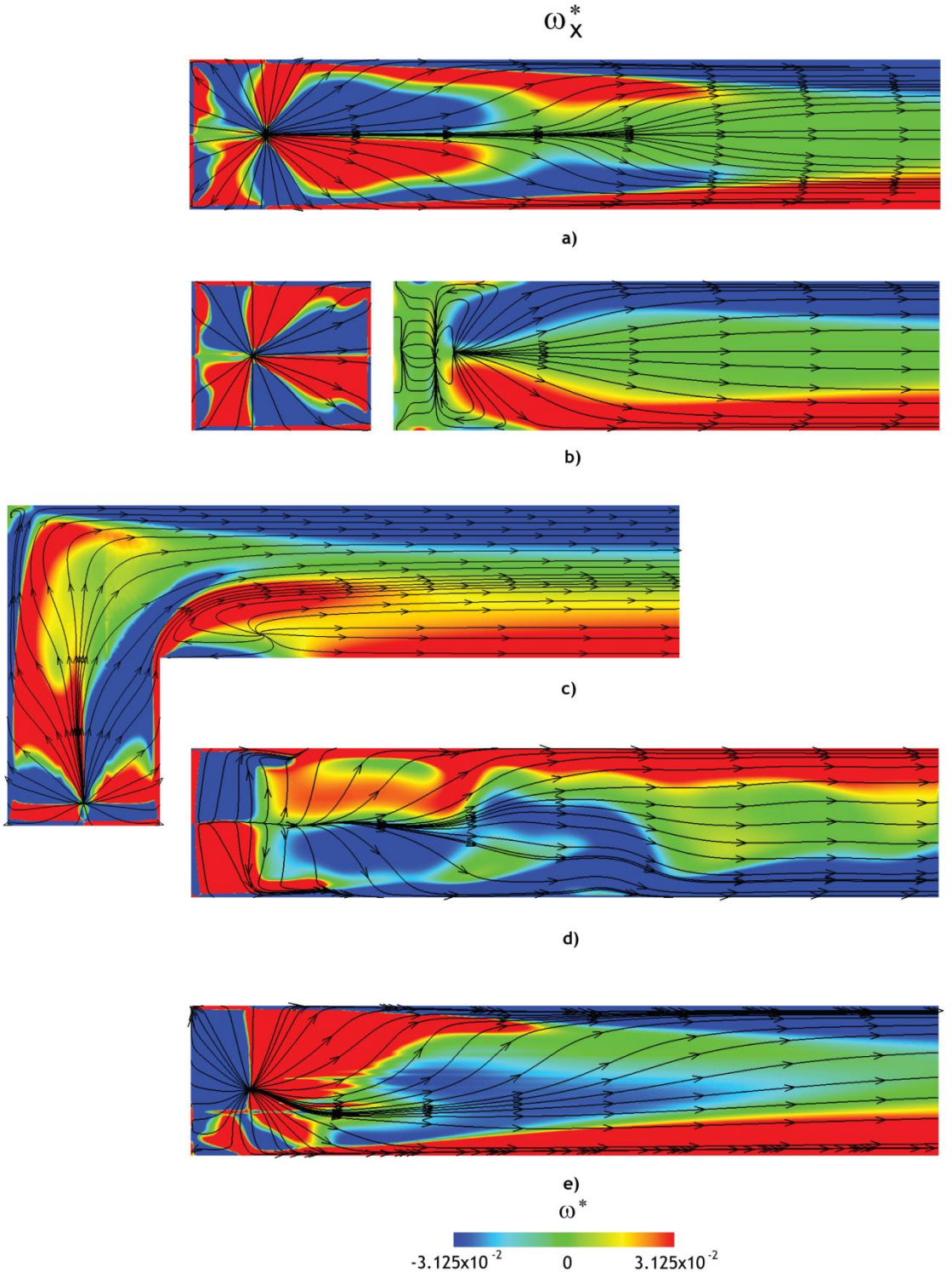

Figure 3-8 Non-dimensional Vorticity maps, with pathlines for a $Re = 300$, at plane YZ a) Opposed jets mixing chamber, b) **Opposed jets mixing chamber with restrictions**, c) **Opposed jets mixing chamber in L configuration**, d) **Vertically angled jets mixing chamber** e) **Horizontally angled jets mixing chamberr**

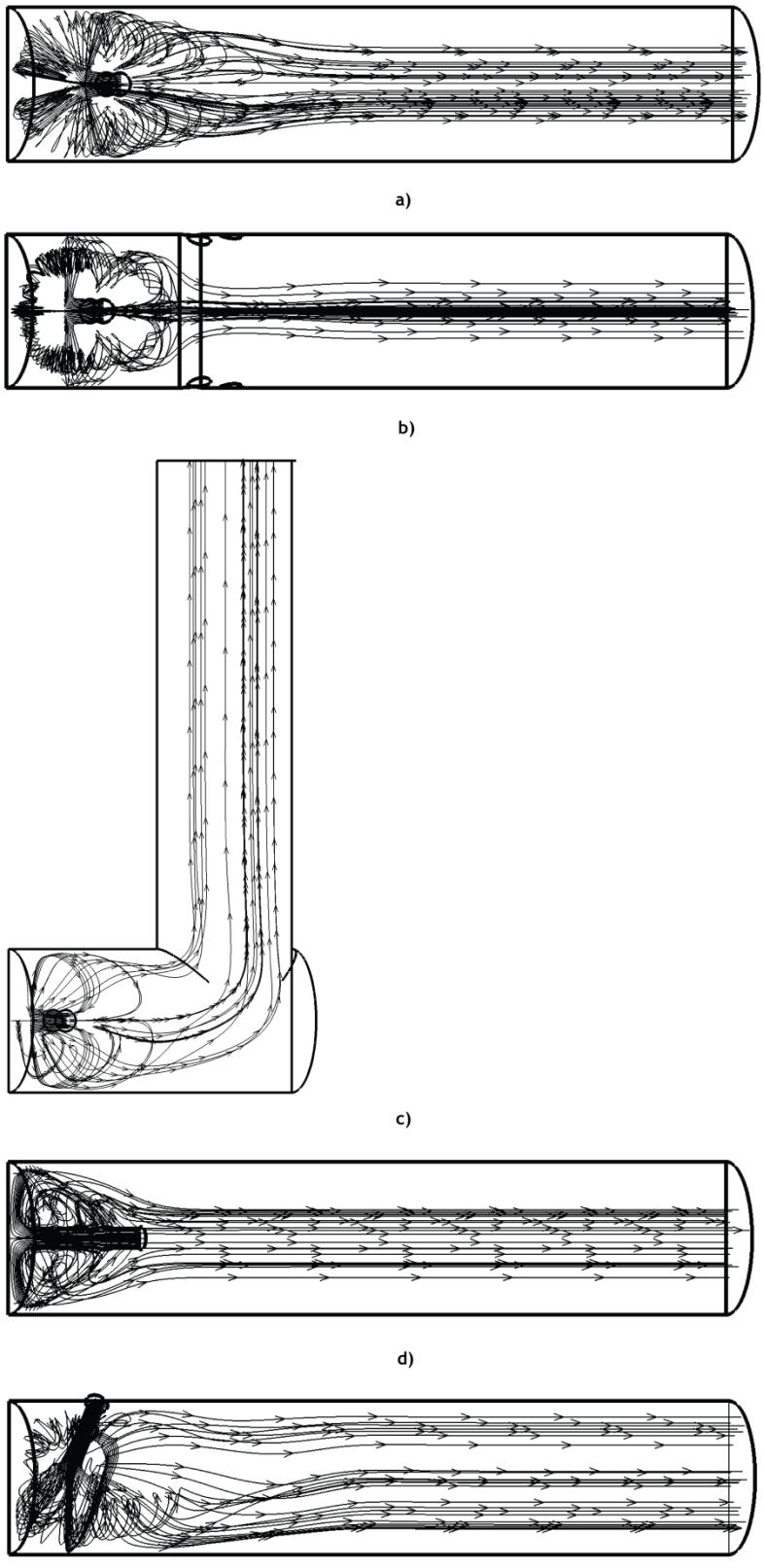

Figure 3-9 Pathlines for $Re = 75$, a) Opposed jets mixing chamber, b) **Opposed jets mixing chamber with restrictions**, c) **Opposed jets mixing chamber in L configuration**, d) **Vertically angled jets mixing chamber** e) **Horizontally angled jets mixing chamber**

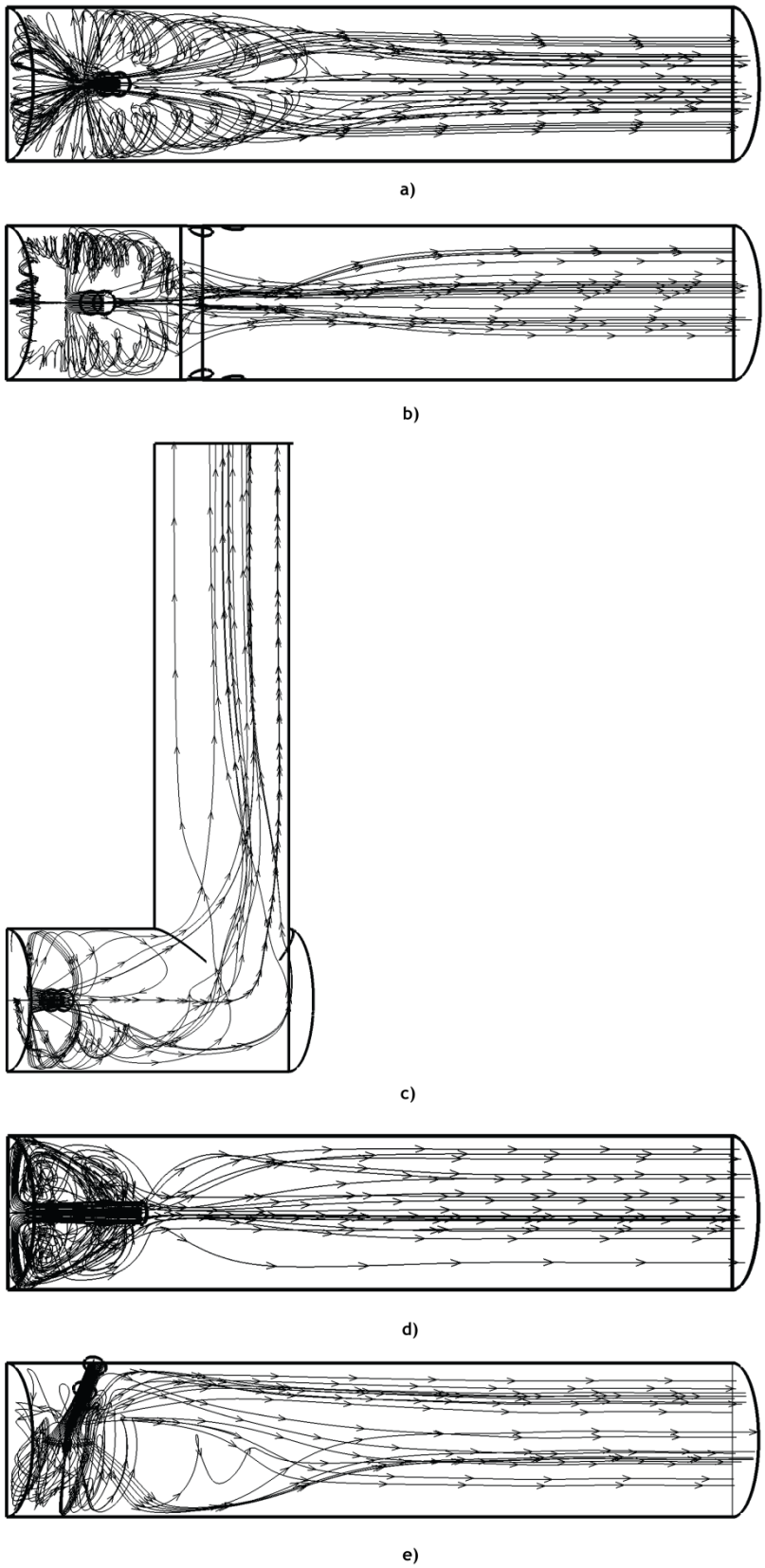

Figure 3-10 Pathlines for $Re = 150$, a) Opposed jets mixing chamber, b) **Opposed jets mixing chamber with restrictions**, c) **Opposed jets mixing chamber in L configuration**, d) **Vertically angled jets mixing chamber** e) **Horizontally angled jets mixing chamber**

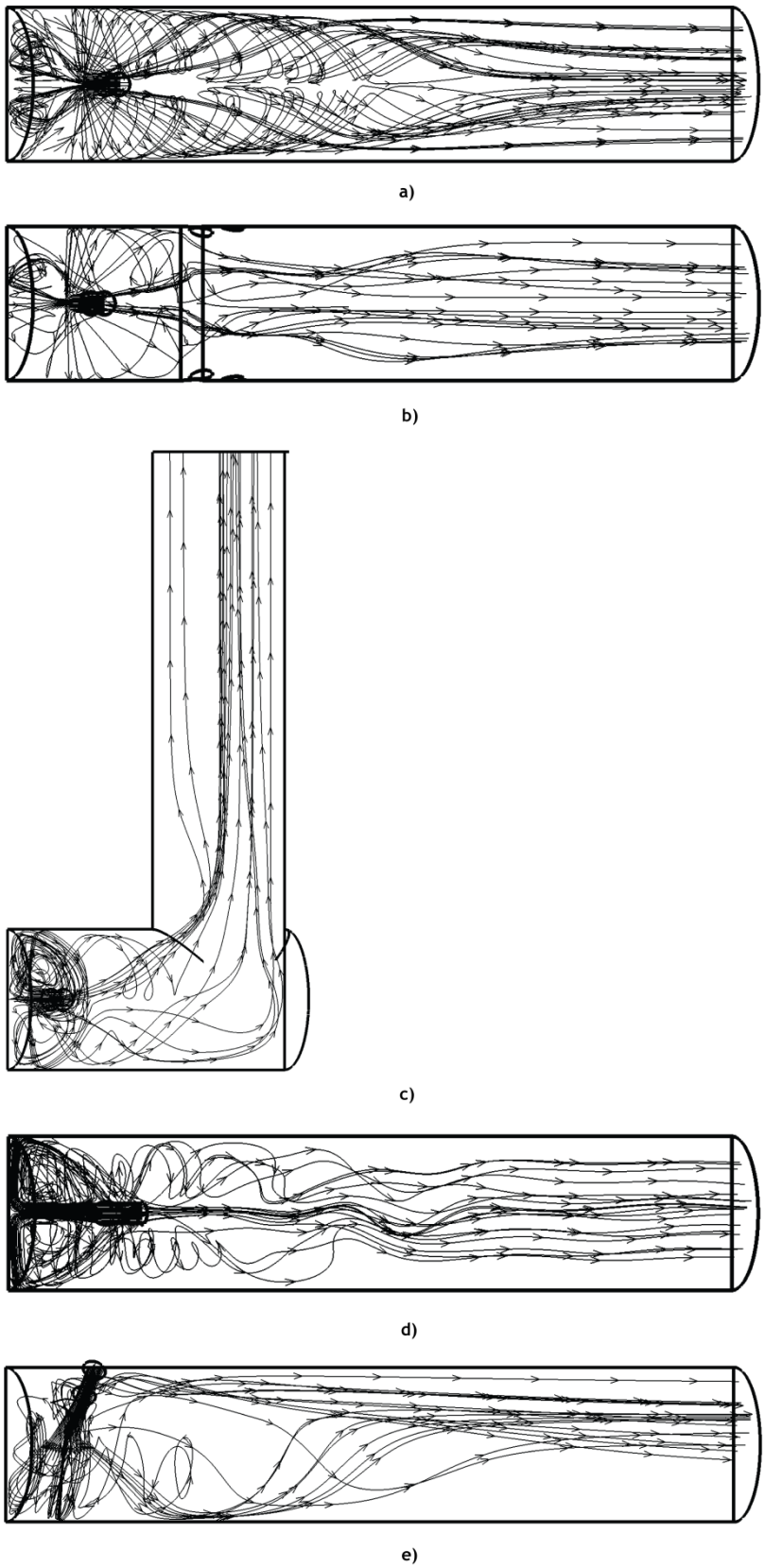

Figure 3-11 Pathlines for $Re = 300$, a) Opposed jets mixing chamber, b) **Opposed jets mixing chamber with restrictions**, c) **Opposed jets mixing chamber in L configuration**, d) **Vertically angled jets mixing chamber** e) **Horizontally angled jets mixing chamber**

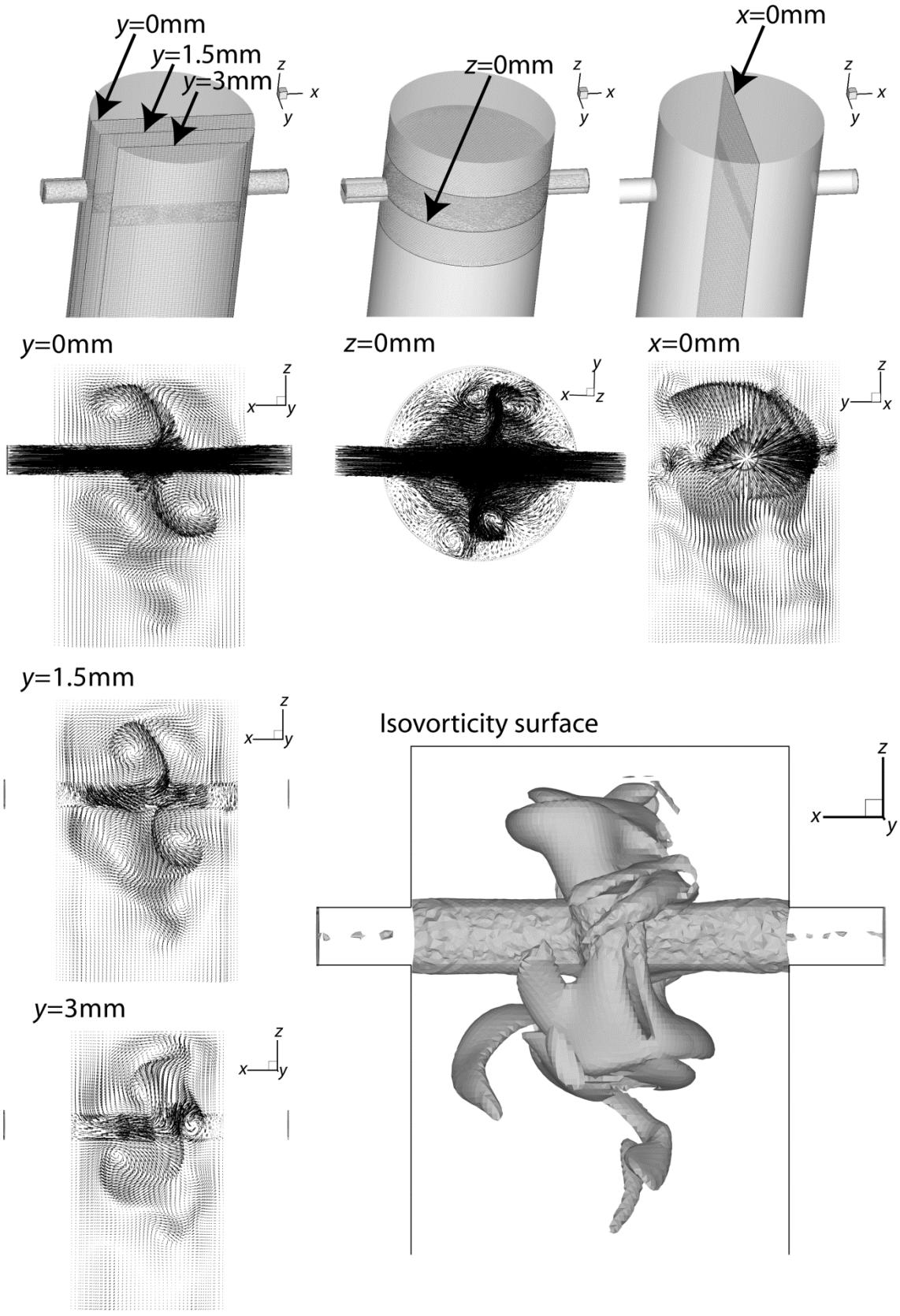

Figure 3-12 Flow imaging: vector maps from dynamic 3D CFD simulation at $Re = 200$ for Opposed jets mixing chamber (Santos et al., 2009)

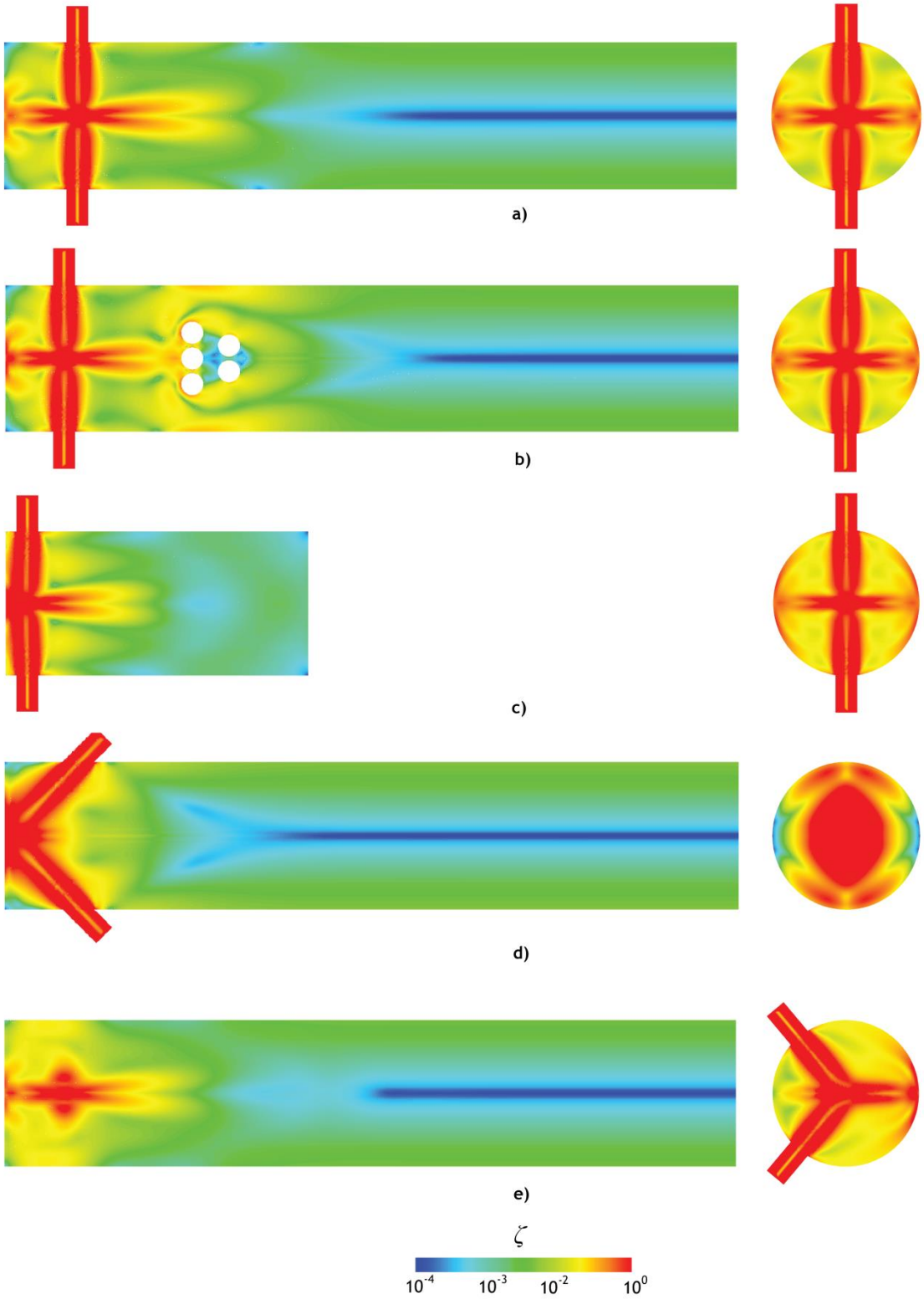

Figure 3-13 Non-dimensional strain rate field maps, with pathlines for a $Re = 75$, at planes XZ and XY a) Opposed jets mixing chamber, b) **Opposed jets mixing chamber with restrictions**, c) **Opposed jets mixing chamber in L configuration**, d) **Vertically angled jets mixing chamber** e) **Horizontally angled jets mixing chamber**

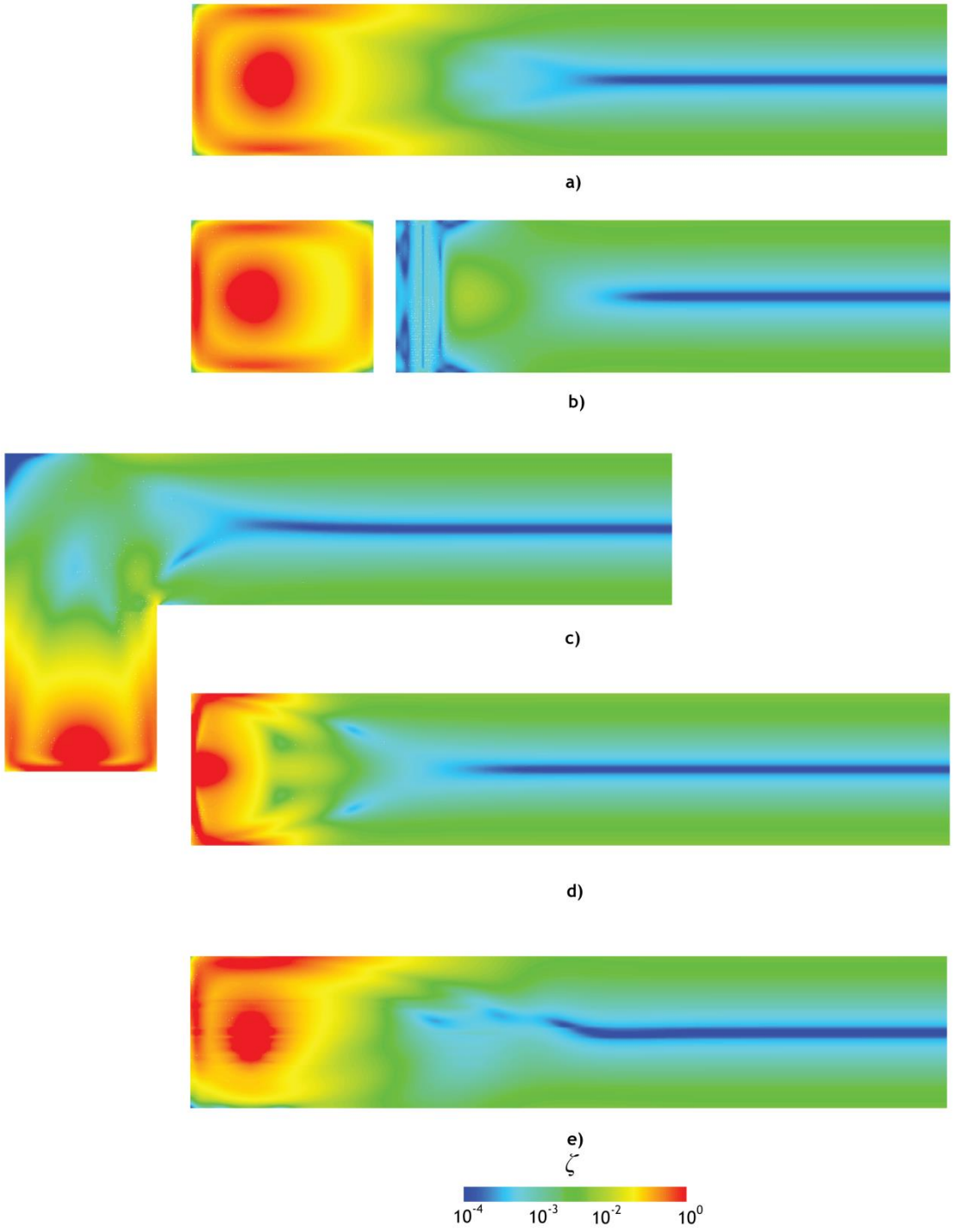

Figure 3-14 Non-dimensional strain rate field maps, $Re = 75$ **, at plane YZ a) Opposed jets mixing chamber**, b) **Opposed jets mixing chamber with restrictions**, c) **Opposed jets mixing chamber in L configuration**, d) **Vertically angled jets mixing chamber** e) **Horizontally angled jets mixing chamber**

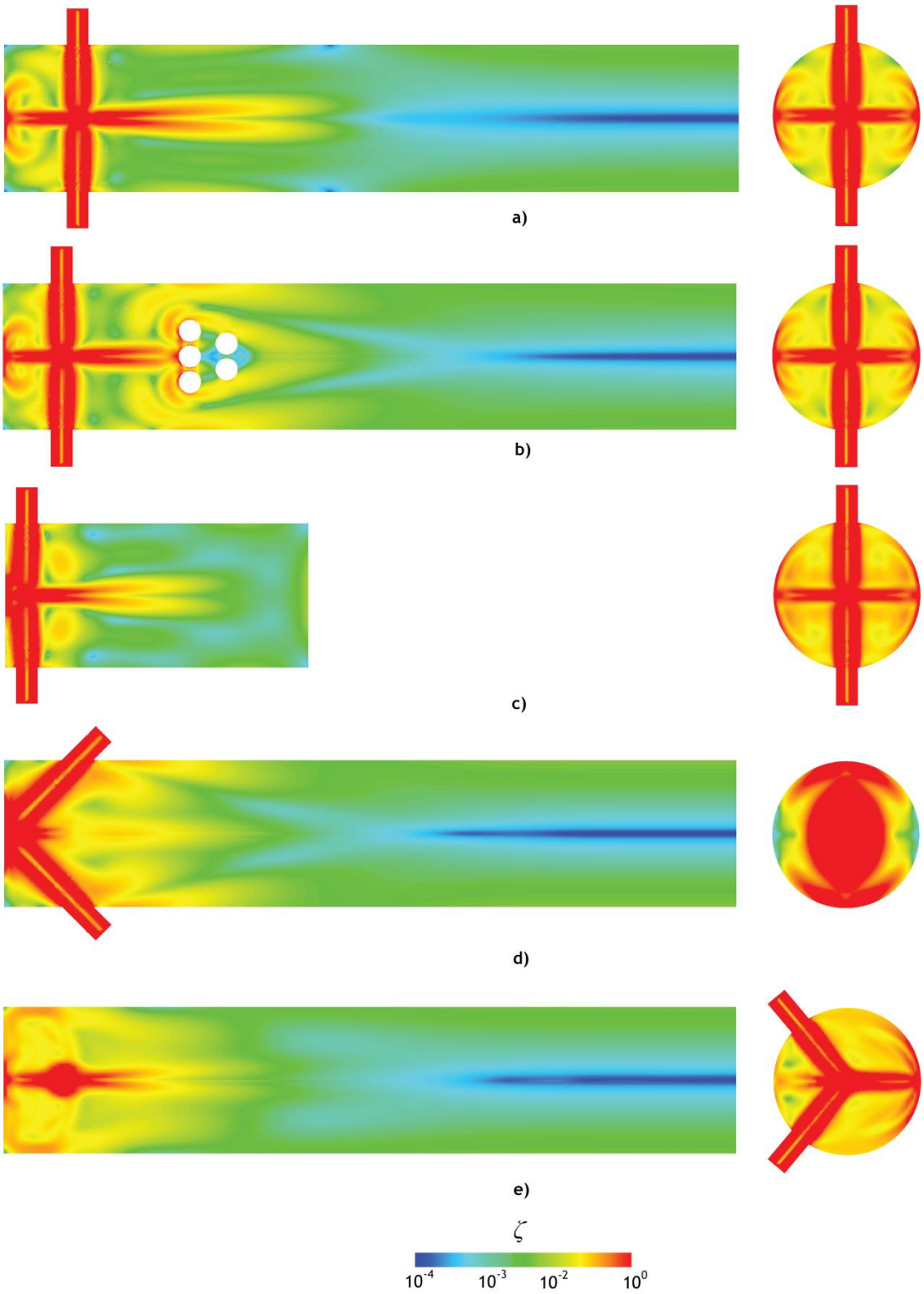

Figure 3-15 Non-dimensional strain rate field maps, with pathlines for a $Re = 150$, at planes XZ and XY a) Opposed jets mixing chamber, b) **Opposed jets mixing chamber with restrictions**, c) **Opposed jets mixing chamber in L configuration**, d) **Vertically angled jets mixing chamber** e) **Horizontally angled jets mixing chamber**

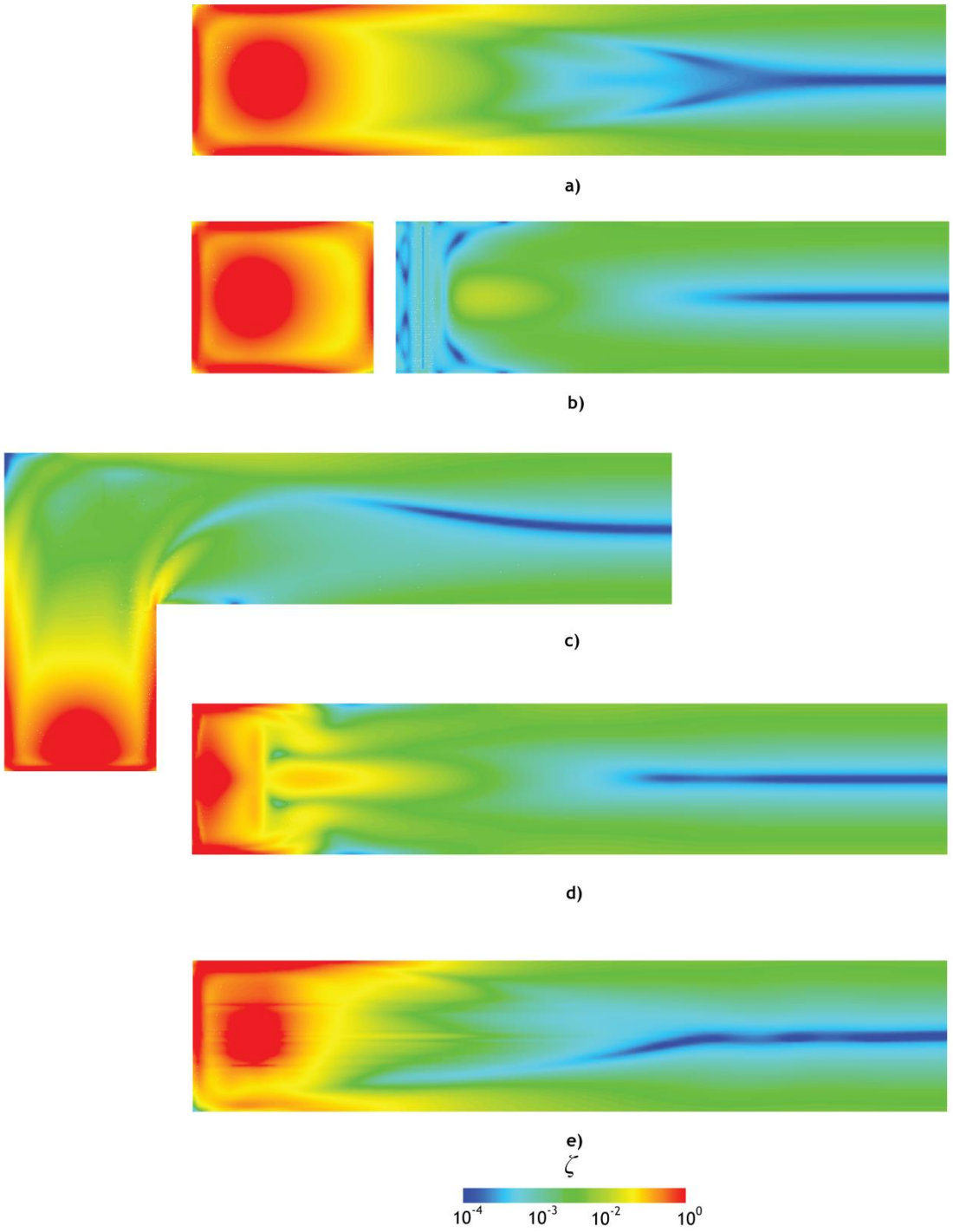

Figure 3-16 Non-dimensional strain rate field maps, $Re = 150$, at plane YZ a) Opposed jets mixing chamber, b) **Opposed jets mixing chamber with restrictions**, c) **Opposed jets mixing chamber in L configuration**, d) **Vertically angled jets mixing chamber** e) **Horizontally angled jets mixing chamber**

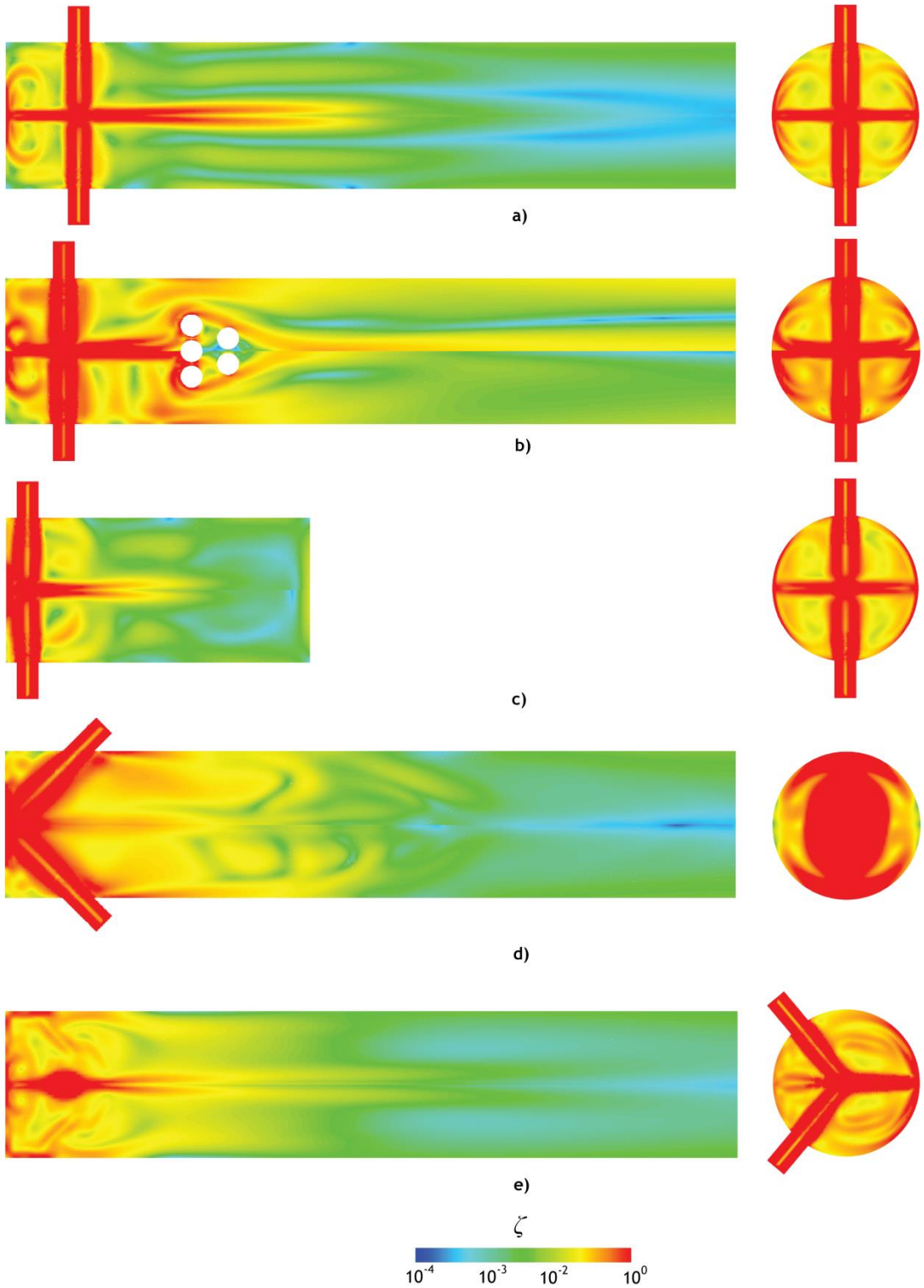

Figure 3-17 Non-dimensional strain rate field maps, with pathlines for a $Re = 300$, at planes XZ and XY a) Opposed jets mixing chamber, b) **Opposed jets mixing chamber with restrictions**, c) **Opposed jets mixing chamber in L configuration**, d) **Vertically angled jets mixing chamber** e) **Horizontally angled jets mixing chamber**

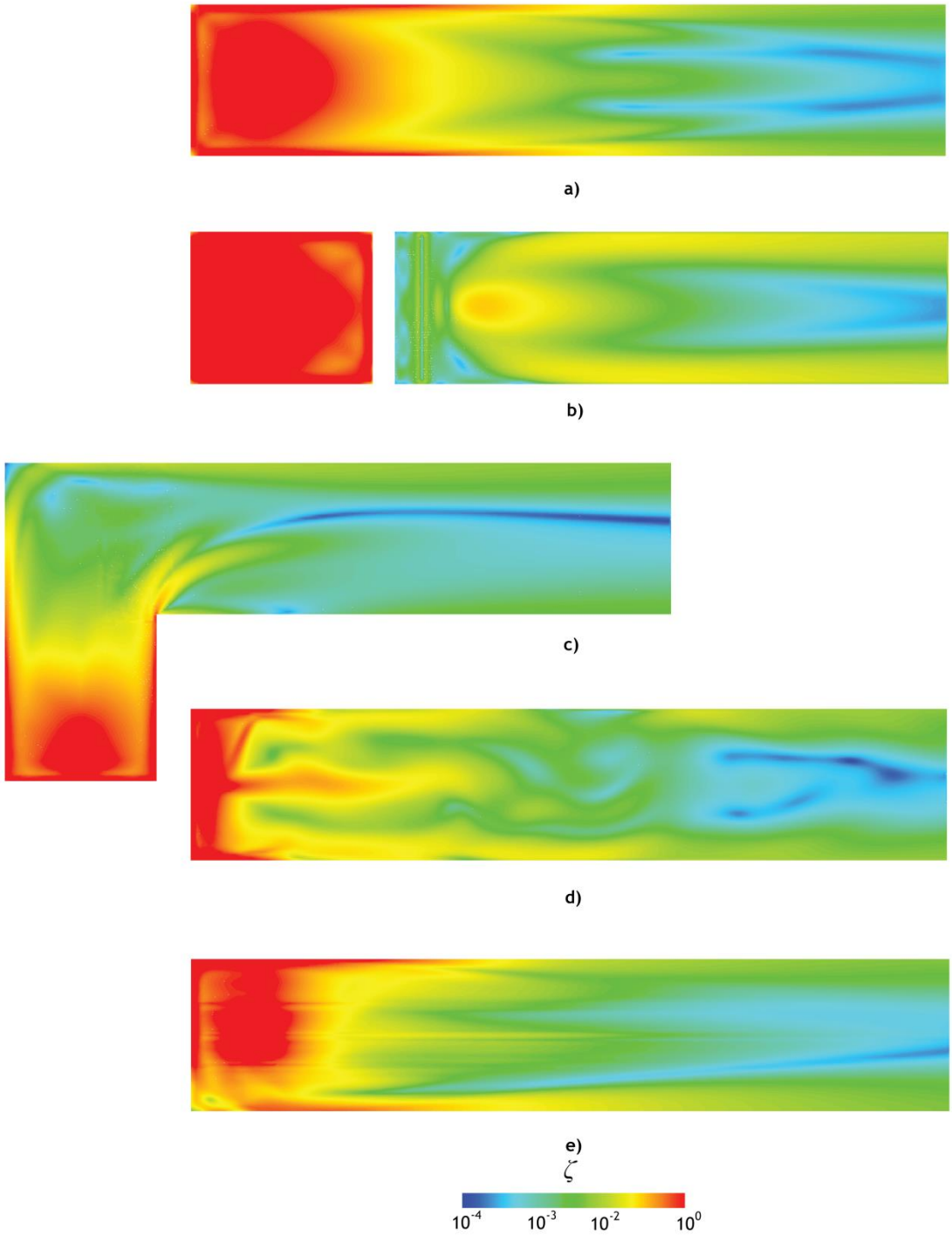

Figure 3-18 Non-dimensional strain rate field maps, $Re = 300$, at plane YZ a) Opposed jets mixing chamber, b) **Opposed jets mixing chamber with restrictions**, c) **Opposed jets mixing chamber in L configuration**, d) **Vertically angled jets mixing chamber** e) **Horizontally angled jets mixing chamber**

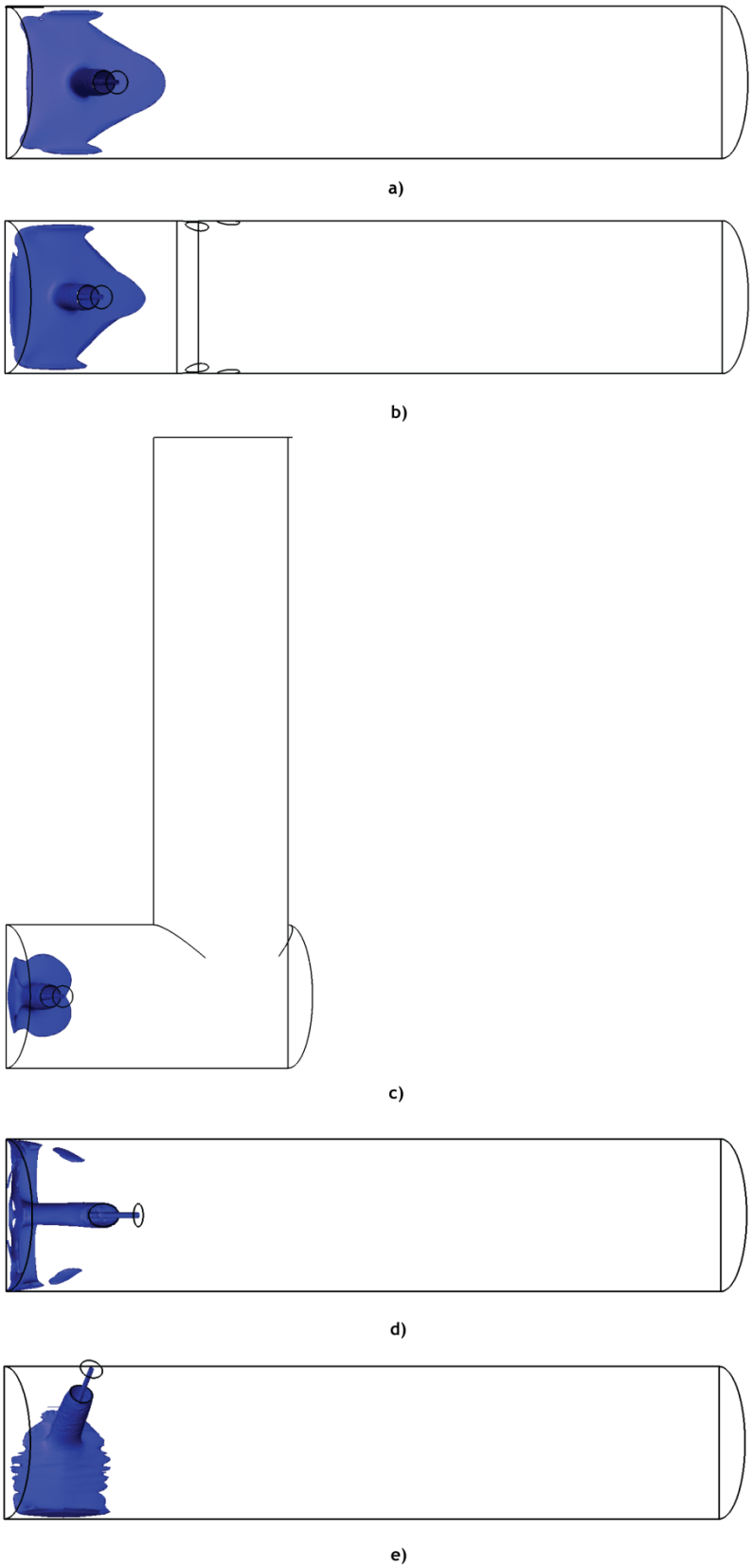

Figure 3-19 Isosurface for a non-dimensional vorticity of $\omega^* = 2$ and a $Re = 300$, a) Opposed jets mixing chamber, b) **Opposed jets mixing chamber with restrictions**, c) **Opposed jets mixing chamber in L configuration**, d) **Vertically angled jets mixing chamber** e) **Horizontally angled jets mixing chamber**

3.2.3 Macroscopic Energy Balance

A macroscopic energy balance is used to compute the energy that could be used for mixing, and benchmark the different mixing chambers geometries. Figure 3-20 shows a scheme of a Reaction Injection Moulding mixing chamber, with volume V. The mixing chamber has two inlets (indices 1 and 2) and one perpendicular outlet (index 3). The assignment of the variables: velocity, pressure, density and diameter to each inlet/outlet is made in Figure 3-20.

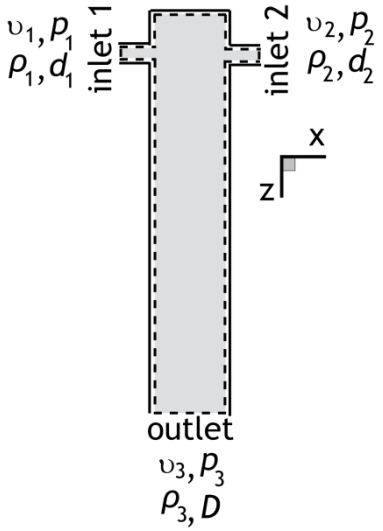

Figure 3-20 Geometric Model with a control volume - grey zone - and control surface – dash line

To obtain the energy balance, it was considered the First Law of Thermodynamics,

$$\frac{dQ}{dt} - \frac{dW_k}{dt} = \frac{DE}{Dt} \qquad 3.13$$

where Q is the net heat added to the system, W_k the total work done by the system on surroundings, and E is the total energy. The net work done by the system, dW_k/dt, is defined by the sum of shaft work, flow work resulting of traction forces and body work, given by

$$\frac{dW_k}{dt} = \frac{dW_s}{dt} - \oiint_{CS} \mathbf{T} \cdot \mathbf{v} dA - \iiint_{CV} \mathbf{B} \cdot \mathbf{v} \rho dV \qquad 3.14$$

where $\mathbf{T}$ are the traction forces, and $\mathbf{B}$ the body forces.

Applying the Reynolds Transport Equation to the substantial derivate of total energy in Equation 3.13 and using the previous equations, the energy balance is expressed by

$$\frac{dQ}{dt}-\frac{dW_s}{dt}+\oiint_{CS}\mathbf{T}\cdot\mathbf{v}dA+\iiint_{CV}\mathbf{B}\cdot\mathbf{v}\rho dV=\oiint_{CS}(e)\rho\mathbf{v}\cdot\mathbf{dA}+\frac{\partial}{\partial t}\iiint_{CV}(e)\rho dV \qquad 3.15$$

The total energy per unit mass is the sum of kinetic energy, $\frac{\upsilon^2}{2}$, potential energy, gz , and internal energy, u , defined as

$$e=\frac{\upsilon^2}{2}+gz+u \qquad 3.16$$

Hence, the general form of the energy balance applied to the mixing chamber over the control-volume V , is given by

$$\begin{aligned}&\frac{dQ}{dt}-\frac{dW_s}{dt}+\oiint_{CS}\mathbf{T}\cdot\mathbf{v}dA+\iiint_{CV}\mathbf{B}\cdot\mathbf{v}\rho dV=\\&=\oiint_{CS}(\frac{\upsilon^2}{2}+u+gz)\rho\mathbf{v}\cdot\mathbf{dA}+\frac{\partial}{\partial t}\iiint_{CV}(\frac{\upsilon^2}{2}+u+gz)\rho dV\end{aligned} \qquad 3.17$$

The following assumptions were considered:

- Steady state flow $\left(\frac{d}{dt}=0\right)$;
- Incompressible flow $\left(\nabla\cdot\mathbf{v}=0\right)$;
- Considering a isothermal case, the internal energy remains constant $\left(\Delta u=0\right)$;
- No body forces act on the system $\left(\iiint_{CV}\mathbf{B}\cdot\mathbf{v}\rho dV=0\right)$;
- Neglect potential energy $\left(\oiint_{CS}(gz)\rho\mathbf{v}\cdot\mathbf{dA}=0\right)$;
- No slip condition on walls $\left(\upsilon_w=0\right)$;
- No shaft work from the system over the surroundings $\left(\frac{dW_s}{dt}=0\right)$;

Based on assumptions made, and considering that dQ/dt is the available power for dissipation, Equation 3.17 transforms into

$$\frac{dQ}{dt}=\oiint_{CS}\mathbf{T}\cdot\mathbf{v}dA+\oiint_{CS}(\frac{\upsilon^2}{2})\rho\mathbf{v}\cdot\mathbf{dA} \qquad 3.18$$

Considering parallel flow at inlet and outlet, the surface forces acting on the boundary of the mixing chamber are only the inlet and outlet pressures, p_1, p_2 and, p_3, the distributed normal stress, p_w and shear stress, τ_w. Since at the walls there is a null velocity, the second term of Equation 3.18 only considers the pressures at inlets and outlet, and becomes

$$\oiint_{CS} \mathbf{T} \cdot \mathbf{v} dA = \oiint_{CS} \mathbf{p} \cdot \mathbf{v} dA \qquad 3.19$$

where $\mathbf{p}$ is the pressure tensor.

Expanding the term of pressures at boundaries, gives

$$\oiint_{CS} \mathbf{T} \cdot \mathbf{v} dA = \iint_{A_1} p_1 \upsilon_1 dA_1 + \iint_{A_2} p_2 \upsilon_2 dA_2 - \iint_{A_3} p_3 \upsilon_3 dA_3 \qquad 3.20$$

It is possible to find the relation between the infinitesimal areas with infinitesimal radius, dr, as state

$$dA = 2\pi r dr \qquad 3.21$$

A variable change is made using Equation 3.21 and the integral gives

$$\oiint_{CS} \mathbf{T} \cdot \mathbf{v} dA = \int_0^{d_1/2} p_1 \upsilon_1 2\pi r dr + \int_0^{d_2/2} p_2 \upsilon_2 2\pi r dr - \int_0^{D/2} p_3 \upsilon_3 2\pi r dr \qquad 3.22$$

Considering a fully developed laminar flow at inlet and outlet, the velocity has a parabolic profile, where υ_1 and υ_2 are the average velocities at inlet 1 and 2, and υ_3 is the average velocity at outlet 3, Equation 3.22 became

$$\begin{aligned} \oiint_{CS} \mathbf{T} \cdot \mathbf{v} dA = & \int_0^{d_1/2} p_1 2\upsilon_1 \left(1 - \frac{r^2}{\left(d_1/2 \right)^2} \right) 2\pi r_1 dr_1 + \int_0^{d_2/2} p_2 2\upsilon_2 \left(1 - \frac{r^2}{\left(d_2/2 \right)^2} \right) 2\pi r_2 dr_2 \\ & - \int_0^{D/2} p_3 2\upsilon_3 \left(1 - \frac{r^2}{\left(D/2 \right)^2} \right) 2\pi r_3 dr_3 \end{aligned} \qquad 3.23$$

Performing the integration, over the surface control at boundaries, gives

$$\oiint_{CS} \mathbf{T} \cdot \mathbf{v} dA = p_1 \upsilon_1 A_1 + p_2 \upsilon_2 A_2 - p_3 \upsilon_3 A_3 \qquad 3.24$$

Flow rate is defined as

$$q = \upsilon A \qquad 3.25$$

And substituting the previous equation at Equation 3.24, it can be defined as

$$\oiint_{CS} \mathbf{T} \cdot \mathbf{v} dA = p_1 q_1 + p_2 q_2 - p_3 q_3 \qquad 3.26$$

The flow rate at inlets and outlet is given by Equation 3.27.

$$2q = 2q_1 = 2q_2 = q_3 \qquad 3.27$$

Considering the previous equality of flow rate between inlets and outlet, Equation 3.26 becomes

$$\oiint_{CS} \mathbf{T} \cdot \mathbf{v} dA = \left(p_1 + p_2 - 2p_3 \right) q \qquad 3.28$$

A compact form can be obtained and is presented in Equation 3.29.

$$\oiint_{CS} \mathbf{T} \cdot \mathbf{v} dA = \sum_{i=1}^{2} \left(p_i - p_3 \right) q \qquad 3.29$$

Expanding the third term on Equation 3.18 at boundaries, it gives

$$\oiint_{CS} \left(\frac{\upsilon^2}{2}\right) \rho \mathbf{v} . dA = -\iint_{A_1} \left(\frac{\upsilon_1^2}{2} \right) \rho_1 \upsilon_1 dA_1 - \iint_{A_2} \left(\frac{\upsilon_2^2}{2} \right) \rho_2 \upsilon_2 dA_2 + \iint_{A_3} \left(\frac{\upsilon_3^2}{2} \right) \rho_3 \upsilon_3 dA_3 \qquad 3.30$$

Using Equation 3.21 and the parabolic velocity profile for a fully developed laminar flow, the integral in order of dr gives

$$\iint_{CS}\left(\frac{\upsilon^2}{2}\right)\rho\mathbf{v}.d\mathbf{A}=-\int_0^{d_1/2}\left(\frac{\left[2\upsilon_1\left(1-\frac{r^2}{\left(d_1/2\right)^2}\right)\right]^2}{2}\right)\rho_1 2\upsilon_1\left(1-\frac{r^2}{\left(d_1/2\right)^2}\right)2\pi r_1 dr_1-$$

$$-\int_0^{d_2/2}\left(\frac{\left[2\upsilon_2\left(1-\frac{r^2}{\left(d_2/2\right)^2}\right)\right]^2}{2}\right)\rho_2 2\upsilon_2\left(1-\frac{r^2}{\left(d_2/2\right)^2}\right)2\pi r_2 dr_2+ \qquad 3.31$$

$$+\int_0^{D/2}\left(\frac{\left[2\upsilon_3\left(1-\frac{r^2}{\left(D/2\right)^2}\right)\right]^2}{2}\right)\rho_3 2\upsilon_3\left(1-\frac{r^2}{\left(D/2\right)^2}\right)2\pi r_3 dr_3$$

Performing the integration of 3.31 results in

$$\iint_{CS}\left(\frac{\upsilon^2}{2}\right)\rho\mathbf{v}\cdot\mathbf{dA}=\left(\upsilon_1^2\right)\left(-\upsilon_1 A_1\right)+\left(\upsilon_2^2\right)\left(-\upsilon_2 A_2\right)+\rho_3\left(\upsilon_3^2\right)\upsilon_3 A_3 \qquad 3.32$$

Considering the relation between the flow rates and a parabolic profile for velocity at inlets and outlets, a compact form is present in Equation 3.33.

$$\iint_{CS}\left(\frac{\upsilon^2}{2}\right)\rho\mathbf{v}\cdot\mathbf{dA}=\sum_{i=1}^{2}\left(\rho_3\upsilon_3^2-\rho_i\upsilon_i^2\right)q \qquad 3.33$$

In the present work, it was assumed the same fluid properties at both inlets and at the outlet, and so

$$\rho=\rho_1=\rho_2=\rho_3 \qquad 3.34$$

Using Equation 3.29, Equation 3.33 and considering the mass flow rate as $\dot{m} = \rho q$, and applied it to the Equation 3.18, the energy balance is

$$\frac{dQ}{dt} = \sum_{i=1}^{2} (p_i - p_3) q + \sum_{i=1}^{2} \left(\upsilon_3^2 - \upsilon_i^2\right) \dot{m} \qquad 3.35$$

The second term from Equation 3.35 is the energy change associated to the pressure drop resulting from the fluid flow, named the pressure energy, PE. Pressure drop can be defined as the average of the pressure drop between the inlets and outlet (Siddiqui et al., 2009), as the follow

$$\Delta p = \frac{(p_1 - p_3) + (p_2 - p_3)}{2} \qquad 3.36$$

The pressure energy is defined by

$$PE = 2q\Delta p \qquad 3.37$$

The third term from Equation 3.35 is associated to the kinetic energy, KE, admits contribution to the energy balance is expressed by Equation 3.38.

$$KE = \left(2\upsilon_3^2 - \upsilon_1^2 - \upsilon_2^2\right) \dot{m} \qquad 3.38$$

The total energy dissipation is sum of pressure energy and kinetic energy. Therefore, the rate of dissipation energy per flux is given by Equation 3.39.

$$\varepsilon_t = \frac{PE + KE}{\dot{m}} \qquad 3.39$$

Direct measurements of energy dissipation are difficult to perform, and so an alternative method was adopted in the present work (Zhao and Kresta, 1996). The total energy dissipation can result from shear dissipation and friction dissipation (Siddiqui et al., 2009; Thakur et al., 2003). Thakur et al. (2003) defines total energy dissipation as

$$\varepsilon_t = \varepsilon_{fe} + \varepsilon_{se} \qquad 3.40$$

where ε_{fe} is the friction energy dissipation and ε_{se} is the shear energy dissipation.

Postulating that mixing results from laminar shear (Bourne and Garcia-Rosas, 1985; Lee et al., 1980; Ottino et al., 1979), the total energy dissipation that could be used for mixing

can be estimated from the shear energy dissipation, that can be calculated from the difference between total energy dissipation and friction energy dissipation, manipulating Equation 3.40.

For the calculation of the friction energy dissipation, the linear momentum conservation is applied to the control volume, V, and is given by (Shames, 1992).

$$\oiint_{CS} \mathbf{T} dA + \iiint_{CV} \mathbf{B} \rho dV = \oiint_{CS} (\mathbf{v}) \rho \mathbf{v} \cdot \mathbf{dA} + \frac{\partial}{\partial t} \iiint_{CV} (\mathbf{v}) \rho dV \qquad 3.41$$

Since the flow is symmetric, the contributions from momentum of jet 1 and jet 2 are matched and so the net contribution in this direction is zero, and due to this, only the orthogonal z-scalar component is studied.

Analysing the conservation of linear momentum equation over the z direction and considering the already stated assumptions, it is possible to find a relation between pressure, at top of mixing chamber, p_{top}, at outlet of mixing chamber, p_3, and wall shear, τ_w,

$$\iint_{A_f} p_{top} dA_f - \iint_{A_3} p_3 dA_3 - \iint_{A_w} \tau_w dA_w = \iint_{A_3} \upsilon_3 \rho_3 \upsilon_3 dA_3 \qquad 3.42$$

where A_f is the flow section or mixing chamber section, that is equal to A_3 and A_w is the lateral wall area.

Relating the pressure difference with mixing chamber's top and outlet pressure, the pressure resulting from friction is described by

$$\Delta p_f = p_{top} - p_3 \qquad 3.43$$

Considering a parabolic velocity profile, the integration of right hand side term in Equation 3.42 gives

$$\iint_{A_3} \upsilon_3 \rho_3 \upsilon_3 dA_3 = \frac{4}{3} \upsilon_3 \rho_3 \upsilon_3 A_3 \qquad 3.44$$

Integrating the left hand side term of Equation 3.42 and using Equation 3.43 and Equation 3.44, the friction pressure drop becomes

$$\Delta p_f = \frac{1}{A_f}\left(A_w \tau_{w_z} + \frac{4}{3}\upsilon_3 \dot{m} \right) \qquad 3.45$$

where τ_{w_z} is wall shear in z direction. The total rate work of the friction acting on the control surface can be define by

$$E_f = \int_0^{D/2} p_{top}\upsilon_f 2\pi r dr - \int_0^{D/2} p_3\upsilon_3 2\pi r dr \qquad 3.46$$

Integrating the previous equation, gives

$$E_f = \Delta p_f \upsilon_f A_f \qquad 3.47$$

Considering that

$$\upsilon_f = \frac{q_3}{A_f} = \frac{2q}{A_f} \qquad 3.48$$

The friction energy dissipation per unit mass is given by

$$\varepsilon_{fe} = \frac{2\Delta p_f q}{\dot{m}} \qquad 3.49$$

In this work, the five geometries studied are shown in Figure 3-1. All geometries have straight cylindrical runners, except for an L shaped geometry, with a $90°$ elbow. For this case, the conservation of linear momentum was calculated for two Cartesian coordinates, as Figure 3-21 shows, and is expressed by

$$\begin{cases} x & \iint_{A_f}(p_l - p_3)dA_f - \iint_{A_{w_1}} \tau_{w_x} dA_{w_1} = \iint_{A_1} \upsilon_1 \rho(-\upsilon_1 dA_1) \\ & \quad + \iint_{A_2} \upsilon_2 \rho(-\upsilon_2 dA_2) + \iint_{A_3} \upsilon_3 \rho(\upsilon_3 dA_3) \\ z & \iint_{A_f}(p_t - p_b)dA_f - \iint_{A_{w2}} \tau_{w_z} dA_{w_2} = 0 \end{cases} \qquad 3.50$$

where A_{w_1} is lateral wall area in first control volume, A_{w_2} is lateral wall area in second control volume and τ_{w_x} is wall shear in x direction. For this geometry two zones were considered at the control volume, the walls of first mixing chamber, denominated Z1 at

Figure 3-21, and the walls of second mixing chamber, Z2 at Figure 3-21. The p_b is the pressure on the base of Z1, and p_l is the pressure on the top of Z2.

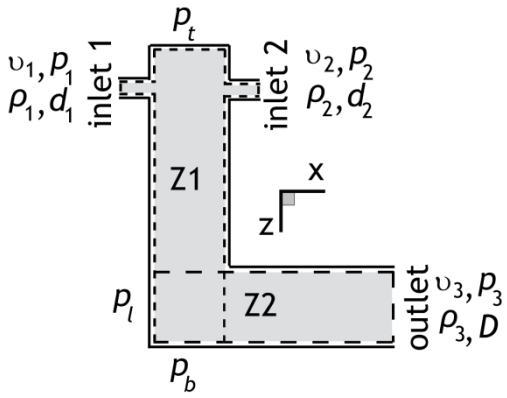

Figure 3-21 Geometric Model of an opposed jets in L, with a control volume - grey zone - and control surface – dashed line. The less sparse dashed line limits the first control volume, and the sparser dashed line limits the second control volume of the mixing chamber.

Integrating Equation 3.50, the pressure drop due the friction gives

$$\begin{cases} x & \Delta p_{f_x} = \dfrac{1}{A_{fl}}\left(A_{w_2}\tau_{w_x} + \dfrac{4}{3}\sum_{i=1}^{2}\left(\upsilon_3 - \upsilon_i\right)\dot{m} \right) \\ z & \Delta p_{f_z} = \dfrac{1}{A_{fl}}\left(A_{w_1}\tau_{w_z} + \dfrac{4}{3}\upsilon_3\dot{m} \right) \end{cases} \qquad 3.51$$

Based on previous equation, the friction dissipation for the oppose jets in L geometry is

$$\varepsilon_{fe} = \frac{\left(\Delta p_{f_x} + \Delta p_{f_z}\right) q_3}{\dot{m}} \qquad 3.52$$

The vertical angled jets mixing chamber has a velocity component in orthogonal z-scalar component, as shown in Figure 3-22. The velocity component in z is defined as

$$\upsilon_{inj_z} = \upsilon_{inj}\cos\theta \qquad 3.53$$

where θ is the angle between the injector axis and the mixing chamber axis.

Applying the conservation of momentum for orthogonal z-scalar component

$$\begin{aligned} &\iint_{A_f} p_{top} dA_f - \iint_{A_f} p_0 dA_f - \iint_{A_w} \tau_w dA_w = \\ &= \iint_{A_1} \upsilon_{1_z}\rho_1\upsilon_{1_z} dA_1 + \iint_{A_2} \upsilon_{2_z}\rho_2\upsilon_{2_z} dA_2 + \iint_{A_3} \upsilon_3\rho_3\upsilon_3 dA_3 \end{aligned} \qquad 3.54$$

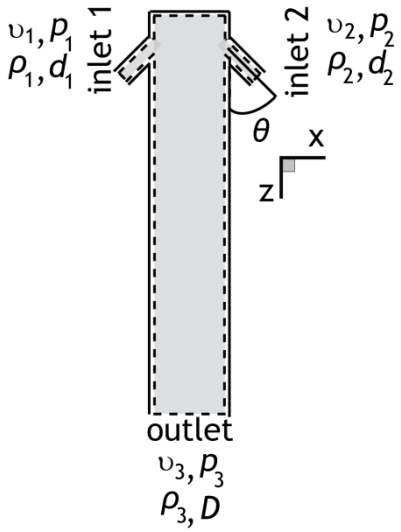

Figure 3-22 Geometric Model of a vertically angled jets mixing chamber, with a control volume - grey zone - and control surface - dash line.

The integration of Equation 3.54, after performing the variable change, using Equation 3.21, and considering the inner product between the velocity and normal vector to the inlets, gives

$$p_{top}A_f - p_0A_{fl} - \tau_w A_w = \frac{4}{3}\upsilon_1^2 \cos\theta\rho_1 A_1 + \frac{4}{3}\upsilon_2^2 \cos\theta\rho_2 A_2 + \frac{4}{3}\upsilon_3^2 \cos\theta\rho_3 A_3 \qquad 3.55$$

The friction pressure drop for this type of mixing chambers is given by

$$\Delta p_f = \frac{1}{A_f}\left[A_w\tau_{w_{zz}} + \frac{4}{3}\dot{m}\left(\upsilon_1\cos\theta + \upsilon_2\cos\theta + \upsilon_3\right)\right] \qquad 3.56$$

In order to compare the different geometries, the shear energy dissipation it is related with total energy dissipation,

$$\varepsilon_{sd} = \frac{\varepsilon_{se}}{\varepsilon_t} \times 100 \qquad 3.57$$

The objective is to achieve high ratios of shear dissipation, ε_{sd}, corresponding to high energy dissipation on shear, and consequently on mechanical mixing. The values for inlet pressure and shear force at the walls were computed from the CFD simulations at steady state. The geometric model, physical model, boundary conditions and numerical methods and discretization are described in Sub-chapters 3.2.1.1 to 3.2.1.4, respectively. The fluid properties are shown in Table 3-6. The analyses were performed for a $Re = 300$, but forcing a stationary flow regime (Santos et al., 2005b). The inlet and outlet pressures were

measured over the surfaces, and shear stress was computed by integration over the surface at mixing chambers walls, as show Equation 3.58. These values are present in Table 3-7.

$$\tau_{w_z} A_w = \int_{A_w} \tau_{w_z} dA_w \qquad 3.58$$

Table 3-6 Fluid properties

Properties	Value
$\rho[\mathrm{kgm^{-3}}]$	1000
$D[\mathrm{m}]$	0.01
$H[\mathrm{m}]$	0.05
$\upsilon_{inj}[\mathrm{ms^{-1}}]$	4
Re_{inj}	300
$q_{inj}[\mathrm{m^3s^{-1}}]$	7.07×10^{-6}
$\upsilon_3[\mathrm{ms^{-1}}]$	0.18
$q_3[\mathrm{m^3s^{-1}}]$	14.13×10^{-6}

Using Equations 3.39, 3.49 and 3.57 the different values of ε were calculated. A small part of the energy is dissipated by friction, as shows Table 3-8. According to Bates et al. (1963), the power number is analogous to the energy dissipation term, and can be defined as the ratio between the total amount of power supplied to the tank, and the power used only for mixing, and is defined in the terms of pressure drop as

$$N_p = \frac{\Delta p_{total}}{\Delta p_{total} - \Delta p_{friction}} \qquad 3.59$$

Table 3-7 CFD values for the different chambers

Mixing chamber	Opposed jets	Opposed jets with restrictions	L	Vertically angled jets	Horizontally angled jets
$p_{in}[10^3\,\mathrm{Pa}]$	5.6	6.2	4.6	10	5.9
$\tau_{w_z} A_w[10^{-3}\,\mathrm{N}]$	1.7	10	15	10	13
$V[10^{-6} m^3]$	3.9	3.9	4.2	3.9	3.9

From Table 3-8 is possible to see that L mixing chamber is the geometry that dissipates more energy by friction, in stationary states. The lowest friction energy dissipation is from the Oppose Jets chamber. On the other hand the mixing chamber with the opposed jets is the one using the largest energy fraction on mixing, having power numbers very close to one.

Table 3-8 Total Energy and Friction Energy for the different chamber

Mixing chamber	Opposed jets	Opposed jets with restrictions	L	Vertically angled jets	Horizontally angled jets
$\varepsilon_t[\mathrm{Jkg}^{-1}]$	21	22	20	26	21
$\varepsilon_{fe}[10^{-2}\,\mathrm{Jkg}^{-1}]$	4.0	17	35	93	20
$\varepsilon_{sd}[\%]$	99.8	99.2	89.8	98.4	99.1
N_p	1.01	1.03	1.83	1.04	1.04

3.2.4 Residence Time Distribution

For the assessment of residence time distribution (RTD) inside a reactor, Danckwerts (1953) proposed the injection of a tracer in the reactor and the monitoring of the evolution of the tracer concentration at the outlet through time. The tracer output curve, the Flow curve, is defined as

$$F\left(t_r\right)=\frac{F_{m_{out}}}{F_{m_{in}}} \qquad 3.60$$

where $F_{m_{in}}$ is the mixing chamber inlet mass flux of tracer, $F_{m_{out}}$ is the outlet mass flux of tracer and $t_r=t/\tau$ is the residence time, where τ is the passage time. The RTD can be calculated as

$$E\left(t_r\right)=\frac{dF\left(t_r\right)}{dt_r} \qquad 3.61$$

for the case where the tracer is injected as a step pulse in the reactor. In this work, the RTD was computed from steady state simulations for each geometry and for the same Re range. The tracer transport was modelled using the Species Transport Equation, where at $t_r=0$, the mass fraction of tracer was set to 1.0 in both inlet nozzles. The values of $F\left(t_r\right)$ at outlet were computed during five passage times, 5τ. Santos et al. (2005b)reported that 5τ is enough to provide information about the macromixing in an opposed jets mixing chamber: the RTD. With this approach, the hydrodynamic solution was kept, and so only the transport equation was solved through time. The tracer diffusivity was set with typical values for liquids, for the case: $10^{-9}\,\mathrm{ms}^2$. The time evolution of the tracer at outlet was computed as

$$F(t_r) = \frac{\int X(t_r)\rho\left|\mathbf{v}(t_r)\cdot\mathbf{dA}\right|}{\int \rho\left|\mathbf{v}(t_r)\cdot\mathbf{dA}\right|} = \frac{\sum_{i=1}^{n} X_i(t_r)\rho_i\left|\upsilon_i(t_r)A_i\right|}{\sum_{i=1}^{n}\rho_i\left|\upsilon_i(t_r)A_i\right|} \qquad 3.62$$

in this equation, X is the mass fraction of tracer at the mixing chamber outlet, ρ is the density, $\mathbf{v}$ is the outlet velocity vector, $\mathbf{dA}$ is the area vector that is normal normal to the outlet, υ is the velocity component normal to the outlet, and A is the outlet area.

In the present work, the $F(t_r)$ values were recorded, and the RTD was computed using second order progressive finite divided differences,

$$E(t_r) = \frac{-F(t_r)_{i+2} + 4F(t_r)_{i+1} - 3F(t_r)_i}{2\left[(t_r)_{i+1} - (t_r)_i\right]} \qquad 3.63$$

Figure 3-23 shows the RTD for each geometry and for the Re range studied. As a comparative example, it was added the RTD of a Continuous Stirred-Tank Reactor (CSTR). The RTD of n CSTRs in series is given by,

$$E(t_r) = \frac{n(nt_r)^{n-1}}{(n-1)!}e^{-nt_r} \qquad 3.64$$

The RTD curves shown in Figure 3-23 peak below the passage time τ and after reaching the peak value show a decrease that is significant up to τ. The jets impinge each other at high speed being spread radially after the impingement point, some of the high speed flow issuing from the impingement point is going directly towards the outlet, this is the reason for the early onset of high concentration of tracer at the outlet, at around 0.2τ. Furthermore, in the opposed jets mixing chamber without mixing restrictors it is clearly seen an early peak of tracer, this is a clear evidence of the existence of a shortcut from the inlet to the outlet.

In all geometries the RTD peak decreases with the Re. The only exception is the opposed jets mixing chamber, where the peak maximum increases with the Re. If in one hand the spreading of tracer can be enhanced by a decrease of viscous forces, which is the reason for the slight decrease on the RTD peaks, on the other hand for higher Re the fluid passes in the mixing chamber in shorter times reducing the time for diffusion thus leading to an increase of the maximum value of the RTD. So in the cases where the fluid is not forced to

engage on some complex paths, the decrease on the fluid passage time can decrease the tracer dispersion.

Phenomena such as channelling, can be assessed from some statistic quantities computed from the RTD. The first and second moment of the RTD were calculated as follows (Fogler, 2002)

$$t_{av} = \int_{t/\tau=0}^{\infty} t_r E(t_r)\, dt_r \qquad 3.65$$

$$\sigma_{t_r}^2 = \int_{t/\tau=0}^{\infty} \left(t_r - t_{avg}\right)^2 E(t_r)\, dt_r \qquad 3.66$$

Because in this work it was not obtained an analytical expression for the $E(t_r)$, the values of t_{av} and $\sigma_{t_r}^2$ were computed numerically as follows

$$t_{av} = \sum_{t/\tau=0}^{\infty} t_r E(t_r)\, \Delta t_r \qquad 3.67$$

$$\sigma_{t_r}^2 = \sum_{t/\tau=0}^{\infty} \left(t_r - t_{avg}\right)^2 E(t_r)\, \Delta t_r \qquad 3.68$$

Table 3-9 shows the first and second moment of the $E(t_r)$ for the geometries and for the range of studied Re. The t_{av} decreases with the Re. The highest values of t_{av} were obtained for the opposed jets and L mixing chambers. The lowest values were obtained for the angled jets mixing chambers.

Although the variance or second moment, $\sigma_{t_r}^2$, which stands for the dispersion distribution of tracer, decreases slightly with Re there is not a clear trend and the slight decrease is probably due to the reduction of the time for diffusion. The effect of geometry on $\sigma_{t_r}^2$ is clear enough to draw some conclusions. The chambers that promote the direct contacting of opposed jets present larger values of $\sigma_{t_r}^2$ than the angled jets chambers, see Table 3-9. The second momentum is mainly associated with the spreading of tracer from diffusion, since in the steady state simulations advective mixing does not play a major role. The mixing chambers with directly opposed jets promote a larger initial contact of the two reactants, than the angled chambers.

The number of $n\,CSTR$ in series that better describes a RTD tanks can be calculated by the inverse of the second moment (Fogler, 2002)

$$n = \frac{1}{\sigma_{t_r}^2} \qquad 3.69$$

An adjustment between the computed values to the cascade of $n\,CSTR$ in series equation, as shown by Equation 3.64, was done using ordinary least square (OLS) method defined as

$$R = \sum_{i=1}^{m} \left(\left(\frac{dF(t_r)}{dt_r} \right)_i - \left(\frac{n(nt_r)^{n-1}}{(n-1)!} e^{-nt_r} \right)_i \right)^2 \qquad 3.70$$

where R is the square sum of the deviation between simulation data and the CSTR cascade model, and m is the total number of time steps. Table 3-9 shows the n CSTR in series used to model each mixing chamber, either by using Equation 3.69 or either by using the value of n that minimizes R.

From CSTR in series model, the opposed jets geometries vary between 3 to 4 CSTRs. The information from this model is the same as from the $\sigma_{t_r}^2$ value, although the n variable is more physically sounded: larger number of reactors represents less dispersion of tracer through the all domain and more compartmentalization. In this case the differences with both the operation Reynolds number and the geometry are not significant with all values of n between 3 and 4.

The results obtained from the fitting between the numerical results and the equation of the RTD from the cascade of $n\,\mathrm{CSTR}$ in series, gave a range for n between 3 and 8 CSTR in series. The results are distinct from those obtained with the model expressed by Equation 3.69, which applies to RTDs that are well represented by a tank in series model. Furthermore from the plots of Figure 3-23 it is clear the poor adjustment of the RTDs to the model. The RTDs from the mixing chambers have a larger concentration of tracer around the peak, because unlike CSTRs where fluid of all ages are being mixed, in the mixing chambers pure fluids are contacted and then flow through a certain path to the outlet without significant back mixing.

Table 3-9 First and second moment for the different geometries for different Re

Mixing Chamber	Re	$t_{av}\left[10^{-1}\right]$	$\sigma_{t_r}^2\left[10^{-1}\right]$	$n\ CSTR$	$n\ CSTR$ using OLS
Opposed jets	75	11	3.1	3	4
	150	9.6	2.4	4	8
	300	9.7	3.4	3	5
Opposed jets with restrictions	75	9.1	3.1	3	4
	150	9.1	2.7	4	5
	300	9.2	3.2	4	4
L	75	8.9	3.2	3	5
	150	9.6	2.9	3	5
	300	9.6	2.7	4	8
Vertically angled	75	8.3	2.8	4	5
	150	8.3	2.8	4	4
	300	7.9	2.4	4	4
Horizontally angled	75	8.8	2.8	4	3
	150	9.5	2.7	4	8
	300	9.5	2.7	4	4

Santos et al. (2005b) computed the RTD of opposed jets mixing chamber from 2D CFD simulations. In 2D simulations the jets cannot spread radially and are pointed to the outlet, which originates an early arrival of tracer at the outlet and an RTD with a similar shape than those obtained from 3D steady state simulation but with most of the tracer passing through the outlet at a time less than 0.4τ. In the 3D simulations the average passage time is close to τ, $t_{av} \approx \tau$, and so the tracer is being spread throughout the entire chamber. The preferential path effect, or shortcuts, which so clearly set the RTD for 2D simulations do not play a major role in the 3D simulations.

Dynamic 2D simulations of Santos et al. (2005b) show that the onset of vortices that engulf fluid from both jets yields an RTD that is well adjusted by the tank in series model, being the best fit obtained for $n = 3$ tanks. The dynamic 3D CFD simulations of opposed jets also show a flow with vortices engulfing both jets, see Figure 3-12, and so it is likely that for dynamic flow regimes with the onset of backmixing flow patterns the RTD becomes better described by the tank in series model. Dynamic CFD simulations of the 3D chamber with mass transfer were not performed due to the large amount of computational resources that would be required.

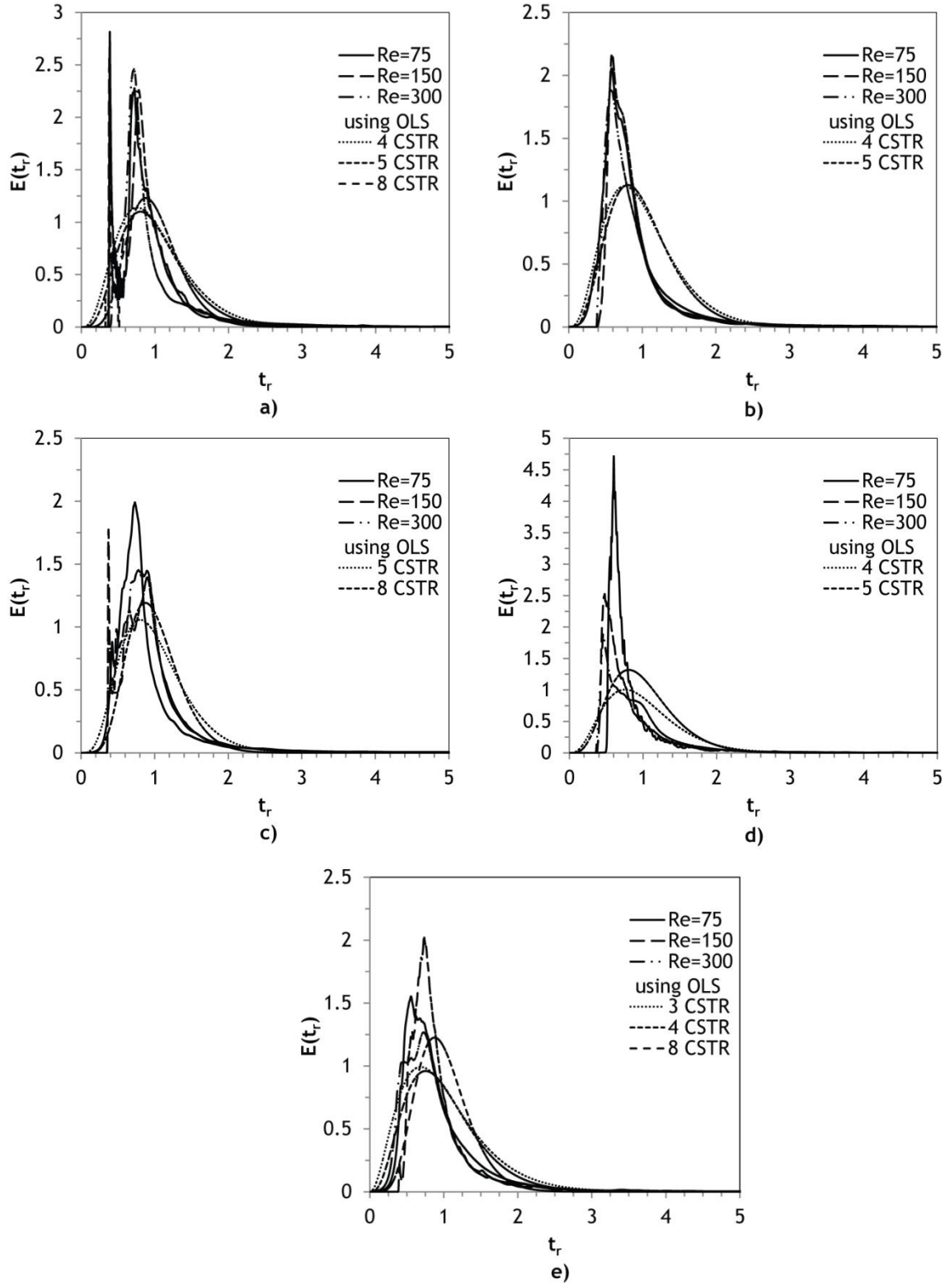

Figure 3-23 Residence Time Distribution for each geometry and Re the studies a) Opposed jets mixing chamber, b) **Opposed jets mixing chamber with restrictions**, c) **Opposed jets mixing chamber in L configuration**, d) **Vertically angled jets mixing chamber** e) **Horizontally angled jets mixing chamber**

3.3 RIMCop System Characterization

Two different RIM equipments were used in the present work. The first one, an in-house built RIM machine at the CDRsp-IPLeiria, and the second equipment an in-house built machine at LSRE-FEUP. This section characterizes both machines.

3.3.1 RIM Equipment Project

The main requirements of a RIM system are:

- Raw material properly conditioned and storage in adequate tanks;
- Accurate reactants dosing or metering;
- Reactants efficient mixing;
- Mixing chamber pressurization, to ensure the required pressure for the mould cavity filling;
- Reactant's recirculation between storage tanks and mixing head;
- Constant reactant's temperature.

Considering the upper requirements, a RIM equipment has the following components:

1. Storage Tanks;
2. Dosing or metering System;
3. Mixing Head;
4. Control System.

Despite the some common components and features between both RIM equipments (at CDRsp-IPLeiria and LSRE-FEUP), the equipments were projected with different requirements, resulting in two different systems.

The CDRsp-IPLeiria prototype, was reformulated for the present work from an equipment previously built under the PLASRIM project with industrial funding from PLASDAN, leadership by CDRsp-IPLeiria, Figure 3-24. PLASRIM was the first Portuguese project for the construction of RIM equipment, in the year 2003. The present work developed and implemented some reformulations to the PLASRIM equipment. One of the reformulations was the changing of the dosing pumps from piston type to gear pumps, to maintain a more constant flow. In addition a new mixing chamber was designed, built and installed in this system. The use of metering pumps reduced the system capacity to supply fluid at high pressure to the mixing chamber, and so the length of the tubing system was shortened. Figure 3-25 shows CDRsp-IPLeiria prototype's scheme. The blue and green lines are the reactants tubes, between the storage tanks and mixing head. The RIM machine at the

CDRsp-IPLeiria enables the raw materials heating, recirculation between mixing-head and tanks, and the reactants mixing.

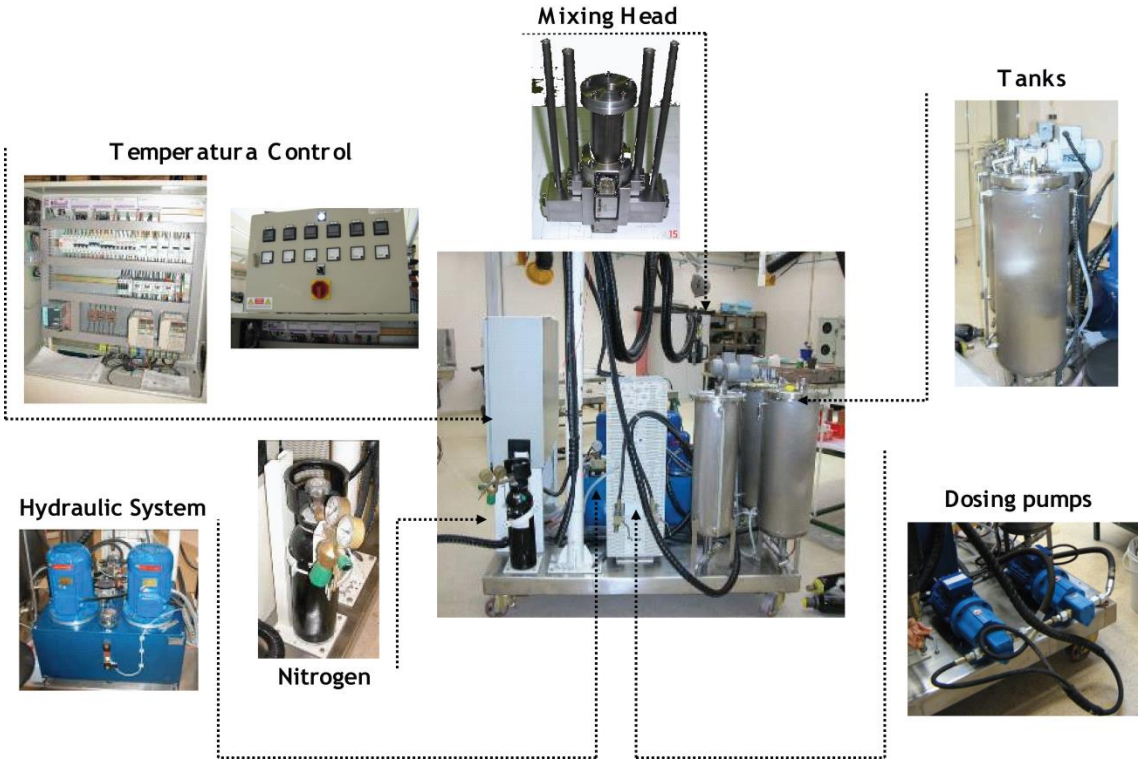

Figure 3-24 Industrial RIM prototype at CDRsp-IPLeiria, adapted from PLASRIM project

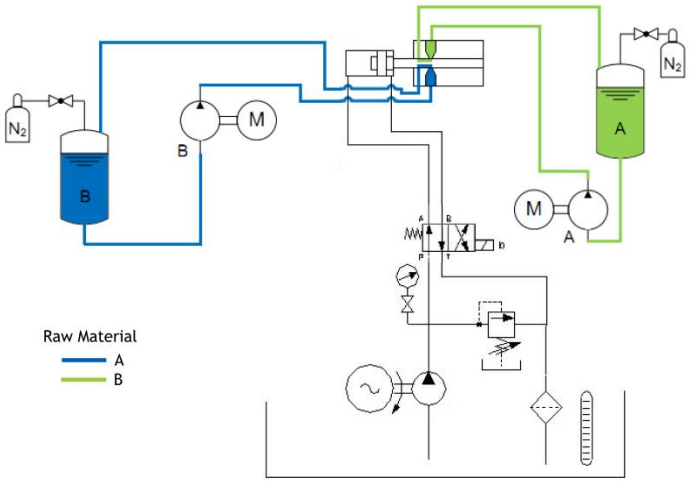

Figure 3-25 Flow scheme of the RIM prototype machine at CDRsp-IPLeiria

On other hand, the LSRE-FEUP prototype was developed from scratch, - Figure 3-26. It has an aluminium structure where all the components were assembled. On the structure were installed the storage tanks, dosing pumps, mixing-head and control system. Figure 3-27 shows the scheme of the LSRE-FEUP's prototype, where blue and green lines are the reactants flow. This system performs the same tasks of the one installed in CDRsp-IPLeiria,

and in addition it allows the recirculation between storage tanks and dosing pumps, without going through the mixing-head. Another key aspect on LSRE-FEUP equipment was the design and implementation of a novel control system, denominated RIMcop®, Reaction Injection Moulding with Control of Oscillation and Pulsation. In this control system, a real-time monitoring of the static pressure in the feeding lines to the mixing chamber is performed, which enables the assessment of mixing during the mould filling. The feasibility of the novel control system was studied from previous works using experimental procedure with inert fluids (Santos, 2003; Santos et al., 2009) and numerical simulations (Erkoc et al., 2007). The aim of the present work, was to proof the RIMcop® process with an actual equipment for the injection of a polyurethane formulation in a mould.

For both equipments, a detailed description of the different components is made over the next sections.

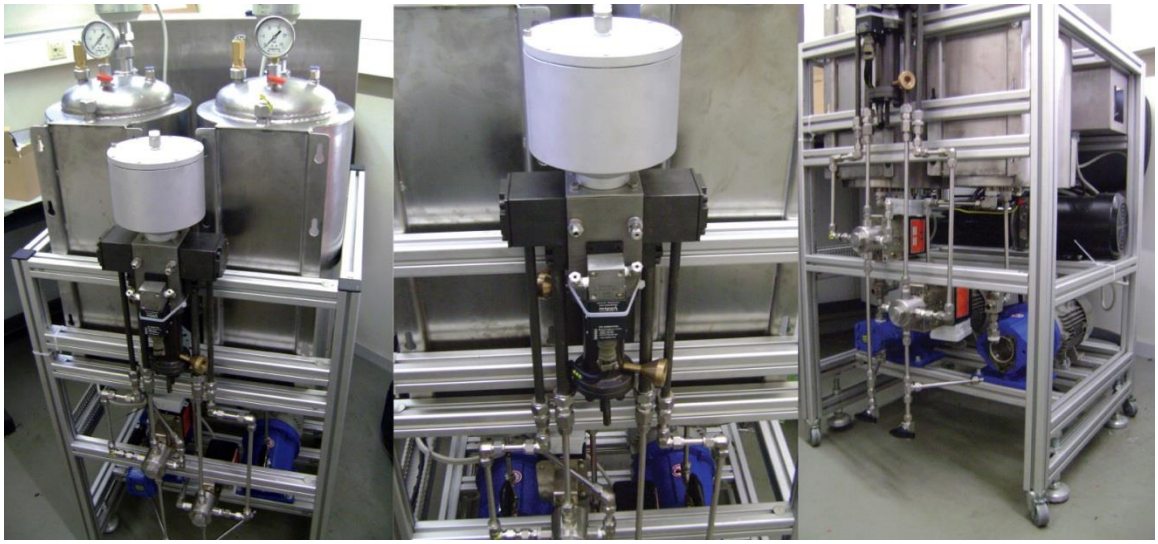

Figure 3-26 Pilot RIMcop® machine at LSRE-FEUP

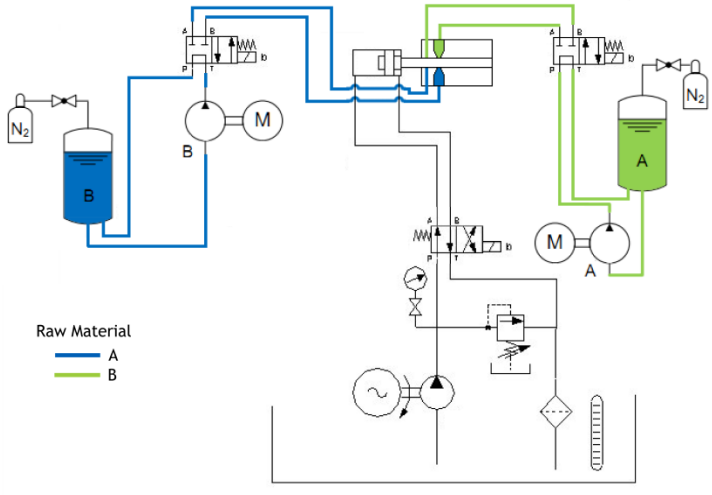

Figure 3-27 Flow scheme of the pilot RIMcop® machine at LSRE-FEUP

3.3.1.1 Mixing Head

A new mixing-head was projected based on the patented RIM technology by Lopes et al. (2005), named RIMCop®, acronym of *Reaction Injection Molding and Control by Oscillation and Pulsation*. This technology uses a mixing chamber with opposed jets, as the one proposed by Keuerleber and Pahl (1972). The main innovation of RIMcop® resides in the real-time measuring of the static pressure difference between the feeding lines to the inlet jets, using a pressure transducer sensor (PTS). Erkoc et al. (2007) showed that the frequency of the static pressure difference can be used as a control variable, since this frequency is a clear indication of the mixing conditions and flow regime in the mixing chamber. Figure 3-28 shows schematically the main concept behind RIMcop®. Using CFD tools and experimental methods, Teixeira (2000) and Santos (2003) studied the flow regime inside a mixing chamber and analysed some geometrical parameters, as the top distance of the injectors and chamber length. The results, were also used in the already mentioned patent (Lopes et al., 2005) as good guidelines for the project of a RIM machine mixing chamber.

The prototype has five big groups:

- Material inlet – this is the kit with the components that deliver the raw materials into the mixing chamber. One of the most important components of this kit are the interchangeable injectors that are designed according to the stoichiometric ratio of each formulation;
- Material outlet – allows the outlet flow of non-mixed material, and recirculates it from the mixing chamber back to the storage tanks;
- Cylinder – actuates the cleaning piston;
- Cleaning piston – it is used to clean the mixing chamber after mould filling. The piston also blocks the mixing chamber after mould filling and forces the raw materials recirculation from the injectors to the recirculation lines that are blocked during mould filling;
- Mixing-head Body – Metallic block with the cylindrical mixing chamber and all the other elements.

Figure 3-29 shows the different groups of the mixing head. In the centre there is an exploded view that shows how all groups are assembled in the Mixing-Head Body. Around the centre view, are shown the different groups.

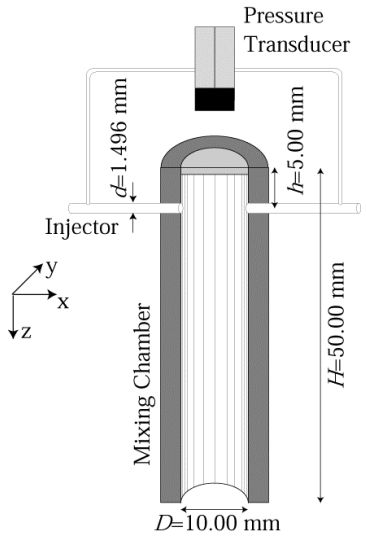

Figure 3-28 Patented scheme of RIMCop mixing-chamber (Lopes et al., 2005)

A key element of the new RIMcop® mixing chamber is the injector, shown in Figure 3-30. The injectors are designed to accelerate the fluid and to maximize the jet's kinetic energy, passing it through a small diameter nozzle upon issuing into the mixing chamber, but taking into count the pressure losses. In the end of injector design is a trade-off between the jets acceleration and the resulting head loss. The diameter also depends on fluid properties and process parameters. To accelerate the flow without creating secondary flow, there is a conical contraction with a gradual slope of $15°$. The length was set to promote a *Poiseulle* profile of the jet when issuing into the mixing chamber. The injector is inside of an isolation body made of *Teflon,* which keeps the temperature stable. The injectors are replaceable so they can be changed when using the machine with different material formulations, in order to maintain the kinetic energy balance between the opposed jets for the specific stoichiometric ratio of each formulation. The kinetic energy ratio between opposed jets is defined as,

$$KE_r = \frac{\rho_1 \upsilon_1^3 d_1^2}{\rho_2 \upsilon_2^3 d_2^2} \qquad 3.71$$

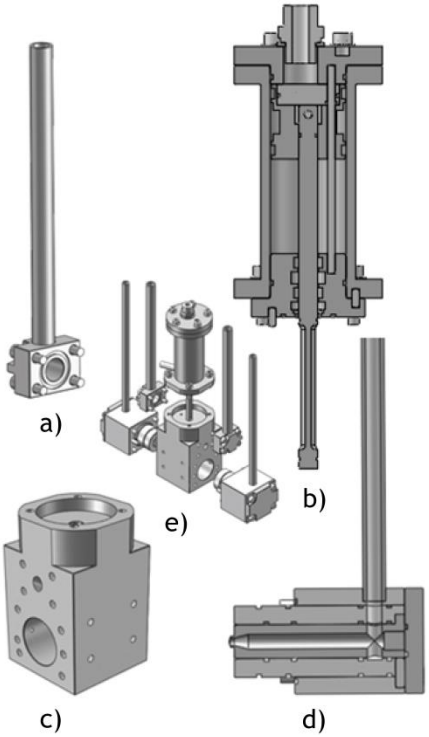

Figure 3-29 Cad drawing of the Mixing-Head groups: a) Material outlet b) cylinder and cleaning piston c) Mixing-Head Body d) Material Inlet e) exploded view of the Mixing-Head

The impact of the balancing of momentum and kinetic energy between the opposed jets will be analysed in Chapter 4 from the results of the experimental data.

Figure 3-30 Cad drawing of the injector.

In the injectors, before the contraction there is a small tip for static pressure measurement. The tips are connect to the PTS. The prototype uses a PTS from Validyne, models P55 and P35, for CDRsp-IPLeiria equipment and LSRE-FEUP, respectively.

Figure 3-31 shows the PTS sensor, and also the pressure tip and channel over different parts, namely the injector, the injector's isolation and the Mixing-Head Body.

Different materials were used in the mixing-head. For the parts in contact with the raw material, was used steel 1.2738. A nitriding was executed to the contact parts, to avoid the oxidation and increase the chemical resistance. For the other parts, was used steel CK45. The parts described before were produced using CNC milling process. However, to minimize the costs, standard pieces were used for screws, dowels and hydraulic

connectors. A complete list of materials is in Appendix A. Figure 3-32 shows the assembled mixing-head.

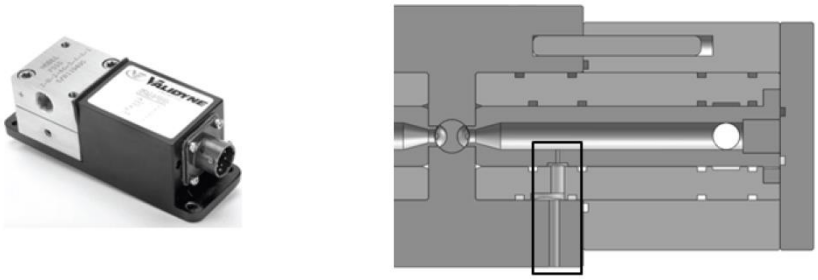

Figure 3-31 a) PTS Validyne P55, b) Model Cad of pressure tip, over the different parts

Figure 3-32 RIMcop® mixing-head

The RIMcop® mixing-head works with two stages: Mixing and Recirculation. During the raw material's recirculation, the cleaning piston is down blocking the mixing chamber, as shown in Figure 3-33a. The cleaning piston has two lateral grooves, which allow recirculating the material from the injector through the recirculating channel back into the storage tank. To start the injection, the cleaning piston is retracted clearing the mixing chamber and allowing the contact and mixing between the raw materials, and flow of the reacting mixture over the outlet into the mould cavity, as shown in Figure 3-33b. When the injection into the mould finishes, the cleaning piston moves forward again blocking the mixing chamber. By doing so, the piston flushes any materials that could exist in the mixing chamber and re-establishes the recirculation circuit that keeps the system operating between injections: pumps working and the temperature in the injectors and feeding lines.

The same mixing-head project was used for both machines, at CDRSP-ILPLeiria and at LSRE-FEUP. The mixing-head at FEUP has an additional hydraulic circuit, which will enable to test the use of a third needle-like injector in systems when the stoichiometric ratio is

larger than 100. This circuit is not described here because no tests were performed with this novel system.

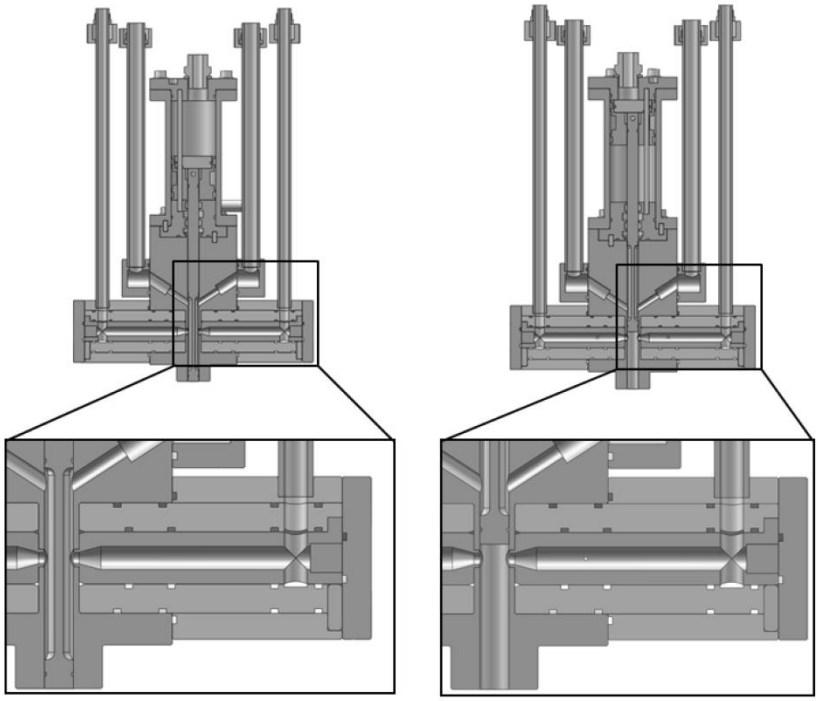

a) b)

Figure 3-33 Work phases: a) Recirculation b) Mixing

3.3.1.2 Meetering Pumps

The meetering pumps used in both equipments, were external gear pump from Viking, model SG80514. The pumps were designed specifically for pumping polyol and isocyanate. Figure 3-34 shows an image of the pump model Figure 3-34a shows the different parts of the pump.

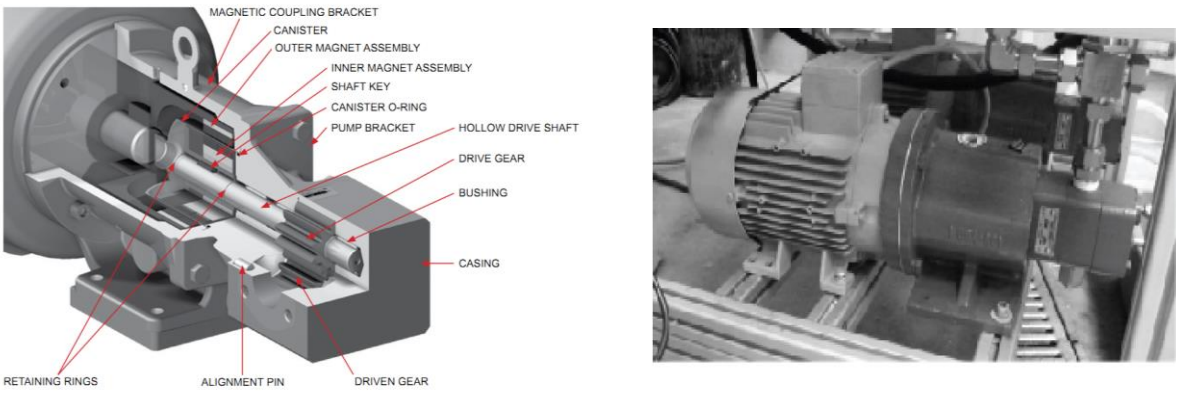

a) b)

Figure 3-34 Viking pump SG80514: a) section (from www.viking.com @ 02/03/2012) b) photo

The pump's selection was based on a project flow rate of $22\mathrm{Lmin}^{-1}$, value defined from the maximum flow rate of the PLASRIM original metering system. Using the Equation 3.72, considering a pressure loss over the system of $\Delta p = 30\mathrm{bar}$ and the volumetric efficiency of $\eta_g = 67\%$, the motor power is computed from

$$P = \frac{q\Delta p}{600\eta_g} \qquad 3.72$$

Is $P = 0.82\mathrm{kW}$. A tri-phasic motor with $P = 1.5\mathrm{kW}$ was used.
One key aspect over the pump selection is the construction material, since the pump will work with raw materials that are quite reactive. Table 3-10 (extracted from www.*pumpschool.com* developed by Viking Pumps and consulted last time at 02/03/2012) shows information on the construction seal materials for pumps, and their chemical compatibility with the fluids used in this work.

Several couplings can be used, but to avoid leakages the best one is the *sealless c*oupling. The *sealless* coupling consists in a magnetic coupling between the motor and pump's spindle, as shown in Figure 3-35, without any mechanical connection between two parts.

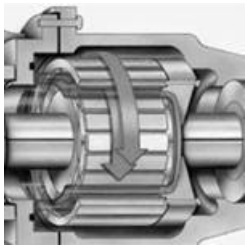

Figure 3-35 Magnetic coupling (www.dst-magnetic-couplings.com @ 02/03/2012)

Table 3-10 Construction material compatibility, advice seals and couplings methods for the used fluids

Fluid	Construction material	Seal	Coupling
Glycerine	Cast iron	Buna-n - acceptable	*any*
Polyol	Cast iron	Buna-n - acceptable	*Sealless*
Isocyanate	Cast iron	Viton®, PTFE, Kalrez®	*Sealless*

Table 3-11 shows the material and material seals used in the pumps from CDRsp-IPLeiria and LSRE-FEUP. This table also shows some of the most important features of this pumps, namely the maximum flow rate, q, the maximum operation pressure, $p_{\max}$, and temperature, T.

Table 3-11 Pumps characteristics

Local	$q\left[\mathrm{Lmin^{-1}}\right]$	$p_{\max}[\mathrm{bar}]$	$T[^{\circ}\mathrm{C}]$	Construction Materials	Seals
CDRsp-IPLEIRIA	22	34	$-40 < T < 230$	Cast iron	PTFE
LSRE/FEUP	22	34	$-40 < T < 230$	Cast iron	PTFE

Table 3-12 Polyurethanes dosing Pump's type

Manufacturing	Model	Type	Magnetic Coupling
Beilinch	THERMOINOX 36/36	Gear	Yes
MAAG		Gear	No
Rexroth	AV2K28	Axial piston	No
Viking	SG80514	External Gear	Yes
Varisco	V25-2	Gear	Elastic Union

3.3.1.3 Storage Tanks

In CDRsp-IPLeiria equipment, the storage tanks used for this work were those from the PLASRIM project, which are shown in Figure 3-36. The storage tanks were made in stainless steel, open at the top and have a rotor to stir the material inside the tank. The tanks have a capacity of $22\mathrm{L}$. The material in the tank is heated by an electrical resistance with $4.5\mathrm{kW}$. The tanks and raw materials temperatures were controlled by a PID system. Several thermocouples were used to control the temperature inside the tanks, namely inside the tanks, in the electrical resistance and closed to mixing-head inlet.

The storage tanks from the LSRE-FEUP prototype, were also made of stainless steel, with a capacity of $20\mathrm{L}$. These tanks are closed at the top, i.e., the top was welded to the tanks and have an oil chamber around the tank with an electrical resistance of $1\mathrm{kW}$. Figure 3-37 shows the tanks from LSRE-FEUP prototype.

a) b)

Figure 3-36 Storage tank from CDRsp Equipment: a) cut from CAD project b) storage tank photography

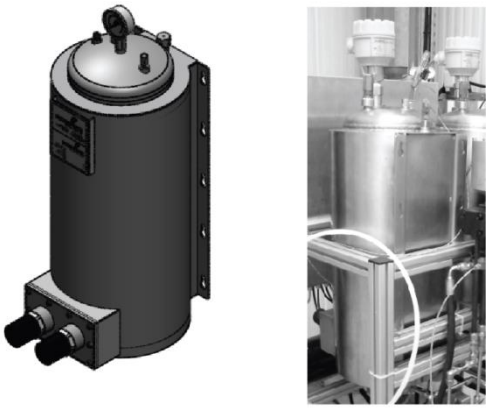

a) b)

Figure 3-37 Storage tank from CDRsp Equipment: a) CAD project b) storage tank photography

A PID temperature controller was developed, and implemented in the tanks of the LSRE-FEUP machine. Applying the First Law of Thermodynamics, and since there is no total work done by the system on surroundings, the following one-dimensional transient energy balance, where Q is the net heat added to the system, and E is the total energy,

$$\frac{dQ}{dt} = \frac{DE}{Dt} \qquad 3.73$$

was made over the tank considering that the tank is filled with fluid and air, as shown in Figure 3-38. In the case of fluid heating, no total work was done and so the work term in Equation 3.13 was dropped in Equation 3.73.

Several assumptions were made to develop the model for the tanks heating:

- Walls are adiabatic ($\frac{dQ_w}{dt} = 0$);
- Heat transfer only occurs by convective heat transfer;
- Kinetic and potential energy are neglect ($\frac{\upsilon^2}{2} = 0$ and $gz = 0$) ;
- Internal walls have a negligible thickness ($\delta \approx 0$);
- Constant pressure ($p = cte$);

Applying the Reynolds Transport Equation to Equation 3.73, and using the enthalpy (Kundu and Cohen, 2004),

$$u = h - p\upsilon \qquad 3.74$$

the energy balance can be defined as

$$\frac{dQ}{dt} = \oiint_{CS} (h - p\upsilon)\rho \mathbf{v} \cdot \mathbf{dA} + \frac{\partial}{\partial t} \iiint_{CV} (h - p\upsilon)\rho dV \qquad 3.75$$

Considering the previous assumptions, and using the equation over the control volume, Equation 3.75 becomes

$$\frac{dQ}{dt} = \frac{\partial}{\partial t} \iiint_{CV} (h)\rho dV \qquad 3.76$$

Considering the enthalpy is given by

$$h = c_p T \qquad 3.77$$

where c_p is the specific heat at constant pressure and T is the fluid's temperature .Using the enthalpy definition, Equation 3.76 gives

$$\frac{dQ}{dt} = \frac{\partial}{\partial t} \iiint_{CV} (c_p T)\rho dV \qquad 3.78$$

Performing the integration of previous equation, the energy balance gives

$$\frac{dQ}{dt} = \frac{dT}{dt} c_p V \rho \qquad 3.79$$

For the heat transfer it was considered the Newton's laws of cooling (Bird et al., 2002) defined by

$$Q = UA\Delta T \qquad 3.80$$

where U is the overall heat transfer coefficient, A is the transversal area and ΔT is the temperature difference.

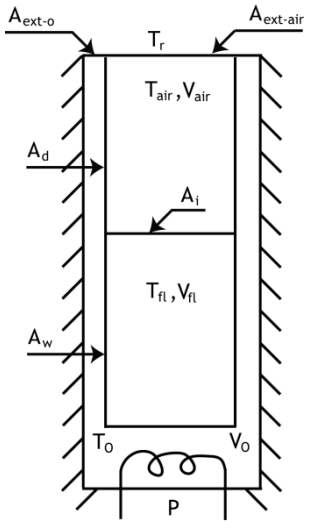

Figure 3-38 Geometric model from tank's temperature modelling

Considering a one-dimensional case, and using Equation 3.79, Equation 3.80 and considering that oil is being heated by the resistances with power P, the energy balance for oil is

$$\frac{dT_o}{dt} = \frac{P - U_{o_w} A_{we} \left(T_o - T_{fl}\right) - U_{o_d} A_d \left(T_o - T_a\right) - U_{o_{ext-o}} A_{ext-o} \left(T_o - T_r\right)}{\rho_o V_o C_{p_o}} \qquad 3.81$$

where T_o is the oil temperature, P is the power transferred to the system, U_{o_w} is the heat coefficient for the wet zone of the oil, A_{we} is the wet zone area, T_{fl} is the fluid temperature, U_{o_d} is the overall heat transfer coefficient for the dry zone of the oil, A_d is the dry zone area, $U_{o_{ext-o}}$ is the overall heat transfer coefficient for the external zone of the oil, A_{ext-o} is the oil area in contact with the air and T_r is the room temperature.

For fluid, the energy balance is given by

$$\frac{dT_{fl}}{dt} = \frac{U_{o_w} A_{we} \left(T_o - T_{fl}\right) - U_{\text{int}} A_{\text{int}} \left(T_f - T_{air}\right)}{\rho_{fl} V_{fl} C_{p_{fl}}} \qquad 3.82$$

where the index int refers to the interior contact zone between air and fluid and the index air refers to air. For the air, the energy balance is

$$\frac{dT_{air}}{dt} = \frac{U_{o_d} A_d \left(T_o - T_{air}\right) + U_{o_d} A_d \left(T_o - T_{air}\right) - U_{air_{ext-air}} A_{ext-air} \left(T_{air} - T_r\right)}{\rho_{air} V_{air} C_{p_{air}}} \qquad 3.83$$

where $A_{ext-air}$ is the external area of the air zone.

From the addition of the resistances the overall heat transfer coefficients are given by Equation 3.84 to 3.87.

$$U_{\text{int}} = h_{air} \tag{3.84}$$

$$U_{o_w} = \frac{1}{\frac{1}{h_{fl}} + \frac{\delta}{k_{steel}} + \frac{1}{h_o}} \tag{3.85}$$

$$U_{o_d} = U_{o_{ext-o}} = \frac{1}{\frac{1}{h_{air}} + \frac{\delta}{k_{steel}} + \frac{1}{h_o}} \tag{3.86}$$

$$U_{air_{ext-air}} = \frac{1}{2\left(\frac{1}{h_{air}}\right) + \frac{\delta}{k_{steel}}} \tag{3.87}$$

Since the aim is to control the oil temperature, to fit the oil temperature from model over the data obtained from experimental values for oil, it was used an Inverse Laplace Transform. A Second Order Plus Time Delay (Sundaresan and Krishnaswamy, 1978), present at Table 3-13, was used.

Table 3-13 Transfer functions based on Sundaresan and Krishnaswamy (1978) model

Transfer Function	Equation
Second Order Plus Time Delay	$G(s) = \frac{K_p}{\tau_{p_1} s + \tau_{p_2} s + 1} e^{\tau_d s}$

The model was implemented at Simulink/Matlab, and the parameters were calculated using the optimization method *Particle Swarm Optimization* (Mendes et al., 2004*)*. Using the calculated parameters, at Table 3-14, the model was fitted to the data, as shown in Figure 3-39 and Figure 3-40, using the second order model.

Table 3-14 PID parameters for the temperature control

K_p	τ_{p_1}	τ_{p_2}	τ_d	τ_{step}
4.90	1.08	100.70	15.00	Variable

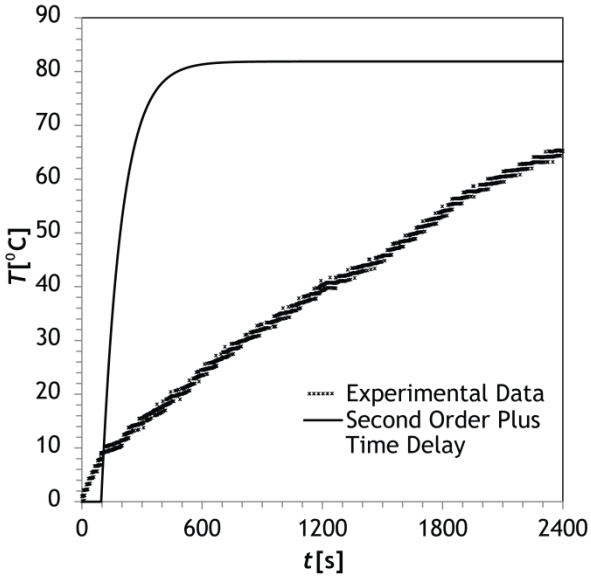

Figure 3-39 First and second order model and experimental data adjustment, with $\tau_{step} = 300$

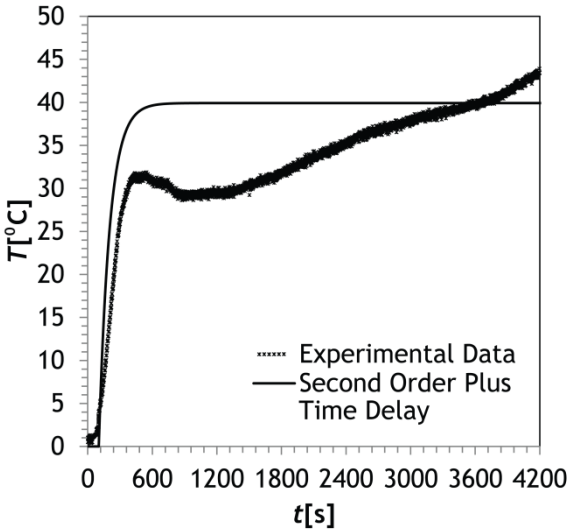

Figure 3-40 First and second order model and experimental data adjustment, with $\tau_{step} = 285$

The Second Order Plus Time Delay, was implemented, due the matching between the model and temperature data.

3.3.1.4 Control System

The control system present at CDRsp-IPLeiria equipment consisted in a PID control from Omrom, E5CN for temperature control, with six channels, two VEV NORDAC 500SE, one for each pump, and an electric control for the hydraulic system of the cleaning piston. The controllers of the CDRsp-IPLeiria RIM machine are shown in Figure 3-41. Besides these controllers the RIM equipment at CDRsp-IPLeiria operates manually with individual setting of the parameters of each component.

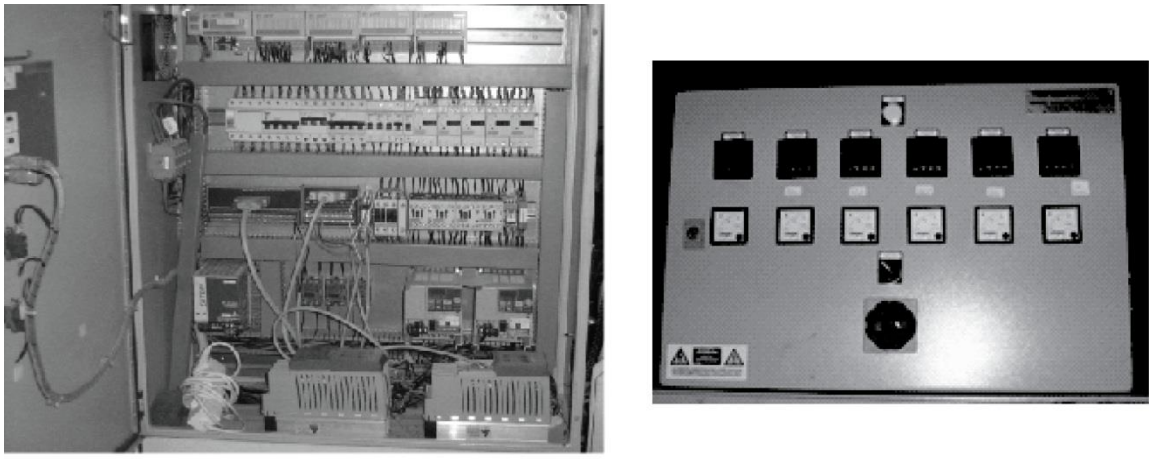

a) b)

Figure 3-41 Control system from CDRsp Equipment: a) VEV NORDAC b) PID Temperature control from Omrom

The LSRE-FEUP equipment, has a more complex control system, based in a implementation of the RIMcop® technology. The idea behind this control technology, is the Real Time monitoring of the differential pressure between the jets, and the analysis of the pressure data dynamic components to assess the operation flow regime, which should ideally be a chaotic regime (Lopes et al., 2005). From CFD results of Erkoc et al. (2007) it was clearly demonstrated that the pressure signal can measure the flow oscillations related to the operation under chaotic flow regimes. The control system of the pumps flow rate and temperature, consists on a PID with an adaptive control system, due to the transient states of the process and to maintain the desired flow regime.

A graphical user interface (GUI) was developed for an easy control of the several systems of the pilot RIMcop® machine, which is shown in Figure 3-42. The control program has several menus: Manual, PID, Temperature, Configuration, which enable to define the operation flow rate manually, or to define a differential pressure set point and control the pumps from this parameter using a PID controller. The PID menu allows defining the accurate proportional K_p, integral K_I and derivative term K_D, that define the control signal as

$$u(t) = K_p i(t) + K_I \int i(t)dt + K_D \frac{d}{dt} i(t) \qquad 3.88$$

where $u(t)$ is a dynamic control signal send to the system. All the processing conditions can be set initially (i.e. flow rate and, filling time) and the program will control the machine operation from those parameters. The terms of the PID controller need to be calibrated in function of the material viscosity and differential pressure. As showed in sub-

chapter 3.3.1.3., a PID controller based on Sundaresan and Krishnaswamy (1978) model was designed and implemented for the tanks. This program also controls the temperature in each of the storage tanks.

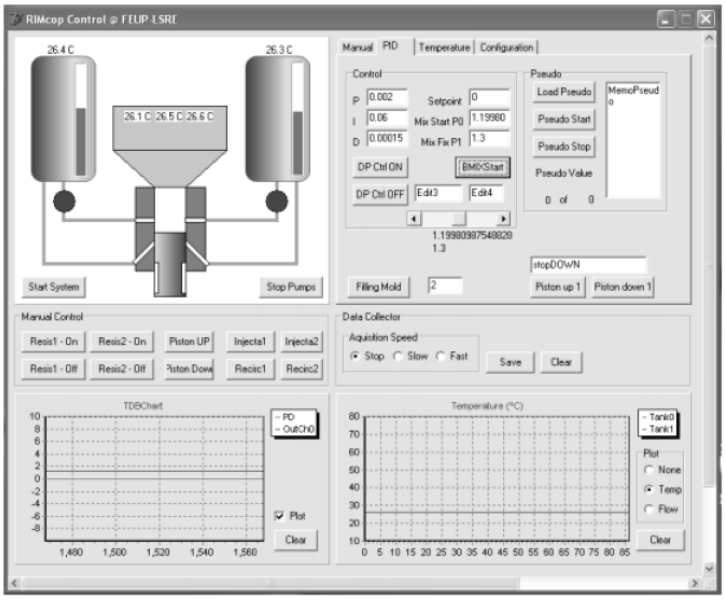

Figure 3-42 GUI from RIMcop equipment, inside the PID menu

The inputs and outputs from the RIM controller can be described as Figure 3-43 shows. In LSRE-FEUP equipment process, one of the pumps is fixed, and the controller performs a variation in flow rate to the other one, according with the information of differential sensor. This flow rate variation is due to the controller actuation over one of the pumps caused by the differential pressure between two jets differs from the reference value. The adjustment allows to balance the jets and sets operation flow regimes with high mixing degree.

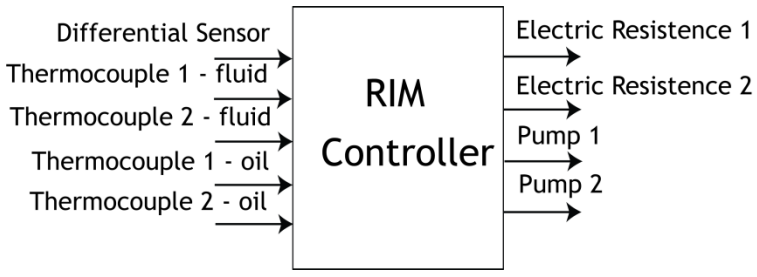

Figure 3-43 Simplified functionality block of LSRE-FEUP RIM Equipment process

A transient state is found during the mixing, and to maintain the optimal mixing conditions based on Equation 3.71, and adaptive model was employed to control the system and respond to changes that occur during the machine operation that stem from dynamics of the process, temperature fluctuations, and so on. The adaptative model implemented is a

Model Identification Adaptive Controllers (MIAC). This model performs an on-line identification to the process, in order to identify it and adjust the parameters. The MIAC uses recursive minimum square with exponential memory to the on-line identification. Figure 3-44 shows the scheme of the process. MIAC is composed by two meshes, the interior mesh, where the controller and the process co-exist, and an external mesh that identifies the model parameters and adjusts the controller parameters.

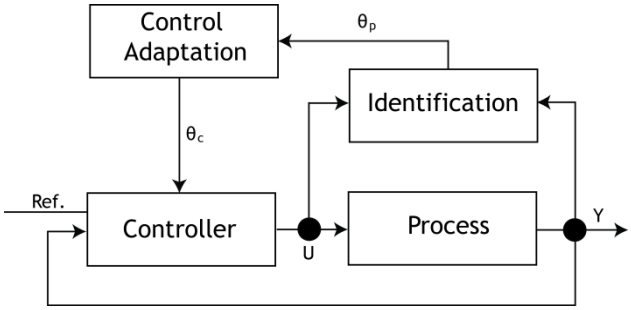

Figure 3-44 Model Identification Adaptive Controllers scheme

The controller model is composed by acquisition boards from Advantech, connected to the PC via USB, as can be seen in Figure 3-45.

Figure 3-45 Acquisition boards from Advantech

A detailed description of the control system can be found in Gonçalves (2008) and Gouveia (2009).

3.4 RIMCop System Calibration

Previous section introduced the RIM machines used in this work. In this section it is described the RIM system calibration, namely the pumps, differential pressure transducer and PID control. First it is presented the calibration performed of the CDRsp-IPLeiria RIM machine. In this machine only the pumps and differential pressure transducer were calibrated since, as shown before, the CDRsp-IPLeiria equipment did not had a control system implemented. In the second part, it is presented the calibration of the LSRE-FEUP RIMcop® machine, where the following systems were calibrated: the differential pressure transducer, the pumps, the system PID controller for the pumps and the tanks temperature controller.

3.4.1 CDRsp-IPLeiria Equipment Calibration

The pumps were calibrated with glycerine, that has a viscosity behaviour, in function of temperature, as described in Figure 3-46.

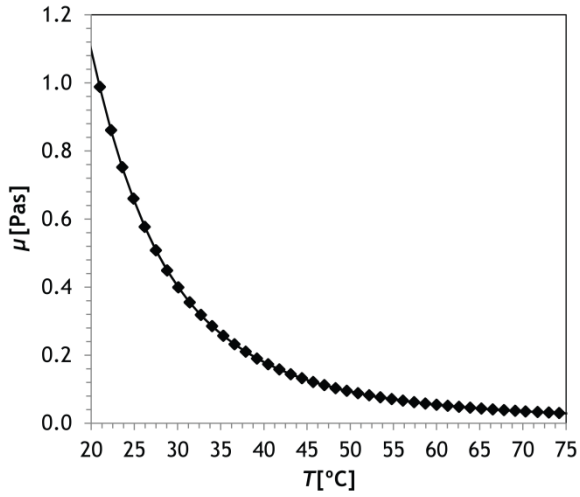

Figure 3-46 Glycerine Viscosity used in CDRsp equipment

The pumps calibration consists in measuring the flow rate at the outlet of recirculation circuit. The procedure adopted consisted in varying the pump's motor rotation speed then using a chronometer and a graduated cylinder, the flow rate was measured. This procedure was repeated for different pressures, varying the flow temperature, and for each processing condition, the flow rate was measured three times. From Figure 3-47 and Figure 3-48, it is possible to compare the flow rate to the manufacturer flow rate charts. From both figures, the points correspond to the experimental data and the lines to the tendency line. Comparing the tendency line with the manufacturer lines is possible to see that there is a close matching of experimental and the manufacturer values.

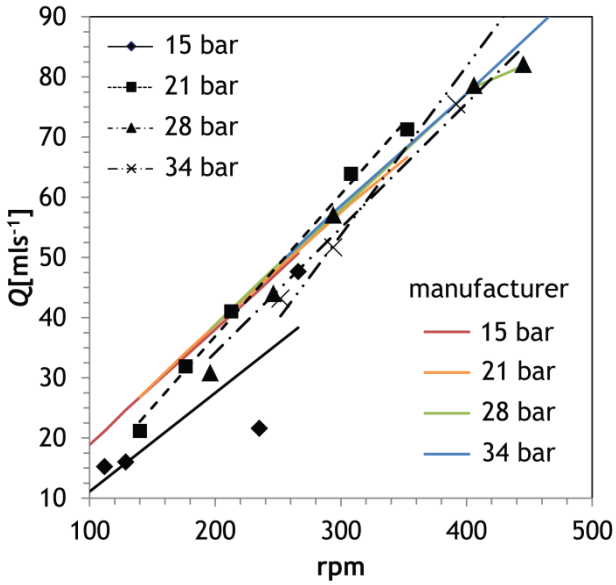

Figure 3-47 Flow rate calibration for pump 1, at CDRsp-IPLeiria

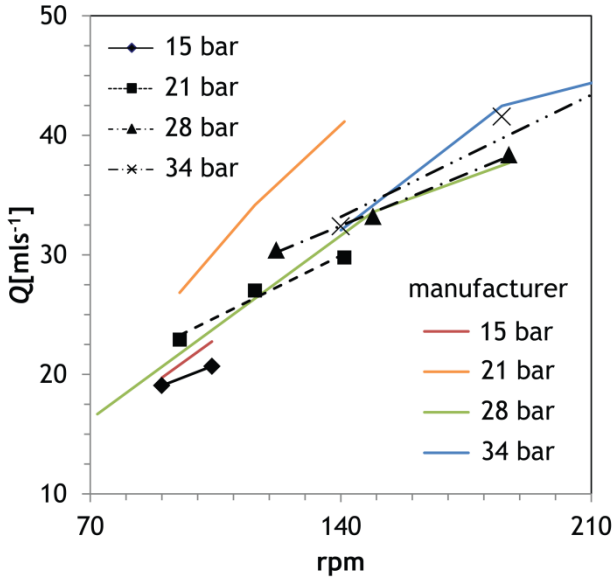

Figure 3-48 Flow rate calibration for pump 2, at CDRsp-IPLeiria

3.4.2 LSRE-FEUP Equipment Calibration

For the calibration performed at LSRE-FEUP, it was also used a glycerol solution. Several aqueous solutions of glycerine with different viscosities were prepared, see Table 3-15. The solutions were prepared with glycerine and water, according to the procedure described by Santos (2003). The first three aqueous solutions from Table 3-15 were used for pump calibration. The other two solutions had an equal viscosity to the raw materials that will be processed in Chapter 4, and were used to calibrate the PID control. The fraction of glycerol is given by,

$$X_g = \frac{\mu^a - \left(A_{wt} e^{\frac{B_{wt}}{T}} \right)^a}{\left(A_g e^{\frac{B_g}{T}} \right)^a - \left(A_{wt} e^{\frac{B_{wt}}{T}} \right)^a} \qquad 3.89$$

where $A_{wt} = 5.17 \times 10^{-4}\,\mathrm{mPa \cdot s}$, $B_{wt} = 2.22 \times 10^{3}\,\mathrm{K}$, $A_g = 7.06 \times 10^{-9}\,\mathrm{mPa \cdot s}$, $B_g = 7.64 \times 10^{3}\,\mathrm{K}$ and $a = -0.320$.

Table 3-15 Glycerol solution viscosities

Solution	$\mu\left[\mathrm{mPa \cdot s}\right]$
1	80.00
2	56.00
3	20.00
4	18.84
5	18.25

At the LSRE-FEUP's RIMCop equipment, the calibration curve for pumps was performed at several voltages, and the flow rate for different viscosities was measured with an identical procedure to the one performed for the CDRsp-IPLeiria's pumps calibration. The calibration was made at the same temperature conditions, and consisted in measuring the flow rate at mixing chamber outlet, for several voltage values. The calibration was set for each isolated pump and for both pumps working with the control system on. Several tests were performed and the maximum error obtained was $\pm 6\%$. From Figure 3-49 to Figure 3-51, is possible to observe the calibration curves for pump 1, pump 2 and both pumps with control, respectively. From these figures, it is possible to identify an increase in the pumps flow rate when the viscosity increases. This trend is clear for higher voltage values and, also, in the lower viscosities range. When the viscosity increases, there is a tendency for a constant flow rate.

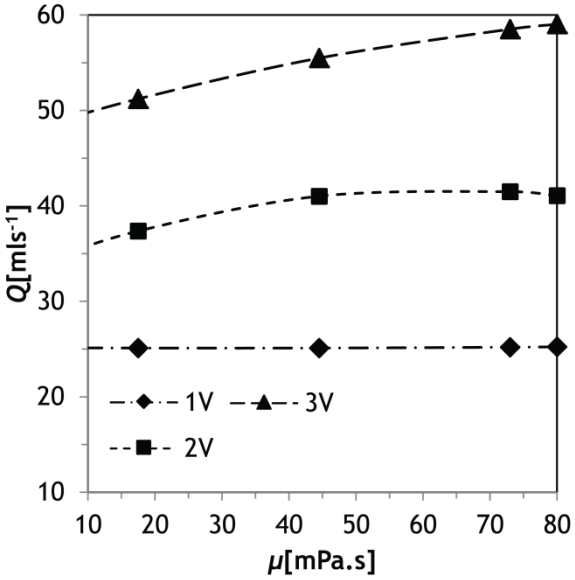

Figure 3-49 Flow rate Calibration for pump 1, at LSRE-FEUP

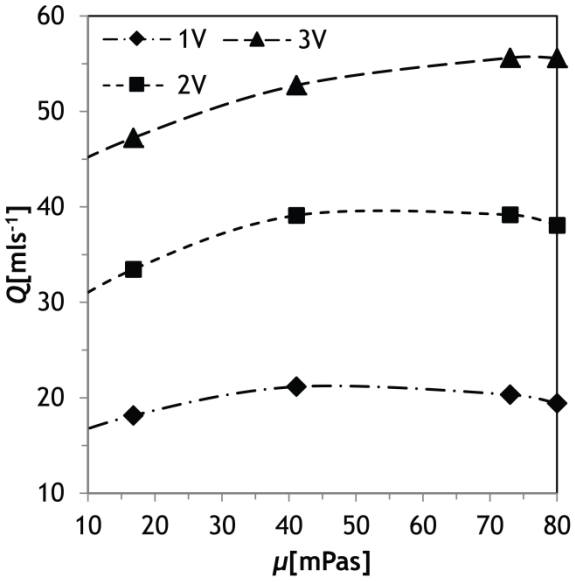

Figure 3-50 Flow rate Calibration for pump 2, at LSRE-FEUP

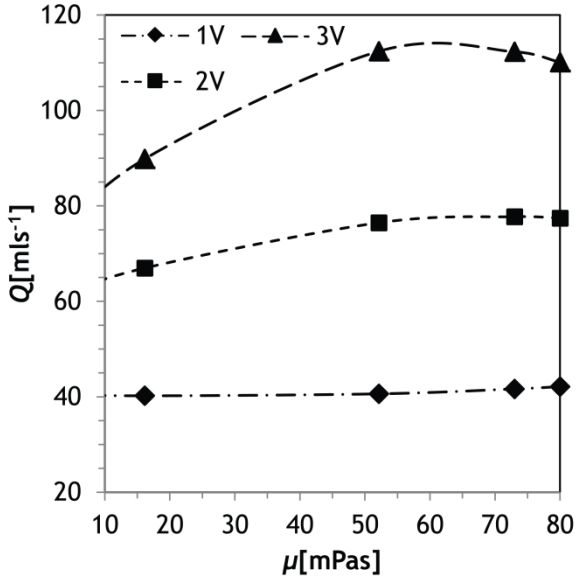

Figure 3-51 Flow rate Calibration for both pumps with control, at LSRE-FEUP

For the pressure transducer, the calibration was made measuring the voltage signal of the SPT when a differencial pressure was imposed between both sides of the pressure transdurcer using two water columns. A column was mounted at each side of the SPT, and the pressure difference was obtained varying the height of water, at each side. The pressure transducer voltage signal varies linearly and presented a linear regression coefficient close to 1. Figure 3-52 presents the calibration curve for the sensor. Based on curve equations from Figure 3-52, the pressure differece was converted to the voltage, using Equation 3.90, since the controller system works with the voltage value.

$$V_{\Delta p} = 3.83\Delta p - 0.66 \qquad 3.90$$

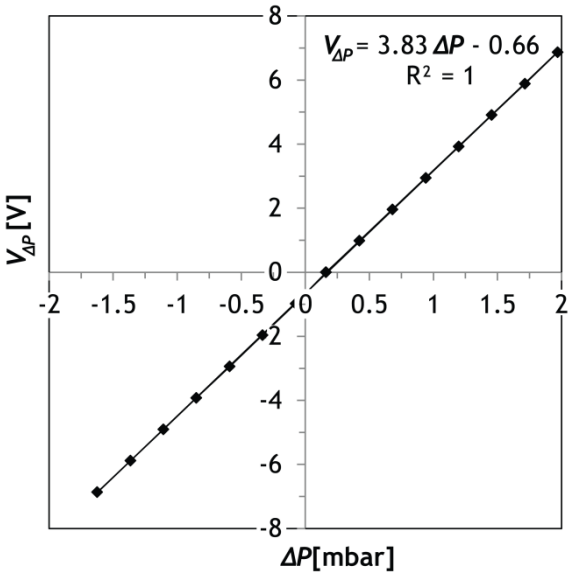

Figure 3-52 Calibration curve for the FEUP's pressure transducer sensor: Pressure drop vs. Voltage

To perform the calibration of the PID controller, it was used pseudo-random values for changing the pump state, in order to identify the model parameters that best fit to the raw material processing conditions. This pseudo-random consists in different stages for pump rotation. Using the values, data is recorded from differential sensor and pump rotation velocity. After, the data are analysed in a Matlab program made that, based on pump delay relatively to the predict value, computes the values for proportional, integral and derivative gain, from Equation 3.88. For the present work, the values are shown in Table 3-16.

Table 3-16 PID parameters for the temperature control

K_p	τ_{p_1}	τ_{p_2}	τ_d	τ_{step}
4.90	1.08	100.70	15.00	Variable

During the injection and tanks clean process an inert and dry atmosphere was assured by filling the tanks with nitrogen and passing a nitrogen stream though the raw materials. The nitrogen was kept recirculating into the tanks after going through an excitator with dry silica. The gas flow rate was controlled with a rotameter.

To calculate the passage time for nitrogen in tanks cleaning, it was assumed that the flow inside the tanks works as a CSTR, then using Equation 3.64 with $n=1$ and considering that 1ppm should be found at tanks, the total number of passages at tank is 14. Based on total volume of the RIMCop® machine, $V_{\text{tank}}=19.6\text{L}$, the clean total time it is 776s, for a relative pressure of 0.25bar.

For other operations, considering a pressure of 0.25bar, it was used a nitrogen gas induction flow rate of $q_g=11\text{Lmin}^{-1}$. The nitrogen required for each experiment was calculated and it is present in Table 3-17, and will result in a total consumption of 5m^3. The procedure used in the samples injections into the mould is explained in Chapter 4 or Appendix B.

Table 3-17 Nitrogen requirements for each operation

Procedure	Tank 1[L]	Tank 2[L]	Total[L]
Tank Clean	330	330	660
Atmosphere inertization	22	22	44
Atmosphere inertization during the raw materials transfer	165	165	330
Raw materials degasification	51	66	117
Tanks pressurization	55	55	110
Tank Clean	330	330	660
Clean Total			1921
Sample's injection	33	33	66
Tanks pressurization	51	66	117
Total by injection			183
Injection Total (18 samples)			3294
Total			5215

3.5 Conclusions

The effect of the geometrical configurations of mixing chamber on hydrodynamic patterns was one of the objects of this chapter. It is possible to resume this work as:

- Using horizontal angles between the injectors different than $180°$, promotes smaller vortices volumes in the top of mixing chamber;
- Vertically angled injectors pointing towards the chamber top, create less vortices, since there is no top vortices;
- Shorter mixing chamber or with restrictions, will produce shorter vortices downstream the jets by breaking them.

The energy balance shows that using directly opposed injectors, with $180°$ angles, promotes the maximum energy dissipation for mixing when compared with other geometries. The vertically angled jets dissipate most of the energy in the top of the energy chamber, while shorter mixing chambers or mixing chambers with restrictions create more energy dissipation throughout the walls.

A macroscopic energy balance was applied over different control volumes for the five geometries. From the momentum conservation were calculated the energy dissipation due to friction and due to mixing. It is possible to observe that for the opposed jets a larger fraction of energy was used on actual mixing than on the other geometries. The geometries with opposed jets favour the efficient use of energy on mixing, except in the

case where obstacles are introduced in the chamber, which cause additional friction. The power numbers, N_p, for the different mixing chambers are very small, indeed, very close to one. This indicates that the supplied energy to the reactor is almost completely used on mixing, and shows the remarkable capacities of the RIM mixing chamber to perform a fast mixing with high level of efficiency. Similar results were obtain by Leblebici (2011). From this result, it is clear that simple mixing chamber geometry can use more energy in the actual mixing.

From RTD it is possible to conclude that, at steady flow regimes, the opposed jets have the tendency to create flow short-circuits from inlet to outlets. The RTD is not well described by tank in series models, being closer to piston like behaviours with axial and radial dispersion, where backmixing patterns are not significant.

RIM equipment was either adapted or built from scratch to demonstrate the RIMcop® technology. The adaptation of existent RIM equipment can be an option for the installation of the RIMcop® technology in existent equipment with lower investment. The RIM system at CDRSP-IPLeiria was prepared to be upgraded to a RIMcop® system, with all the components related with this technology, such as the PTS or the computer boards for the components controller. Nevertheless, the controller was not tested in this machine. This chapter presented and described the different components of the RIM system in CDRsp-IPLeiria, and the calibration of all the system components.

The machine at LSRE-FEUP is a new RIM equipment built and designed from scratch to operate a RIMcop® machine. All the main components in the machine were described in present chapter, including the controller system, as well as the calibration of the different components of the system.

3.6 References

Bates, R.L., Fondy, P.L., Corpstein, R.R., 1963. Examination of Some Geometric Parameters of Impeller Power. Industrial & Engineering Chemistry Process Design and Development 2, 310-314.

Berger, E., Wille, R., 1972. Periodic Flow Phenomena. Annual Review of Fluid Mechanics 4, 313-340.

Bird, R.B., Stewart, E.W., Lightfoot, E.N., 2002. Transport Phenomena, 2nd ed. John Wiley & Sons.

Bourne, J.R., Garcia-Rosas, J., 1985. Laminar Shear Mixing in Reaction Injection Moulding. Polymer Engineering and Science 25, 1-5.

Danckwerts, P.V., 1953. Continuous Flow Systems: Distribution of Residence Times. Chemical Engineering Science 2, 1-13.

Erkoc, E., Santos, R.J., Nunes, M.I., Dias, M.M., Lopes, J.C.B., 2007. Mixing dynamics control in RIM machines. Chemical Engineering Science 62, 5276-5281.

Fogler, H.S., 2002. Elementos de Engenharia das Reacções Químicas. LTC.

Fonte, C., 2012. Mixing Studies with Impinging Jets - PIV/PLIF Experiments and CFD Simulation, Ph.D. Thesis, Deparment of Chemical Engineering, Universidade do Porto, Porto, Portugal.

Fonte, C., Santos, R., Dias, M., Lopes, J.C., 2011. Quantification of Mixing in RIM Using a Non-Diffusive Two-Phase Flow Numerical Model. Internation Journal of Chemical Reactor Engineering 9, A114.

Gomes, N., Mateus, A., Bártolo, P., Santos, R., Dias, M.M., Lopes, J.C., 2009. Projecto de Cabeça de Mistura RIM, com conceitos Inovadores de mistura e controlo, ConfEng UBI, Covilhã, Portugal.

Gomes, N., Santos, R.J., Dias, M.M., Gouveia, A.F., Sousa, C.C., Bártolo, P.J., Lopes, J.C.B., 2010. Assessment of the effect of controlling mixing using RIMCop® technology on the production of polyurethanes, RPD 2010, Industrial Knowledge for Innovation, Marinha Grande, Portugal.

Gonçalves, R., 2008. Self Tuning e Controlo de Máquinas RIM, Master Thesis, Deparment of Electrical and Computer Engineering, University of Porto, Porto, Porto.

Gouveia, A., 2009. Identificação e Controlo Adaptativo de Máquinas RIM, Master Thesis, Deparment of Electrical and Computer Engineering, University of Porto, Porto, Portugal.

Harris, R.F., Anderson, R.M., Shannon, D.M., 1992. Speciality Polyurethane Soft Segments. II. Mixing Studies in Micro-RIM Using Polyether Diamine Oligomers Containing Backbone Urea Moieties. Journal of Applied Polymer Science 46, 1547-1560.

Johnson, D.A., Wood, P., 2000. Self-Sustained Oscillations in Opposed Impinging Jets in an Enclosure. Canadian Journal of Chemical Engineering 78, 867-875.

Johnson, D.A., Wood, P., Hrymak, A.N., 1996. The Effect of Geometrical Parameters on the Flow Field of an Opposed Jet RIM Mix Head: Equal Flow and Matched Fluids. Canadian Journal of Chemical Engineering 74, 40-48.

Keuerleber, R., Pahl, F., 1972. Devide for feeding flowable material to a mold cavity. Patent US3706515.

Kundu, P.K., Cohen, I.M., 2004. Fluid Mechnics. Elsevier Academic Press, USA.

Leblebici, E.N., 2011. Comparative Study of NETmix® and T-jets Reactors Based on Pressure Dynamics Master Thesis, Chemical Department, University of Porto, Porto, Portugal.

Lee, L.J., Ottino, J.M., Ranz, W.E., Macosko, C.W., 1980. Impingement Mixing in Reaction Injection Molding. Polymer Engineering and Science 20, 868-874.

Lopes, J.C.B., Santos, R.J., Teixeira, A.M., Costa, M.R.P.F.N., 2005. Production Process of Plastic Parts by Reaction Injection Moulding, and Related Head Device. Patent WO 2005/097477.

Macosko, C.W., McIntyre, D.B., 1984. RIM Mixhed with High Pressure Recycle. Patent US4479531.

Malguernera, S., Suh, N., 1977. Liquid Injection Molding I. An Investigation of Impegiment Mixing. Polymer Engineering and Science 17, 111-115.

Mendes, R., Kennedy, J., Neves, J., 2004. The fully informed particle swarm: simpler, maybe better. Evolutionary Computation, IEEE Transactions on 8, 204-210.

Nakamura, S., Brodkey, R.S., 2000. Direct and Large Eddy Simulation of the Three-Dimensional Unsteady Flows in the Counter-Jet Mixing Vessel, ASME Fluids Engineering Summer Conference, Boston, Massachusetts.

Nishioka, M., Sato, H., 1978. Mechanism of determination of the shedding frequency of vortices behind a cylinder at low Reynolds numbers. Journal of Fluid Mechanics 89, 49-60.

Ottino, J.M., Ranz, W.E., Macosko, C.W., 1979. A lamellar model for analysis of liquid-liquid mixing. Chemical Engineering Science 34, 877-890.

Ranz, W.E., 1979. Applications of a Stretch Model to Mixing Diffusion, and Reaction in Laminar and Turbulent Flows. AIChE Journal 25, 41-47.

Ranz, W.E., 1986. Analysis of Reaction Processes in Which Microscopic Heterogeneities Appear: Scale-Up and Scale-Down of Polymerization Reactions. Industrial & Engineering Chemistry Fundamentals 25, 561-565.

Santos, R.J., 2003. Mixing Mechanisms in Reaction Injection Moulding - RIM - An LDS/PIV Experimental Study and CFD Simulation, Ph.D. Thesis, Deparment of Chemical Engineering, Universidade do Porto, Porto.

Santos, R.J., Erkoc, E., Dias, M.M., Lopes, J.C., 2009. Dynamic Behavior of the Flow Field in a RIM Machine Mixing Chamber. AIChE Journal 55, 1338-1351.

Santos, R.J., Erkoc, E., Dias, M.M., Teixeira, A.M., Lopes, J.C.B., 2008. Hydrodynamics of the mixing chamber in RIM: PIV flow-field characterization. AIChE Journal 54, 1153-1163.

Santos, R.J., Teixeira, A., Costa, M.R., Lopes, J.C., 2005a. Production Process of Plastic Parts by Reaction Injection Moulding and Related Head Device. Patent.

Santos, R.J., Teixeira, A.M., Costa, M.R., Lopes, J.C.B., 2002. Operational and design study of RIM machines. International Polymer Processing 17, 387-394.

Santos, R.J., Teixeira, A.M., Erkoç, E., Sultan, M.A., Karpinska, A., Dias, M.M., Lopes, J.C.B., 2010. Validation of a 2D CFD Model for Hydrodynamics' Studies in CIJ Mixers. International Journal of Chemical Reactor Engineering 8, A32.

Santos, R.J., Teixeira, A.M., Lopes, J.C.B., 2005b. Study of mixing and chemical reaction in RIM. Chemical Engineering Science 60, 2381-2398.

Schluter, K., 1976. System for Filling a Mold with Reactive Synthetic-Resin Components. Patent US3975128.

Shames, I., 1992. Mechanics of Fluids. MvGraw-Hill, Inc, New York.

Siddiqui, S.W., Zhao, Y., Kukukova, A., Kresta, S.M., 2009. Characteristics of a Confined Impinging Jet Reactor: Energy Dissipation, Homogeneous and Heterogeneous Reaction Products, and Effect of Unequal Flow. Industrial & Engineering Chemistry Research 48, 7945-7958.

Sundaresan, K.R., Krishnaswamy, P.R., 1978. Estimation of time delay time constant parameters in time, frequency, and laplace domains. The Canadian Journal of Chemical Engineering 56, 257-262.

Taubenmann, P., 1986. Mixing Head for Producing a Preferably Chemically Reactive Mixture of Two or More Plastics Components. Patent US4592657.

Teixeira, A.M., 2000. Escoamento na Cabeça de Mistura de uma Máquina RIM, Ph.D. Thesis, Deparment of Chemical Engineering, University of Porto, Porto.

Thakur, R.K., Vial, C., Nigam, K.D., Nauman, E.N., Djelveh, G., 2003. Static Mixers in the process industries - A review. Trans IChemE 81, 787-826.

Wood, P., Hrymak, A.N., Yeo, R., Johnson, D.A., Tyagi, A., 1991. Experimental and Computational Studies of the Fluid Mechanics in an Opposed Jet Mixing Head. Physics of Fluids A 3, 1362-1368.

Zhao, Y., Brodkey, R.S., 1998a. Averaged and Time-resolved Full-field (three-dimensional), Measurements of Unsteady Opposed Jets. The Canadian Journal of Chemical Engineering 76, 536-545.

Zhao, Y., Brodkey, R.S., 1998b. Particle Paths in Three-dimensional Flow Fields as a Means of Study: Opposing Jet Mixing System. Powder Technology 100, 161-165.

Zhao, Y., Kresta, S.M., 1996. Distribution of Energy Between Convective and Turbulent Flows Frequently Used Impellers. Chemical Engineering Research and Design 74, 379-389.

4 Application of RIMCop Machine

4.1 Introduction

Although being one of the fastest steps of the RIM process, mixing has a huge impact on the mechanical properties of the injected part (Kolodziej et al., 1982; Malguarnera and Suh, 1977; Nguyen and Suh, 1985), such that under poor mixing conditions the obtained part may be rejected or may have to be subjected to several post-moulding operations.

Previous chapter compared different mixing chambers used commercially and proved that there is no mixing efficiency gain when increasing the complexity of the chamber geometry, and so the best technical solution would be the simplest one: the original mixing chamber from Keuerleber and Pahl (1972). Here, using a mixing chamber similar to Keuerleber and Pahl (1972), the mechanical properties of an injected part were related with mixing inside the chamber, which is assessed from the static pressure difference between the two injectors.

The RIM mixing chambers need to be tuned frequently, which is mainly an empirical method based on trial and error. The state-of-art equipment does not have any means to control mixing, and problems on it are only detected after demoulding the parts. Previous chapter introduced the RIMCop technology, that consists in on-line monitoring during the mixing phase, using the differential pressure between the injectors. The results were studied by *in-situ* and *ex-situ* techniques.

4.2 Assessment of Mechanical Properties in RIM

The relation between mixing and mechanical properties is still not completely established. Some of the few works on the effect of mixing in the reacted polymer were made by Kolodziej et al. (1982); Kolodziej et al. (1986); Nguyen and Suh (1985). Although these works use a parameter known to affect mixing, there was no actual measurement of a mixing inside the mixing chamber that could be used to relate mixing with the mechanical properties. Kolodziej, Macosko et al. (1982) added a carbon black tracer to one of the monomer streams and measure the thickness of the formed *strias* in the moulded part. In a Re range between 80 and 450, it was observed that the striation thickness decreases until $Re = 200$ and after this value, the striation thickness remains constant. This decrease in striation thickness is a clear indication of an increase in the dynamics of mixing mechanisms. Kolodziej et al. (1986) studied the molecular weight distribution, for a Re range between 80 to 210. It was observed that for high Re, the molecular weight distribution was also higher, relating it to the degree of mixing. Nguyen and Suh (1985) determined the quality of mixing by injecting a third stream with an inert material into the mixing chamber, and measuring the gap size formed by the inert material that was removed after the cure reaction. When the Reynolds number of the polyol stream increases it is observed a decrease in the gap size. These early works proved that one of the operational parameters with biggest impact on mixing is the Reynolds number, defined as (Malguernera and Suh, 1977)

$$Re = \frac{\rho \upsilon_{inj} d_{inj}}{\mu} \qquad 4.1$$

where ρ is the fluid density, υ_{inj} is the mean velocity at the injector nozzle, d_{inj} is the injector diameter and μ is the fluid viscosity. In industrial operations the Re range is between $100 < Re < 500$ (Santos et al., 2005). Previous studies (Teixeira et al., 2005) demonstrated that the impingement point of the opposed jets oscillates when the operation Reynolds number is above a critical Reynolds number, which was observed to be $Re_{cr} = 120$ (Santos et al., 2008; Santos et al., 2002).

Malguernera and Suh (1977) reported the existence of two flow regimes in RIM. Below the critical Reynolds number, the flow is steady: the streams of fluid from each jet flow segregatedly through parallel paths and present none or very weak dynamics of mixing, namely advective mixing mechanisms. Between the two symmetric flow streams, mixing

mainly occurs by diffusion through the interface formed between these streams. This flow regime is referred to as *steady flow regime*. Above the critical Reynolds number, vortices that break the flow symmetry are formed immediately downstream the jets impingement point. These vortices detach from the jets and evolve towards the outlet forming a *vortex street*. This dynamic flow regime is referred to as the *self-sustainable chaotic flow regime* (Erkoc et al., 2007a; Santos et al., 2002; Santos et al., 2005). The vortices formed in the self-sustainable chaotic flow regime are the main mixing mechanism in RIM (Santos et al., 2005), and when the vortices are formed they impose an oscillatory behavior on the jets impingement point. The chaotic mixing enables the reduction of segregation scales from the jet diameter to smaller scales (Fonte et al., 2011; Ranz, 1979).

The formation of a vortex street generates an oscillation of the static pressure with a frequency related to the vortex formation rate by Santos et al. (2009a). The concept that chaotic flow could be monitored from the static pressure, was the main idea underlying the introduction of a new technology for the control of mixing in RIM in Real Time, the RIMcop® - RIM with control of oscillation and pulsation. In the RIMcop® the static pressure is measured in the opposed injectors and the pressure difference is used as a control variable to check if the system is mixing correctly. In this chapter this concept is explored with several experiments where the pressure signal is related with mechanical characteristics of injected parts into a mould.

Up to this day, the path taken to assure that mixing in RIM was enough for the reaction to be chemically controlled, has been the increase on the complexity of mixing chamber geometries to force the flow into complex patterns, which promote striation mechanism (Gomes et al., 2009). However, Santos et al. (2002) proved that the traditional mixing chamber design, closer to Keuerleber and Pahl (1972) original idea, can achieve the required mixing degree for RIM. The first RIM mixing chambers introduced by Keuerleber and Pahl (1972) were cylindrical with two opposite injectors. The main problem faced by these mixing chamber geometries is that they require an extremely tight control of the equilibrium of the two jets of monomer when issuing into the mixing chamber, small deviations of less than 1% on the jets balancing compromise mixing (Santos et al., 2010), and deviations of 10% can make one of the jets to completely push the other jet into their injector making it to clog. The jets balancing is given by the *jets momentum ratio* that is defined as (Malguernera and Suh, 1977)

$$M_r = \frac{\rho_{iso} \upsilon_{iso}^2 d_{iso}^2}{\rho_{pol} \upsilon_{pol}^2 d_{pol}^2} \qquad 4.2$$

where the indices iso refers to isocyanate and pol refers to polyol.

In addition to controlling the jets balancing, the jets flow rate should be set to ensure that the monomers are mixed under the stoichiometric ratio of the specific formulation.

The present work aims to establish the relation between the final mechanical properties of injected parts with the operational conditions that are related with mixing dynamics.

4.2.1 Experimental Setup

The experimental work was performed in an industrial prototype of a RIM machine, Figure 4-1. The prototype is equipped with two heated storage tanks, two metering pumps, a mixing head and a discharged mould. To control the heating of storage tanks, and consequently the raw materials temperature a manual PID control was used.

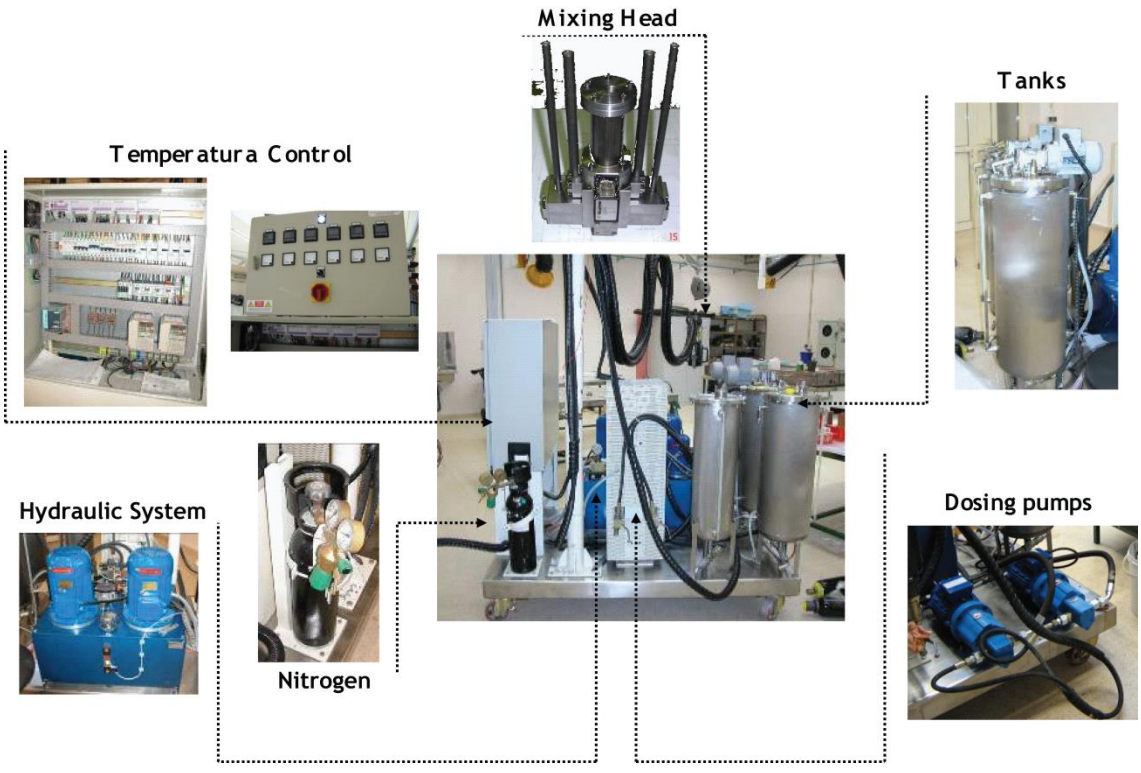

Figure 4-1 Industrial Prototype of RIM Machine

The metering pumps were external gear pumps model SG80514 from Viking Pump Inc. The flow rates were set using a calibration curve from manufacturer, based on the rotation frequency of the gear pumps. The calibration was assessed during experiments, and the deviation was less than 13%. The pump flow rate is adjusted from the motor rotation frequency, which is set using a Nord SK 500E frequency inverter.

A cylindrical mixing chamber with two opposed nozzles was used, having a geometry design very close to Keuerleber and Pahl (1972). The mixing chamber has 10mm diameter and 50mm long. The nozzles are placed at 5mm from the closed top of the mixing chamber and have 1.5mm of diameter, as shown in Figure 4-2. This mixing chamber has the same geometry than those used in previous works that studied flow and mixing dynamic in RIM at LSRE (Erkoc et al., 2007b; Santos et al., 2009a; Santos et al., 2008; Santos et al., 2002; Santos et al., 2005; Teixeira et al., 2005).

The top of the mixing chamber is confined by a cleaning piston that moves backward to clear the chamber and let mixing and mold filling start. When the piston moves forward to clean the chamber stops mixing by blocking the jets and forcing them into the recirculation circuit. The injectors have 50mm length with an inlet section of 8mm and after a smooth conical reduction the injectors diameter drops to 1.5mm, which is the jets diameter when they enter the mixing chamber. The dimensions of the injectors were checked using Computational Fluid Dynamics (CFD) simulation to ensure a Poiseuille flow at the nozzle tip. Just before the conical section of the injector, there is a pressure tap, connected to the Differential Pressure Transducer (DPT). The DPT records dynamically the static pressure difference between the nozzles, Δp, according to the patented operational procedure (Lopes et al., 2005), see Figure 4-2. The used pressure transducer was a Validyne P55. The data recorded from the DPT was acquired with a personal computer using a National Instruments USB-6008 data acquisition card that has a sample rate of 10kHz.

The procedure of the industrial prototype used in the RIM machine is similar to the industrial operation mode of a RIM machine, and the one found in Macosko (1989). It can be divided in three stages:

- First the raw materials are heated to the processing temperature. This stage includes the circulation of the raw materials through the hydraulic circuits, passing through the metering pumps, mixing head and back to the tanks. During the recirculation the cleaning piston is blocking the mixing chamber and so the raw materials are not mixed and injected into the mold, instead they are directed to a recirculation circuit that is connected to the storage tanks.
- The second stage consists on the start of the raw materials mixing and the mould filling. The cleaning piston is retracted allowing the jets of raw materials to enter in the mixing chamber through the two opposed injectors and to impinge each other. This reacting mixture of the two monomers is injected into an open mould, where the foam cures and rises up freely.

- In the third stage the mixing chamber is cleaned by the piston that also stops the streams from mixing. The raw materials are then going into the recirculation circuit until the next shot.

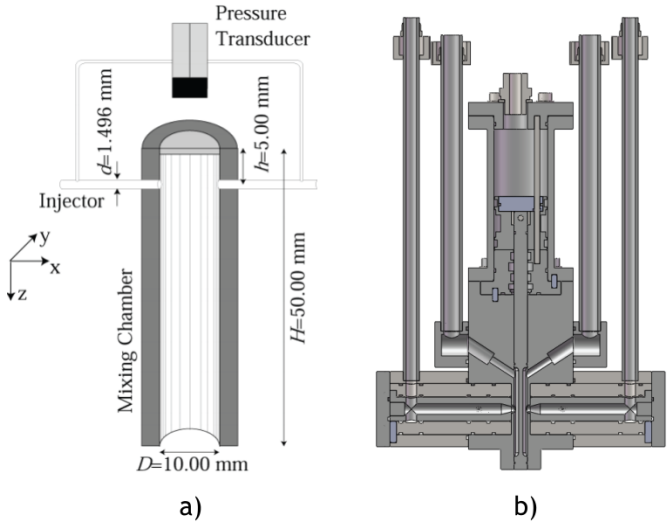

Figure 4-2 Mixing chamber: a) scheme and b) mixing head drawing

The raw materials used in the present work are an isocyanate, diphenyl methane diisocyanate (MDI, Suprasec 5025), and a polyol, DaltoRim ED12160. This commercial formulation from Hunstman originates a polyurethane structural foam. The polymerization runs with $1{:}1.02$ weight ratio of MDI/ ED12160, as a stoichiometry reference. The main properties are present in Table 4-1. The materials were recirculated until a steady temperature was achieved, $48°C$ for the poliol and $34°C$ for the isocyanate. These temperature values were chosen to set the viscosities and Reynolds number values shown in Table 4-1 and Table 4-2.

Table 4-1 – Raw materials properties

Material	$\rho\left[\mathrm{Kgm^{-3}}\right]$	$\mu\left[\mathrm{Pa\cdot s}\right]$	$T\left[°\mathrm{C}\right]$
Suprasec 5025	1230	0.153	34
DaltoRim ED12160	1055	0.148	48

In this work four runs were done, with a fixed Re number of 389 for the isocyanate stream, corresponding to a flow rate of $3.42\mathrm{L\,min^{-1}}$. For each run, three experiments were done, under the same processing conditions.

Table 4-2 shows processing conditions of the PU. The momentum ratio was varied by changing the stoichiometry, starting at 1:1 and varying it by 2% up to $1{:}1.05$.

Table 4-2 Processing Conditions

Run	*Stoichiometry* MDI/ ED12160	Re_{pol}	$q_{pol}\left[\mathrm{Lmin}^{-1}\right]$	M_r
1	1:1	345	3.42	1.17
2	1:1.02	339	3.36	1.21
3	1:1.04	333	3.30	1.25
4	1:1.05	328	3.25	1.29

From the samples, the apparent modulus from a compressive test was calculated. The compressive test was performed based on ASTM standard D1621-10 *Standard Test Method for Compressive Properties of Rigid Cellular Plastic* (ASTM, 2000) and ran in a Universal Test Machine Zwick Z100. The apparent modulus is defined as (ASTM, 2000)

$$E_c = \frac{FH_s}{Aw} \tag{4.3}$$

where W is the load, H_s the initial specimen height, A the initial cross-sectional area and D the deformation, which correspond to the decrease in the initial specimen height by a compressive load.

4.2.2 CFD Model

A 3D model of the mixing chamber was implemented in Ansys Fluent to get further data enable better insight in to the flow dynamics assessed from the Δp^*. The set of governing equations used for the flow are:

- continuity equation

$$\nabla.\mathbf{v} = 0, \tag{4.4}$$

where, $\mathbf{v}$ is the velocity vector.

- and Navier-Stokes equations

$$\rho\frac{D\mathbf{v}}{Dt} = -\nabla\mathbf{p} + \mu\nabla^2\mathbf{v} + \rho\mathbf{g} \tag{4.5}$$

where $\mathbf{v}$ is the velocity vector, $\mathbf{p}$ is the pressure, and $\mathbf{g}$ is the gravitational acceleration vector.

The SIMPLEC scheme was used for the pressure-velocity coupling, the PRESTO! and MUSCL schemes were used for pressure and momentum, respectively.

The simulated 3D geometry is identical to the mixing chamber described on experimental setup, as shown in Figure 4-3. The boundary conditions used were:

- Constant pressure at outlet
- No slip conditions at walls
- Constant velocity at inlet, according to Table 4-3 .

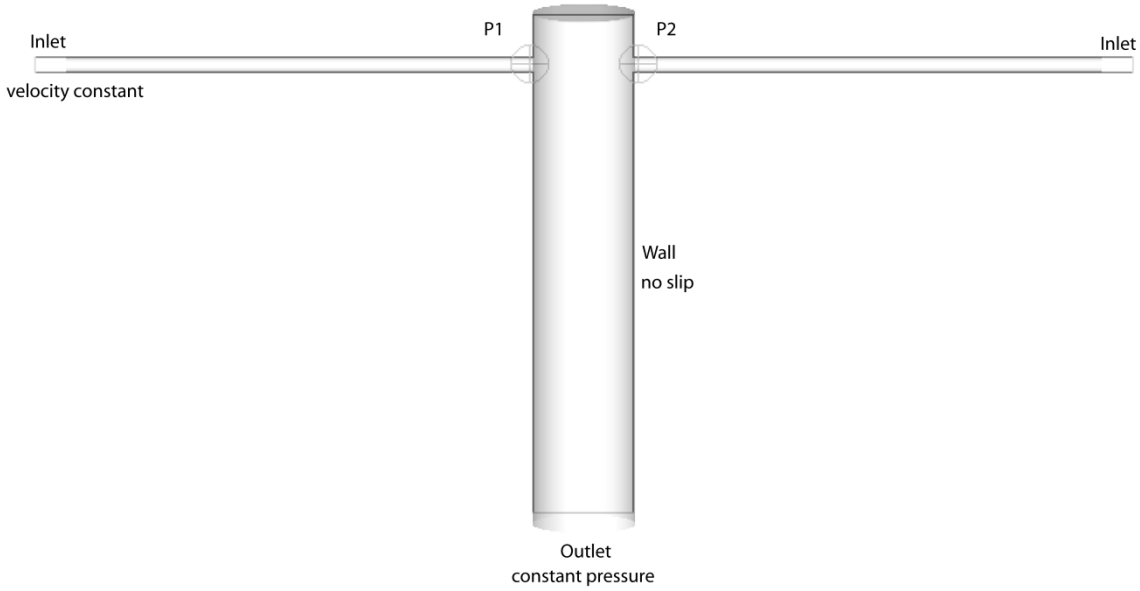

Figure 4-3 Geometrical model of a mixing chamber

Table 4-3 Boundary conditions for the CFD simulation

Material	Re	$q_{pol}\left[\mathrm{Lmin^{-1}}\right]$	$\upsilon\left[\mathrm{ms^{-1}}\right]$
Polyol	339	3.36	30.65
Isocyanate	389	3.42	33.71

The discretization grid was made of quadrilateral elements with $0.15\mathrm{mm}$ and 1.3 million uniformly sized hexahedral finite volume. The static nozzle one pressure, p_1, the nozzle two pressure, p_2, and the pressure difference between the nozzles, $\Delta p = p_1 - p_2$, shown in Figure 4-3 was dynamically recorded during the CFD simulation, considering a transient simulation. The numerical and experimental ΔP were normalized according to

$$\Delta p^* = \frac{\Delta p}{\frac{1}{2}\rho_{iso}\upsilon_{iso}^2} \qquad 4.6$$

where ρ is the density, υ is the velocity at the injector. The index iso refers to isocyanate stream.

4.2.3 Results

4.2.3.1 Mechanical Properties

Samples were taken from the part injected into a mould in the RIM machine, under the conditions shown in Table 4-2. The apparent modulus of the samples, E_C, calculated from Equation 4.3, was related with normalized differential static pressure data obtained during the mould injection, Δp^*, see Equation 4.6. The average value of normalized differential static pressure data: $\overline{\Delta p^*}$, was computed from the complete recorded time series of Δp^* obtained during mould filling.

From Figure 4-4, is possible to observe that the value of $\overline{\Delta p^*}$ is clearly related with final mechanical properties E_C. For each run, the larger values of E_C are consistently observed for the values of $\overline{\Delta p^*}$ closer to zero. When varying the stoichiometry, the $\overline{\Delta p^*}$ value increases due to the larger deviation of the unitary momentum ratio, and in consequence E_C decreases. The run with the stoichiometry ratio indicated by the vendor for this formulation, $1{:}1.02$, run number 2, Figure 4-4b, yielded the larger value of E_C and lower $\overline{\Delta p^*}$. The results presented agree with Erkoc et al. (2007b), where in their work, had been proven that $\overline{\Delta p^*}$ is a direct measure of mixing. Santos et al. (2002) showed that jets should be balance in RIM process and when $\overline{\Delta p^*}$ differs from 0, one of the jet is pushing the other to one side of the chamber. This will compromise the flow dynamics inside the mixing chamber, and consequently the chaotic mixing phenomena (Santos, et al. 2005). From the present results, one question arises: Why similar processing conditions will originate different mechanical properties? To understand this, a study inside of the flow dynamics is made from the recorded Δp^* data series.

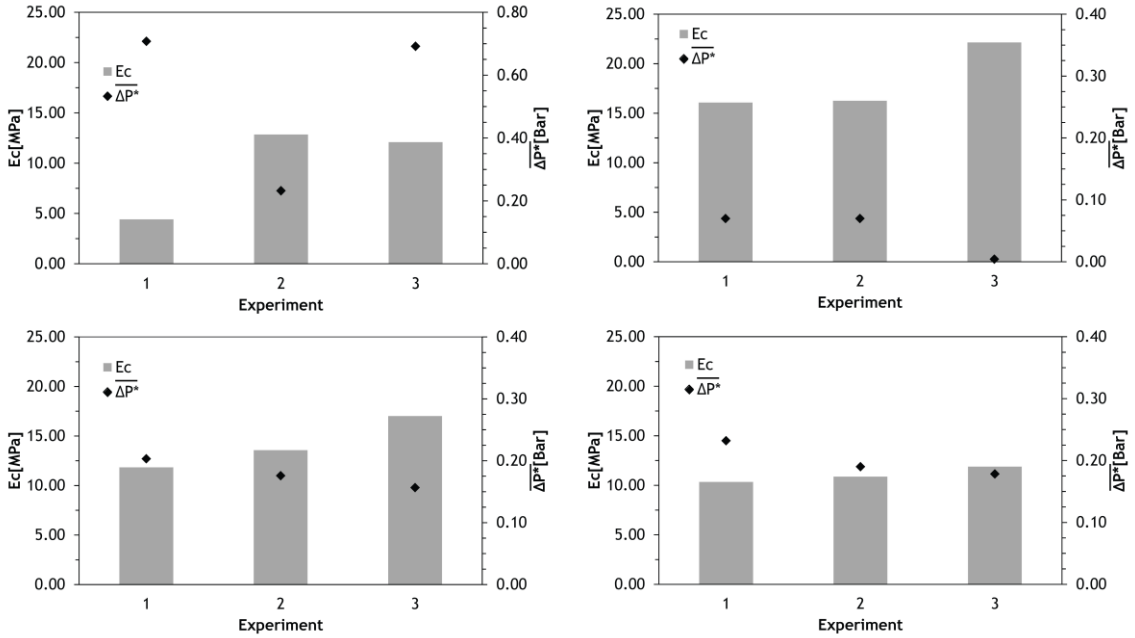

Figure 4-4 Static pressure difference and Apparent Modulus values from experiments using the following stoichiometric ratios: a) $1{:}1$ **b)** $1{:}1.02$ **c)** $1{:}1.04$ **d)** $1{:}1.05$

4.2.3.2 Spectral Analysis

The power spectra of Δp^* data recorded during mould filling were computed and are shown from Figure 4-5 to Figure 4-8. The Δp^* was measured experimentally using the DPT and it was transformed into frequency domain using the Fast Fourier Transforms (FFT). The data analysis procedures were previously described by Santos et al. (2009a).

The power spectra shown from Figure 4-5 to Figure 4-8 are from experiments made for the different stoichiometric ratios covered in this work. It is shown that for all experiments, the oscillatory behavior of the flow is complex, with occurrence of more than one energy peak for each data series. The energy peaks at a certain frequency in the power spectra are associated with particular flow oscillatory behaviors that have typical frequencies (Santos et al., 2009a). The two peaks having higher energy value in each spectra are identified and shown in Table 4-4.

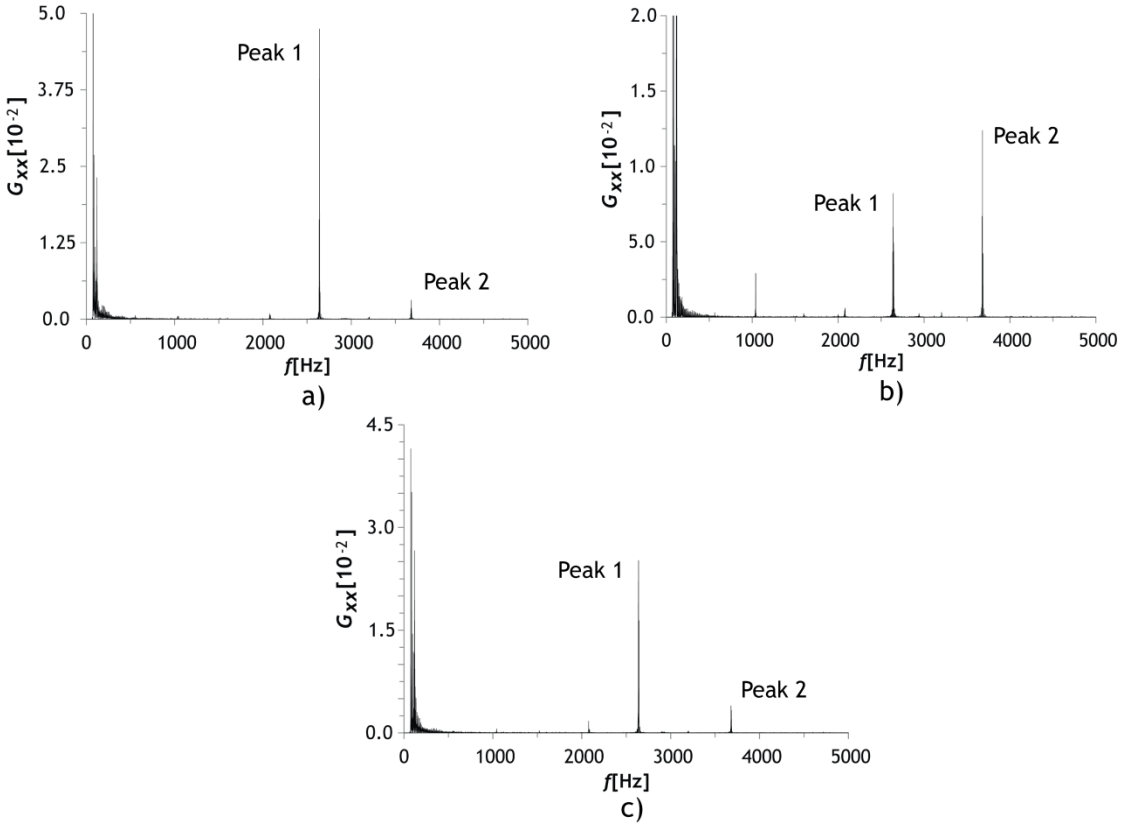

Figure 4-5 Power spectra from experimental data and for stoichiometry of $1:1$: a) Experiment 1, b) Experiment 2, c) Experiment 3)

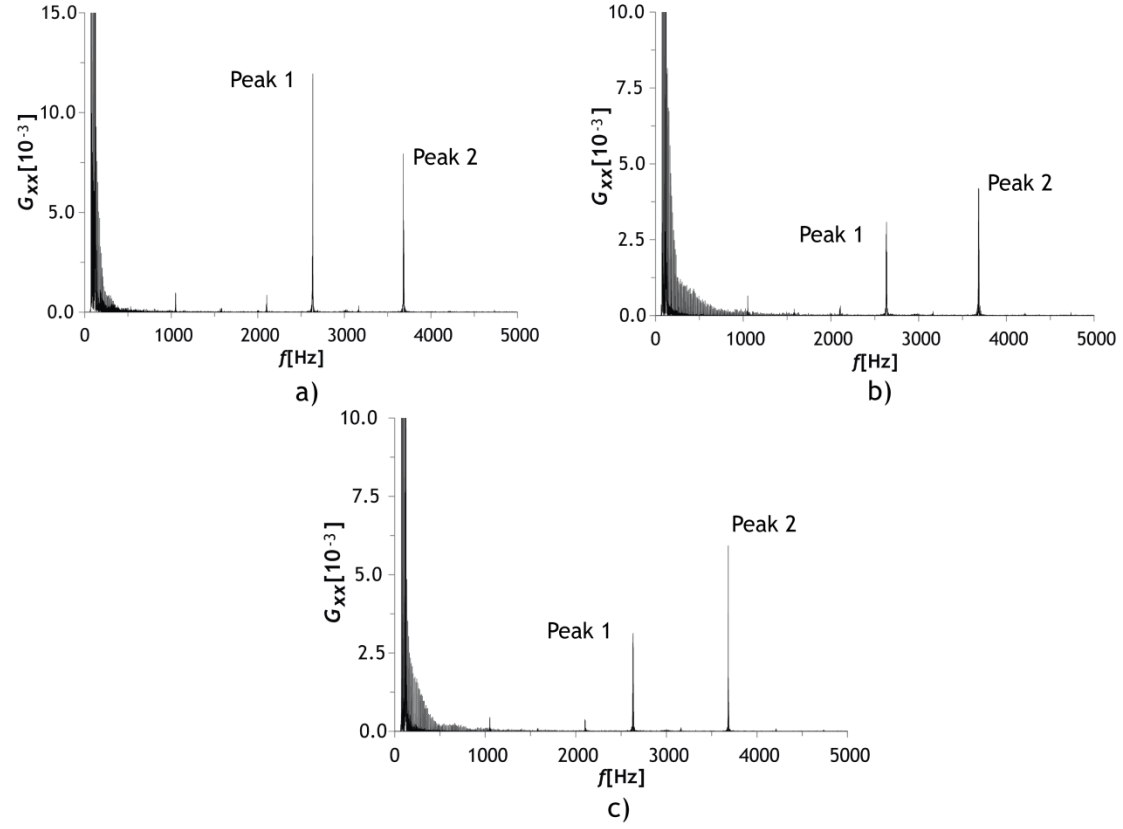

Figure 4-6 Power spectra from experimental data and for stoichiometry of $1:1.02$: a) Experiment 1, b) Experiment 2, c) Experiment 3)

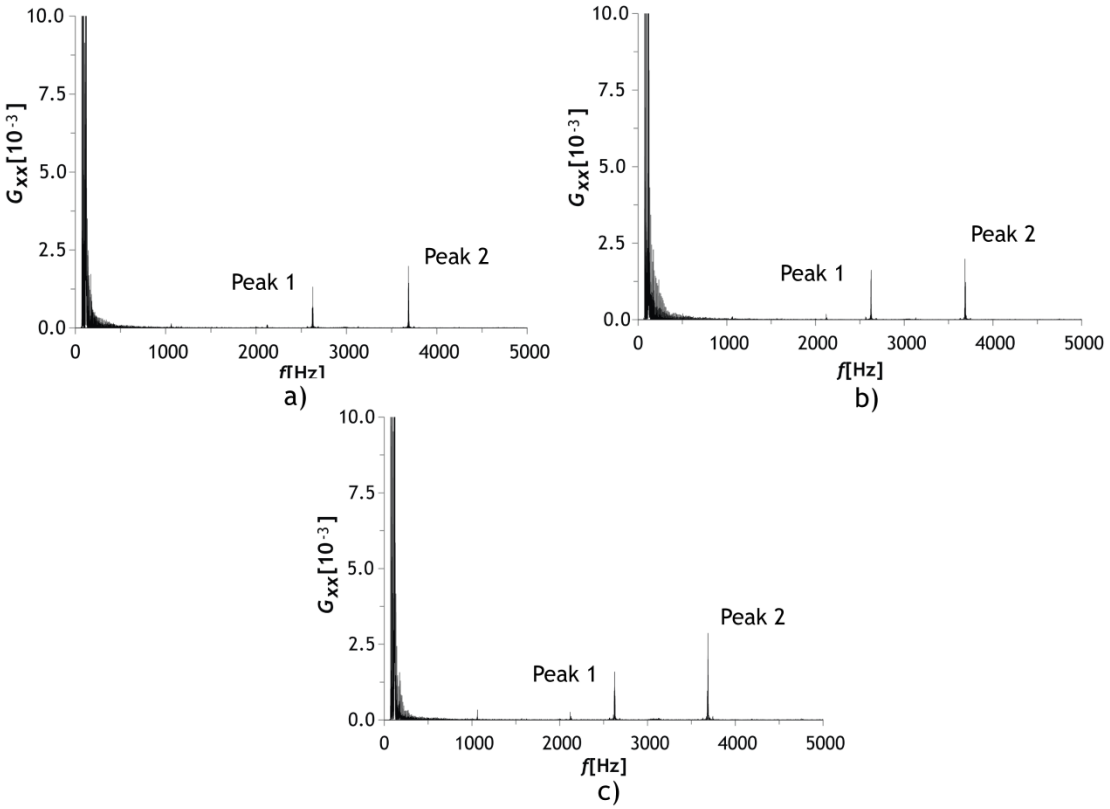

Figure 4-7 Power spectra from experimental data and for stoichiometry of $1{:}1.04$: a) Experiment 1, b) Experiment 2, c) Experiment 3)

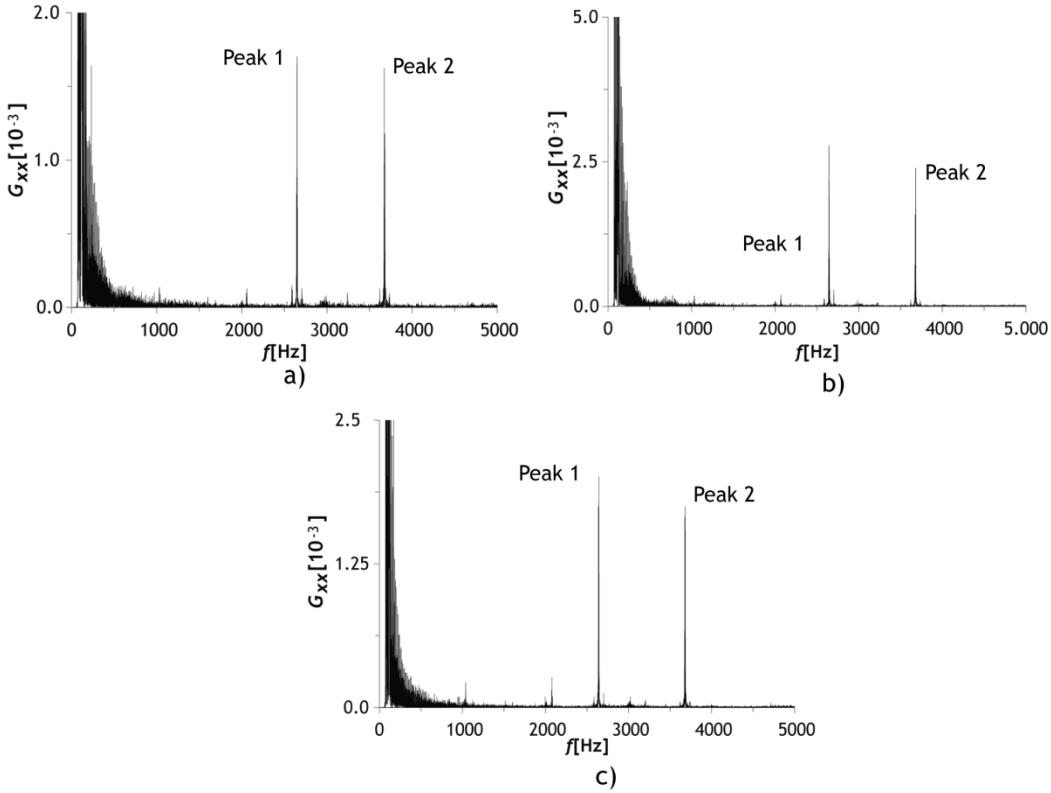

Figure 4-8 Power spectra from experimental data and for stoichiometry of $1{:}1.05$: a) Experiment 1, b) Experiment 2, c) Experiment 3)

The presence of two peaks indicates the existence of two main vortices with different size and structure. When relating the mechanical properties from Figure 4-4, with the energy peaks, the best apparent modulus is achieved when the power spectra of the highest frequency have a higher value than the others. The values of frequencies and spectra energy of the highest power spectra peaks are present in Table 4-4. The ratio between the energy spectra of the highest peak energy, $G_{xx\,peak\,2}/G_{xx_{peak1}}$, is considered. From Figure 4-4 and Table 4-4, an increasing apparent modulus, E_c, with an increasing ratio between the energy of each peak, $G_{xx\,peak\,2}/G_{xx_{peak1}}$, is observed. According to Silva et al. (2006), there is an increase on mechanical properties with a decrease of polyol percentage, phenomena that could be found on unbalanced flow during the mixing inside the chamber, as the case of present work. This could be associated to a fluctuation in instantaneous flow rate ratio of the raw materials into the mixing chamber, and consequently to the size of vortex associated to an oscillatory frequency. From Figure 4-16, it is propose a hypothesis that the ratio between the highest energy peaks, $G_{xx\,peak\,2}/G_{xx_{peak1}}$, is correlated with the quantity of each raw material into the mixing chamber; however, it is not a directly measured from the stoichiometry inside the mixing chamber and only could be used as a qualitative measure of the mixing quality.

CFD simulation with the same conditions of the $1{:}1.02$ experiment was ran, with a data recording procedure of Δp^* similar to the experimental ones. This serves the double purpose of validating the CFD model and of eliminating the hypothesis that the experimental data dynamics is hindered by errors or is being driven by external vibration sources such as flow pulsation by the pumps, which do not affect CFD simulations. The Δp^* FFT from the CFD data, is shown in Figure 4-9. A similar behavior to experimental data in Figure 4-6 is observed, particularly the two peaks having higher energy relatively to the others. The similar trend of both experimental and CFD data, shows that there is no influence from external mechanisms on the power spectra and that the CFD simulations make a good description of the flow dynamics. Table 4-4 also shows the energy peaks from CFD data, which have frequency values close to those observed experimentally, and also a very close match of $G_{xx\,peak\,2}/G_{xx_{peak1}}$ value with the one observed in the third experiment for the 1:1.02 ratio.

Table 4-4 Frequency energy and power spectra for experimental and CFD data, measured from Δp*

	Ratio	Exp	Peak1				Peak2				
			f_n[Hz]	G_{xx}	St Pol	St Iso	f_n[Hz]	G_{xx}	St Pol	St Iso	$\frac{G_{xx_{peak2}}}{G_{xx_{peak1}}}$
Exp.	1:1	1	264×10^{1}	4.7×10^{-2}	0.12	0.12	368×10^{1}	3.1×10^{-3}	0.17	0.17	0.07
		2	264×10^{1}	8.2×10^{-3}	0.12	0.12	368×10^{1}	1.2×10^{-2}	0.17	0.17	1.46
		3	264×10^{1}	2.5×10^{-2}	0.12	0.12	368×10^{1}	4.0×10^{-3}	0.17	0.17	0.16
Exp.	1:1.02	1	264×10^{1}	1.2×10^{-2}	0.13	0.12	368×10^{1}	8.0×10^{-2}	0.17	0.17	0.66
		2	263×10^{1}	3.1×10^{-3}	0.13	0.12	368×10^{1}	4.2×10^{-2}	0.17	0.17	13.55
		3	263×10^{1}	3.1×10^{-3}	0.13	0.12	368×10^{1}	6.0×10^{-2}	0.17	0.17	19.35
Exp.	1:1.04	1	263×10^{1}	1.3×10^{-3}	0.13	0.12	369×10^{1}	2.0×10^{-3}	0.18	0.17	1.54
		2	263×10^{1}	1.6×10^{-3}	0.13	0.12	369×10^{1}	2.0×10^{-3}	0.18	0.17	1.25
		3	263×10^{1}	1.6×10^{-3}	0.13	0.12	369×10^{1}	2.9×10^{-3}	0.18	0.17	1.81
Exp.	1:1.05	1	265×10^{1}	1.7×10^{-3}	0.13	0.13	367×10^{1}	1.6×10^{-3}	0.18	0.17	0.94
		2	264×10^{1}	2.8×10^{-3}	0.13	0.13	368×10^{1}	2.4×10^{-3}	0.18	0.17	0.85
		3	264×10^{1}	2.0×10^{-3}	0.13	0.13	368×10^{1}	1.8×10^{-3}	0.18	0.17	0.90
CFD	1:1.02	-	257×10^{1}	2.6×10^{-4}	0.12	0.12	371×10^{1}	5.1×10^{-4}	0.18	0.17	1.96

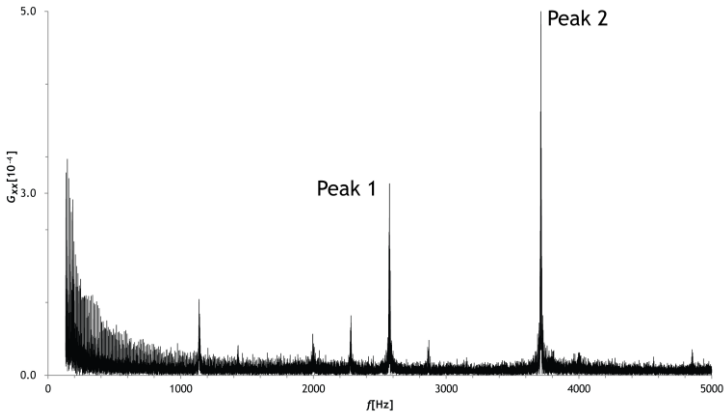

Figure 4-9 Power spectra from CFD data and for stoichiometry ratio 1:1.02

Previous works (Santos, 2003; Santos et al., 2009a) proposed the hypothesis that the oscillation of typical frequencies is associated with a structural formation. For a direct comparison of typical frequencies f_n for different Re , it was used the Strouhal number defined as

$$St = \frac{f_n d_{inj}}{\upsilon_{inj}} \qquad 4.7$$

The value of f_n is one of the energy peaks obtained for each experiment from the power spectra of Δp^*. The value of υ_{inj} is different for each jet and so in Table 4-4 are reported both in terms of the polyol and the isocyanate stream. Because both streams have very similar velocities, the St value for both streams reported with two significant figures is the same. The St numbers normalize the frequencies by the velocity, and so they are independent of flow velocity and are generally related to different structure sizes and shapes during the mixing process.

From computational and experimental work, Santos et al. (2009a) observed that elongated ellipsoids or prolate spheroid are the main flow structures being formed after the jets impingment point. For this case the vortices volume is defined by

$$\mathrm{V}_{vortex} = \frac{\pi d_2 d_1^2}{6} \qquad 4.8$$

Where d_1 is the equatorial diameter and d_2 the polar diameter, see Figure 4-10. The frequency of the oscillation of the jets impingement point is related to the injection flow rate and to the vortex volume, is was proposed by Santos et al. (2009a) that the injected

flow fills two vortices, one in each side of the chamber and when these vortices detach they cause half an oscillation, so the frequency induced by the vortices is given by

$$\phi_{vortex} = \frac{1}{2}\frac{q_{inj}}{\mathrm{V}_{vortex}} \qquad 4.9$$

where q_{inj} is the flow rate for each injector.

From PIV and CFD data the equatorial diameter is considered to remain constant with flow conditions, namely with the Re, with a value equal to $d_1 = 3\mathrm{mm}$ (Santos et al., 2009a). The volume of the vortices, and consequently the polar diameter could be estimated from Equation 4.9 using Δp^* frequency data.

The polar diameter was computed for both frequencies taken from the power spectra and are presented in Table 4-5. The polar diameter is different for the two frequencies obtained from the power spectra, with the flow structures closer to a prolate spheroid with longer major axis to an almost equidimensional spheroid. 2D CFD simulations also show two typical frequencies, a higher frequency caused by the detachment of smaller vortices next to the jets impingement point, and a lower frequency caused by larger vortices resulting from the engulfment of the smaller vortices. The same phenomena could be causing here two distinct frequency values, one associated to the smaller vortices and the other to vortices being formed further downstream in the mixing chamber.

Table 4-5 Polar diameter for proposed flow structures obtained from experimental and CFD, for stoichiometry $1{:}1.02$

Data from	Exp	$d_2[\mathrm{mm}]$	
		Peak 1	Peak 2
Experimental	1	4.55	3.26
	2	4.55	3.26
	3	4.56	3.25
CFD	-	4.66	3.23

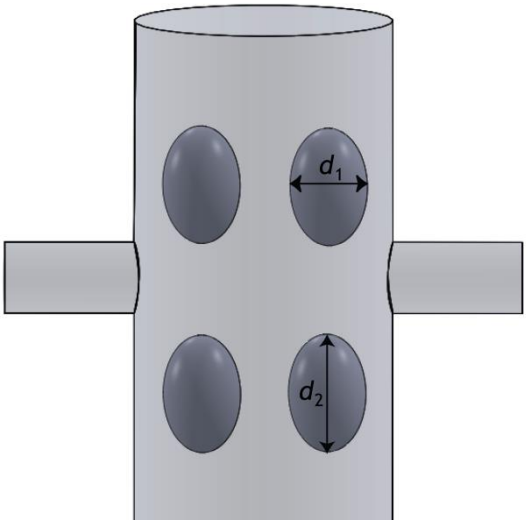

Figure 4-10 Flow structures based on oscillatory frequency

4.2.3.3 Models for the jets equilibrium

It has been observed in the industrial practice of RIM that even when the operation conditions are kept the process shows some variation. This is here related to the unstable equilibrium of the jets at the jets impingement point.

Rockwell and Naudascher (1979) had stated that pressure fluctuation can be used to assess the amplitude of oscillation, and Erkoc et al. (2007b) had shown that the pressure signal can be used to determine the frequency of oscillation of the jets impingement point. Santos et al. (2009b) showed that the jets impingement point vibrates at the same frequency of the vortices formation rate and the present work shows that the vortices formation frequency can be studied by the spectral analysis of the differential static pressure in an actual reactive polymerization process with mixing of two components. Based on the previous idea, a relation between the impingement point position and the pressure difference between the injectors was developed. First are considered the forces acting in each injector that are given by

$$\mathbf{F} = \oiint_{cs} \mathbf{T}\, d\mathbf{A} + \oiint_{cs} \mathbf{v}\left(\rho \mathbf{v} \bullet d\mathbf{A}\right) \qquad 4.10$$

where $\mathbf{T}$ are the normal stresses to the injector, $\mathbf{A}$ is the injector area, $\mathbf{v}$ is the velocity vector, and the index cs refers to control surface. The control surface comprises the jet from inlet to impingement plane, and it is show in Figure 4-11.

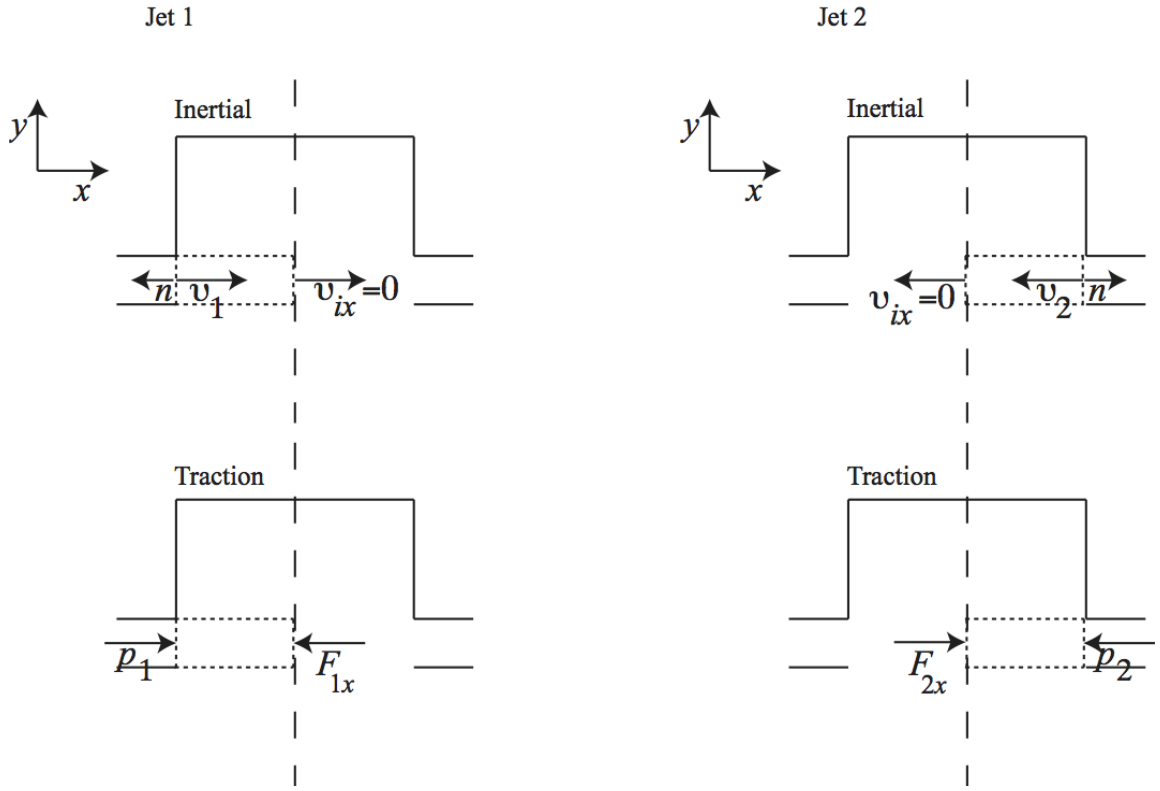

Figure 4-11 Control volume for the momentum balance

The drag forces from the vortices rotating around the jet are not considered, and no *X* velocity component is also considered on the jet after the impingement point, and so from the forces balance, it results for the jet 1 that the traction forces, T, in the *X* direction is:

$$\int_0^{d/2} T\,2\pi dr = \pi\frac{d_1^2}{4}p_1 - F_{1x} \qquad 4.11$$

where F_{1x} is the traction force from the opposed jet, jet 2.

The inertial terms are given by,

$$\oiint_{cs}\mathbf{v}\rho(\mathbf{v}\bullet d\mathbf{A}) = \int_0^R \rho_1 v_i^2\,2\pi r\,dr - \int_0^{d_1/2}\rho_1 v_{1x}^2\,2\pi r\,dr \qquad 4.12$$

The jets have a parabolic flow profile, $\upsilon_{1x} = 2\upsilon_1\left(1-\left(2r/d_1\right)^2\right)$, where υ_1 is the average velocity at injector 1. The *X* velocity component at the impingement plane is zero, thus

$$\oiint_{cs}\mathbf{v}\rho(\mathbf{v}\bullet d\mathbf{A}) = -\int_0^{d_1/2}\rho_1 v_{1x}^2\,2\pi r\,dr = -\pi\rho_1 v_1^2\frac{d_1^2}{3} \qquad 4.13$$

The balance of traction and inertia terms,

$$F_{1x} = \pi \frac{d_1^2}{4} \rho_1 + \pi \rho_1 \upsilon_1^2 \frac{d_1^2}{3} \qquad 4.14$$

For the second jet, we get:

$$F_{2x} = \pi \frac{d_2^2}{4} \rho_2 + \pi \rho_2 \upsilon_2^2 \frac{d_2^2}{3} \qquad 4.15$$

To balance the jets, the momentum of the jets must be matched, $F_{1x} l_1 = F_{2x} l_2$, where l_1 and l_2 are the distances from injector 1 and 2, respectively, to the jets impingement point. Applying the momentum balance and replacing by Equation 4.14 and Equation 4.15, it results,

$$\frac{d_1^2}{4} \rho_1 l_1 + \rho_1 \upsilon_1^2 \frac{d_1^2}{3} l_1 = \frac{d_2^2}{4} \rho_2 l_2 + \rho_2 \upsilon_2^2 \frac{d_2^2}{3} l_2 \qquad 4.16$$

The injectors diameter ratio is defined as $\phi_d = d_1 / d_2$. Since $l_1 + l_2 = D$, it results that $l_2 = D - l_1$. The momentum ratio, similarly to the definition used for the experiments in Equation 4.2, is defined as

$$KE_R = \frac{\rho_1 d_1^2 \upsilon_1^2}{\rho_2 d_2^2 \upsilon_2^2} \qquad 4.17$$

A dimensionless pressure defined as

$$p^* = \frac{p}{\rho_1 \upsilon_1^2} \qquad 4.18$$

Replacing these terms in Equation 4.16, it gives,

$$p_1^* \frac{l_1}{D} - \phi_d^2 p_2^* \frac{D - l_1}{D} = \frac{4}{3} KE_R \frac{D - l_1}{D} - \frac{4}{3} \frac{l_1}{D} \qquad 4.19$$

If a dimensionless distance $l_1^* = l_1 / D$ is defined, from Equation 4.19

$$l_1^* = \frac{\phi_d^2 p_2^* + \frac{4}{3} KE_R}{p_1^* + \phi_d^2 p_2^* + \frac{4}{3} KE_R + \frac{4}{3}} \qquad 4.20$$

The distance of the jets impingement point from the mixing chamber axis is $\xi = 1/2 - l_1^*$ and so

$$\xi = \frac{p_1^* - \phi_d^2 p_2^* - \frac{4}{3} KE_R + \frac{4}{3}}{2p_1^* + 2\phi_d^2 p_2^* + \frac{8}{3} KE_R + \frac{8}{3}} \qquad 4.21$$

For the present case, where the values of $\phi_d = 1$ and $KE_R = 1$,

$$\xi = \frac{1}{2} \frac{p_1^* - p_2^*}{p_1^* + p_2^* + \frac{8}{3}} \qquad 4.22$$

If p_1 is assumed as the reference pressure, $p' = p' - p_1'$, then $p_1' = p_1 - p_1 = 0$ and $p_2' = p_2 - p_1 = \Delta p$. From Equation 4.22, it results,

$$\xi = \frac{1}{2} \frac{\Delta p^*}{\Delta p^* + \frac{8}{3}} \qquad 4.23$$

Figure 4.12 also shows the relation between Δp^* value and l^*. Only when $\Delta p^* > 0.1$ there is an observable displacement of the jets impingement point from the mixing chamber axis. For the conditions used in the experimental work $\Delta p^* = 0.1$ is around 1bar. So, small amplitude oscillations of the jets impingement point cause an easily measurable pressure fluctuation.

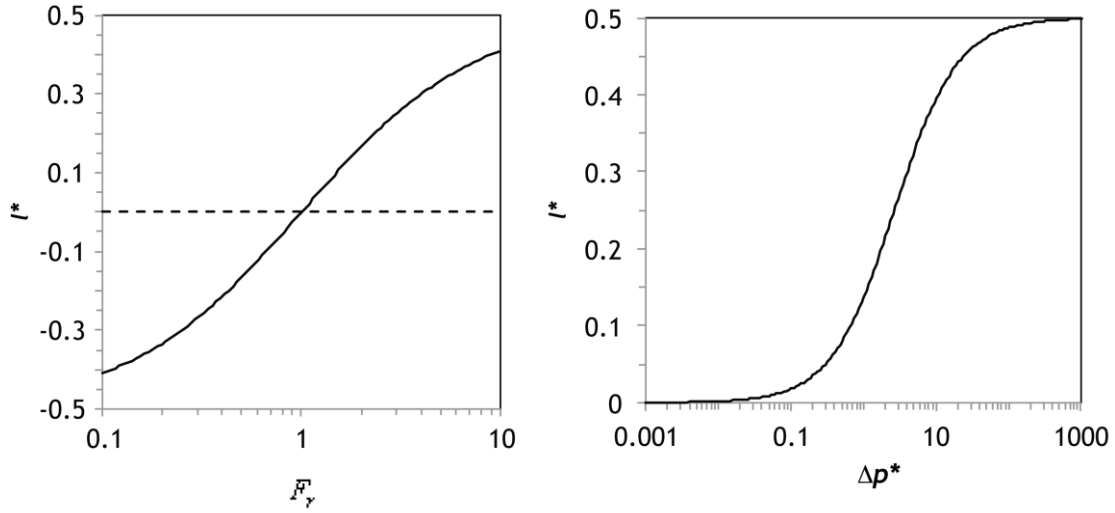

Figure 4-12 Influence of F_r and Δp^* on the normalized impingement position, l^*, for a mixing chamber with equal injectors

The displacement of the jets impingement point is computed from Δp^* time series using Equation 4.23. Figure 4.13 shows the impingement point position over time and the average impingement point position for Experiment 3 in the run with a stoichiometry ratio of 1.02:1. From Figure 4.13 it is possible to observe that the impingement point, for all experiments, oscillates between both sides of the chamber, by no more than 2.5% of the mixing chamber diameter from the mixing chamber axis. This result is corroborated from PIV results that clearly showed that the oscillations of the jets impingement point have low amplitude (Santos et al., 2008). This is also clearly seen from Figure 4.13, where despite the imaged flow regime is chaotic with flow oscillations the deviation of the impingement point from the mixing chamber axis is relatively small.

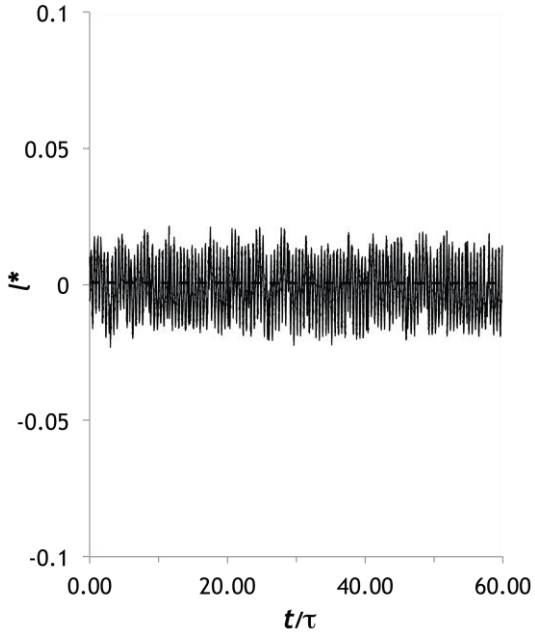

Figure 4-13 Average impingement point position (dashed line) and time series of impingement point time position (continuous line) computed from Δp^* for the Experiment with the stoichiometric ratio of 1.02:1.

4.3 Mixing Under Controlled Conditions - RIMCop

Previous section shows that the variations of mechanical properties in a polyurethane formulation are associated with the static pressure difference between the opposed injectors.

The quality of RIM parts strongly depends on the interaction between the monomer jets, mainly ensuring the proper operational conditions to maintain continuously the jets oscillation and the associated formation of vortices that engulf both fluid streams. These phenomena are responsible for the stretching and folding of the monomers interface, promoting the mixing scale reduction.

Fonte et al. (2011) and Santos et al. (2005) reported the existence of a critical Reynolds number, Re_{cr}, that onsets the dynamic regime, but as Fonte (2012) showed in his work, even above the Re_{cr}, mixing can be hindered due to slight differences in monomers' physical properties or small deviations on the flow rate of one injector. These problems can affect the part quality, as structural aesthetical defects of the part.

Mixing under controlled conditions has been studied since the 1970s. Using ATR, Sebastian and Boukobbal (1986) proved that higher adiabatic temperature rise is obtained when the

jets of polyol and isocyanate have unitary momentum ratio. Significant changes in the flow field were observed by Johnson (2000) for unequal flow conditions between the opposed jets in RIM, both numerical and experimental observations. Computational and experimental results from Santos et al. (2002) and Santos et al. (2010) also proved that unitary value of the jets momentum ratio is a critical parameter for the self-sustainable oscillation of the jets impingement point, which only occurs in a very narrow interval of jets momentum ratios. Santos et al. (2002) and Santos et al. (2010) also proved that if the unitary momentum ratio between the opposed jets was set by changing the jets diameter, the flow dynamics was not compromised, regardless of the flow rate ratio. Schütz et al. (2009) studied the viscosity ratio between the jets, and observed that the impingement point is shifted from the mixing chamber axis to the injector with higher viscosity, for the same mass flow rate of the opposed. A non-unitary deviation in jets' flow rate ratio decreases the mixing quality, as observed by Nunes et al. (2012) in a RIM mixing chamber. Fonte (2012) offered a deeper insight about the mixing dynamics in the RIM mixing chamber under the unbalanced flow, and introduced a model that can be directly applied on the design of RIM mixing chambers and RIM machines operation.

The Re for the isocyanate jet was kept constant, and was computed from the viscosity curve of the isocyanate and from the minimum flow rate that the used metering system could provide. Due to this the Re used in present work is considerable higher, as shown below, than in industrial RIM processes where Re values are usually in a range of 300 to 600 and the monomers viscosities are typically well above $100\mathrm{mPas}$ (Santos et al., 2009a), Nevertheless, this formulation was the one used to study the influence of momentum ratio, the kinetic energy ratio of the jets and the RIMcop controller system.

For jets of equal diameter injectors, $d_{iso} = d_{pol}$, the jets' momentum ratio(Malguarnera and Suh, 1977), the jets' kinetic energy ratio and the jets' flow rate ratio become

$$\mathrm{M}_r = \frac{\rho_{iso} \upsilon_{iso}^2}{\rho_{pol} \upsilon_{pol}^2} \qquad 4.24$$

$$\mathrm{KE}_\mathrm{r} = \frac{\rho_{iso} \upsilon_{iso}^3}{\rho_{pol} \upsilon_{pol}^3} \qquad 4.25$$

$$\mathrm{F}_r = \frac{\rho_{iso} \upsilon_{iso}}{\rho_{pol} \upsilon_{pol}} \qquad 4.26$$

where the index iso refers to isocyanate and pol to polyol.

In RIM, the materials can solidify either by crosslinking or by phase separation according to the nature of the material processed (Yang, 1987). During the process of solidification in RIM, the structure developed can lead to a phase separation into hard segmented, crystalline and glassy regions that reinforce the soft rubbery phase (Camargo et al., 1985). However, in the commercial RIM formulations triols are used as a soft segment, there is some crosslinking, since the hard segments associate into domains, raising the viscosity and act to build up the modulus. Two processes control the RIM final part properties: the polymerization of liquid monomers to produce high molecular weight polymers and the phase separation of hard and soft segments, responsible to build up the mechanical properties. These two processes are highly coupled in RIM and a careful balance between the speed of both phases is necessary to obtain optimal results (Yang, 1987), which will influence the final part properties (Camargo et al., 1985; Macosko, 1989).

Previous studies (Benoit and Hadziioannou, 1988; Camberlin and Pascault, 1984; Christenson et al., 1986; Eisenbach et al., 1985; Leibler, 1980; Leung and Koberstein, 1986) have related the polymerization and phase separation processes with thermodynamics of phase separation, i.e., it were analysed the influence of catalyst, hard segment content, hard segment cristinallity, polyol molecular weight and polyol type. Nevertheless, the properties in RIM polyurethanes do not only depend on the thermodynamics but also strongly on dynamic aspects of the interplay of polymerization kinetics and phase separation. Present work concerns the relation of mixing mechanics and flow regimes with the polymerization and phase separation that occurs in RIM. The polymerization can be studied using thermal techniques, which can be related with extension of reaction, namely differential scanning calorimetry and the adiabatic reactor method. The present work use the adiabatic reactor method as an *in-situ* characterization during mould filling, where further details are present in Section 4.3.3. For phase separation studies, this work applied several techniques to characterize the physical, mechanical and morphological properties of the final polymer, as presented in Section 4.3.4.

4.3.1 List of Experimental Conditions

A Hunstmann mixing activated castable polyurethane formulation is tested to validate the RIMCop technology. The formulation is a solid polyurethane, with a commercial name of Rencast FC52. It is polymerized upon the mixing of a blend of isocynates, composed by 2,4 diphenyil methane diisocyanate and 4,4 diphenyil methane diisocyanate, with a polyolo

containing $5-15\%$ light hydrotreated petroleum distillates, $5-15\%$ propoxylated ethylenediamine, $1-10\%$ hydrogenated terphenyl and $0.1-1\%$ terphenyl. Main properties are present in Table 4-6. The stoichiometry is $1{:}1.14$ for polyol:isocyanate ratio. A carbon black tracer was added to the polyol, in order to observe the mixing scale from the striation thickness in the moulded part (Kolodziej et al., 1982).

Table 4-6 Rencast FC52 raw material properties

Property	Material	
	polyol	isocyanate
Commercial name	Rencast FC52 polyol	Rencast FC52 isocyanate
$\rho\left[\mathrm{Kgm^{-3}}\right]$	980	1120
$\mu\left[10^{-3}\mathrm{Pa\cdot s}\right]$	18.88	18.25
$T_{inj}\left[^{\circ}\mathrm{C}\right]$	55	25

A list of experiments and conditions is given in Table 4-7, where it is possible to see the voltage of the control signal for each pump and the injection time for each experiment. The temperature of the monomers had slight oscillations, particularly due to the fact that this formulation is processed at approximately the room temperature, $T=23^{\circ}\mathrm{C}$ and so the Re_{iso} varied as shown in Table 4-7 due to the change in viscosity caused by the temperature fluctuations.

Table 4-7 Processing conditions for Rencast FC52

Experiment	Re_{iso}	M_r	KE_r	F_r	$t_{inj}\left[\mathrm{s}\right]$
1	1525	0.97	0.89	0.92	7
2	1418	1.00	0.93	0.93	7
3	1474	1.04	0.99	0.95	7
4	1596	1.13	1.13	1.00	7
5	1550	1.26	1.33	1.05	7
6	1642	1.42	1.58	1.11	7

4.3.2 Experimental Setup

In the RIMCop prototype-equipment, it was used an oscilloscope to capture the high frequencies of Δp^{*} associated to the vortices formation, since the acquisition boards sample rate was not enough to get this job done. It was used a Tektronix TDS2002

oscilloscope with a sample rate in the range of Giga samples per second, GHz . Since, for the flow conditions need to inject the parts the frequencies are lower, only a $2.5kHz$ was acquired.

Also a thermocouple is placed inside the mould, in the axis of the mould, as shown in Figure 4-18. The purpose is to acquire the adiabatic temperature rise from the cure reaction of the polymerization. To make demoulding easier, the thermocouple surface is covered with mould releasing agent.

The first step is the preparation of the raw materials, starting with the blending of the polyol with carbon black particles. A small amount, $0.25L$, of polyol and carbon black were mixed using ultrasound system from Dr Hielscher, model UP50H. After a second mixing step is made in a rotating mixer, adding more $0.25L$ of polyol. The final mixing step is made in the polyol storage drum. After the polyol is transferred to the tanks of the RIMcop machine and it is circulated several times to ensure a good homogenization.

The raw materials, polyol and isocyanate, were transferred from the storage drum to the storage tanks of the RIMcop machine. Particular care was taken to avoid that humidity did not contaminate the isocyanate and polyol. To this end, the storage tanks were filled under an inert atmosphere of nitrogen. A peristaltic pump Watson Marlow 323 was used for the transfer of the raw materials to the tanks. After the transfer, the raw materials were left, inside the tanks over the inert atmosphere of nitrogen for $12h$, while nitrogen was being bubbled through the bottom of the tank for degassing and drying. A detailed procedure is present in Appendix. Special attention was also paid to the DPT, where the connection lines to the injectors were filled with inert oil. This procedure was done to prevent the contact of the raw materials with the DPT membrane.

Before the injection, the raw materials inside the storage tanks, were heated up to the injection temperature. The conical mould's surface was covered with a mould releasing agent that avoids the injected part to get stuck to the mould walls. The mould was close without a clamp sealing the cover to the moulds, which assures a small gap from where air escapes from the mould cavity. After all the equipment is set, the storage tanks are depressurized, but a nitrogen flow stream is kept inside the tanks to assure that the raw materials are not contaminated by air humidity.

Parts with a volume of $0.4L$ were injected, according to the processing conditions in Table 4-7. After the polyurethane cure, the parts were extracted, according to the times present in Table 4-8. Differential pressure was recorded using the system control during

mixing and mould filling. Temperature was recorded with a thermocouple inside the mould during the curing process. A detailed procedure of the RIMcop pilot machine operation is presented in Appendix B.

Table 4-8 Process characteristics time

$V_{inj}\left[\mathrm{L}\right]$	$t_{gel}[\mathrm{min}]$	$t_{cure}[\mathrm{min}]$	$t_{extraction}[\mathrm{min}]$
0.4	17	60	60

After the part injection and to empty the storage tanks, a clean procedure was performed. It is extremely important to clean the machine to avoid possible damages on the tubes, or other components, due to the crystallization of the raw materials. After to ensure the purge of all liquids and cooling of the system, the tank's internal walls were sprayed with dichloromethane. The solvent that drops in the tanks bottom, was recirculated over the entire installation both through the injection and recirculation lines. These procedures were performed several times to assure a proper cleaning of the pilot RIMcop machine. After the purge of all dichloromethane, the tanks were dried using, first acetone, and after nitrogen. Also, a complete and detailed procedure for the RIMcop pilot machine cleaning is presented in Appendix B.

4.3.3 Polymerization Kinetics

Since the polymerization reaction of polyurethane is fast and exothermic, the heat released by the reaction can be used as an assessment of the reaction kinetics and thus, in the case of mixing controlled reactions, of the degree or fastness of mixing. Although several techniques can be used to assess the reaction kinetics (Bártolo, 2001), the thermal methods are a valuable option for the determination of global kinetic parameters that govern the cure reaction. Furthermore in an industrial machine, where it is not practical to have laboratorial equipment, and considering that cure is a fast reaction, it is not feasible to analyse it *ex-situ*. For that reason, the adiabatic temperature rise is a valuable thermal method for the analysis of polyurethane reaction *in-situ*. Figure 4-14 shows a typical temperature curve and rate of temperature variation curve associated with the polymerization reaction.

In order to relate the conversion of the reaction with temperature, several assumptions where made:

- Constant heat of reaction
- No temperature gradients (adiabatic reactor)

- Conversion of the reaction is assumed as simple second order kinetics and Arrhenius temperature dependence according to

$$\frac{d\alpha}{dt} = A_0 e^{-E_a/RT} \qquad 4.27$$

where E_a is the energy of activation, R is the Universal Gas constant and T is the absolute temperature.

From the above assumptions and the overall energy balance

$$\frac{dQ}{dt} - \frac{dW_k}{dt} = \frac{DE}{Dt} \qquad 4.28$$

for the adiabatic case the rate of temperature change is related with the heat generation due to the rate of reaction as

$$\rho c_p \frac{dT}{dt} = -\Delta H_r \frac{d[NCO]}{dt} \qquad 4.29$$

where Q is the heat transferred to the system, W_k the work made by the system, E the energy of the system, and c_p is the specific heat capacity, ΔH_r the heat released and $[NCO]$ is the isocyanite functional group concentration. This equation assumes that all energy released from the chemical reaction is used to increase the internal energy of the mixture, at a constant pressure p. Due to the irreversibility of the reaction, the rate of change of the NCO concentration can be expressed in terms of the fractional conversion, as

$$\frac{d[NCO]}{dt} = [NCO]_0 \frac{d\alpha}{dt} \qquad 4.30$$

and so

$$\rho c_p \frac{dT}{dt} = -\Delta H_r [NCO]_0 \frac{d\alpha}{dt} \qquad 4.31$$

Then, integrating the previous equation for a constant c_p and ΔH_r, with the limits of $T = T_0$ for $\alpha = 0$ and $T = T_{max}$ for $\alpha = 1$, it results in

$$T_{max} - T_0 = \frac{\Delta H_r \left[NCO\right]_0}{\rho c_p} \tag{4.32}$$

and

$$T - T_0 = \Delta T_{ad} \alpha \tag{4.33}$$

As the reaction is considered a simple second order reaction, substituting Equation 4.27 and Equation 4.32 into 4.31 results

$$\frac{1}{\left(T_{max} - T_0\right)} \frac{dT}{dt} = -Ae^{-E_a/RT} \tag{4.34}$$

Based on this balance and considering a $n-th$ order reaction, Camargo et al. (1982) proposed a simpler kinetic model, described by

$$E_a = \frac{T_m^2 n}{\left(1-\alpha_m\right)\Delta T_{ad}} \tag{4.35}$$

$$A_0 = \frac{\left(dT/dt\right)_m e^{E_a/T_m}}{\left(1-\alpha_m\right)^n} \tag{4.36}$$

$$\alpha_m = \frac{\left(T_m - T_0\right)}{\Delta T_{ad}} \tag{4.37}$$

where index m refers to the point where dT/dt is maximum and A is a constant.

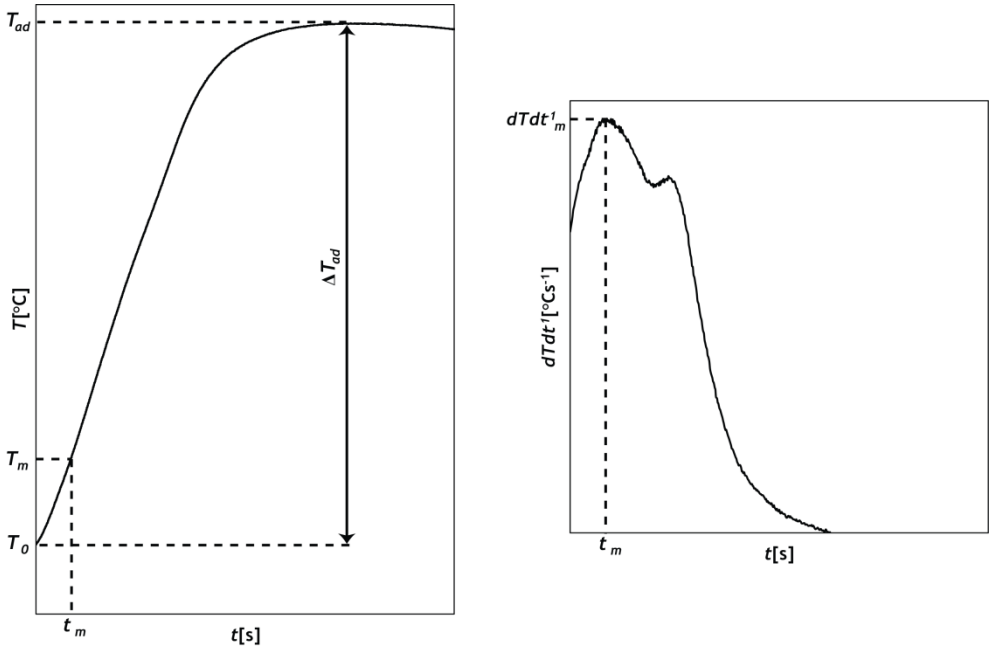

Figure 4-14 Polymerization kinetics variables adapted from Camargo et al. (1982)

The characterization of the polymerization kinetics is a fundamental aspect on the RIM process, namely for processing studies such as the definition of the production cycle time, energy consumption, and for product development (Camargo, 1984). In the present work, the kinetic model, described previously, was applied to experimental data. The results show the dependence of the cure reaction on operation conditions, namely on the balancing of the jets impingement point.

Previous works (Fonte, 2012; Santos, 2003; Santos et al., 2009a; Santos et al., 2010)) agreed that higher mixing efficiency is achieved when the monomer jets' impinge in the center of the mixing chamber. More recently, Fonte (2012) reported that optimum conditions are obtained when kinetic energy ratio of both jets are balanced, rather than the momentum ratio as was reported previously (Malguarnera and Suh, 1977).

4.3.3.1 Adiabatic Reactor

In order to measure the adiabatic temperature rise, it was needed assure that the mold and polymer behave as an adiabatic chamber. A computational model was proposed, in order to estimate the time necessary to cool the part. Figure 4-15 shows the mold and the volume that was filled for the experiment. The part volume was $0.4\mathrm{L}$, due to the requirement of samples' size for further testing.

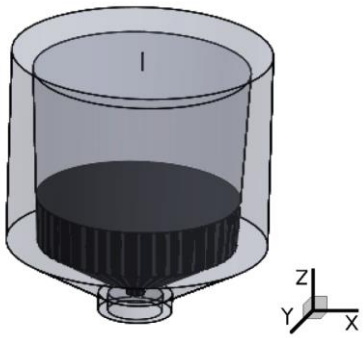

Figure 4-15 Part and mold: Opaque – part, transparency - mold

For the experimental adiabatic temperature rise measurement, a thermocouple is placed inside the mold. This position, $\mathbf{r}$, was calculated based on the center of mass of the part, $\mathbf{r}_{cm}$, defined as (Pratap and Ruina, 2002),

$$\mathbf{r}_{cm} = \frac{1}{\sum m_i}\int \mathbf{r}dm = \frac{1}{\sum m_i}\int \rho(r)\mathbf{r}dv \qquad 4.38$$

where m_i is mass of geometry with index i. Highest temperature, T_{max}, is found at center of mass. The part is obtained from the revolution of a 2D geometry, so only the z axis is considered, and for this axis the center of mass is $z_{CM} = 3.78\times10^{-2}\,\mathrm{m}$.

The time that the center of the part will take to cool down to the room temperature is predicted from an energy balance (Shames, 1992). Equation 4.28, was applied to the part volume, see Figure 4-15, and the heat added to the system can be defined as

$$\frac{dQ}{dt} = -\oiint_{CS}\mathbf{q}.\mathbf{dA} + \iiint_{CV}\dot{\Theta}\rho dV \qquad 4.39$$

where $\mathbf{q}$ is the heat flux vector and $\dot{\Theta}$ is the rate of energy production per unit mass,

Assuming that:

- no external work is done by the system $\frac{dW_k}{dt}$;
- neglecting the body forces $\left(\iiint_{CV}\mathbf{B}\rho dV = 0\right)$;
- potential flow;

Considering Equation 4.39 and the previous assumptions, using the Gauss theorem the differential form is defined as

$$q = -k\frac{\partial T}{\partial x_i} \qquad 4.40$$

where q is the stored energy per mass and k is the effective conductivity.

A simple axisymmetric model was developed, and implemented in Ansys Fluent. Only the energy equation was discretized using a Third-order MUSCL scheme. The grid elements have the following dimension: $\Delta x = 10^{-3}\,\mathrm{m}$.

The boundary conditions considered are present in Figure 4-16. The geometric model has identical dimensions to the mold from Figure 4-17. The materials properties are present in Table 4-9. Heat flux through the wall depends on temperature gradient between inside and outside tank and is proportional to heat transfer coefficient(Fluent, 2010). The wall was considered to be made of steel, originating a parallel thermal resistance composed by the fluid convective effect, $1/h_f$, wall conduction, $\Delta x/k_{stell}$ and convective effect of the air, $1/h_{air}$, the heat transfer coefficient is computed by

$$k = \frac{1}{1/h_f + \Delta x/k_{steel} + 1/h_f} \qquad 4.41$$

where h_f is the convective coefficient of fluid, Δx is the wall thickness, k_{steel} thermal conductivity of steel and h_{air} convective coefficient of air.

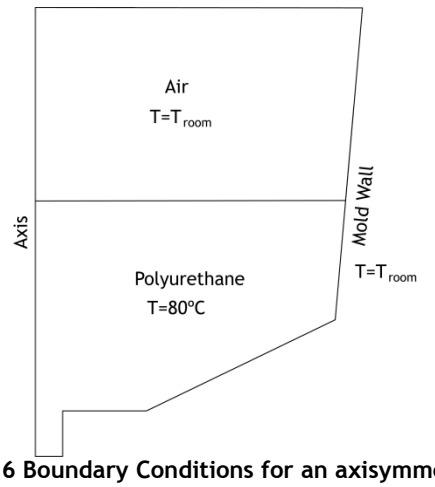

Figure 4-16 Boundary Conditions for an axisymmetric case

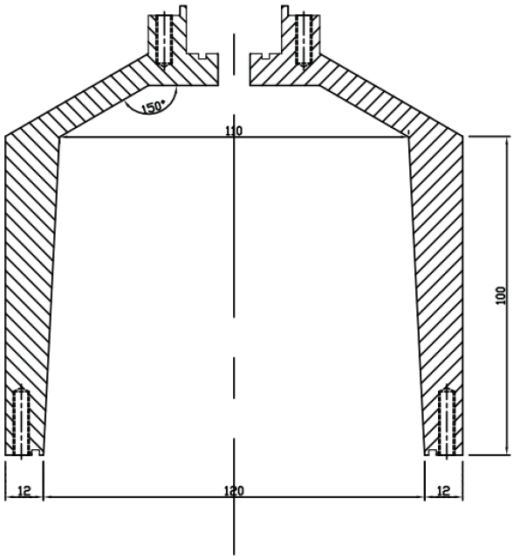

Figure 4-17 Dimensions of the mold used, in mm

To a proper convergence it was used the heat transfer's criteria according to Patankar (1980), where the time step for a heat transfer simulation is defined by

$$\Delta t \leq \frac{\rho c_p \Delta x^2}{2k} \qquad 4.42$$

For this case, it was used $\Delta x = 10^{-3}\mathrm{m}$ and so the time step should be bellow $\Delta t \leq 5.5\mathrm{s}$. The chosen value was $\Delta t = 5s$.

Table 4-9 Material Properties

Material	Air	Polyurethane (Castro and Macosko, 1982)	Steel
$\rho[\mathrm{kgm^{-3}}]$	1.2	1.0×10^{3}	8.0×10^{3}
$c_p\left[\mathrm{Jkg^{-1}K^{-1}}\right]$	1×10^{3}	1.9×10^{3}	5.0×10^{2}
$k[\mathrm{Wm^{-1}K^{-1}}]$	2.4×10^{-2}	1.7×10^{-1}	1.6×10^{1}

From Figure 4-18 is possible to see the adiabatic behavior of the mould center of mass, since the temperature at the center point decreases during approximately $20\mathrm{h}$, with a maximum temperature loss of $2\times10^{-3}\,^{o}\mathrm{C/s}$, until the room temperature is reached. A map of the temperature evolution over the time is presented in Figure 4-19.

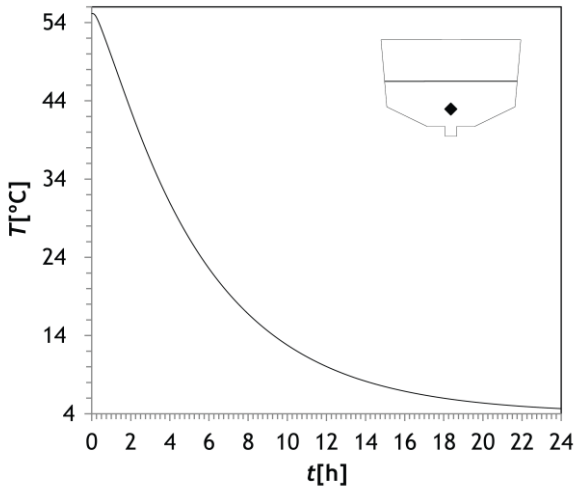

Figure 4-18 Temperature at center of mass over the time, where the black point is the thermocouple tip localization

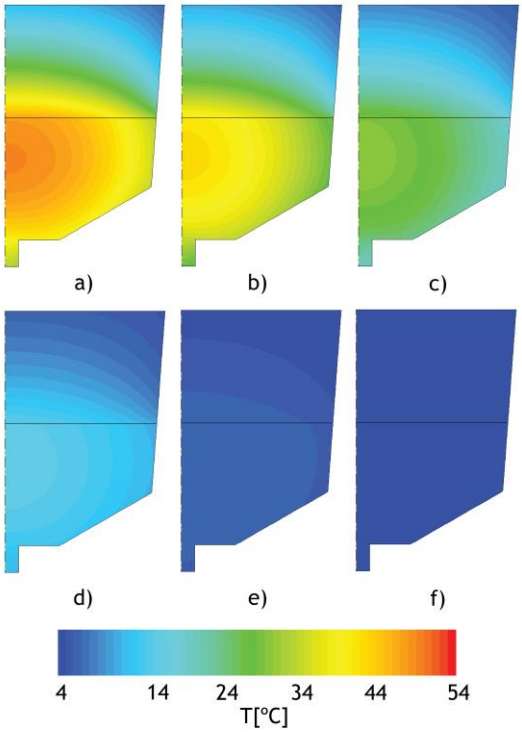

Figure 4-19 Temperature contours after: a) 3600s **b)** 7200s **c)** 14400s **d)** 28800s **e)** 57600s **f)** 86400s

4.3.3.2 Results and Discussion

The effect of kinetic energy ratio of the jets in RIM on the reaction kinetics of polyurethane polymerization was studied using the adiabatic temperature rise. Figure 4-20 shows the temperature rise over the time for different kinetic energy ratio values of the opposed jets (Figure 4-20a) and for unitary momentum ratio, and kinetic energy ratio and flow rate ratio of the jets (Figure 4-20b). The temperature rises in all samples, however, has a different behavior that depends on the operational conditions. Figure 4-20a shows

the temperature behavior for different kinetic energy ratios. The rates of temperature rise are similar for every kinetic energy ratio of the jets, except for $KE_r = 1.13$, which corresponds to the unitary flow rate ratio. An increase in the maximum temperature is observable when the KE_r tends to the unitary value, as $\lim_{KE_r \to 1^{\pm}} T = T_{\max}$. For the unitary KE_r, a maximum of $107°C$ is achieved. The exception to the trend of T_{max} is observed for KE_r values close to 1.13, where the flow rate ratio tends to the stoichiometric ratio of the used formulation ($KE_r = 1.68$). However, accordingly to the elastic analogue model of the jets (Fonte, 2012) there is a limited range for KE_r that allows the RIM machine operation without clogging any injector. For the present work this range is $0.85 \leq KE_r \leq 1.60$.

From Figure 4-20b, it is possible to observe that a higher temperature is achieved for unitary kinetic energy ratio, rather than unitary momentum and flow rate ratio. From the fastest temperature rise and higher temperature achieved, it is clear that balancing the kinetic energy of the jets is more important than balancing momentum ratio, for enhancement of mixing. This results agrees with findings of Fonte (2012) who showed that the unitary kinetic energy ratio promotes a lower scale of segregation of the monomers at the RIM mixing chamber outlet.

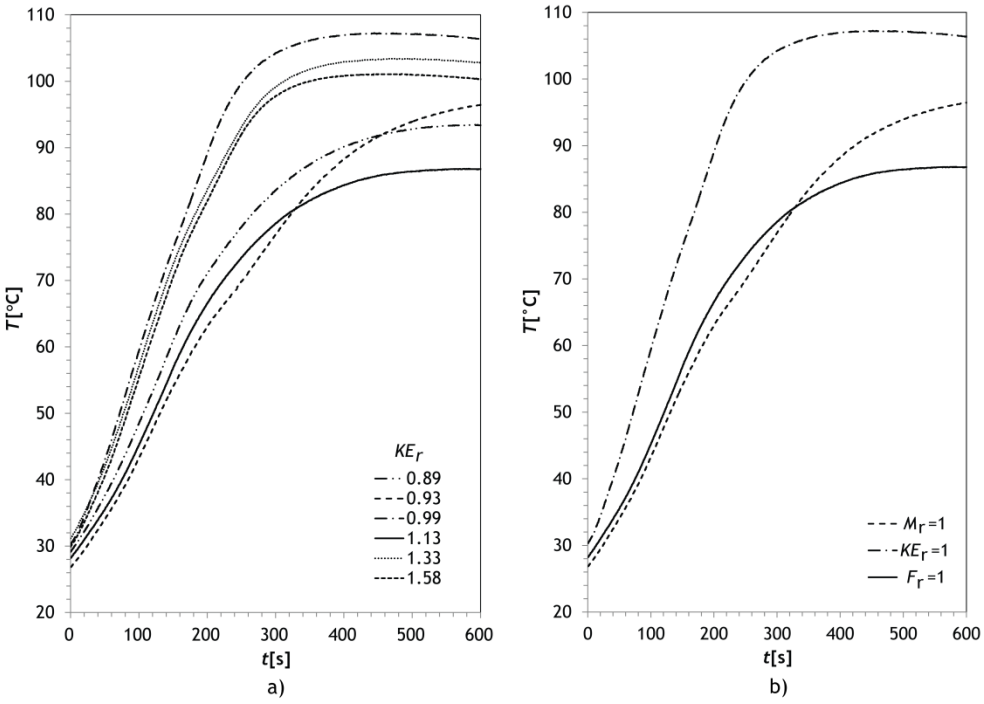

Figure 4-20 Temperature rise along the time: a) for different kinetic energy ratios and b) for unitary momentum ratio, kinetic energy ratio and flow rate ratio.

The adiabatic temperature rise, ΔT_{ad} , was calculated from

$$\Delta T_{ad} = T_{max} - T_0 \qquad 4.43$$

where $T_{\max}$ is the maximum temperature measured in the moulds and T_0 is the initial temperature inside the empty mould. Figure 4-21 shows the ΔT_{ad} as a function of KE_r and relates it with the $\overline{\Delta p^*}$, calculated by Equation 4.6, and obtained from experimental data from the DPT. The ΔT_{ad} behaviour is equal to the one presented in Figure 4-20, since it is function of $T_{\max}$. From Figure 4-21a, it is possible to observe that for unitary values of the kinetic energy ratios the values of ΔT_{ad} are higher, and for unitary flow rate ratio the lowest ΔT_{ad} is observed. Figure 4-21b, compares the ΔT_{ad} from the unitary ratio for momentum, kinetic energy and flow rate, where a clear higher temperature is achieved for unitary kinetic energy ratio.

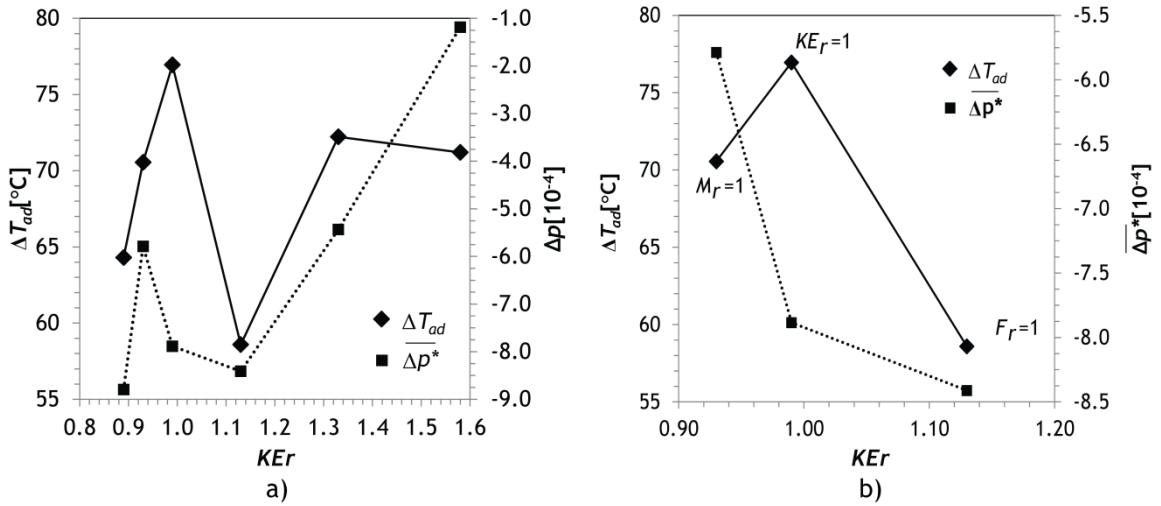

Figure 4-21 Adiabatic temperature rise and average pressure drop between the injectors along kinetic energy ratio: a) for different kinetic energy ratios and b) for unitary momentum ratio, kinetic energy ratio and flow rate ratio.

According to Castro et al (Castro et al., 1981; Castro et al., 1983) the RIM systems can be classified in heat activated and mixing activated, where the heat active system cures from the walls towards to the center of the mould and the mixing activated system, cures in the opposite direction and the initial temperature of mold wall and polymer are small. This difference leads to a low activation energy in mixing activated systems and high activation energy in heat activated systems. Figure 4-22 shows the activation energy, E_a, variation through the KE_r. For the higher ΔT_{ad} it is achieved the lowest value of E_a, where for $\lim_{KE_r \to 1^{\pm}} E_a = E_{a_{\min}}$.

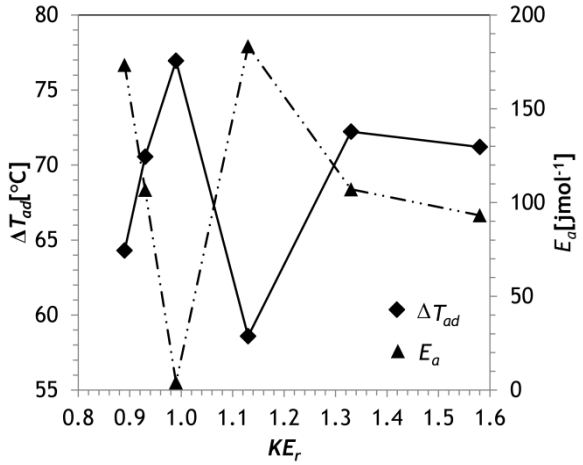

Figure 4-22 Activation energy and Adiabatic temperature rise along kinetic energy ratio

Mixing activated systems present a high reaction rate after mixing due to the low activation energy needed. Reaction rate is directly related with rate of temperature rise, dT/dt , and it was calculated from experimental temperature data using a moving average differentiation with 20 points distance, as

$$dT/dt_i = \frac{T_{i+19} - T_i}{t_{i+19} - t_i} \qquad 4.44$$

This behaviour is observed in all samples for the system used in the present work, see Figure 4-23, where the rate of temperature, dT/dt , increases fast until it reaches a peak value and after is decreases slowly. Major differences can be observed in the maximum peaks, where $\lim_{KE_r \to 1^{\pm}} dT/dt = dT/dt_{\max}$. Also the higher dT/dt corresponds to fastest reactions.

This temperature rise, dT/dt , is directly related to the reaction rate, since, in a reaction under adiabatic conditions, the temperature is an intensive property that characterizes the conversion extent.

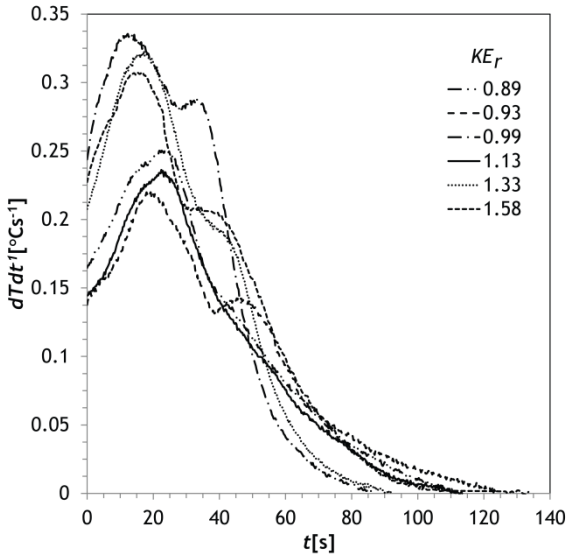

Figure 4-23 Rates of temperature rise vs. time, in function of kinetic energy ratio

4.3.4 Physical Characteristics of the Final Polymer

The mechanical properties of segmented polyurethanes are originated from the properties of the two phase morphology generated due to the microphase separation between the hard and soft segments, as also on the type of hard and soft segments, the volume fraction of each segment, intermolecular bonding, molecular weight and molecular weight distribution (Yang, 1987). Also, the phase separation controls the viscosity rise, since during the reaction the hard segments separation will increase. If the phase separation occurs in an early stage, will increase the viscosity, compromise the polymerization kinetics and produce a low molecular weight polymer, and consequently the phase separation will occur to a lesser extent. Phase separation is very important to achieve the best mechanical properties. High content of hard segments during the reaction promotes the increase of modulus and stress behaviour (Ferguson and Ahmad, 1977; Ferguson and Patsavoudis, 1972; Turner et al., 1983; Zdrahala et al., 1980). However, it is important to limit the hard segments content, since it will decrease the packing order and, consequently, the crosslinking effect (Harrell, 1969). Also the hard segment content increases the reaction exothermic heat, raising the temperature (Blake et al., 1987; Castro et al., 1981; Castro et al., 1984). However, for adiabatic conditions, the phase separation is delayed, while for isothermal conditions there is a greater likelihood of phase separation due to the presence of more urethane groups (Blake et al., 1987; Castro et al., 1981; Castro et al., 1984).

The phase separation during the RIM process can be classified into two categories: no phase separation occurs during the polymerization step; or the phase separation occurs in the polymerization step (Yang, 1987). The first situation occurs when the polymerization

reaction rate is too fast, and the second situation occurs for a slow rate reaction. PU system used for the present work has a viscosity rise behaviour, along the reaction time, according to Figure 4-24 (Torres et al., 2012). In the same figure the storage, E', and loss modulus, E'', are shown, and the intersection of both curves represent the gelation time, after this point, the mixture flow is difficult. For the present PU system, the gelation time is around 18min, which is an indication that in this system phase separation occurs during the polymerization. From Figure 4-23, is possible to see a double peak in dT/dt. According to Camargo (1984), the double peak is due to phase separation and occurs during polymerization reaction.

To analyse the phase separation, several techniques, as Fourier transform infrared spectroscopy or small angle X-ray scattering can be used. However, in an industrial environment it is difficult to have these techniques close to the equipment for an *in-situ* characterization. To overcome it, an *ex-situ* techniques can be used, such as the measurement of physical properties of the polymer, since the phase separation is associated with mechanical properties. In the literature, several techniques were used such as: measuring the tensile strength (Fruzzetti et al., 1977), elongation to break (Fruzzetti et al., 1977), flex life (Fruzzetti et al., 1977), compressive properties (Gomes et al., 2010), among others. Although, there is an extensive body of literature on final mechanical properties of segmented polyurethanes as a function of various formulation parameters (Macosko, 1989), no information can be found about the influence of mixing kinetics on the phase separation, and consequently on final polyurethane properties.

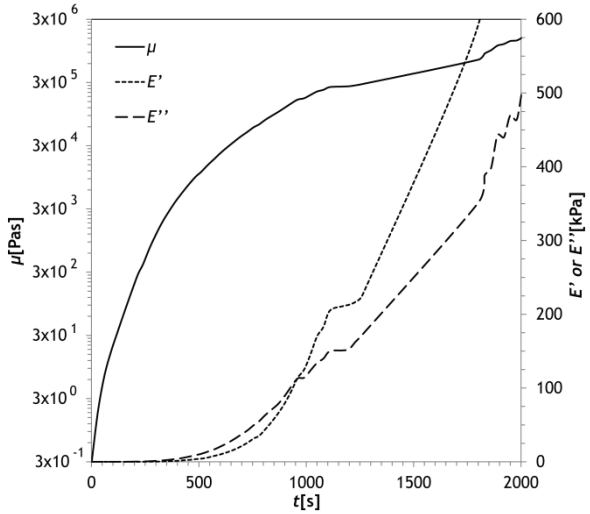

Figure 4-24 Rencast FC52 viscosity rise in function of reaction time (Torres et al., 2012)

From the injected parts, several samples were extracted by milling using a Roland MDX-500 3D modeling machine, which has an accuracy of 0.1mm in each axis. Figure 4-25 shows

the positioning of the samples cut from the injected samples. These samples were milled according to the standards used in each test, which are specified in the corresponding sub-chapter. In order to cut the maximum number of samples possible, they were cut with length perpendicular to the main flow direction. But in fact, the samples orientation does not affect the measured mechanical properties due to the fact that most of the polymerization reaction occurs after the mould filling and is fairly isotropic (Camargo, 1984).

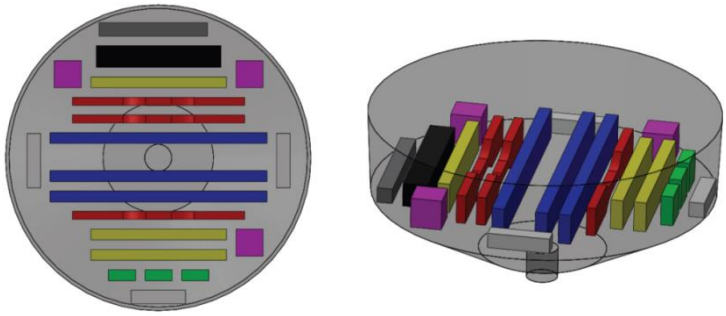

Figure 4-25 Specimens collected from the injected part: blue) flexural specimens; red) tensile specimens; yellow) compressive modulus specimens; green) compressive strength specimens; pink) density specimens; black) deflection temperature specimen; dark grey) glass temperature transition specimen; light grey) SEM specimens.

4.3.4.1 Physical Properties

Three physical properties were measured and compared as function of KE_r: density, deflection temperature and glass transition temperature.

Density

The density for each sample was calculated, using an analytical balance from *Mettler Toledo AG 204*. The density determination was based on Archimedes' principle, which states that a body immersed in a fluid apparently loses weight by an amount equal to the weight of the fluid it displaces. The procedure ASTM D792 (ASTM, 2001b) procedure was used to calculate the density of the samples, and it is shown in Figure 4-26.

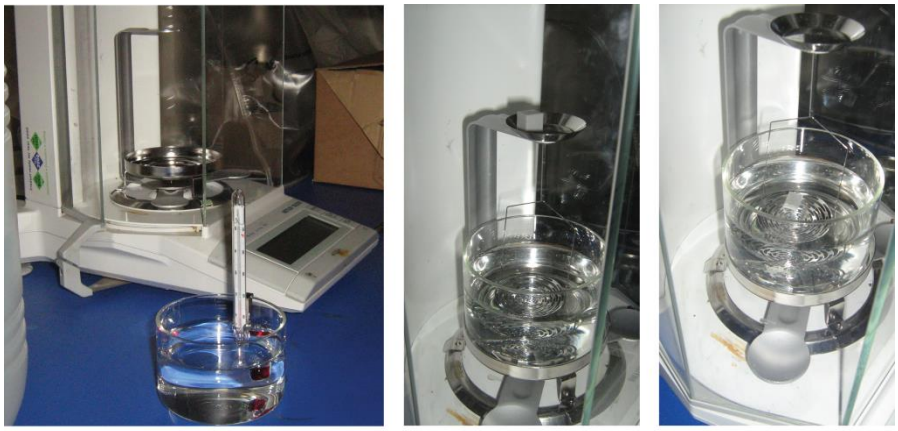

Figure 4-26 Density measurement according to ASTM D792 (ASTM, 2001b): a) distilled water temperature measurement, b) measurement of dry mass of the sample and c) measurement of wet mass of the sample.

According to the standard (ASTM, 2001b) the sample density is determined by

$$\rho_{pu} = \frac{m_d}{m_d - m_{we}} \rho_{H_2O@T_{measurement}} \qquad 4.45$$

where m is the mass, the index d refers to dry and we to wet, $\rho_{H_2O@T_{measurement}}$ is the water density at the mass measurement temperature.

Figure 4-27 shows the density as a function of KE_r. It can be observed that the density increase when $\lim_{KE_r \to 1^{\pm}} \rho_{pu} = \rho_{pu_{\max}}$ which is the local maximum. After the density decreases until $KE_r = 1.13$ and after it can increase again, due to the fact that the injection is made close to the stoichiometric ratio, which is achieved for $KE_r = 1.68$. Notice that the variation between the lower and higher ρ_{pu} values is less then 4% .

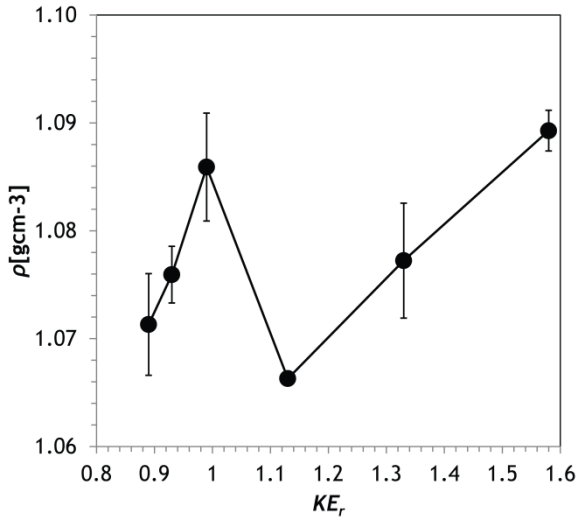

Figure 4-27 Density as function of kinetic energy ratio

Deflection temperature, T_d

The defelection temperature T_d is the maximum temperature at which a polymer can be used as a rigid material (Nielsen and Landel, 1984). Up to this temperature the material is able to support a load for some appreciable time. To determine the T_d, the sample is placed under a specified load and its temperature is raised. The T_d is the temperature when the sample deflects 0.25mm. This method, normally is performed according to the ASTM D648 (ASTM, 2001a) standard. The present work used a *Dynamical Mechanical Analyzer* (DMA), model Tritec 2000 from Triton, where a three-point bending deformation was used to perform the measurements with equivalent conditions to the ASTM D648 (ASTM, 2001a) standard. However, the samples dimensions for DMA are smaller than those used in the ASTM D648 (ASTM, 2001a), and to perform the test under the same load conditions, the DMA's sample must perform the same strain induced by a characteristic load. For the present work it was used a stress of 0.455MPA, defined in the standard (ASTM, 2001a), and the DMA deflection was calculated according to

$$s_{DMA} = \varepsilon_{ASTM} \frac{L_{DMA}^2}{6t_{h_{DMA}}} \qquad 4.46$$

where ε is the strain, s is the deflection, t_h and L are the thickness and the length of the samples, the index DMA refers to the sample size used in DMA. In the present work it was used an $L = 20\text{mm}$, where the samples have a dimensions of $20\times 8\times 8\text{mm}$. The strain from ASTM standard is given by

$$\varepsilon_{ASTM} = \frac{6s_{ASTM}t_{h_{ASTM}}}{L_{ASTM}^2} \qquad 4.47$$

where index $ASTM$ refers to the standard dimensions (ASTM, 2001a). For the present work, was used a temperature scan with single strain and frequency where $\varepsilon = 0.05\%$ and the oscillatory frequency was 1Hz. The temperature range was from room temperature, $23°\text{C}$ until $120°\text{C}$, with a ramp rate of $2°\text{Cmin}^{-1}$. Due to the analysis type all the runs were stopped before the maximum temperature value due to the fact that the material stiffness was out of the equipment's stiffness range. However, the tests were stopped at values that did not jeopardize the calculation of T_d. The test conditions were chosen in order to maintain the linear viscoelasticity.

From Figure 4-28 it is possible to observe a decrease in T_d with an increase in KE_r, $\lim_{KE_r \to +\infty} T_d = T_{d_{\min}}$, however for $KE_r = 1$ there is a local minimum.

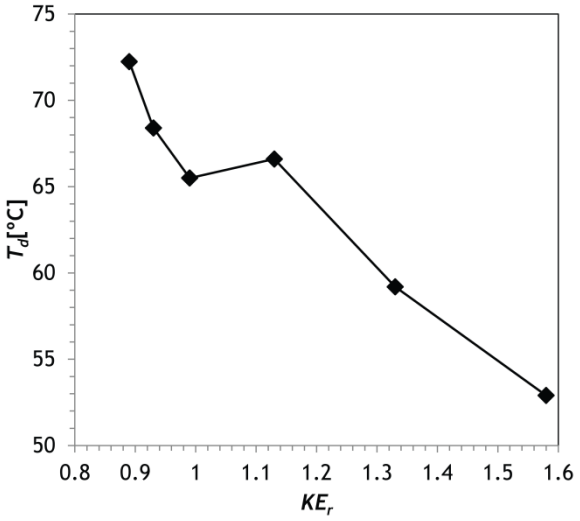

Figure 4-28 Deflection temperature as function of kinetic energy ratio

Glass transition temperature, T_g

Glass transition temperature, T_g, represents a major transition for material's physical properties from a hard glassy to a rubbery state. The T_g was measured using DMA, using a single strain and frequency value and a single cantilever bending deformation. The sample dimensions were $10 \times 5 \times 5\text{mm}$, with a strain of $\varepsilon_{ASTM} = 0.05\%$ and an oscillatory frequency of 1Hz. The temperature range was from room temperature, $23°\text{C}$, to $120°\text{C}$ with a ramp rate of $2°\text{Cmin}^{-1}$. The T_g was determined from the peak of the damping factor, $\tan\delta$

$$\tan\delta = \frac{E''}{E'} \qquad 4.48$$

For the T_g, shown in Figure 4-29, it is found a similar trend to the one found for the T_d, where $\lim_{KE_r \to +\infty} T_g = T_{g_{\min}}$. However, two peaks are noticed, for $KE_r = 0.99$ and $KE_r = 1.13$, with a maximum value for $KE_r = 0.99$. These clearly show that the KE_r plays an important role for the phase transition in RIM, and consequently, on the range of operation temperatures of the produced material.

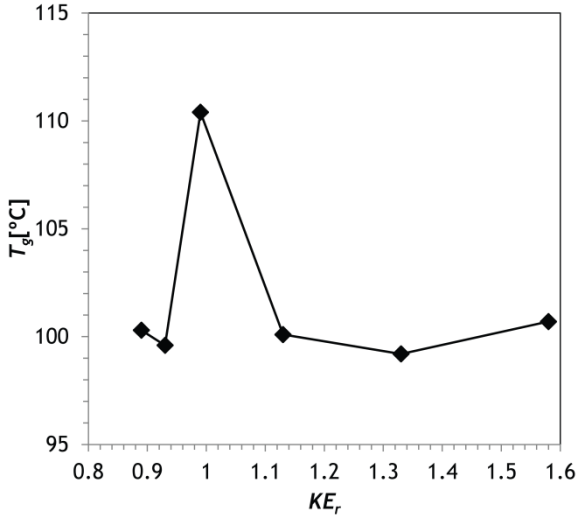

Figure 4-29 Glass transition temperature as function of kinetic energy ratio

4.3.4.2 Mechanical Properties

The material behavior under load was studied from the stress-strain curves. Present work studied the samples under an axial force, originating a tensile and compressive performance. The tensile test consists in elongation of the specimens, as shown in Figure 4-30e and Figure 4-30f, and the compressive test consists in specimens compression, as shown in Figure 4-30c and Figure 4-30d. Also samples under a transversal force were studied, originating a flexural performance, as shown in Figure 4-30b. The stress-strain tests performed were:

- Tensile test, according to the standard ASTM 638 (ASTM, 2002)
- Compressive test, according to the standard ISO 604 (ISO, 2002)
- Flexural test, according to the standard ISO 178 (ISO, 2003)

Three specimens, for each test, were cut from the injected parts, according to the position of the specimens with the colors blue, red, yellow and green from Figure 4-25. The dimensions used are present in Table 4-10 with the specified tolerance for each.

Table 4-10 Specimens Dimensions

Test	Dimension
Tensile*	$63.5\times9.53\pm0.08\times3\pm0.4$
Compressive Modulus	$50\pm2\times10\pm0.2\times4\pm0.2$
Compressive Strength	$10\pm0.2\times10\pm0.2\times4\pm0.2$
Flexural	$80\pm2\times10\pm0.2\times4\pm0.2$

* main dimensions

All experiments were performed using a universal test machine from Zwick model Z100, and according to the respective standard, with a pre-stress of 100N and the velocity used for the tests was $1 \mathrm{mm min^{-1}}$, except for the flexural test that was performed at $2 \mathrm{mm min^{-1}}$. Figure 4-30a shows the equipment and Figure 4-30b to Figure 4-30f show the mechanical test. For each test, three specimens were analyzed. The mean, $\bar{x}$, can be defined by

$$\bar{x} = \frac{1}{n} \sum_{i=1}^{n} x_i \qquad 4.49$$

where n is the number of samples, for these work 3 samples were used, x is the value of the measured property, e.g., compressive modulus, and index i is the sample number. Standard deviation, s_d , is defined as

$$s_d = \sqrt{\frac{1}{n-1} \sum_{i=1}^{n} \left(x_i - \bar{x} \right)^2} \qquad 4.50$$

The lower and upper limits of confidence interval of 97.5%, for the results were computed according to Bendat and Piersol (1971), and using

$$\bar{x} \pm \frac{t_{0.975}}{\sqrt{n}} s_d \qquad 4.51$$

where $t_{0.975}$ is the t-Students parameter, and for the present work it is equal to $t_{0.975} = 4.303$, according to the standard ISO (1980).

Figure 4-30 Measurement of the mechanical properties: a) Zwick model Z100 DMA, b) flexural test , c) compressive modulus test, d) compressive strength test, e) tensile test f) break of specimen in tensile test.

In the elastic region, identifiable in Figure 4-31, the material behaviour is linear and follows the Hooke's law, where the stress, σ, is proportional to the strain, ε, according to

$$\sigma_i = E_i \varepsilon_i \qquad 4.52$$

Based in the previous relation, the modulus, E_i, is calculated from the values in the elastic region,

$$E_i = \frac{\sigma_{0.025} - \sigma_{0.005}}{\varepsilon_{0.025} - \varepsilon_{0.005}} \qquad 4.53$$

where the index i corresponds to a test indicative letter, in the present f is used for the flexural test, c for compressive test and t for tensile test. From the last equation, the terms $\varepsilon_{0.005} = 0.0005$, $\varepsilon_{0.025} = 0.0025$, $\sigma_{0.005}$ is the strength at $\varepsilon_{0.005}$ and $\sigma_{0.025}$ is the strength at $\varepsilon_{0.025}$.

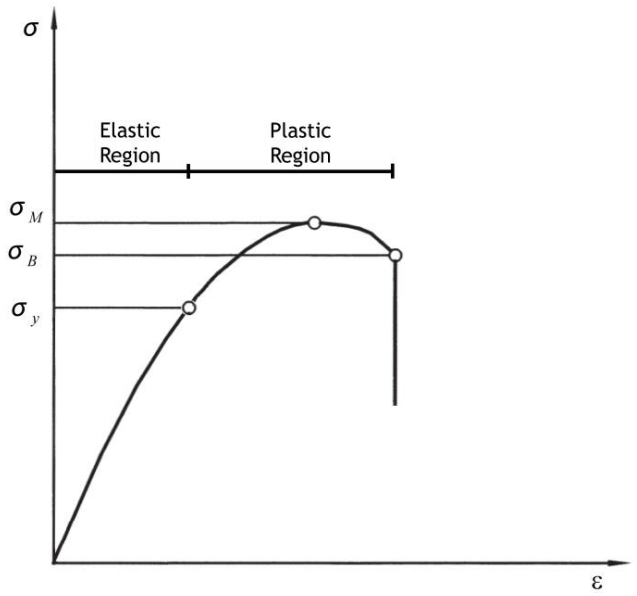

Figure 4-31 Typical curve of strain-strength

From a stress-strain curve under an axial force, were measured the follow material properties, according to Figure 4-31:

- yield strength, σ_y , is the limit of elastic region;
- maximum strength, σ_M , is the maximum strength;
- break strength, σ_B , is the limit of plastic region and is achieved when the specimen breaks.

Figure 4-32 shows the tensile test results. The highest E_t and σ_{B_t} are obtained when the jet's kinetic energy ratio is closer to one, $KE_r = 0.99$. The lowest value of σ_{y_t} and the highest E_t indicate the existence of a smaller elastic region. Both E_t and σ_{B_t} increase with KE_r until a maximum value is reached at $KE_r = 0.99$, $\lim_{KE_r \to 1^{\pm}} E_t = E_{t_{\max}}$ and $\lim_{KE_r \to 1^{\pm}} \sigma_{B_t} = \sigma_{B_t \max}$. For the σ_{y_t} , the maximum value occurs when $KE_r = 0.93$, where the jet's momentum are in equilibrium. For the $KE_r = 0.99$, there is a local minimum value in σ_{y_t} . From the present results, the maximized stretching effects, i.e., $KE_r \approx 1$, promote an earlier phase separation and it suggests that the increase of the interfacial area between the monomers can promote a better inter-domain cohesion of hard segments (Macosko, 1989). The Mean, standard deviation and lower and upper limits of confidence of 97.5%

of the strength and modulus are shown in Table 4-11, and it is observable that all values are inside the limits of confidence of 97.5%.

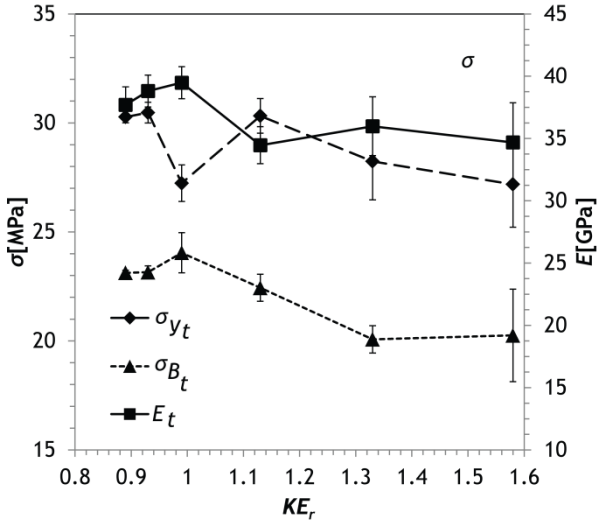

Figure 4-32 Tensile properties as function of kinetic energy ratio

Compressive strengths, σ_{y_c}, σ_{M_c} and σ_{B_c}; and modulus, E_c, which are shown in Figure 4-33 exhibit a similar behaviour, with the values increasing until their maximum value for a specific $KE_r = 1.13$, and after decreasing, i.e. $\lim_{KE_r \to 1.13^{\pm}} y = y_{\max}$, where y represents the compressive properties measured. However, there is a local minimum for the strengths when $KE_r = 0.99$ and another one for the E_c. The Mean, standard deviation and lower and upper limits of confidence of 97.5% of the strength and modulus are shown in Table 4-12 and Table 4-13, respectively. From the tables is observable that all values are inside the limits of confidence of 97.5%.

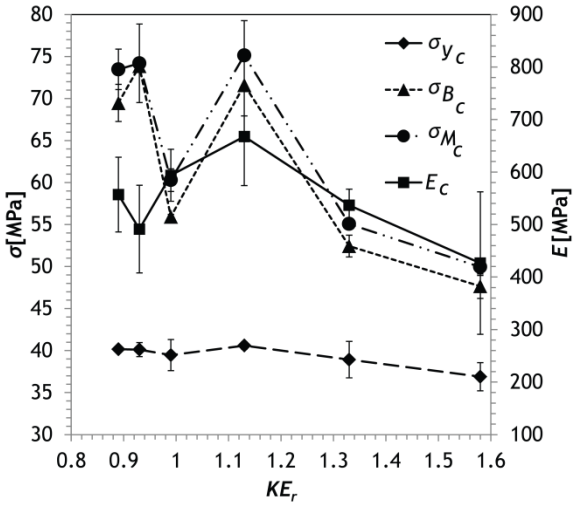

Figure 4-33 Compressive properties in function of kinetic energy ratio

Table 4-11 Mean, standard deviation and lower and upper limits of confidence of 97.5% for the tensile test

KE_r	σ_{y_t} [MPa]				σ_{B_t} [MPa]				E_t [GPa]			
	$\overline{\sigma_{y_t}}$	s_d	$\overline{\sigma_{y_t}} - \frac{t_{0.975}}{\sqrt{n}} s_d$	$\overline{\sigma_{y_t}} + \frac{t_{0.975}}{\sqrt{n}} s_d$	$\overline{\sigma_{B_t}}$	s_d	$\overline{\sigma_{B_t}} - \frac{t_{0.975}}{\sqrt{n}} s_d$	$\overline{\sigma_{B_t}} + \frac{t_{0.975}}{\sqrt{n}} s_d$	$\overline{E_t}$	s_d	$\overline{E_t} - \frac{t_{0.975}}{\sqrt{n}} s_d$	$\overline{E_t} + \frac{t_{0.975}}{\sqrt{n}} s_d$
0.89	30.3	0.1	29.6	30.9	23.1	0.1	22.6	23.6	37.7	1.4	31.5	43.9
0.93	30.5	0.5	28.4	32.5	23.2	0.3	21.9	24.4	38.8	1.3	33.3	44.3
0.99	27.2	0.8	23.6	30.8	24.0	0.9	20.1	28.0	39.5	1.3	33.9	45.0
1.13	30.3	0.8	26.9	33.7	22.4	0.6	19.8	25.1	34.5	1.5	28.1	40.8
1.33	28.2	1.8	20.6	35.8	20.1	0.6	17.4	22.8	36.0	2.4	25.8	46.1
1.58	27.2	2.0	18.7	35.6	20.3	2.1	11.1	29.4	34.7	3.2	21.0	48.4

Table 4-12 Mean, standard deviation and lower and upper limits of confidence of 97.5% for the compressive test

KE_r	σ_{y_c} [MPa]				σ_{M_c} [MPa]				σ_{B_c} [MPa]			
	$\overline{\sigma_{y_c}}$	s_d	$\overline{\sigma_{y_c}} - \frac{t_{0.975}}{\sqrt{n}} s_d$	$\overline{\sigma_{y_c}} + \frac{t_{0.975}}{\sqrt{n}} s_d$	$\overline{\sigma_{M_c}}$	s_d	$\overline{\sigma_{M_c}} - \frac{t_{0.975}}{\sqrt{n}} s_d$	$\overline{\sigma_{M_c}} + \frac{t_{0.975}}{\sqrt{n}} s_d$	$\bar{x}$	s_d	$\overline{\sigma_{B_c}} - \frac{t_{0.975}}{\sqrt{n}} s_d$	$\overline{\sigma_{B_c}} + \frac{t_{0.975}}{\sqrt{n}} s_d$
0.89	40.2	0.3	38.8	41.5	73.5	2.2	64.0	82.9	69.5	2.4	59.1	79.8
0.93	40.1	0.8	36.5	43.7	74.2	0.4	72.5	75.8	73.9	4.7	53.7	94.0
0.99	39.5	1.8	31.5	42.5	60.3	0.3	59.1	61.4	55.9	1.3	50.2	61.7
1.13	40.6	0.4	38.7	48.3	75.1	3.7	59.4	90.9	71.6	4.1	53.8	89.4
1.33	38.9	2.2	29.6	48.3	55.1	1.3	49.5	60.7	52.4	0.6	49.8	55.1
1.58	36.9	1.7	29.7	44.1	49.9	1.4	43.7	56.2	47.7	1.0	43.4	52.0

Table 4-13 Mean, standard deviation and lower and upper limits of confidence of 97.5% for the compressive test

KE_r	$E_C\,[MPa]$			
	$\overline{E_c}$	s_d	$\overline{E_c}-\frac{t_{0.975}}{\sqrt{n}}s_d$	$\overline{E_c}+\frac{t_{0.975}}{\sqrt{n}}s_d$
0.89	557.0	71.2	250.6	863.3
0.93	491.3	83.6	131.5	851.1
0.99	593.8	49.3	381.5	806.1
1.13	667.6	93.5	265.1	1070.1
1.33	536.8	30.7	404.9	668.7
1.58	426.6	125.7	0.0	1010.6

The classic formula for determining the bending stress in a beam under simple bending was calculated from the Euler-Bernoulli beam equation,

$$E_i I \frac{d^4 w(x)}{dx^4} = F(x) \tag{4.54}$$

where E is the Young modulus, I is the cross-sectional beam moment of inertia, w is the deflection of the beam x is the position along the axial axis of the beam and F is the applied force over the beam.

The maximum cross-sectional bending stress in a beam under simple bending is defined by

$$\sigma_{\max} = \frac{M_{\max} c}{I} \tag{4.55}$$

where $M_{\max}$ is the maximum torque and c the distance to the neutral plane of the beam. For a simple supported beam, the $M_{\max}$ is given by

$$M_{\max} = \frac{FL}{4} \tag{4.56}$$

where F is the applied force and L is the beam span.

The cross-sectional beam moment of inertia for a rectangular section is

$$I = \frac{b t_h^{\,3}}{12} \tag{4.57}$$

where b is the width, and t_h is the thickness.

According to the ISO (2003), Equation 4.56, Equation 4.57 and considering $c = t/2$ are used into Equation 4.55, originating the flexural strength given by

$$\sigma_f = \frac{3FL}{2bt^2} \qquad 4.58$$

From flexural results, present in Figure 4-34, is possible to see that the flexural strength, σ_f, achieve a maximum for $KE_r = 0.93$ and a minimum for $KE_r = 1.13$. For the flexural modulus, E_f, the maximum is for $KE_r = 0.99$ and the minimum for $KE_r = 0.93$. The tendency is $\lim_{KE_r \to 1.13^{\pm}} y = y_{\max}$, where y represents the any flexural properties analysed. For both properties, the local minimum is when $KE_r = 1.13$, i.e., for equal flow rate. The results are inside the limits of confidence of 95%, as shown in Table 4-14. In the same table the mean and standard deviation are shown also.

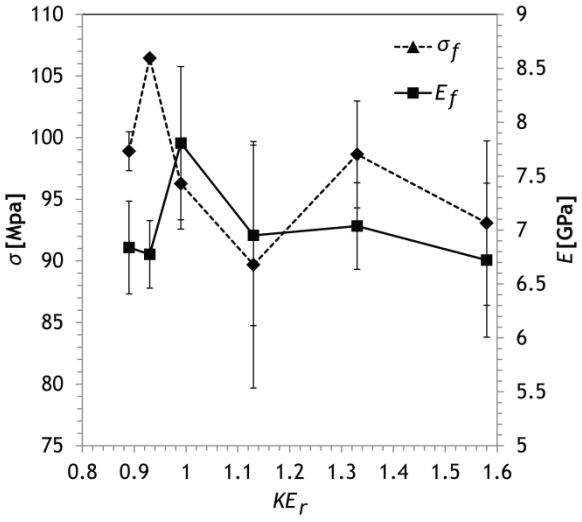

Figure 4-34 Flexural properties in function of kinetic energy ratio

From the stress-strain curves, the toughness can be calculated. This property measures the ability of a material to absorb energy before the fracture, under the plasticity domain, and is a relation between strength and ductility, that is defined by

$$K_i = \int_0^{\varepsilon_{b_i}} \sigma_i d\varepsilon_i \qquad 4.59$$

where the index i corresponds to the type of mechanical test, and the ε_b to the break strain.

Table 4-14 Mean, standard deviation and lower and upper limits of confidence of 97.5% for the flexural strength and modulus

KE_r	$\sigma_f\,[MPa]$				$E_f\,[MPa]$			
	$\overline{\sigma_f}$	s_d	$\overline{\sigma_f}-\frac{t_{0.975}}{\sqrt{n}}s_d$	$\overline{\sigma_f}+\frac{t_{0.975}}{\sqrt{n}}s_d$	$\overline{E_f}$	s_d	$\overline{E_f}-\frac{t_{0.975}}{\sqrt{n}}s_d$	$\overline{E_f}+\frac{t_{0.975}}{\sqrt{n}}s_d$
0.89	98.9	1.6	92.1	105.7	6.8	0.4	5.0	8.7
0.93	106.4	0.1	106.0	106.9	6.8	0.3	5.4	8.1
0.99	93.6	3.7	80.5	112.0	7.8	0.7	4.7	10.9
1.13	89.7	10.0	46.7	132.7	7.0	0.8	3.3	10.6
1.33	98.6	4.3	80.0	117.3	7.0	0.4	5.3	8.8
1.58	93.1	6.7	64.4	128.1	6.7	0.7	3.6	9.8

Figure 4-35 shows the toughness variation with KE_r. The first observation from Figure 4-35 is that the tensile tests have more energy absorption capacity. For the tensile tests, the K_t has an increasing trend with KE_r until $KE_r = 1.33$ and after it decreases. However, two local minima exist for $KE_r = 0.93$ and $KE_r = 0.99$, suggesting that both kinetic energy balance, maximum temperature in the mold or raw materials stoichiometry will affect the material ability to absorb energy. For the K_c, the trend is not so perceptible in the studied KE_r range, and some local minima for $KE_r = 0.99$ and $KE_r = 1.33$, and peaks for $KE_r = 1.13$ can be found. Regarding the flexural test, there is a decrease in K_f for the increasing in KE_r.

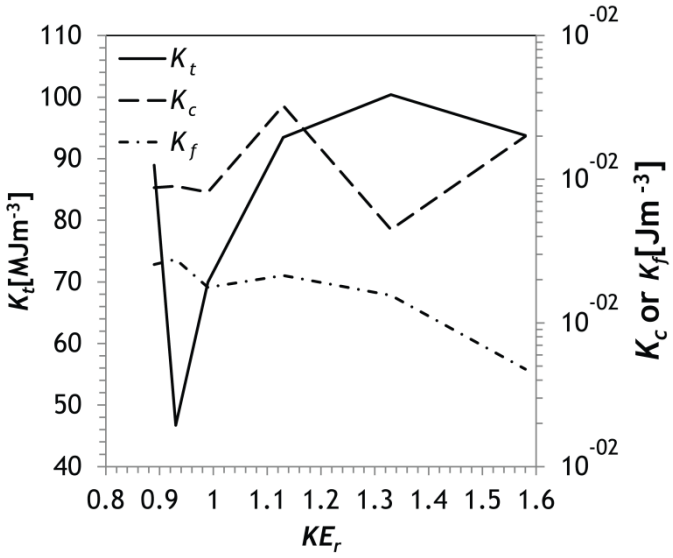

Figure 4-35 Toughness in function of kinetic energy ratio.

To get a better insight into the effect of mixing on the microstructure of the PU, the viscoelastic properties, storage modulus E' and loss modulus E'' were measured using DMA, with a test specification equal to the ones used to calculate the T_g. The viscoelastic properties are fingerprints of the molecular behaviour, and are an important key to understand the polymerization and phase separation.

The E' represents the elastic response of the material, while the E'' is the viscous behaviour and is related with energy losses.

Figure 4-36a and Figure 4-36b show E' and E'', and the damping factor, $\tan\delta$. Observing Figure 4-36a and Figure 4-36b it is found that the modulus behaviour have a similar temperature dependence for the different KE_r except for $KE_r = 0.99$, where the rubbery plateau is achieved later and with higher mechanical properties. According to Menard (2008), these shifts in achieving the rubbery plateau correspond to an increase in the crosslinking between the chains, and the upward shift in rubbery plateau increase the cristallinity of hard segments (Menard, 2008), since it works as additional driving force to phase separation besides the thermodynamic incompatibility (Macosko, 1989). In highly separated material, the transitional behaviour of each phase will work as a pure component, and that can be seen by a existence of a plateau in E', denominated rubbery plateau (Camargo, 1984). This pure component behaviour is related with the different solubility between both phases, and their incompatibility (Macosko, 1989). Figure 4-36a shows the existence of the plateau in all samples, and demonstrates that there is a high phase separation. The interdomain and phase boundary mixing can be assessed by dynamical mechanical response. Hashimoto et al. (1983) and Camargo et al. (1985) reported that the interdomain and phase separation boundary are increased when the temperature dependence is increased. As stated before, the present system has a larger temperature dependence when the processing parameters are close to unit, notedly for $KE_r = 0.99$. The results suggest that the kinetic energy ratio is of outmost importance to stretch and fold the monomers blend, down to a scale thin enough for diffusion to be able to contact the materials at the molecular level. The increasing modulus in rubbery plateau of E', represents more narrow hard segments (Eisenbach et al., 1985).

For $KE_r = 1.58$ and $KE_r = 1.33$ the modulus values on the plateau are lower than for other KE_r values, where the variation between them is very small. However, the higher modulus value for rubbery plateau is for $KE_r = 0.99$.

Looking to the loss modulus, E'', from Figure 4-36b, it is possible to observe that the peaks are shifted when compared to the peak of $KE_r = 0.99$. For all KE_r, the peaks occur at the same locations, with the exception of $KE_r = 0.99$, pointed out before. These shifts correspond to the interdomain increase (Camargo et al., 1985; Hashimoto et al., 1983), again for the values of processing parameters close to unitary value.

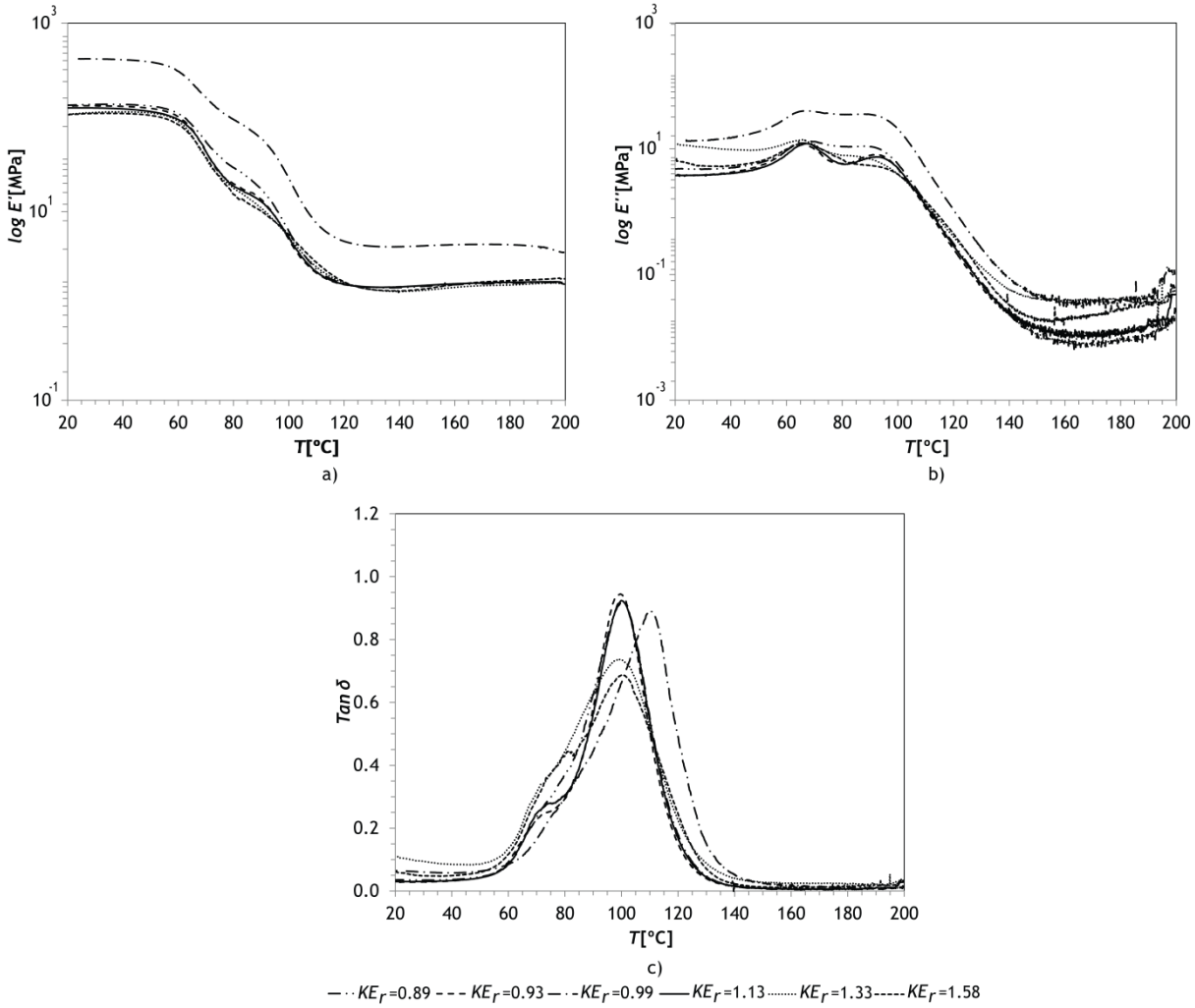

Figure 4-36 Viscoelastic properties as function of kinetic energy ratio: a) storage modulus b) loss modulus and c) $\tan\delta$.

Despite the complexity of the relationship between mechanical properties and microstructure, from the results above shown, there is a clear relation between the scale of mixing and the mechanical properties. With a decrease of the striation thickness and, consequently, the increase of interfacial area, for the $KE_r \approx 1$, the inter-domain between segments and the dilution of the soft segments, will improve the growth of hard segments, which is the responsible for the materials mechanical response.

4.3.4.3 Morphological Studies

From the previous studies, the effects of the processing conditions at the molecular scale were assessed. However, one question arises: how is the morphology of the samples and how it is affected by the monomer jets' balance? For that purpose, optical microscopy and scanning electron microscopy (SEM) photos of material samples were taken. The optical microscopy was used to study the sample free surface, and SEM was used for the internal morphology.

The free surface of the molded part was imaged using an optical microscope Axiotech 100 from Zeiss. The samples were cut from the free surface and were cleaned to guarantee a surface without any contamination.

Figure 4-37 shows the images taken with a magnification of $500\times$. Two images were taken from different positions in the sample. For the balanced KE_r , i.e. $KE_r = 0.99$, the darker structures in figures are highly orientated, for other KE_r the orientation is not the same in different photos, e.g., $KE_r = 0.93$ and $KE_r = 1.13$ or it is completely disorientated, as can be seen for $KE_r = 1.33$ and $KE_r = 1.58$. Hashimoto et al. (1983) showed that for a phase separated material, the relation between microdomain and their boundaries can result in more or less orientated domain phases. From Figure 4-37, these effects are observed. However, it is not possible to sustain that the contrast seen in the figure has any relation with the different domains that are a much smaller scale process.

The thicknesses of the dark structures were calculated using a Matlab program, after image processing. For the image processing, five images with $700\times1000\text{pixels}$ were cut from Figure 4-37. The five images were selected randomly from the main image, however it was tried to select the zones with higher colour contrast between the dark structures and the yellow ones. After the selection, the brightness and contrast were adjusted in order to improve the figures quality. To increase the colour difference between the structures, all the image colours were inverted, as shown in Figure 4-38.

Figure 4-38 images were processed using an algorithm (ISIS, 2012) to separate the horizontal stripes, which consists in using a low and high filter to remove padding from images. Figure 4-39 shows an example of this procedure. Using the identical images to Figure 4-39b, the dark structure thickness was calculated.

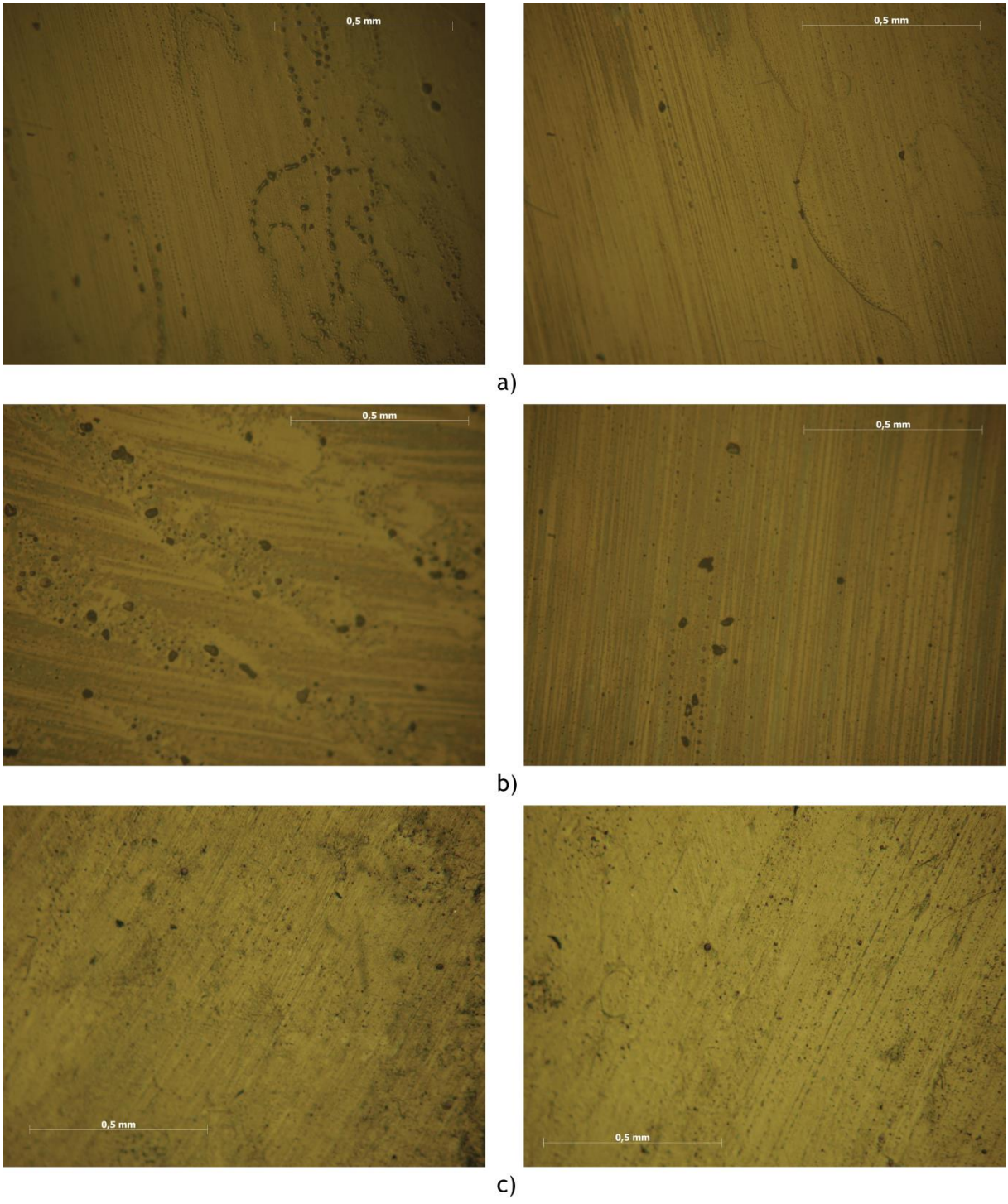

Figure 4-37 Optical microscopy images with a magnification of $500\times$: a) $KE_r = 0.89$ b) $KE_r = 0.93$ c) $KE_r = 0.99$

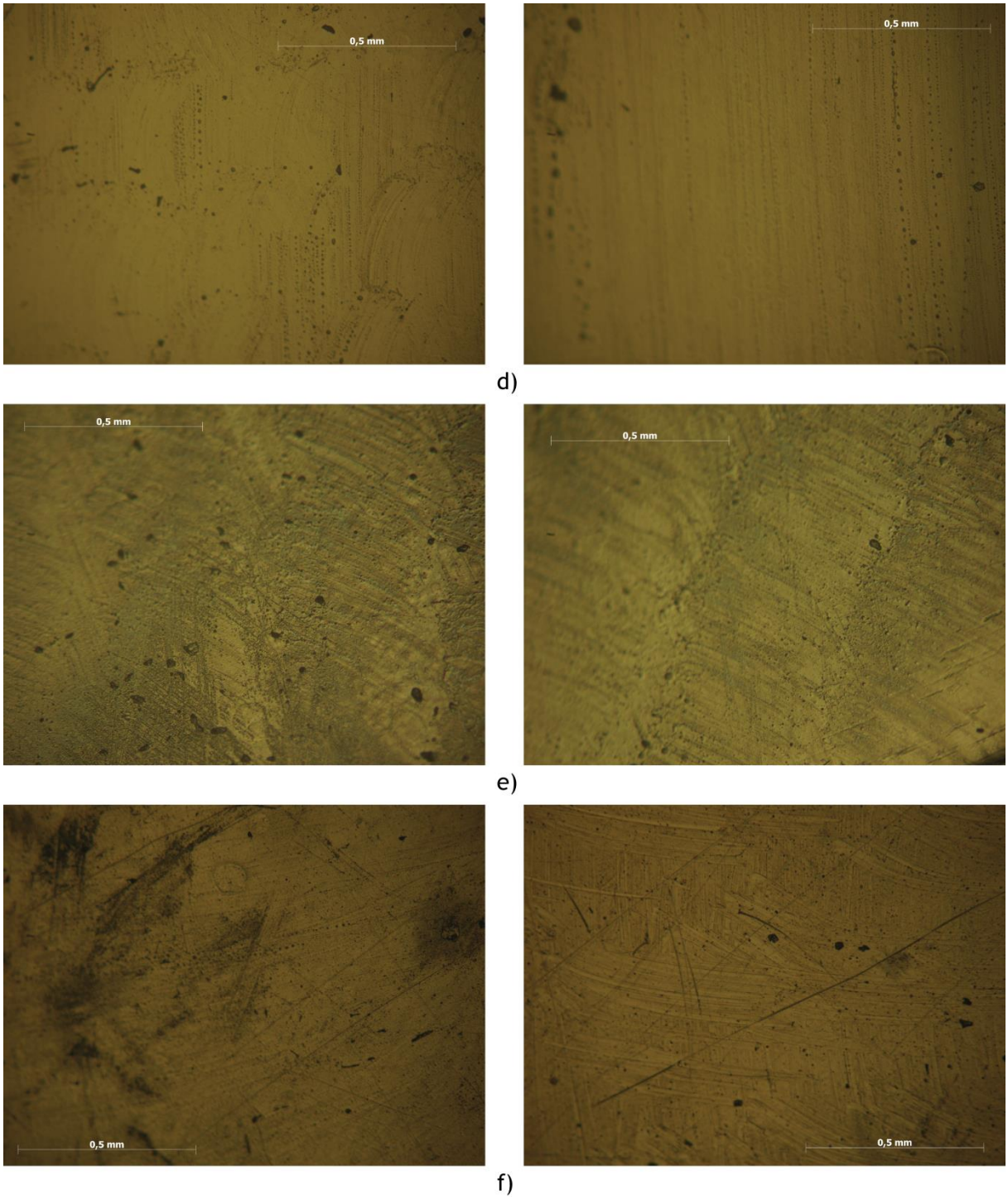

Figure 4-37 (continuation) Optical microscopy images with a magnification of $500\times$: d) $KE_r = 1.13$ e) $KE_r = 1.33$ f) $KE_r = 1.58$

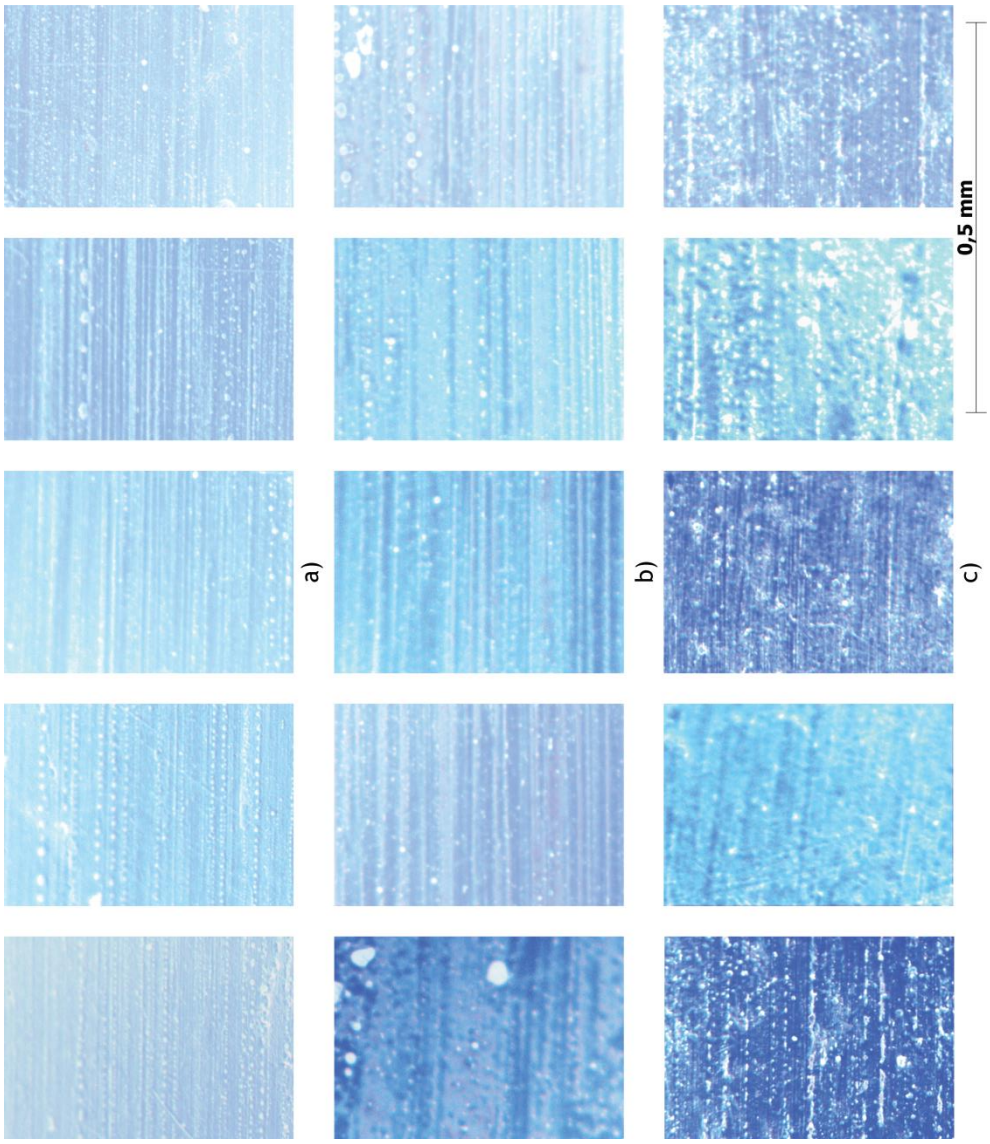

Figure 4-38 a)KE_r=0.89 b) KE_r=0.93 c) KE_r=0.99

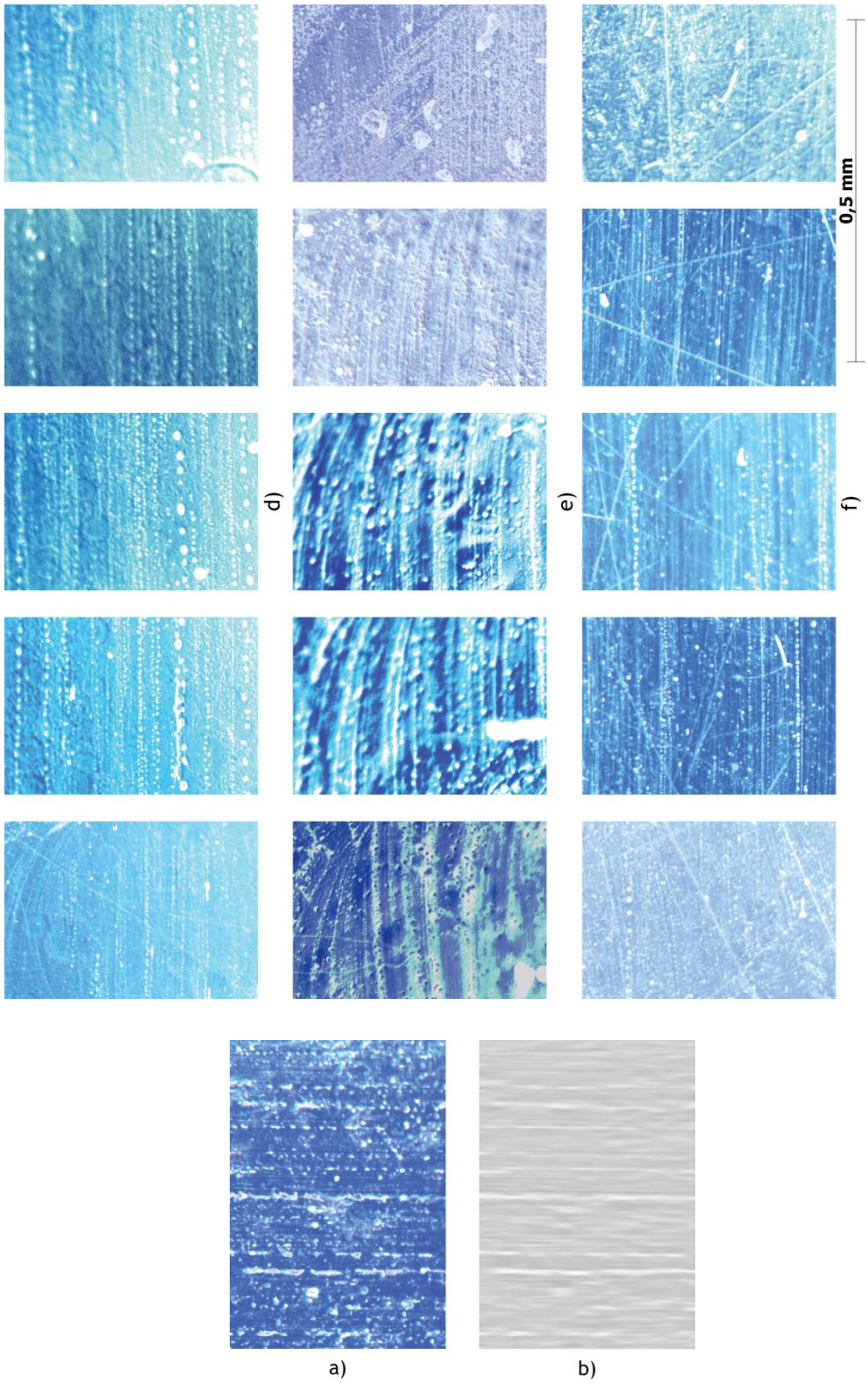

Figure 4-38 (Continuation): d)KE_r=1.13 e) KE_r=1.33 f) KE_r=1.58

Figure 4-39 Cutted image from optical microscopy for $KE_r = 0.99$ where a) inverted imaged b) processing image with ISIS (2012)

Considering that both structures were two immiscible phases, the scale of segregation, s_L, as defined by Danckwerts (1952) was used. This scale is related to the size of strias of two

phases in a mixture. According to Tucker III (1991), the s_L is defined as the integral of the correlation function of the volume fractions, $R(r)$, from zero, i.e. $R(0)=1$, to a distance ξ at which there is no correlation, $R(\xi)=0$, according to

$$s_L = \int_0^{\xi} R(r)\,\mathrm{d}r \qquad 4.60$$

To calculate the correlation function it was used the power spectrum of the imaged domain using the Fast Fourier Transform technique, identical to the one proposed by Tucker III (1991), where the power spectrum $P(n)$ is defined as

$$P(n) = \left| \int_{-\infty}^{\infty} \left(\alpha(x) - \bar{\alpha}\right) e^{-2\pi i n x} \mathrm{d}x \right|^2 \qquad 4.61$$

n is the wave number in m^{-1}.

The coefficient of correlation function, $R(r)$, was calculated from the inverse of the power spectrum, according to

$$R(r) = \int_{-\infty}^{\infty} P(n) e^{2\pi i n r} \mathrm{d}n \qquad 4.62$$

The computation of s_L is performed in pixels, to compute the striation thickness, s, the s_L is scaled from pixels to $\mu\mathrm{m}$.

The number density distribution function was defined as (Lopes, 1984)

$$f^N(s) = \frac{d}{dt_d} n(s) \qquad 4.63$$

where t_d is in the range of $0 < t_d < t_{d_{\max}}$, $n(t_d)$ is the number fraction of the thickness of dark part, t_d, and f^N is subject to

$$\int_0^{t_{d_{max}}} f^N(s)\,dt_d = 1 \qquad 4.64$$

The number cumulative distribution function is (Lopes, 1984)

$$F^N(s) = \int_0^{t_{d_{max}}} f^N(s)\,ds \qquad 4.65$$

where for $F^N(s_{max}) = 1$. This value expresses the fraction of the dark strias with a thickness smaller or equal than t_d.

Figure 4-40 shows the number density and cumulative distribution functions for the striation thickness, where it is observable a range between $1.25\mu m$ to $4\mu m$, with more than half of the strias thickness below $2.5\mu m$. These values are according to the ones predicted numerically by Fonte (2012) from CFD simulations, and are below the $10\mu m$ of mixing scale that were defined has the limit to avoid diffusional limitations during the polymerization (Lee et al., 1980).

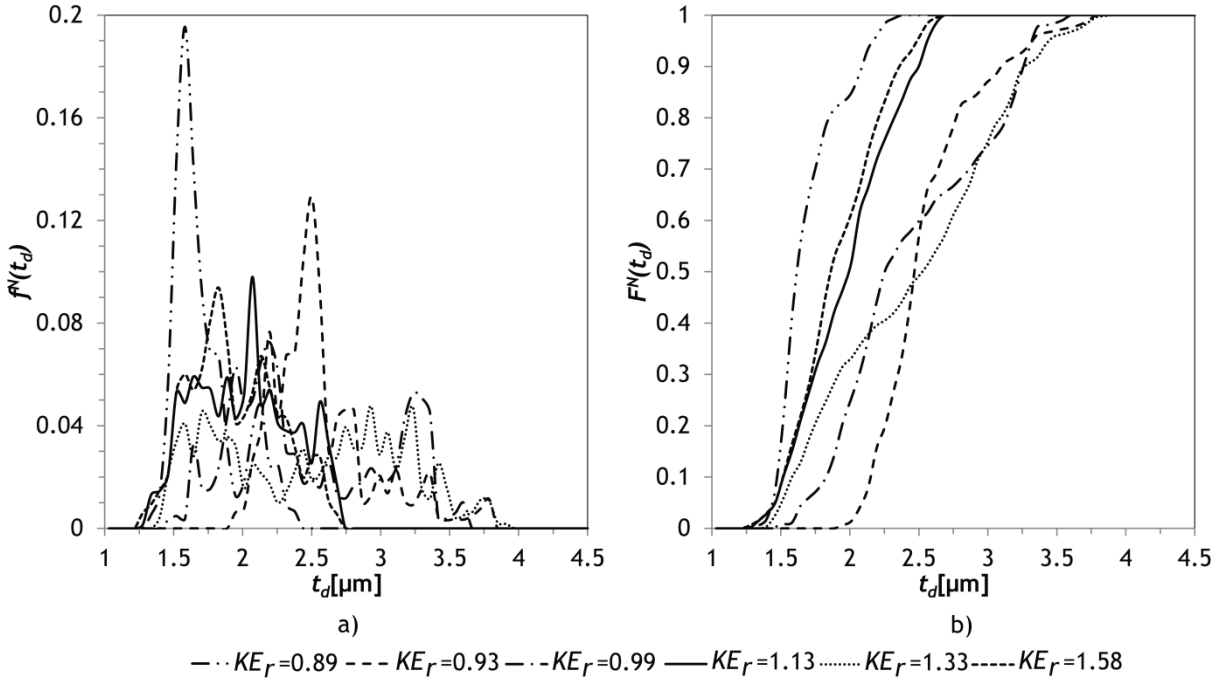

Figure 4-40 Number based dark structure thickness: a) density function b) cumulative distribution function

To understand the morphology that the dark strias represet, it was observed some internal surfaces using Scanning Electron Microscopy (SEM). Samples were extracted from the moulded part and a V-notch was made on it. For a fracture without any plastic deformation, the samples were quenched using liquid nitrogen and then the sample was broken on the V-nocth. After, the sample was put in a vacuum atmosphere, and was observed using a SEM FEI Quanta 400 FEG ESEM. The image, Figure 4-41, was obtained from a fracture of a sample from a part obtained with $KE_r = 1.13$, for a magnification of 1000X.

From the SEM figure, an algorithm from Wepf (2012) was used in ImageJ to determine the cell size distribution.

Figure 4-41 shows that the structure is highly cellular, with narrow cell size variation and without any observable cell arrangement pattern. To validate these observations, the number density for cell diameter, d_c, were calculated using

$$f^N(d_c) = \frac{d}{dd_c} n(d_c) \qquad 4.66$$

Cumulative distribution functions for cell size, d_c, were calculated using

$$F^N(d_c) = \int_0^{t_{d_{max}}} f^N(d_c)\, dd_c \qquad 4.67$$

The results are shown in Figure 4-42. From this figure, it is observable that the range of d_c values are the same of t_d, shown in Figure 4-40, which is the indication that the dark structures shown in optical microscopy are focus in depth and picturing the cell structure that exist just below the free surface.

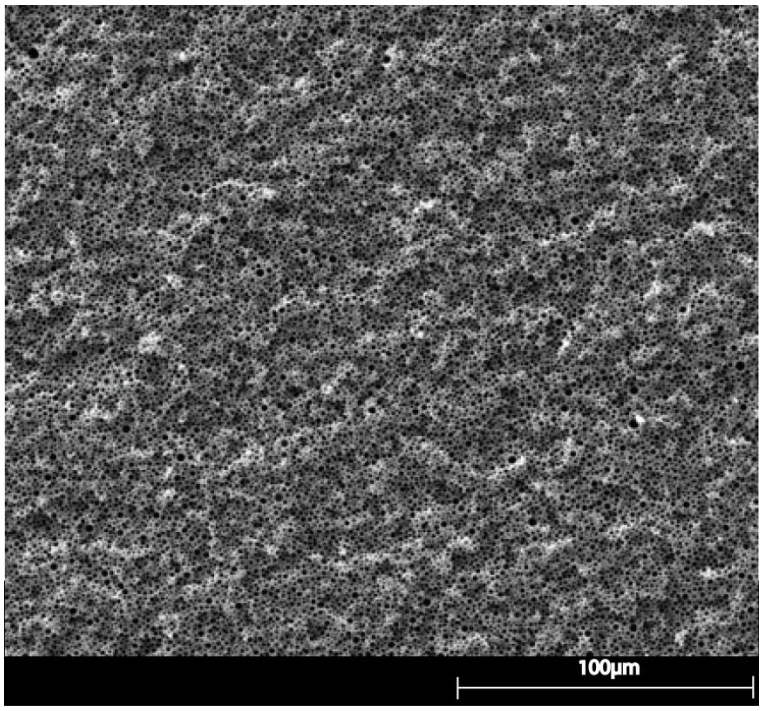

Figure 4-41 SEM image for a sample with $KE_r = 1.13$, with a magnification of $1000\mathrm{X}$

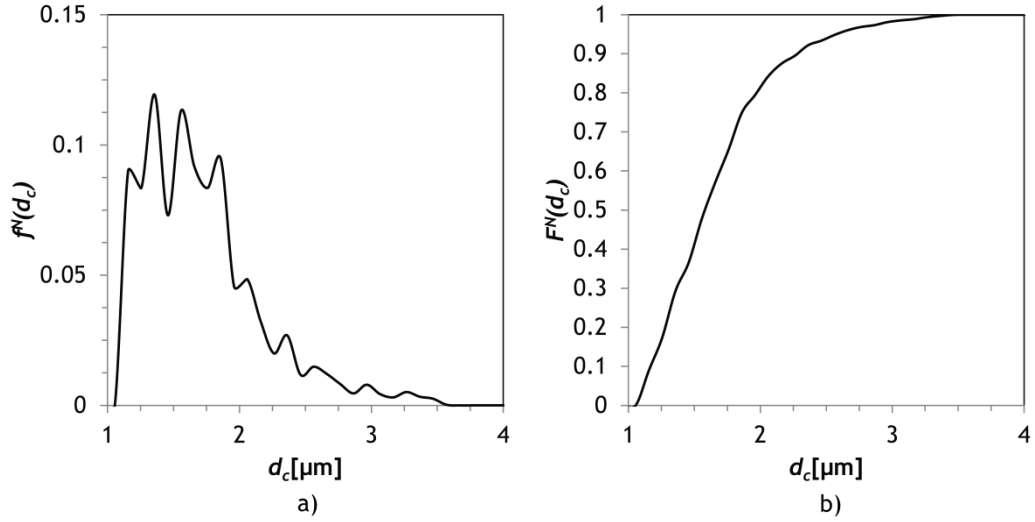

Figure 4-42 Number based cell diameter for sample with $KE_r = 1.13$: a) density function b) cumulative distribution function

4.4 Conclusions

It was demonstrated that $\overline{\Delta p^*}$ can be used as a control variable at RIM process, since the mechanical properties varied with it. Better mechanical performances are related to values of $\overline{\Delta p^*}$ closer to zero, corresponding to an impingement of the opposed jets of monomer at the axis of the mixing chamber, a condition associated with better mixing of the streams, as previous works had stated (Erkoc et al., 2007b). The impingement point position plays a fundamental role on mixing quality.

From the present work is possible to conclude that mixing in the RIM process is generally a process that is not controlled with the level of accuracy that the influence of some parameters on final properties would ask for, since for the same processing conditions, different impingement point locations were found. The hydrodynamics behavior inside the mixing chamber can carry the impingement point between the jets to an oscillatory position, unbalancing the mixing and originating different mechanical properties, even with equal processing conditions. This led to the different mechanical parts properties for the same conditions. In an extreme situation, when the streams are too unbalanced one jet can penetrate the opposed injector causing it to clog. This work proves that state-of-art mixing chamber are working as black box processes as far as mixing is regarded.

Experimental work presented, suggests that the monomers' jet balance, whether by momentum or kinetic energy ratio plays an important role on mixing with a major impact on the curing reaction. From the ATR experiments, a clear influence of the balanced

kinetic energy ratio is shown. This suggests that for $KE_r = 1$, the striation length scales are sufficiently thin originating for the polymerization reaction to become chemically controlled.

Although it is not suitable to report mechanical properties as poor or good, since such a classification depends on the application, from the mechanical analysis it is shown that the kinetic energy ratio, namely close to 1, can influence the final mechanical properties.

From the morphological structure of the samples, it was observed a cell distribution under the skin. From the optical and SEM analysis, it was shown that the cell sizes are smaller for $KE_r = 1$, a value predicted numerically by Fonte (2012) for striation thickness. The results suggest that the cell size formation, are associated to the striation mechanism, however it is difficult to prove this from the available data.

4.5 References

ASTM D1621-10, 2000. Standard Test Method for Compressive Properties of Rigid Cellular Plastic. ASTM.

ASTM D648, 2001a. Standard Test Method for Deflection Temperature of Plastic Under Flexural Load in the Edgewise Position. ASTM.

ASTM D792, 2001b. Standard Test Methods for Density and Specific Gravity (Relative Density) of Plastics by Displacement. ASTM.

ASTM D638, 2002. Standard Test Method for Tensile Properties of Plastics. ASTM.

Bártolo, P., 2001. Optical approuches to macroscopic and microscopic engineering, Ph.D. Thesis, Department of Physics, University of Reading, Reading, UK.

Bendat, J.S., Piersol, A.G., 1971. Random Data: Analysis and Measurement Procedures. John Willey & Sons, New York.

Benoit, H., Hadziioannou, G., 1988. Scattering theory and properties of block copolymers with various architectures in the homogeneous bulk state. Macromolecules 21, 1449-1464.

Blake, J.W., Yang, W.P., Anderson, R.D., Macosko, C.W., 1987. Adiabatic reactive viscometry for polyurethane reaction injection molding. Polymer Engineering & Science 27, 1236-1242.

Camargo, R., 1984. Kinetics and Phase Segregation Studies on the RIM Polymerization of Urethane Elastomers, Ph.D. Thesis, Department of Chemical Engineering, University of Minnesota, Minnesota, USA.

Camargo, R.E., Gonzalez, V.M., Macosko, C.W., 1982. Bulk Polymerization Kinetics by The Adiabatic Reactor Method, 2nd Internation Conference on Reactive Processing of Polymers, Pittsburgh, p. 22.

Camargo, R.E., Macosko, C.W., Tirrell, M., Wellinghoff, S.T., 1985. Phase separation studies in RIM polyurethanes catalyst and hard segment crystallinity effects. Polymer 26, 1145-1154.

Camberlin, Y., Pascault, J.P., 1984. Phase segregation kinetics in segmented linear polyurethanes: Relations between equilibrium time and chain mobility and between

equilibrium degree of segregation and interaction parameter. Journal of Polymer Science: Polymer Physics Edition 22, 1835-1844.

Castro, J.M., Gonzalez, V.M., Macosko, C.W., 1981. Process Behavior Differences Between Thermally Activated and Mixing Activated RIM Type Chemical Systems. Society of Plastics Engineering Tehcnical Papers 27.

Castro, J.M., Gonzalez, V.M., Macosko, C.W., 1983. Mixing and Thermally Activated Reaction Injection Molding (RIM) Type of Chemical Systems. Process Behavior Differences. Latin american journal of chemical engineering and applied chemistry 13, 12.

Castro, J.M., Macosko, C.W., 1982. Studies of mold filling and curing in the reaction injection molding process. AIChE Journal 28, 250-260.

Castro, J.M., Macosko, C.W., Critchfield, F.E., 1984. Effect of processing conditions on premature gelling, knit line strength, and physical properties for the RIM process. Journal of Applied Polymer Science 29, 1959-1969.

Christenson, C.P., Harthcock, M.A., Meadows, M.D., Spell, H.L., Howard, W.L., Creswick, M.W., Guerra, R.E., Turner, R.B., 1986. Model MDI/butanediol polyurethanes: Molecular structure, morphology, physical and mechanical properties. Journal of Polymer Science Part B: Polymer Physics 24, 1401-1439.

Danckwerts, P.V., 1952. The Definition and Measurement of Some Characteristics of Mixtures. Applied Science Research 3, 279-196.

Eisenbach, C.D., Baumgartner, M., Gunter, C., 1985. Synthesis and Properties of Polyurethane Elastomers with Monodisperse Segment Length Distribution ACS Polymer Preprints 26, 7-9.

Erkoc, E., Santos, R.J., Lopes, J.C.B., 2007a. Onset of turbulence in T-jet mixers, in: Palma, J., Lopes, A.S. (Eds.), Advances in Turbulence Xi. Springer-Verlag Berlin, Berlin, pp. 728-728.

Erkoc, E., Santos, R.J., Nunes, M.I., Dias, M.M., Lopes, J.C.B., 2007b. Mixing dynamics control in RIM machines. Chemical Engineering Science 62, 5276-5281.

Ferguson, J., Ahmad, N., 1977. Chemical structure and physical properties in polyester based segmented polyurethanes—II: Tensile properties. European Polymer Journal 13, 865-869.

Ferguson, J., Patsavoudis, D., 1972. Chemical structure-physical property relationships in polyurethane elastomeric fibres; property variations in polymers containing high hard segment concentrations. European Polymer Journal 8, 385-396.

Fluent, 2010. FLUENT 13.0 User's guide. Fluent, Inc, Lebanon, USA.

Fonte, C., 2012. Mixing Studies with Impinging Jets - PIV/PLIF Experiments and CFD Simulation, Ph.D. Thesis, Deparment of Chemical Engineering, Universidade do Porto, Porto, Portugal.

Fonte, C., Santos, R., Dias, M., Lopes, J.C., 2011. Quantification of Mixing in RIM Using a Non-Diffusive Two-Phase Flow Numerical Model. Internation Journal of Chemical Reactor Engineering 9, A114.

Fruzzetti, R., Hogan, K., Murray, F., White, J., 1977. Factors Affecting the Quality of Impingment Mixed RIM Urethanes. SAE Technical Paper.

Gomes, N., Mateus, A., Bártolo, P., Santos, R., Dias, M.M., Lopes, J.C., 2009. Projecto de Cabeça de Mistura RIM, com conceitos Inovadores de mistura e controlo, ConfEng UBI, Covilhã, Portugal.

Gomes, N., Santos, R.J., Dias, M.M., Gouveia, A.F., Sousa, C.C., Bártolo, P.J., Lopes, J.C.B., 2010. Assessment of the effect of controlling mixing using RIMCop® technology on the production of polyurethanes, RPD 2010, Industrial Knowledge for Innovation, Marinha Grande, Portugal.

Harrell, L.L., 1969. Segmented Polyurethans. Properties as a Funcation of Segment Size and Distribution. Macromolecules 2, 607-612.

Hashimoto, T., Tsukahara, Y., Tachi, K., Kawai, H., 1983. Structure and properties of tapered block polymers. 4. "Domain-boundary mixing" and "mixing-in-domain" effects on microdomain morphology and linear dynamic mechanical response. Macromolecules 16, 648-657.

ISIS, 2012. The Power of Spatial Filters.

ISO 2602, 1980. Statistical interpretation of test results - Estimation of the mean - Confidence interval. ISO.

ISO 604:2002, 2002. Plastics - Determination of compressive properties. ISO.

ISO 178, 2003. Plastics - Determination of flexural properties. ISO.

Johnson, D.A., 2000. Experimental and Numerical Examination of Confined Laminar Opposed Jets. Part I Momentum Imbalance. International Communications in Heat and Mass Transfer 27, 443-454.

Keuerleber, R., Pahl, F., 1972. Devide for Feeding Flowable Material to a Mold Cavity. Patent US3706515.

Kolodziej, P., Macosko, C.W., Ranz, W.E., 1982. The Influence of Impingement Mixing on Striation Thickness Distribution and Properties in Fast Polyurethane Polymerisation. Polymer Engineering and Science 22, 388-392.

Kolodziej, P., Yang, W.P., Macosko, C.W., Wellinghoff, S.T., 1986. Impingement Mixing and its Effect on the Microstructure of RIM Polyurethanes. Journal of Polymer Science 25, 2359-2377.

Lee, L.J., Ottino, J.M., Ranz, W.E., Macosko, C.W., 1980. Impingement Mixing in Reaction Injection Molding. Polymer Engineering and Science 20, 868-874.

Leibler, L., 1980. Theory of Microphase Separation in Block Copolymers. Macromolecules 13, 1602-1617.

Leung, L.M., Koberstein, J.T., 1986. DSC annealing study of microphase separation and multiple endothermic behavior in polyether-based polyurethane block copolymers. Macromolecules 19, 706-713.

Lopes, J.C., 1984. Droplet Sizes, Dynamics and Deposition in Vertical Annular Flow, Ph.D. Thesis, Department of chemical Engineering, University of Texas, Houston, Texas, USA.

Lopes, J.C.B., Santos, R.J., Teixeira, A.M., Costa, M.R.P.F.N., 2005. Production Process of Plastic Parts by Reaction Injection Moulding, and Related Head Device. Patent WO 2005/097477.

Macosko, C., 1989. RIM Fundamentals of Reaction Injection Molding. Hanser Publishers, Munich, Germany.

Malguarnera, S.C., Suh, N.P., 1977. Liquid injection molding II. Mechanical design and characterization of a RIM machine. Polymer Engineering & Science 17, 116-121.

Malguernera, S., Suh, N., 1977. Liquid Injection Molding I. An Investigation of Impegiment Mixing. Polymer Engineering and Science 17, 111-115.

Menard, K., 2008. Dynamic Mechanical Analysis - A Pratical Introduction. CRC Press.

Nguyen, L.T., Suh, N.P., 1985. Effect of High Reynolds Number on the Degree of Mixing in RIM Processing. Polymer Process Engineering 3, 37-56.

Nielsen, L.E., Landel, R.F., 1984. Mechanical Properties of Polymers and Composites 2. Marcel Dekker, New York, USA.

Nunes, M.I., Santos, R.J., Dias, M.M., Lopes, J.C.B., 2012. Micromixing assessment of confined impinging jet mixers used in RIM. Chemical Engineering Science 74, 276-286.

Patankar, S.V., 1980. Numerical Heat Transfer and Fluid Flow. Tayler&Frances, Philadelphia.

Pratap, R., Ruina, A., 2002. Introduction to Statics and Dynamics Oxford. University Press London.

Ranz, W.E., 1979. Applications of a Stretch Model to Mixing Diffusion, and Reaction in Laminar and Turbulent Flows. AIChE Journal 25, 41-47.

Rockwell, D., Naudascher, E., 1979. Self-Sustained Oscillations of Impinging Free Shear Layers. Annual Review of Fluid Mechanics 11, 67-94.

Santos, R.J., 2003. Mixing Mechanisms in Reaction Injection Moulding - RIM - An LDS/PIV Experimental Study and CFD Simulation, Ph.D. Thesis, Deparment of Chemical Engineering, Universidade do Porto, Porto.

Santos, R.J., Erkoc, E., Dias, M.M., Lopes, J.C., 2009a. Dynamic Behavior of the Flow Field in a RIM Machine Mixing Chamber. AIChE Journal 55, 1338-1351.

Santos, R.J., Erkoc, E., Dias, M.M., Lopes, J.C.B., 2009b. Dynamic Behavior of the Flow Field in a RIM Machine Mixing Chamber. Aiche Journal 55, 1338-1351.

Santos, R.J., Erkoc, E., Dias, M.M., Teixeira, A.M., Lopes, J.C.B., 2008. Hydrodynamics of the mixing chamber in RIM: PIV flow-field characterization. AIChE Journal 54, 1153-1163.

Santos, R.J., Teixeira, A.M., Costa, M.R., Lopes, J.C.B., 2002. Operational and design study of RIM machines. International Polymer Processing 17, 387-394.

Santos, R.J., Teixeira, A.M., Erkoç, E., Sultan, M.A., Karpinska, A., Dias, M.M., Lopes, J.C.B., 2010. Validation of a 2D CFD Model for Hydrodynamics' Studies in CIJ Mixers. International Journal of Chemical Reactor Engineering 8, A32.

Santos, R.J., Teixeira, A.M., Lopes, J.C.B., 2005. Study of mixing and chemical reaction in RIM. Chemical Engineering Science 60, 2381-2398.

Schütz, S., Kissling, K., Piesche, M., 2009. Operational Behavior of Impingement Mixers, 8th World Congress of Chemical Engineering, Montréal, Canada.

Sebastian, D.H., Boukobbal, S., 1986. Mixhead Parameters Governing Impingement Mixing Effectiveness for Polyurethane Reactive Injection Molding Processes. Polymer Process Engineering 4, 53-70.

Shames, I., 1992. Mechanics of Fluids. MvGraw-Hill, Inc, New York.

Silva, M., Mateus, A., Bártolo, P., Pouzada, A., Pontes, A., 2006. Assessment of the performance of products moulded by RIM, Rapid Product Development 2006: Building the Future by Inovation, Marinha Grande, Portugal.

Teixeira, A.M., Santos, R.J., Rui, M., Costa, P.F.N., Lopes, J.C.B., 2005. Hydrodynamics of the mixing head in RIM: LDA flow-field characterization. AIChE Journal 51, 1608-1619.

Torres, M.V., Winter, U., Santos, R.J., Costa, M.R., Dias, M.M., Lopes, J.C., 2012. Rheology of a Reactive System of Polyurethanes for Production in RIMcop®, Polychar 20, Dubrovik.

Tucker III, C.L., 1991. Principles of Mixing Measurements, in: Rauwendaal, C. (Ed.), Mixing in Polymer Processing. Marcel Dekker, New York.

Turner, R.B., Spell, H.L., Vanderhider, J.A., 1983. The effect of Hard Segment Content on a Crosslinked Polyurethane RIM System, in: Kresta, J.E. (Ed.), 186th Meeting of the American Chemical Society. American Chemical Society, Wahsington, D. C.

Wepf, R., 2012. "Automatic" determination of particle size distribution The Electron Microscopy Site.

Yang, W.P., 1987. Dynamics of phase separation and its effect on polyurethane structure and properties, Ph.D. Thesis, Chemical Departament, University of Minnesota, Minnesota, USA.

Zdrahala, R.J., Hager, S.L., Gerkin, R.M., Critchfield, F.E., 1980. Polyether Based Thermoplastic Polyurethanes Effect of the Soft Segment Molecular Weight. Journal of Elastomers and Plastics 12, 225-244.

5 RIM mould design

5.1 Introduction

The longest step on RIM cycle is the part curing until enough mechanical properties are built up to proceed with the part extraction. This stage occurs inside a mould, previously designed to conform the filled fluid to the desired part design. For the part quality and homogenization, mould design should be careful. A good mould design can shorten the RIM cycle, as it reduces the curing time, and/or reduces/eliminate post-operations, as trim and sanding.

Besides the importance of moulding, up to nowadays, only a few studies about moulds design are found in literature (Cohnen and Osswald, 1992; Mohammed et al., 1994; Müller et al., 1985; Silva, 2007), and at the industrial level, the design is still pretty much based on empirical processes, and made following the guidelines or design experience from TIM moulds. Unlike TIM, mould filling in RIM is largely affected by flow phenomena inside RIM moulds, which needs to be accounted for in order to improve the design of RIM moulds.

Present chapter aims to understand the filling phenomena, regarding the fluid mechanics elementary laws, and create some helpful information for the mould designers. First introduces a Volume of Fluid (VOF) coupled with Finite Volume Method (FVM) model, using Ansys Fluent™, where the numerical results obtained were compared with literature, first using a 2D model with experimental work of Coyle et al. (1987) and last a 3D model, compared with numerical work of Chang and Yang (2001). The validation set enough

confidence on the model that was then used for further studies on the effect of flow phenomena on mould filling.

In second part, the fluid filling was studied and some phenomena were encountered, using the main forces that drive filling: inertial, gravitational and surface forces. Using fluid mechanics parameters, the forces were studied in several ranges and the results were used to understand the forces effects and create flow patterns maps. Also velocity and pressure profiles along the filling where studied for several fluid mechanics parameters.

Last part of chapter adds some new project suggestions to improve the mould project, and consequently improving of cycle time and part quality.

5.2 VOF Model for Reaction Injection Moulding's Flow Front

During the flow front advancement, there are two flow regions: the main flow and fountain flow – Figure 5-1 (Manas-Zloczower et al., 1987). The velocity field in main flow is parabolic and parallel to the walls, this occurs in regions away from the flow front. When the fluid is close to the flow front, it decelerates in the flow direction, to acquire a perpendicular component (Manas-Zloczower et al., 1987). Schmidt (1974) showed experimentally this phenomenon, injecting a color tracer into the flow. Due to the RIM process relevance, several authors have been studying the flow front in mould filling for this process, where the viscous forces are dominant but are not enough to prevent instabilities that can cause imperfections (Macosko, 1989).

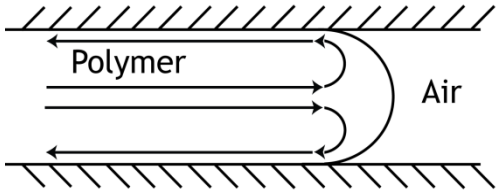

Figure 5-1 Flow Front

One of the main problems in simulating the injection process is the determination of the free surface positions at each instant, where it can be used a fixed or a moving mesh. If a moving mesh is used the simulation method is called Lagrangian (Silva, 2001). This formulation discretizes only the fluid domain and the free surface is calculated through the mesh's movement. When the mesh is fixed, the simulation method is called Eulerian formulation (Silva, 2001). All the domain is discretized, and the free surface moves through the mesh. A hybrid method called Arbitrary Lagrangian-Eulerian (ALE) combines the independent movement of material and mesh.

For unsteady free surface problems, the Lagrangian methods are more common, and in the injection process several authors use a quasi-Lagrangian formulation (Behrens et al., 1987; Lee, 1997; Mavridis et al., 1988; Mori et al., 1996), which consists in fixing the boundary points.

Relatively to the Eulerian formulations, the tracking of the free surface can be employed on the definition of the free surface – *surface tracking* – or when the free surface is computed from the determination of the filled volumes by the several phases – *volume tracking*. Due to its importance in the present work, a detailed study about these methods will be done.

In *surface tracking* works, the free surface is computed using a relation with a reference line. For example, for the bidimensional case, the free surface mapping can be performed using one boundary side as reference (Pichelin and Coupez, 1998). Several works have been done using this method (Cuniot et al., 1989; Hieber and Shen, 1980; Kuei and Burton, 1987).

A large number of works has been made using *volume tracking* methods, mainly *Marker-And-Cell* (MAC) and VOF. MAC consists in using an Eulerian mesh, where some particles representing the fluid are set. The free surface is defined by the calculation of the velocity field, consisting in an average of neighbor particle's velocities. After that, the particles are defined as empty, fill or free surface. Huang and Usmani (1994) used the coupling of a CFD simulations using Finite Difference Method (FDM) and a MAC, in injection moulding. More recently, Shiojima et al. (1989) and Zaidi et al. (1997) coupled MAC with Finite Element Method (FEM) for injection moulding simulations.

As far as VOF is regarded, the free surface is defined by a function, which enables identifying if the mesh elements are filled with material or not. This function acquires, for each element, a value between 0 and 1. The element is considered empty, filled or free surface, if the element has a value of 0, 1 or in-between 0 and 1, respectively. Thermodynamic equilibrium in interface is required for a mono-fluid approximation, due to the requirement of a previous knowledge of free surface shape (Chen et al., 1996; Hirt and Nichols, 1981; Shen, 1992). Another approach used in injection moulding is the simulation of two fluids, where the VOF function defines a value, between 0 and 1, for all the mesh volumes. Several authors have been employing this method, using FEM (Codina et al., 1994; Dhatt et al., 1990; Hetu and Garcia-Rejon, 1995; Thompson, 1986).

Also some works using ALE are present in literature. Fauchon et al. (1991) used this method, for the domain discretization, and search for the mesh's velocity field, to minimize the deformation between two consecutive time steps. Another approximation,

was used by Pichelin and Coupez (1998), and consisted in an Eulerian formulation in all domain, but domain was actualized for each time step.

Using a commercial Computational Fluid Dynamics code, ANSYS Fluent™, it is proposed in this thesis a model that couples VOF and FVM. Some previous work, using the same model was applied to polyurethane foam expansion (Geier et al., 2009; Silva, 2007).

5.2.1 Physical Model

During the injection phase, before the polymer cure, the flow is considered incompressible and has a Newtonian behavior. Several authors, as Tucker and Dessenberger (1994) and Torres et al. (2012), observed this behavior, in an initial curing phase. Stress in Newtonian fluids is related to the deformation in the fluid flow as

$$\boldsymbol{\tau} = -p\mathbf{I} + 2\mu\mathbf{D} \tag{5.1}$$

where $\boldsymbol{\tau}$ is the stress tensor, p is the the pressure, $\mathbf{I}$ is the identity tensor and $\mathbf{D}$ is the deformation tensor, given by

$$\mathbf{D} = \frac{1}{2}\left(\nabla\mathbf{v} + \nabla\mathbf{v}^T\right) \tag{5.2}$$

where $\mathbf{v}$ is the velocity vector, and index T corresponds to transpose matrix.

The flow of Newtonian fluids is described by the following equations:

- Continuity

$$\nabla\mathbf{v} = 0 \tag{5.3}$$

- Navier-Stokes

$$\rho\frac{D\mathbf{v}}{Dt} = -\nabla p + \mu\nabla^2\mathbf{v} + \rho\mathbf{g} \tag{5.4}$$

where $\frac{D\mathbf{v}}{Dt}$ is the material derivative of the velocity field.

For the Pressure-velocity coupling was used the SIMPLEC scheme (Doormaal and Raithby, 1984), where the PRESTO! Scheme (Peyret, 1996) and MUSCL scheme (Van Leer, 1977), were used for pressure and momentum, respectively. A VOF model was used for the flow

front. This model was chosen due to its ability to deal with superficial tension, and it is designed for immiscible phases, as in the case of RIM mould filling. The velocity field is common for both phases, and the free surface distribution is calculated from the distribution equation,

$$\frac{\partial \alpha_i}{\partial t} + \nabla \cdot \left(\alpha_i \mathbf{v} \right) = 0 \qquad 5.5$$

where α_i is the volumetric fraction of phase i. The sum of all volumetric fractions is equal to 1,

$$\sum_i \alpha_i = 1, \quad i = \{\text{air}, \text{liquid}\} \qquad 5.6$$

This work tested the following interpolation schemes for the interface:

- Geometric Reconstruction (Youngs, 1982);
- Compressive Interface Capturing Scheme for Arbitrary Meshes (CICSAM) (Ubbink and Issa, 1999);
- Compressive Scheme;
- Modified High Resolution Interface Capturing (modified HRIC) (Muzaferija et al., 1998);
- QUICK (Leonard and Mokhtari, 1990).

For the superficial tension it was considered a Continuum Surface Force (CSF) model (Brackbill et al., 1992). This model uses the interfacial surface curvature to calculate the pressure drop at the interface, corresponding to the superficial tension,

$$F_{ST} = \gamma_{g-l} \frac{\rho k_{cs_i} \nabla \alpha_i}{\frac{1}{2}\left(\rho_g + \rho_{liq} \right)} \qquad 5.7$$

where the indices g and liq represent the different phases, γ_{g-l} is the superficial tension between both phases and k is the superficies curvature. The pressure drop will add a font term in the continuity equation. The interfacial surface curvature, is calculated from the local gradient of normal vector to the interfacial surface,

$$k_{sc} = \nabla \cdot \hat{n} \qquad 5.8$$

where $\hat{n}$ is the unitary normal vector computed by $\hat{n} = \frac{n}{|n|}$, being n the normal vector to the surface

$$n = \nabla \alpha_i \qquad 5.9$$

In this work, the unitary normal vector is adjustable to the surface using a contact angle with the walls (Brackbill et al., 1992), as show Equation 5.10.

$$\hat{n} = \hat{n}_p \cos\theta_p + \hat{t}_p \sin\theta_p \qquad 5.10$$

where $\hat{n}_p$ and $\hat{t}_p$ are the normal and tangential unitary vectors to the interfacial surface, respectively and θ_p the contact angle with the wall.

5.2.2 Results

To prove that the model is adjustable to the RIM process, the following case studies are tested:

- Filling of a symmetric rectangular pipe;
- Filling of a 3D symmetric cavity.

The first case was used to study the different parameters and schemes, in order to obtain a better adjustment to the physical process simulation. Validation using experimental data was also done. The second case study was used to study the applicability to a 3D case. Both cases were simulated in a Dell XEON Dual-core with 12Gb of RAM.

5.2.2.1 Filling of symmetric rectangular pipe

To study the flow front, the filling of a symmetric rectangular pipe was simulated. The geometry model used is shown in Figure 5-2. A uniform quadrangular mesh with 100×3500 elements was used, with the geometrical parameters presented in Table 5-1. During the injection, the air is pushed out by the polymer front. Several approaches have been used to model boundary conditions in walls close to the flow front. Haagh and Van De Vosse (1998) used different boundary conditions for the different phases, where it was employed a slip condition for polymeric phase and a no-slip condition for air. Other authors (Coyle et al., 1987; Manas-Zloczower et al., 1987) used a no-slip condition for the walls in both phases. For this work, it was adopted a no-slip condition, due to the fact that with the VOF model it is computed a common velocity field for both phases, and it is not possible to set

different boundary conditions for each phase. Other boundary conditions are present in Figure 5-2 and filling velocity in Table 5-1. Physical properties of the fluids are present in Table 5-2.

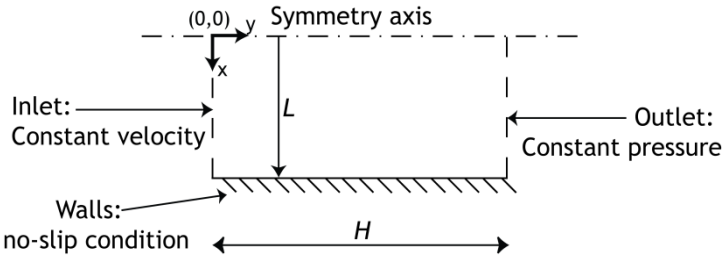

Figure 5-2 Geometry and boundary conditions of rectangular tube

Table 5-1 Geometrical parameters and injection velocity

$H[\mathrm{m}]$	1.00×10^{-2}
$L[\mathrm{m}]$	3.50×10^{-1}
$\upsilon_f[\mathrm{ms^{-1}}]$	1.50

Table 5-2 Physical properties of the fluids

	$\rho_{air}[\mathrm{kgm^{-3}}]$	$\rho_{liquide}[10^2\,\mathrm{kgm^{-3}}]$	$\mu_{air}[\mathrm{Pa\cdot s}]$	$\mu_{liquide}[10^1\,\mathrm{Pa\cdot s}]$	$\gamma_{g-l}[10^{-2}\,\mathrm{N.m}]$
Experimental (Coyle et al., 1987)		9.70		5.25	2.10
VOF	1.23	9.70	1.79×10^{-5}	5.25	2.10

As mentioned in Section 5.2.1, several interpolation schemes for the flow front were tested. Figure 5-3 shows the volumetric fraction of air, for the different interpolation schemes at $93.75\mathrm{s}$. Observing the Figure, it is possible to see slight differences in flow front position between the different schemes, however they are not significant. Also the computational times used for each scheme are very close. Since there are no significant differences, the high resolution CICSAM scheme was chosen, due to the ability of this scheme to work with high viscosity ratios between the phases (Geier et al., 2009), as is the case of RIM where $\mu_{polymer} \gg \mu_{air}$.

During the polymer injection in RIM, the flow front is influenced by the superficial tension (Cohnen and Osswald, 1992), being the capillarity the main cause of air bubble imprisonment (Cohnen and Osswald, 1992). Due to this, it is important to analyse the interaction between the phases during the flow. For that purpose, the contact angle between the interface polymer-air with walls, was defined. In literature, several values are found, varying between $90°$ (Castro and Macosko, 1982; Manas-Zloczower et al., 1987) and $180°$ (Coyle et al., 1987). In this work, contact angles of $0°$ and $45°$ were studied. For the superficial tension, the value was defined by Macosko (1989) and is shown at Table

5-2 (Macosko, 1989). Figure 5-4 shows that for the different contact angles there is no difference on flow front. A contact angle of $90°$ was defined, since this is the most referred value in literature and considers a flat flow front.

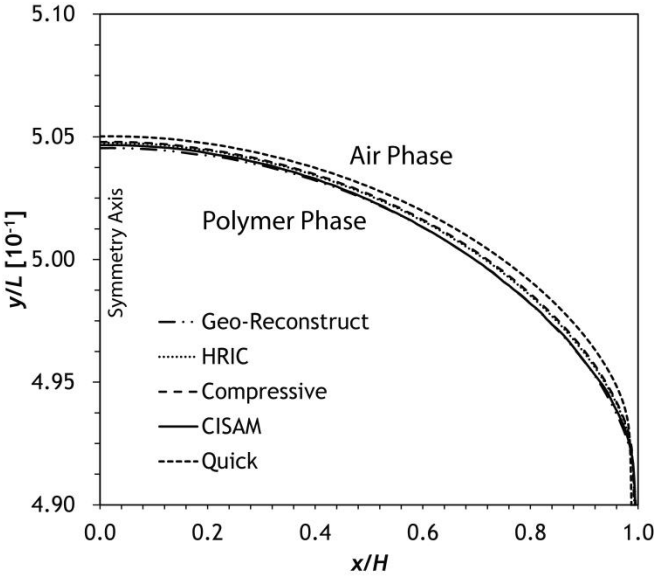

Figure 5-3 Volumetric fraction of air, for the different interpolation schemes at $93.75s$

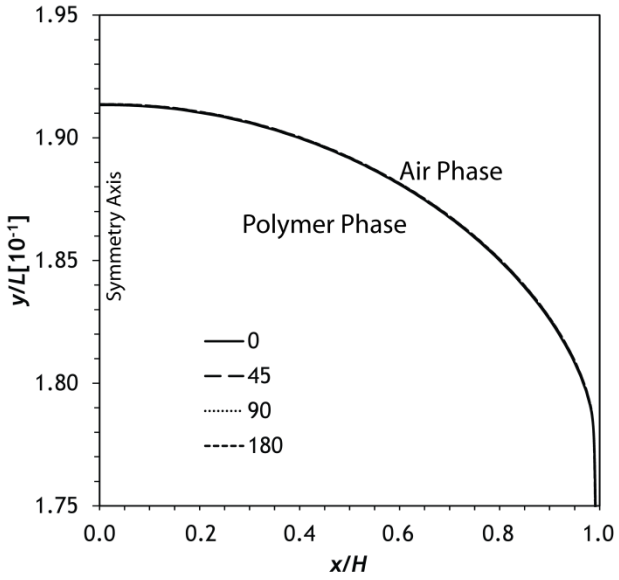

Figure 5-4 Flow front for different contact angles

The numerical results of this work were compared with the experimental data from Coyle et al. (1987). For this case, it was used a quadrangular uniform mesh with 100×7500 elements. The geometry model used is the same from Figure 5-2, and the geometrical dimensions and boundary parameters are present in Table 5-3. From Table 5-2 it is possible to observe the physical properties of the fluids used experimentally and numerically. For the numerical case, the wall was considered as a moveable wall, without slip, to the flow front remaining spatially constant. The gravity action is simulated, and the main flow direction is defined in the opposite direction to the gravity vector.

Table 5-3 Geometrical parameters

	$L[\mathrm{m}]$	$H[10^{-2}\mathrm{m}]$	$\upsilon_{fl}[10^{-3}\mathrm{ms}^{-1}]$	$10^{-4}Re_{fl}$
Experimental (Coyle et al., 1987)	1.02×10^{0}	1.89	1.89	7.00
VOF	7.50×10^{-1}	2.00	2.00	7.00

To observe the fountain flow, a third phase was added, working as a tracer, analog to the experimental method of Coyle et al. (1987). This allowed a better visualization of the fountain flow, and is a reproduction of the experimental method. Observing Figure 5-5, the flow front has a similar surface, and the flow front pattern is identical in both the simulation and experiment.

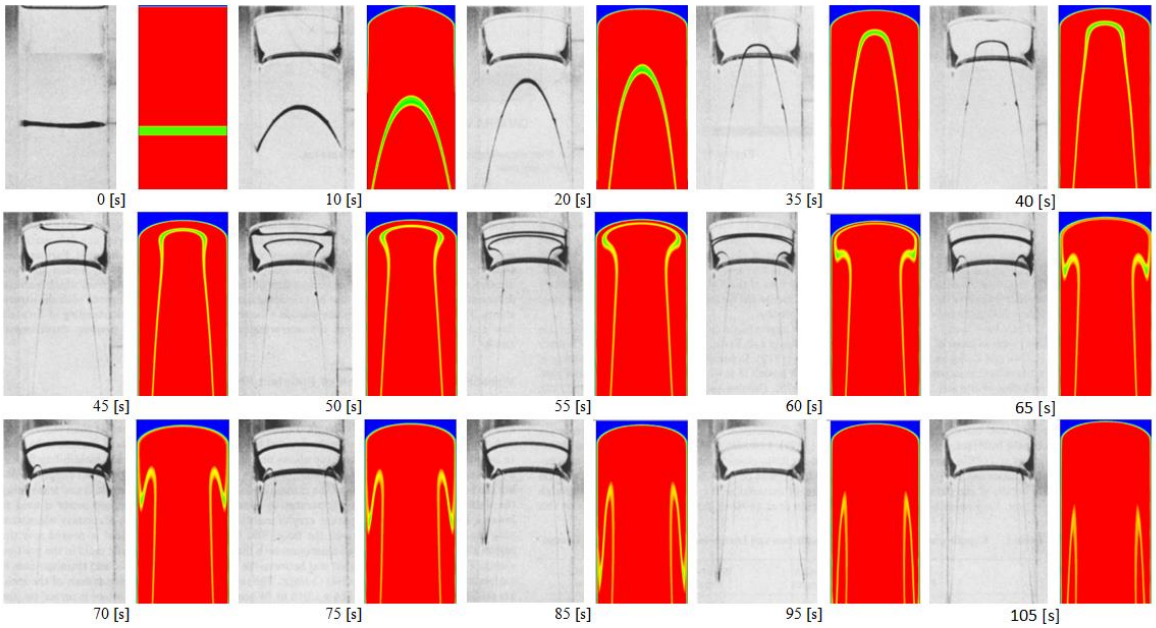

Figure 5-5 Fountain effect in flow front - monochromatic images from experimental data of Coyle et al. (1987), polychromatic images from MVF-VOF model.

5.2.2.2 Filling of 3D symmetric cavity

The VOF model was applied to a 3D case, the filling of a 3D symmetric cavity with an obstacle in the middle and $2\mathrm{mm}$ of thickness - Figure 5-6. Using the same geometric model, Chang and Yang (2001) applied a Hele-Shaw model and a 3D MVF model, using a fractional volume function to track the flow front. The results from that work are compared to the present work. It were considered two different phases, air and polymer, whose main properties are in Table 5-4.

Table 5-4 Physical properties

Fluid	Air	Polymer
$\rho[\mathrm{kgm}^{-3}]$	1.23×10^{0}	1.00×10^{3}
$\mu[\mathrm{Pa}\cdot\mathrm{s}]$	1.79×10^{-5}	5.05×10^{-2}

The boundary conditions are identical to the previous case study. It was considered a constant velocity profile at inlet, with a mean velocity of $\bar{\upsilon} = 3.70 \times 10^{-1} \mathrm{ms}^{-1}$. It was used a quadrangular uniform mesh of $600 \times 200 \times 4$ elements. This case, with an obstacle, also allows to study the ability of the model to handle with the splitting and re-merging of the flow front (Chang and Yang, 2001). From Figure 5-7, it can be seen the similarity between the 3D MVF-VOF model and Chang and Yang (2001) models, with a time of $0.33\mathrm{s}$ between iterations. A closer similarity is obtained for Hele-Shaw model. A slight divergence, from Chang and Yang (2001), is observed when the actual model needs to work with re-merging of the flow.

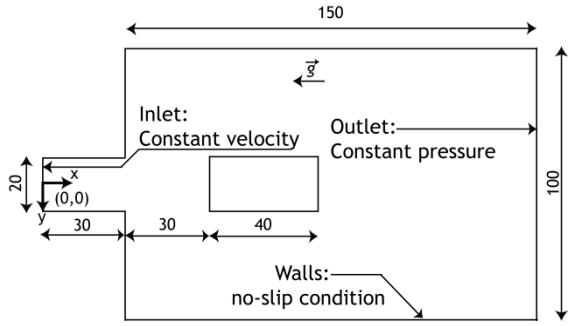

Figure 5-6 Geometric model and dimensions

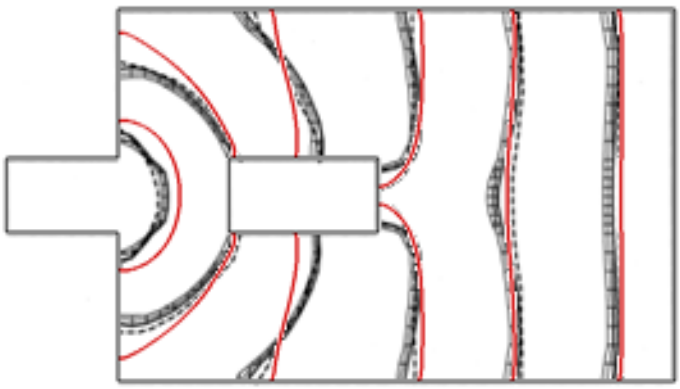

Figure 5-7 Flow front comparison between the 3D MVF-VOF model and the Chang and Yang (2001) models (red line correspond to 3D MVF+VOF model, dash line correspond to Hele-Shaw model and mesh surface to 3D model)

5.3 Filling phenomena and flow maps in thickness variation

Nowadays, the world is living in the plastic era, where most of the objects used are derived from the plastics materials. These spread originate a large number of parts with sizes, materials and forms that have increasing shape complexity. Unless a constant section part, e. g. a ruler, the flow during the filling needs to overcome several singular regions, as show in Figure 5-8. From this figure, it is possible to observe that the flow needs to pass: a) around an object; b) a thickness variation and change direction.

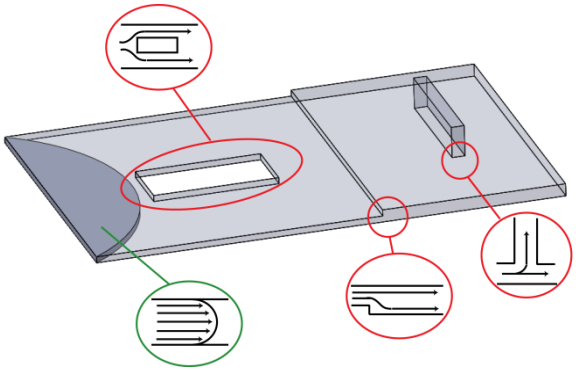

Figure 5-8 Typical obstacles during a mould filling

Although, the modern techniques to deal with the increasing complexity in plastic parts are quite advanced, the tools used require long time and, sometimes high computational power.

As seen before, during a mould filling the flow needs to pass over several variations of thickness. Even if the part thickness is constant, a thickness variation can occur in the injection point, where the flow is constrained. Considering this, the contraction and expansionof the flow is studied in this chapter. The initial study was performed on $2{:}1$ contractions and $1{:}2$ expansions. The aim is to observe and understand how the different forces can influence the flow and how it could affect the final part quality, in addition to the processing conditions.

For the present work, a 2D model was used, based on the set of governing and constitutive equations for multiphase flow introduced in Section 5.2.1. The model is similar to the one found in Cohnen and Osswald (1992); Mohammed et al. (1994). For both works, were considered the following assumptions:

- The fluid is Newtonian and incompressible;
- Viscosity, μ, and density, ρ, are pressure independent;
- Curing effects are neglected.

In their work, they neglect the gravity effects, however for the present work this is considered, due to the low viscosities of the raw materials used in RIM (Macosko, 1989).

A simpler 2D geometric model was used, due to the high computational resources needed to perform a considerable number of simulations. In Figure 5-9 it is show the geometric model. Salient corner(Owens and Phillips, 2002), an important parameter used along this work, can be seen in Figure 5-9. Geometric dimensions are presented in Table 5-5. Physical properties of the fluids are presented in Table 5-2.

Table 5-5 Geometric dimensions for contraction and expansion geometry

$D_1[\mathrm{m}]$	2.00×10^{-2}
$D_2[\mathrm{m}]$	4.00×10^{-2}
$L_1[\mathrm{m}]$	1.75×10^{-1}
$L_2[\mathrm{m}]$	1.75×10^{-1}

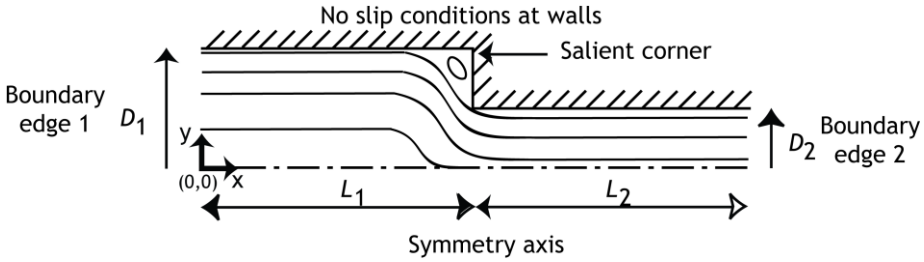

Figure 5-9 Geometric model used for contraction and expansion studies

The following boundary conditions were imposed to the 2D model:

- Symmetry axis $\left(\tau_{ij}=0\right)$;
- No slip conditions at walls were considered $\left(\mathbf{v}_{wall}=0\right)$;
- At mould inlet, was set a constant and uniform velocity $\left(\upsilon_x=\upsilon_f=\text{constant}\right)$;
- At mould outlet was set a constant and uniform gauge pressure $\left(\mathbf{p}=0\right)$.

Depending on the geometry being a contraction or an expansion, the inlet boundary conditions were set on boundary edge 2 or 1 of Figure 5-9, respectively. The inlet velocity and the fluid properties as viscosity and surface tension, were defined according to the dimensionless analysis, which is presented in the next section. Despite in Figure 5-9, the positive x axis is considered from the boundary edge 1 to boundary edge 2, this is only valid for contraction flows. For the expansion flow, the positive x axis is from boundary edge 2 to boundary edge 1. This consideration does not affect the flow, and is only used for map presentation purposes, in order to considering in all maps and graphics the flow as going from left to right.

It was used a quadrangular mesh with $\Delta x=1\times10^{-4}\,\mathrm{m}$, resulting in 526266 elements. A sensibility analysis to mesh size was performed, using similar flow conditions to $Fr=1$, $Re=1$ and $We=100$. From Figure 1-10, it is possible to observe that a mesh size bigger than used in present work, don't affect significantly the pressure drop and increase, exponentially, the computational time.

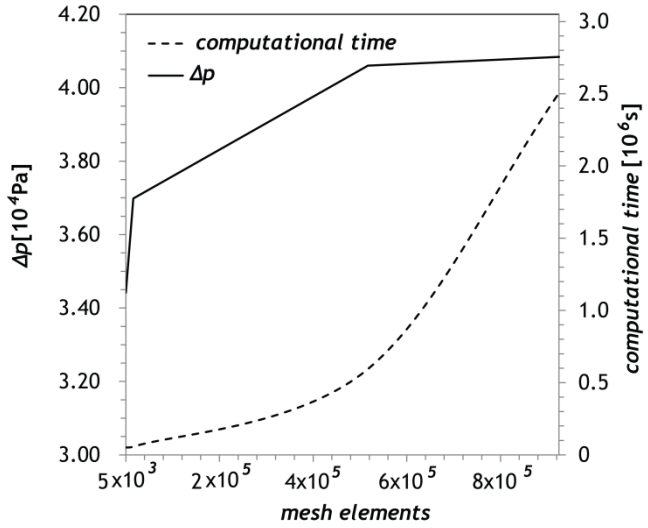

Figure 5-10 Mesh size sensibility and computational time

The simulations were performed in NxPy cluster from FEUP, with 2 Intel Xeon EM64T 3GHz and 4GB RAM, per node. Each simulation was executed using 2 nodes, and the main advantage of using NxPy cluster resided in the simultaneous simulation of several cases. The stability criterion of a Courant–Friedrichs–Levy number equal to 1 was fulfilled.

5.3.1 Dimensionless analysis

The first approach to analyse mould filling was to identify the relevant dimensionless numbers for this flow. The Buckingham's π Theorem is applied to the flow shown in Figure 5-9, which is governed by the variables in Table 5-6.

The same table presents the primary dimensions for each variable. The velocity used dimensionless analysis is the downstream average velocity, where for contraction case is the velocity in bigger zone, and for expansion is the average velocity in smaller zone.

Using the Buckingham's π Theorem, four dimensionless numbers were identified, according to the calculation present in Table 5-7, and for contraction are defined as:

Reynolds number $$Re = \frac{\rho \upsilon_1 D_1}{\mu} \quad (5.11)$$

Froude number $$Fr = \frac{\upsilon_1^2}{g D_1} \quad (5.12)$$

Weber number $$We = \frac{D_1 \upsilon_1^2 \rho}{\gamma_{g-l}} \quad (5.13)$$

Thickness ratio $$Tr = \frac{D_2}{D_1} \quad 5.14$$

Table 5-6 Main Variables over a contraction in RIM injection

Variable	Symbol	Primary Dimension
Edge 1	D_1	L
Edge 2	D_2	L
Velocity	υ	LT^{-1}
Density	ρ	ML^{-3}
Viscosity	μ	$MT^{-1}L^{-1}$
Gravity	g	LT^{-2}
Superficial Tension	γ_{g-l}	MT^{-2}

Table 5-7 – Dimensionless Factors' and calculations

π_i	Variable				a	b	c	d	Dimensionless Factors'
π_1	D_2^a	υ^b	ρ^c	D_1^d	-1	0	0	1	$\frac{D_1}{D_2} = Tr$
π_2	D_2^a	υ^b	ρ^c	μ^d	-1	-1	-1	1	$\frac{\mu}{\rho\upsilon D_2} = \frac{1}{Re}$
π_3	D_2^a	υ^b	ρ^c	g^d	1	-2	0	1	$\frac{gD_2}{\upsilon^2} = \frac{1}{Fr}$
π_4	D_2^a	υ^b	ρ^c	$\gamma_{g-l}{}^d$	-1	-2	-1	1	$\frac{\gamma_{g-l}}{D_2\upsilon^2\rho} = \frac{1}{We}$

The Reynolds number - Equation 5.11- is a ratio between Inertial Forces and Viscous Forces, the Froude number Equation 5.12 is a ration between Inertial and Gravitational Forces and Weber number Equation 5.13 is a ratio between Inertial and Superficial Forces.

An identical result is obtained for the expansion, however the index 2 in variables to calculate Fr and Re numbers is 1, and it is used the inverse of Tr, calculated by Equation 5.14.

The dimensionless numbers identified as important during the flow in RIM are the ones found in literature (Castro and Lee, 1989; Castro and Macosko, 1982).

For typical surface tension values in RIM process, the capillary number is defined as

$$Ca = \frac{\upsilon_{inj}\eta}{\gamma} \quad 5.15$$

and it gives values in the range from 1 to 10 (Macosko, 1989).

The critical Reynolds number should be in the range 1 to 100 (Macosko, 1989). Using these ranges and according to the Equation 5.16, the Weber number for typical filling in RIM is in the range between 10 to 1000 .

$$We = Ca\,Re \tag{5.16}$$

Müller et al. (1985) suggested that the reactant mixture should be injected against the walls, in the direction of gravity. In this way, the air is pushed out of the cavity in opposite way of the injection point and against the gravity. Other way, gravity could promote some air entrapment. However, it is pointed that the injection against the gravity can be more favourable to the flow patterns preventing any backflow. Nevertheless, Martinho et al. (2003) experimentally found worst visual aspect and defects in injection trials in the direction of gravity. Based on this idea, the present work will focus on study of flow in opposite direction to the gravity forces, and all the simulations performed according to it.

5.3.2 Flow phenomena

Using the VOF model developed in Section 5.2 and the geometry from Figure 5-9, it was possible to study the filling of a part and to identify several flow phenomena that can affect the filling and consequently the part quality.

The flow phenomena were described by plotting the volume fraction of the fluid, α_f , and the streamlines, that for a bidimensional case, were computed as

$$\frac{dx}{\upsilon_x} = \frac{dy}{\upsilon_y} \tag{5.17}$$

The maps were taken for the following dimensionless flow time (c.f. Equation 5.18):

- $0.50\tau^*$, corresponds to the flow entry in the contraction section, $x = L_2$, and for entry in the expansion section, $x = L_1$;
- $0.61\tau^*$, corresponds to a distance of two smaller diameters after the contraction, $x = L_2 + 2D_1$, and two bigger diameters after the expansion $x = L_1 + 2D_2$;
- $0.73\tau^*$, corresponds to a distance of four smaller diameters after the contraction, $x = L_1 + 4D_1$, and four bigger diameters after the expansion $x = L_1 + 4D_2$.

$$\tau^* = \frac{t}{t_{inj}} \qquad 5.18$$

where t_{inj} is the total filling time.

From the simulations performed, the flow phenomena identified are presented in Figure 5-11 to Figure 5-17.

The first phenomenon identified was a stable flow front, shown in Figure 5-11 for $Fr = 10^{-3}$, $Re = 10$ and $We = 1000$. In this figure, it is possible to observe the flow front passing through the contraction and its advancement. After passing the contraction, the flow front suffers a little perturbation, as shown in the map at $0.5\tau^*$, where also the streamlines show some instabilities in air flow. After it, the flow front recovers the surface geometry, and the streamlines are straight and parallel to the flow. For a better comprehension about what is a stable front, Figure 5-12 shows what it is named unstable front, for $Fr = 10^{-3}$, $Re = 100$ and $We = 1000$. Here, it is possible to see the irregular shape of the flow front, during all the flow advancement.

The presence of a stable or unstable shape in the flow front is, mainly, due the existence of an interface between two phases. On this boundary, there is a surface tension between the working fluid and air that plays an important role in the thermodynamic equilibrium in the boundary between the two different phases. For these equilibrium, the free energy is minimum, and for a isothermal condition, the Helmholtz free energy over the surface can be defined as (Batchelor, 2009)

$$F = \rho_g V_g F_g + \rho_l V_l F_l + A\gamma \qquad 5.19$$

where F is the free energy, V is phase volume, g and l indices refer to gas and liquid phase, respectively, and A refers to the interface area. From the previous equation, it is possible to understand that the total work done on the system, is equal to the gain in total free energy, and equal to $\gamma \delta A$, that is equivalent to the tensile forces exerted on an interface surface.

Considering that the *Marangoni effect,* between phases is null, for a moving fluid front, there is a discontinuity of momentum across the boundary of the interface (Batchelor,

2009). Using the constitutive equation for a Newtonian fluid, cf. Equation 5.1, and considering the surface equation as function of position defined as

$$\zeta\left(x,y\right)=0 \qquad 5.20$$

the force continuity equation at the interface can be adopted from Batchelor (2009) and defined as

$$\rho\mathbf{g}\cdot\mathbf{z}+\boldsymbol{\sigma}_{g}\cdot\mathbf{n}-\boldsymbol{\sigma}_{liq}\cdot\mathbf{n}=-\gamma\oint\mathbf{n}\times d\mathbf{x} \qquad 5.21$$

where $\mathbf{n}$ is the normal vector to the surface of interface with components $\frac{\partial\zeta}{\partial x},\frac{\partial\zeta}{\partial y}$, $\boldsymbol{\sigma}$ is the normal stress tensor of each phase, and $d\mathbf{x}$ is a line element of the closing bounding surface.

For present geometries and flow, the velocity field is predominantly unidirectional in both phases and the continuity equation at the interface can be considered as

$$-\rho gz+\left(-p_{1}\right)-\left(-p_{2}\right)=-\gamma\left(\frac{1}{R_{1}}+\frac{1}{R_{2}}\right) \qquad 5.22$$

Another phenomenon found is air entrapped at the salient corner, as shown in Figure 5-13 for $Fr=1$, $Re=1$ and $We=1000$. For a contraction, or expansion, monophasic flows exhibit a vortex in the salient corner, where the occurrence of some secondary flow vortex upstream the contraction, or, downstream in the case of an expansion, will originate a closed region (Sousa et al., 2009). For the present work, and under certain flow conditions, this close region will promote the air entrapment. As Figure 5-13 shows, during the flow front advancement, the fluid that is forced to bend in the contraction region does not have the ability to fill the corner vortex, and some air get stuck in the mould cavity.

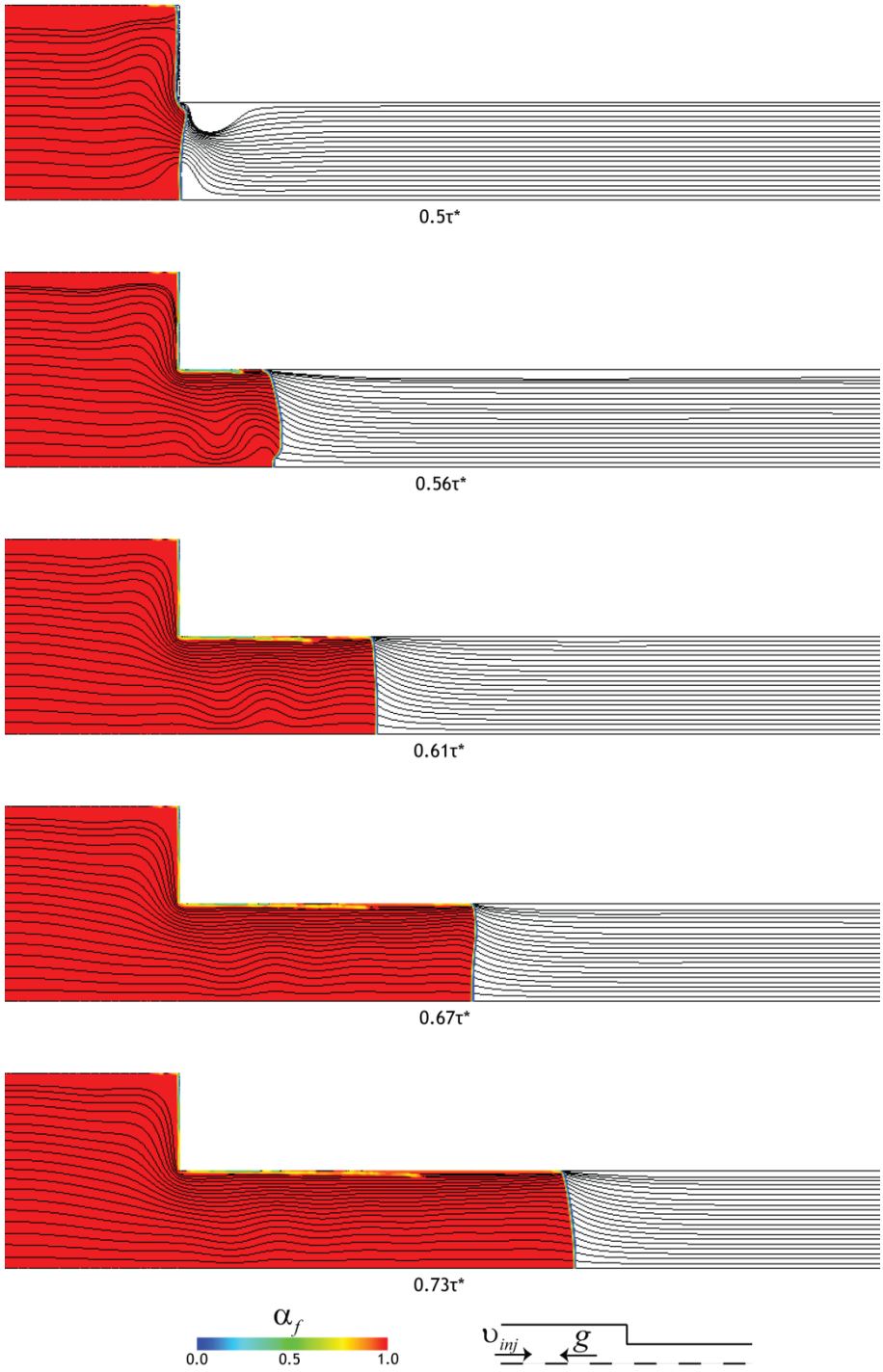

Figure 5-11 Stable flow front for $Fr = 10^{-3}$, $Re = 10$ and $We = 1000$

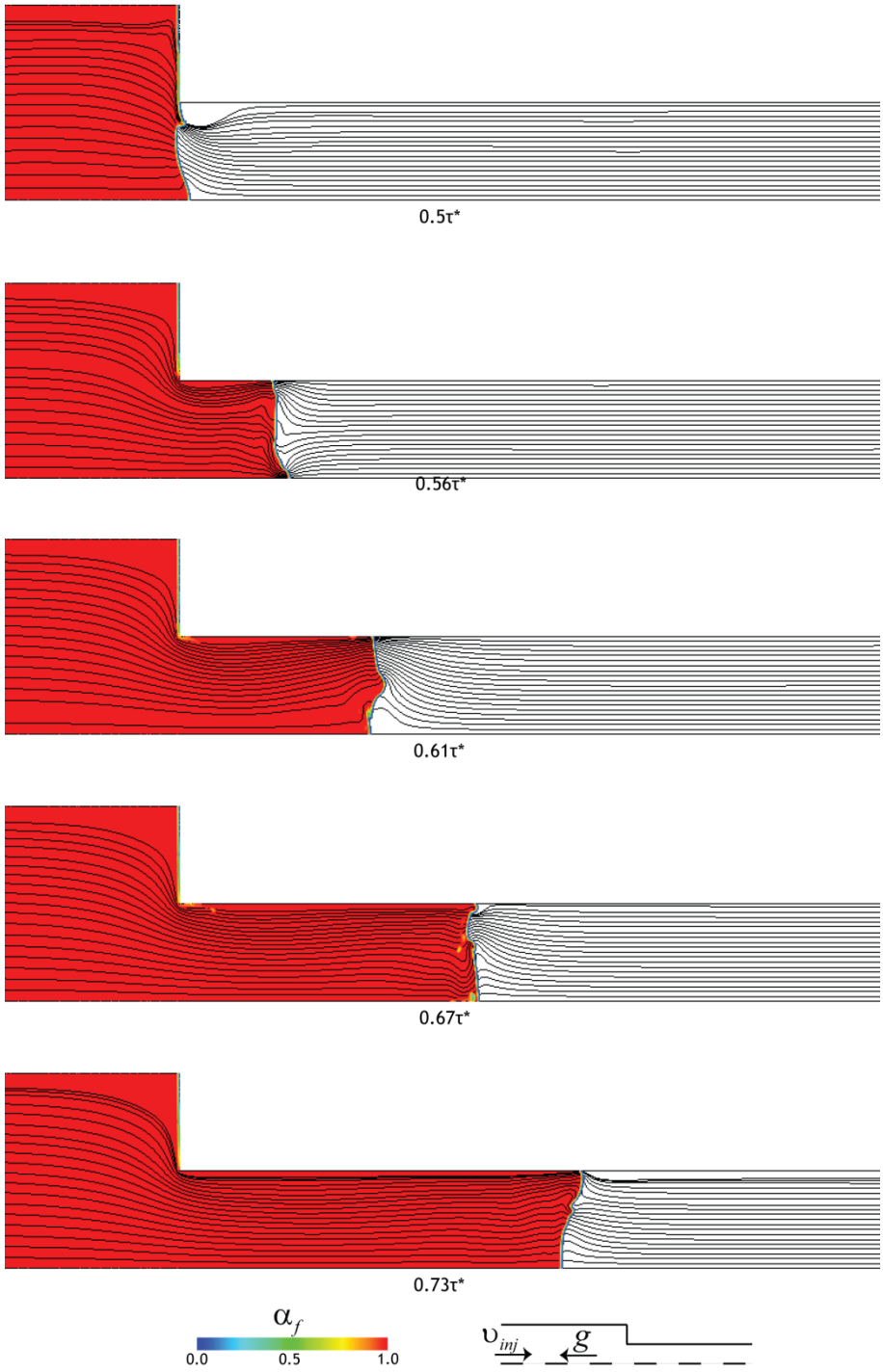

Figure 5-12 Unstable flow front for $Fr = 10^{-3}$, $Re = 100$ and $We = 1000$

The existence, of at least, one solid boundary is crucial for the formation of eddies (Moffatt, 1964). Analytically, Moffatt (1964) demonstrated that the flow in the corner can be induced by an arbitrary disturbance at a larger distance, independently of the energy input by the flow at large distance, and is implying by the existence of an infinite sequence of vortices, called Moffat eddies. Also the mathematical solution was derived from previous works (Dean, 1936; Dean and Montagnon, 1949), where Stokes flow on the

corner was considered, because in the corner the velocity tends to zero (Dean and Montagnon, 1949). The biharmonic equation for the stream function, ψ, in the corner is defined as (Dean, 1936; Dean and Montagnon, 1949)

$$\left(\frac{\partial^2}{\partial x^2} + \frac{\partial^2}{\partial y^2} \right)^2 \psi = 0 \qquad 5.23$$

where the boundary conditions at walls are

$$\psi = 0 \qquad 5.24$$

$$\frac{\partial \psi}{\partial \upsilon} = 0 \qquad 5.25$$

The Moffat eddies diminish in size and strength as the apex of the corner is approached (Moffatt, 1964). For the presence of air in the salient corner, viscous forces play an important role, however even if the velocities near the corner are small enough for Stokes approximation, the inertial forces must be taken into account (Moffatt, 1964).

Considering the same assumptions in Section 5.2.1 and a constant viscosity during the contraction or expansion flow (Vrentas and Duda, 1973), Equation 5.4 can be defined according to dimensionless numbers as

$$\frac{D\mathbf{v}}{Dt} = -\nabla p + \frac{1}{Re}\nabla^2 \mathbf{v} + \frac{\mathbf{g}}{Fr\|\mathbf{g}\|} \qquad 5.26$$

Similar conclusions can be considered for contraction and expansion flow, besides the differences of reattachment length of the corner vortex (Musarra and Keunings, 1989; van de Griend and Denn, 1989), as shown in Figure 5-14, both obtained for $Fr = 1$, $Re = 1$ and $We = 1000$.

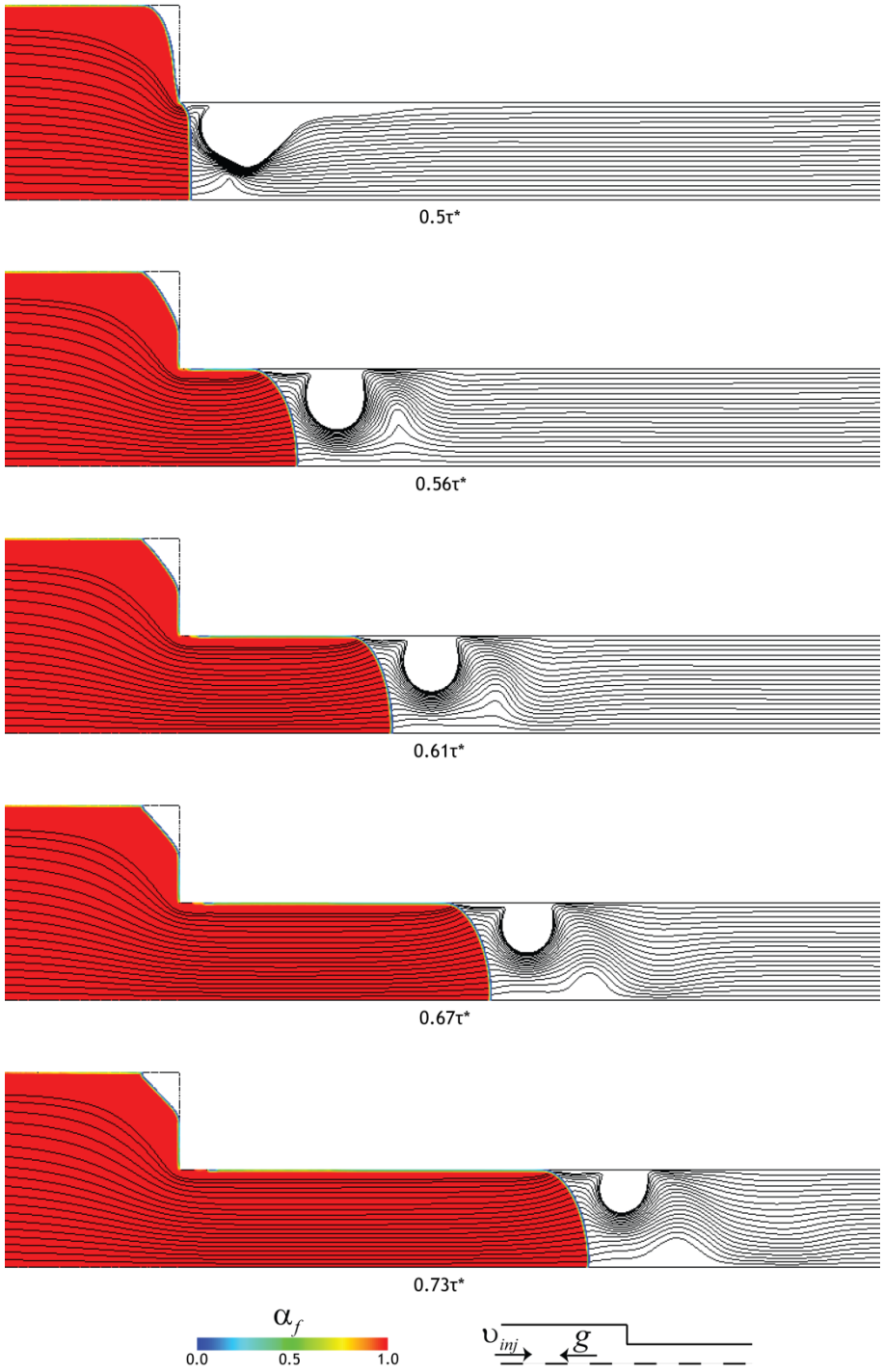

Figure 5-13 Air entrapped at the salient corner for $Fr = 1$, $Re = 1$ and $We = 1000$

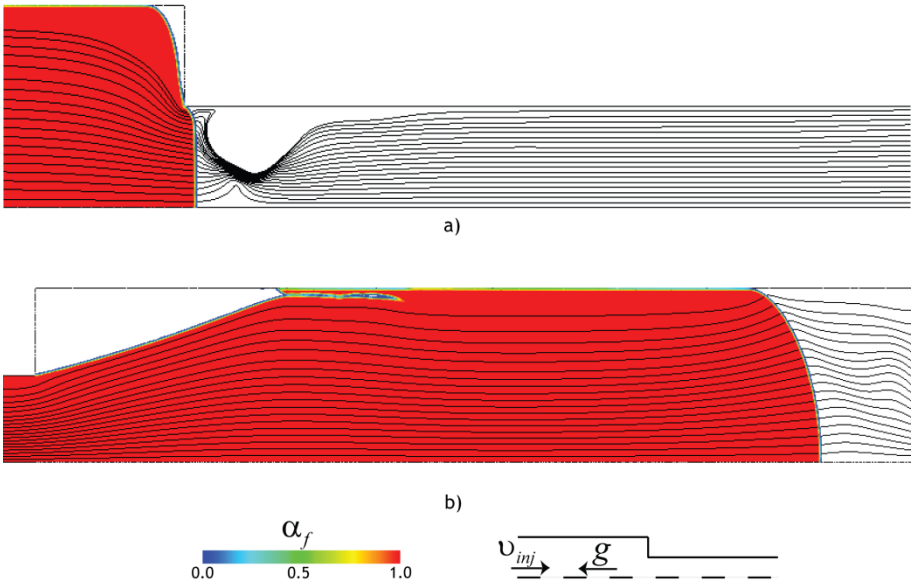

Figure 5-14 Air entrapped at the salient corner for $Fr=1$, $Re=1$ and $We=1000$: a) contraction b) expansion

The presence of the vortex at salient corner alone does not imply an air imprisonment. The flow depends on inertial, viscous and gravitational forces. Influenced by the ratio of these forces, for some flow conditions, the fluid flow can push forward the air from the salient corner, originating some clean salient corner equal to those shown in Figure 5-11 and Figure 5-12. However, as will be shown below on Section 5.3.4, the air moves forward with the filling front creating some air entrapment, Figure 5-15 to Figure 5-17, that could be responsible for part defect.

Commonly referred by several authors (Kundu and Cohen, 2004; Muralidhar and Biswas, 2011; Shames, 1992), for parallel and laminar flows, there is a separation of the flow in the entrance of the duct. Stüer et al. (1999) refers that the entrained fluid can make the closed two-dimensional vortex in the salient corner to release as a blob. In the present work, it is observed a similar behaviour when the air flows directly from the corner vortex to the fluid medium, it originates the entrapment of gas, as shown in Figure 5-15 with the following flow conditions: for $Fr=10^{-1}$, $Re=1$ and $We=10$. Analysing the time evolution, it is possible to see that as the liquid flows, the air is pushed into the liquid and the gas entrapment becomes bigger.

It is well know that sudden changes in the flow section can originate separation, although this depends on the flow conditions. Astarita and Greco (1968) suggest that above a critical Re number, that was found to be 186 for $Tr\approx 2.5$, a *vena contraction* is formed. In Figure 5-16, for a flow conditions of $Fr=10^{-1}$, $Re=1000$ and $We=100$, *vena contraction*

is formed after the flow front reaches the geometric constriction. With the flow advancement, the front tends to the walls, forming a close zone in the *vena contracta* region that remains in the same position regardless of the fluid flow.

In the present work, both phenomena from Figure 5-15 and Figure 5-16 are named air entrapment and engulfment, besides the different formation kinetics: air comes directly from the salient corner (cf. Figure 5-15) or the air gets stuck between the liquid and the wall due to the formation of a *vena contracta* (cf. Figure 5-16).

Flow separation creates a boundary layer, initially of zero thickness, that will grow in size downstream until it becomes equal to half the length of the channel, achieving a fully developed profile(Muralidhar and Biswas, 2011). At the entrance, the flow assumes a uniform velocity profile. Experimentally, Armaly et al. (1983), observed, for a simple backward-facing step flow, a single separation region attached to the step. The reattachment length of the primary separation region is dependent on Re number, on the step height and on the momentum of the oncoming flow (Armaly et al., 1983). Despite the results were obtained for a backward-facing step flow, a deeper insight of the dynamics in the primary recirculation region can be found on Schäfer et al. (2009) and some extrapolation can be done for expansions or contractions.

Figure 5-17 shows the air flowing from the salient corner to the small channel, originating an air boundary layer, for $Fr = 10$, $Re = 1000$ and $We = 100$. Observing the evolution of the flow, when it reaches the contraction, some air is still in the corner vortex, however with the flow advancement, this air also advances for the smaller channel allowing the liquid front to fully fill the top corner. However, downstream the step a gas boundary layer is formed that the fluid cannot fill. Due to the presence of air, the gas boundary layer can originate some instability in the flow, as shown from the streamline maps, which perturb the flow front that becomes unstable.

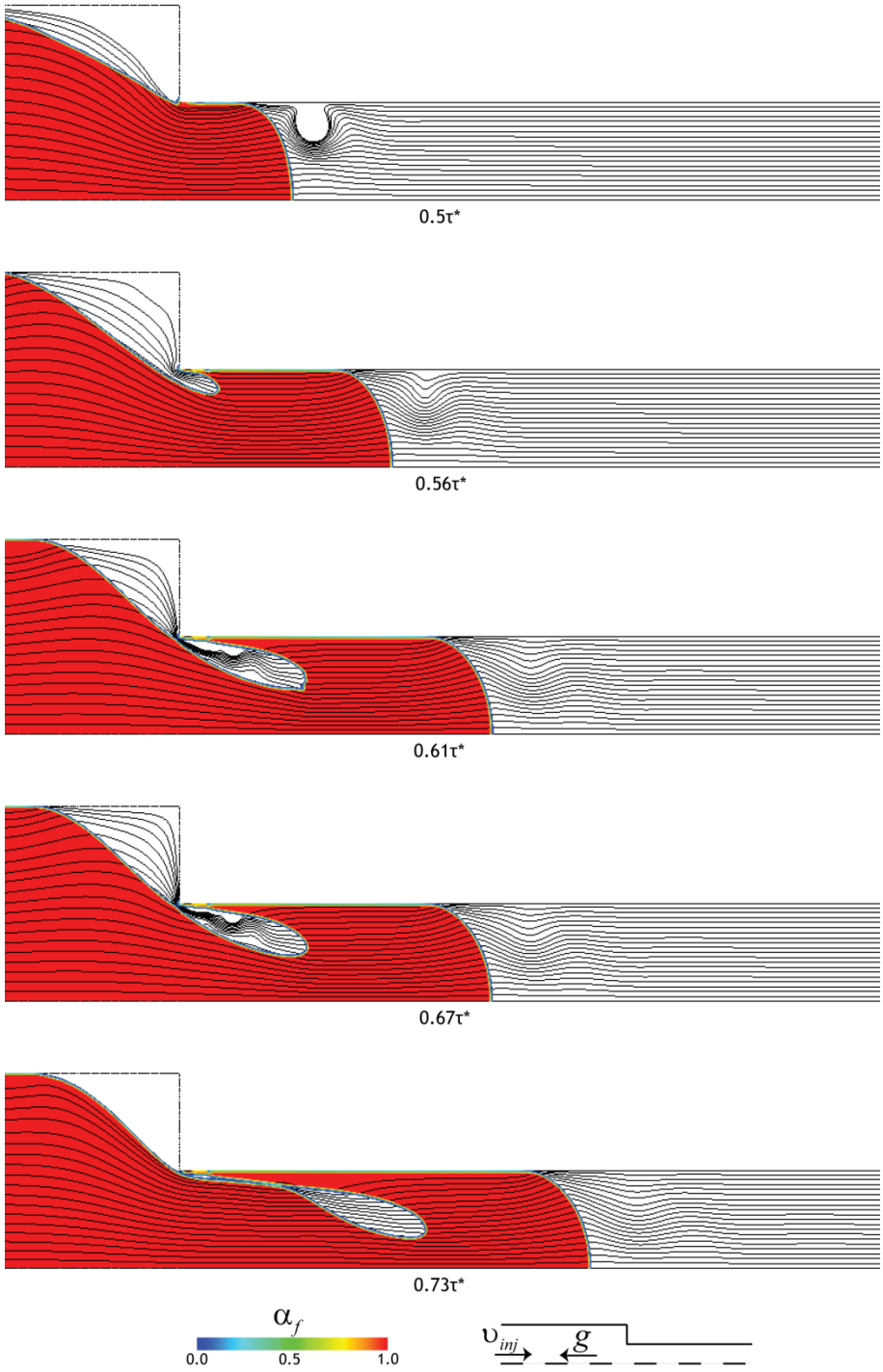

Figure 5-15 Air entrapment and engulfment, originated from the air in the corner vortex for $Fr = 10^{-1}$, $Re = 1$ and $We = 10$

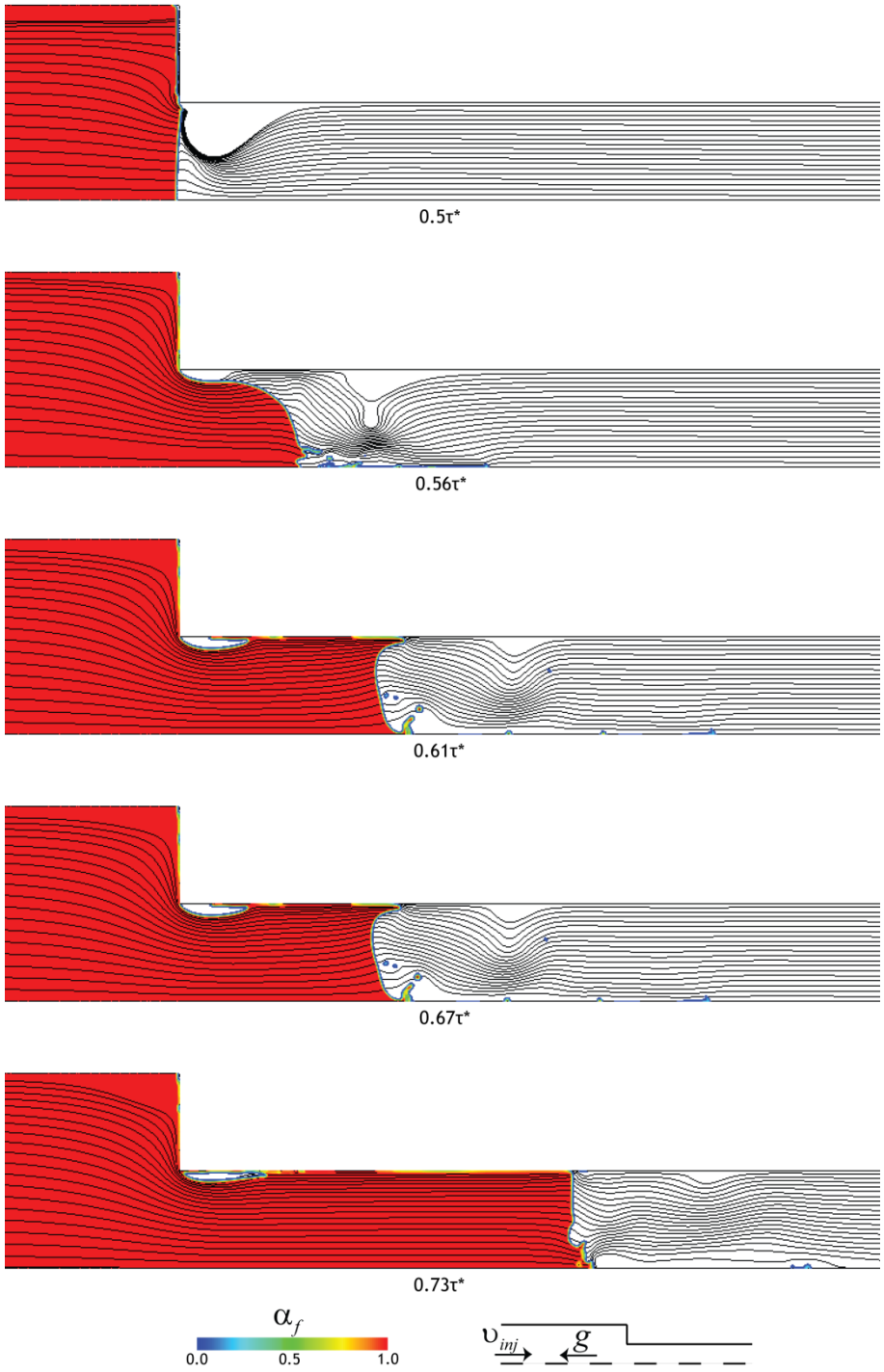

Figure 5-16 Air entrapment and engulfment, originated from a closed gas boundary layer for $Fr = 10^{-1}$, $Re = 1000$ and $We = 100$

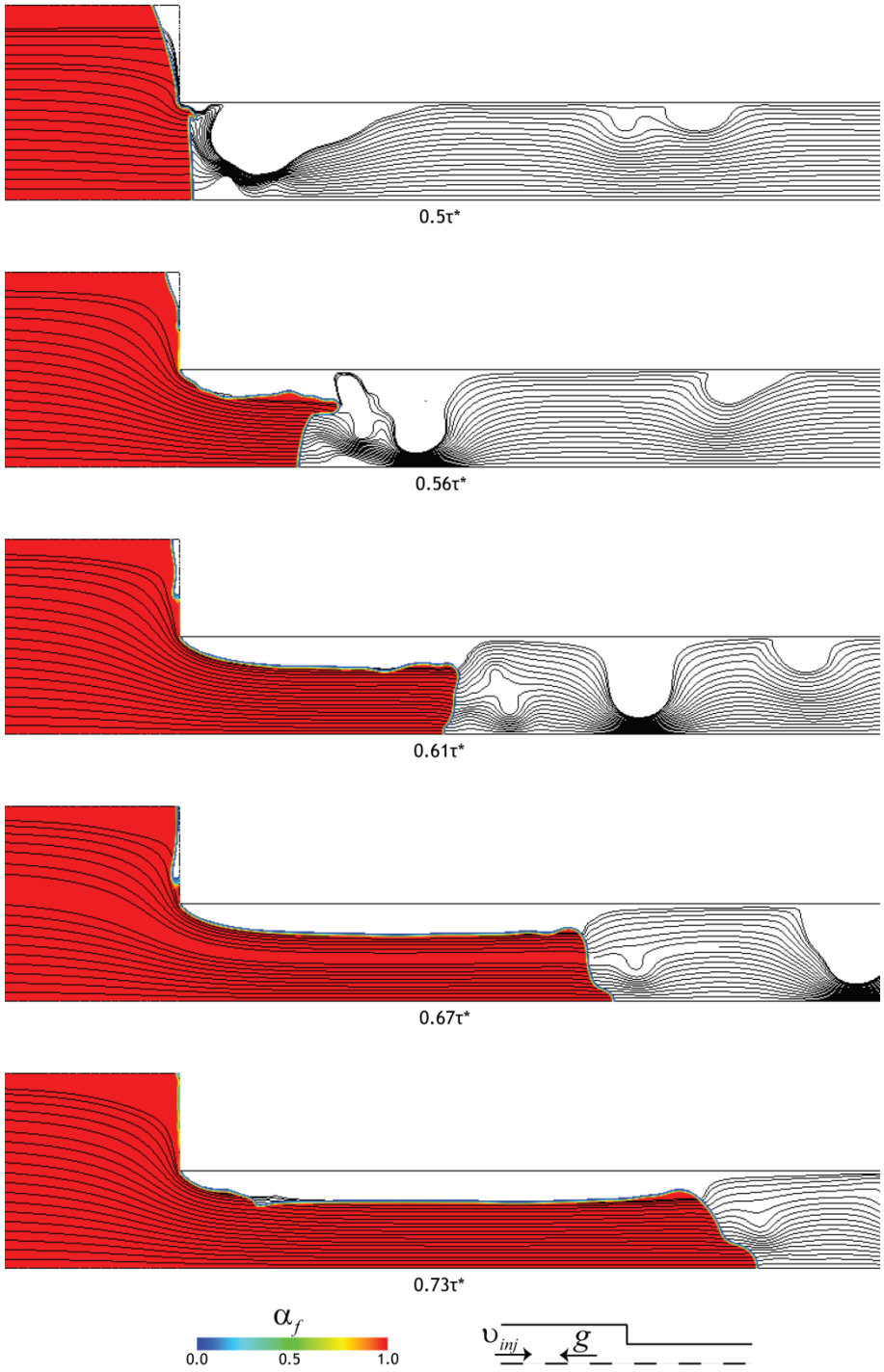

Figure 5-17 Air boundary layer for $Fr = 10$, $Re = 1000$ and $We = 100$

5.3.3 Fluid mechanics parameters effects

Castro and Macosko (1982) carried out several experiments that showed the impact of inertial effects on mould filling in RIM. Cohnen and Osswald (1992) quantified experimentally the inertial, viscous and surface forces effects in terms of the dimensionless numbers Re, Ca and We for what they considered, realistic industrial cases, and concluded that the filling pattern is greatly influenced by inertia and the air or gas entrapment depends on capillary effects. Numerically, Mohammed et al. (1994) shown that inertia plays an important role for defining the recirculation zones and the velocity flow field.

The present work studies the individual effect of fluid mechanics parameters that affect the mould filling, introduced in Section 5.3.1.

5.3.3.1 Effect of gravity – Froude number

Due to the low viscosity of fluids used in RIM, the gravitational force can play an important role during filling. The importance of gravitational force over the inertial force in RIM moulds flows is studied in this section. A relation between these forces is already known, the Froude number, Fr, which is defined by Equation 5.12. For lower Fr, the presence of gravity cannot be neglected, whenever the injection is performed in the opposite direction to gravity or not.

Considering the geometry of Figure 5-9, and for a fixed Reynolds number of $Re=1$ and Weber number of $We=10^3$, the multiphase flow filling was studied. From the CFD simulation results the flow front shape was analysed at $0.50\tau^*$ (contraction or expansion zone), $0.61\tau^*$ and $0.73\tau^*$.

A range of Froude numbers between $Fr=10^{-3}$ to $Fr=10$ was studied in order to identify the flow phenomena. The fluid fraction maps, α_f, shown at Figure 5-18 regard the $Fr<1$ simulations, i.e., when the gravity effects are dominant over the inertial forces in the flow. From the maps shown in this figure and for $0.73\tau^*$, it is possible to observe that for lower Fr numbers, the gravity will affect the shape of flow front surface, changing from flat surface to a convex meniscus surface with the increasing in Fr. The flow in the maps of Figure 5-18 is always in the opposite direction to gravity.

For Fr number equal or larger than 1, shown in Figure 5-19, the convex meniscus, for $0.73\tau^*$, remain constant due to the inertial forces that have a dominant effect over the gravitational forces. The increase in Fr number allows a larger removal of the air in the salient corner, due to the increasing velocity values of the liquid and consequently larger dynamic pressure of the filling front, which enabled that a larger fraction of air is pushed out of the corner before the filling front blocks the thinner channel. Regarding Equation 3.15, the velocity increase will lead to an increase in viscous dissipation, due to shear dissipation in the walls. However this is not analysed in the present case, it should be noted that an over-raised value in viscous dissipation could lead to burns in final part. High shear stress is known to cause damage/burn thermoplastics during the flow. One should notice that the flow front keeps its well defined shape when it passes the contraction. As shown by Equation 5.26 pressure gradient is affected by gravitational force, and consequently so the flow front deformation, as present in Equation 5.22.

When the inertial forces are small, the flow have time to fill the salient corner, however, as Figure 5-20 shows, the salient corner is not totally filled and some air is still trapped in that zone and after it flows into the liquid. From the same figure, it is possible to observe that for lower We number (Figure 5-20a) and lower Re number, there is an increase in the area of the air stuck in the salient corner, which decreases for Froude numbers larger than $Fr=1$. When the Re and Fr increase there is an increase in the area of air. Similar trend is observed in Figure 5-20c, for the highest We number studied. Regarding the values present in Figure 5-20b, for a $We=100$, for the all range of Re number studied, there is an increasing in air area in the salient corner when Fr rises until close to $Fr=1$, and after it decreases. This trend is present in all We range. The presence of air in salient corner could lead to part defects. CFD results aim the prediction of air presence and to a convenient air escape project to exhaust these quantities from the cavity.

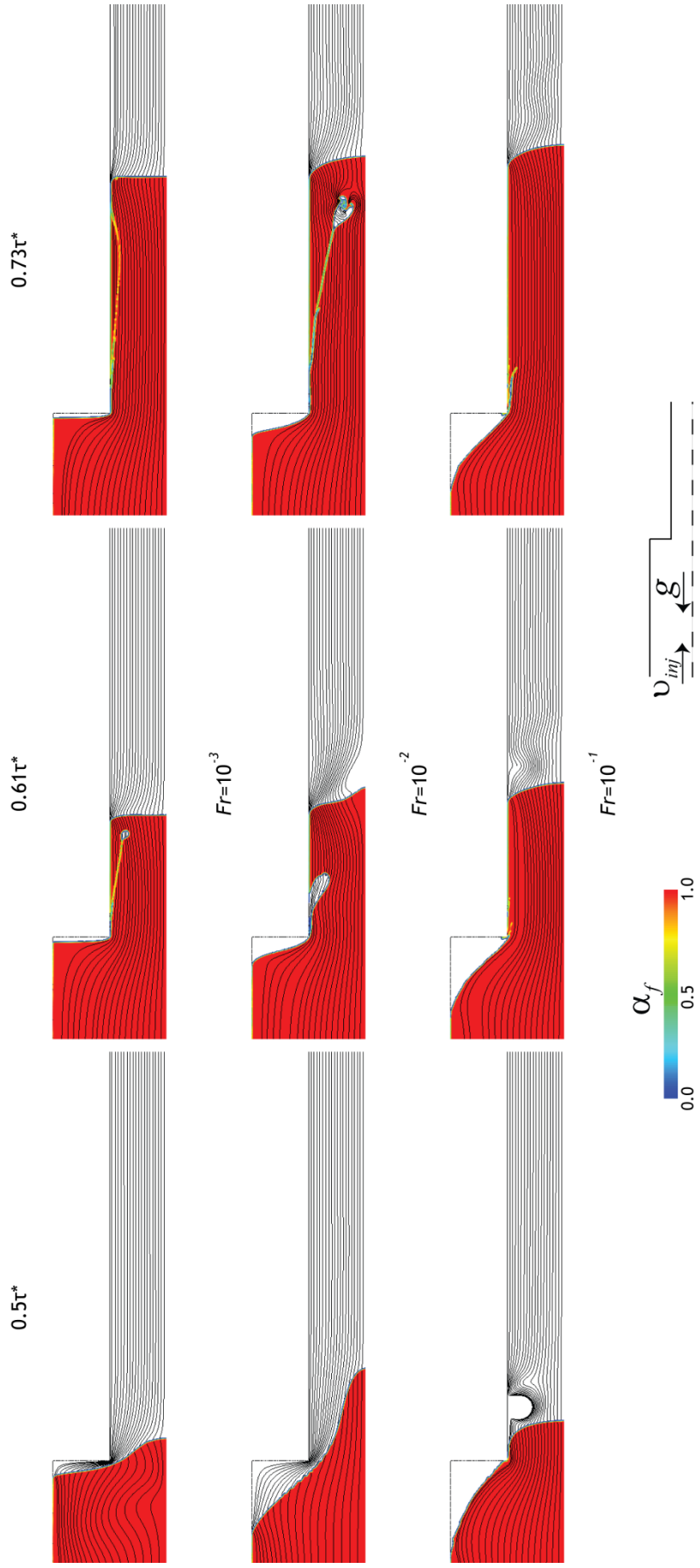

Figure 5-18 Flow front shape for contraction flow 2:1 for different *Fr*, below *Fr*=1 , at *Re*=1 and *We*=1000 , taken at different filling times. The red colour corresponds to the fluid phase, and colourless to the air phase.

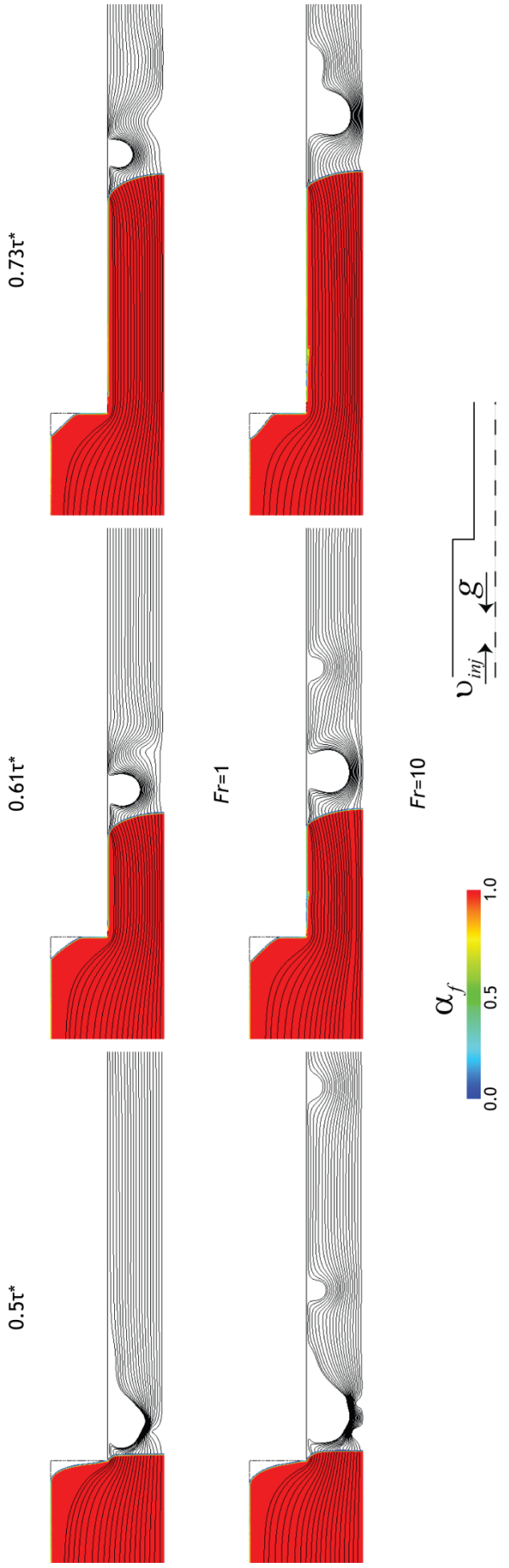

Figure 5-19 Flow front shape for contraction flow 2:1 above $Fr>1$, at $Re=1$ and $We=1000$, taken at different fillingtimes. The red colour corresponds to the fluid phase, and colourless to the air phase.

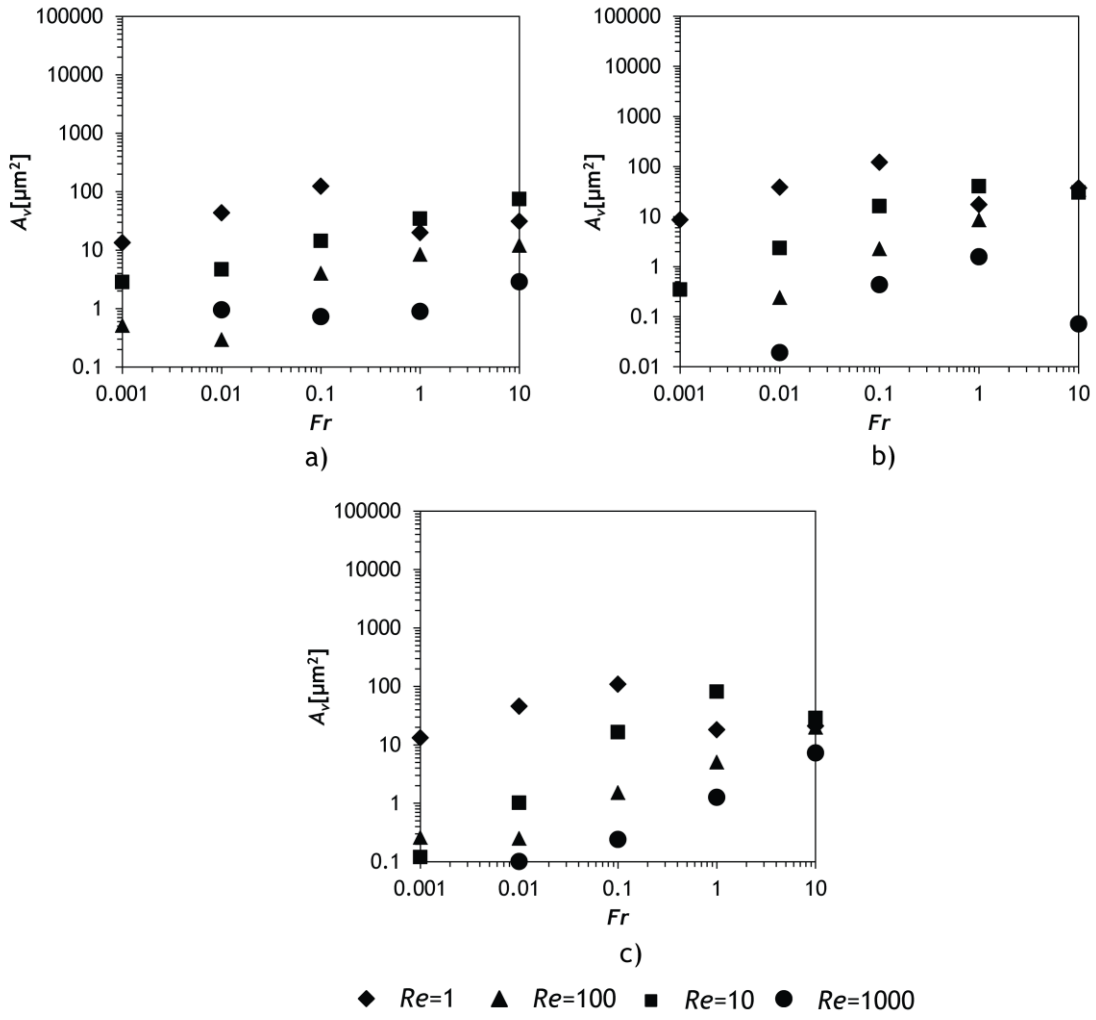

Figure 5-20 Effect of the Froude number on air entrapped area in salient corer at contraction flow 2:1, for different Reynolds number and Weber number: a) $We=10$ **b)** $We=100$ **and c)** $We=1000$

Similar behaviour is observed in expansion flow. For numbers lower than $Fr<1$ and higher than $Fr>1$, respectively Figure 5-21 and Figure 5-22. For $Fr<1$ it is observed a flatness of the flow front surface due to the gravity force dominance over inertia. When the fluid passes a contraction, an extrudate swell occurs. For lower values of Fr, the gravity attracts the fluid that fill the salient corner and the extrudate swell is not visible. However, increasing the Fr the salient corner tends to be not fully filled with liquid, and air gets stuck. For Fr numbers higher than 1, the flow swells into the size of the D_2, creating a salient corner with air inside, since the gravity does not affect the flow enough to fill that zone. The figures suggest that the swelling ratio increases with Fr numbers. The swelling ratio is the ratio between downstream flow diameter by the upstream flow diameter, and it is depending on the re-arrangement of the velocity and stress fields (Richardson, 1970).

Similar to contraction, expansion flow shown to be influenced by gravity forces on pressure gradient, as in Equation 5.26, and consequently on the flow front deformations, as shown in Equation 5.22.

The air entrapment area, shown in Figure 5-23, clearly increases with the Fr number and also with the Re number.

5.3.3.2 Effect of viscous forces – Reynolds number

A broad range of material with different properties can be used in RIM process. Regarding the mould filling, the viscosity has an important role since it influences the energy consumption during the process, the specifications of the RIM machine in terms of operation pressure and minimum required throughput, and the final parts quality. To assess the importance of the viscous forces on filling the Reynolds number effect on mould filling is studied. The Reynolds number gives the ratio between fluid's inertia and viscous forces, described by Equation 5.11. In order to understand the influence of each force during the mould filling, the following Re of 1, 10, 100 and 1000 were studied. This set of Reynolds numbers in the mould, where set considering the Re number range for a typical RIM process is between 1 to 100.

The geometry used was the one in Figure 5-9. It was fixed a Froude number of $Fr = 1 \times 10^{-3}$ and a Weber number of $We = 1 \times 10^{3}$, and the same time instants of the previous section were chosen.

The shape of the flow front for a contraction, is shown in Figure 5-24. The front evolves from the meniscus shape to an instable flow front shape when the Reynolds number increases. In these simulation the gravitational force has an equal influence to the inertial force, in the flow front and so it is not enough to "stabilize" the front. Regarding the effect of the viscous forces, in flow regimes where they are dominant, i.e., lower Re, it is possible to observe the resistance that viscous forces pose to the deformation of the flow front shape. Increasing the Re number, this resistance decreases and an instable front appears. Also some air instabilities appear close to the flow front, as shown form the streamlines, and an increasing gas boundary layer is observable when the inertial forces become more important, i.e. for rising Re values.

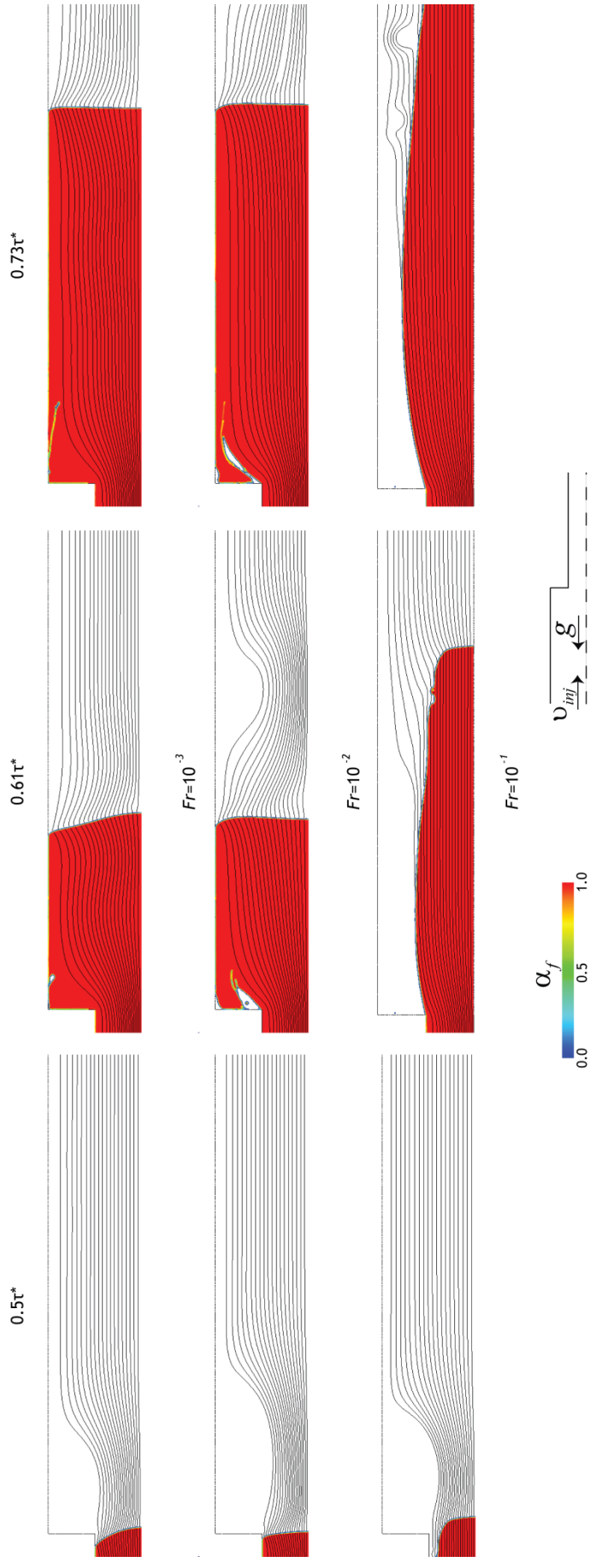

Figure 5-21 Flow front shape for flow expansion 1:2 for different *Fr*, below *Fr*<1 , at *Re*=1 and *We*=1000 , taken at different filling times. The red colour corresponds to the fluid phase, and colourless to the air phase.

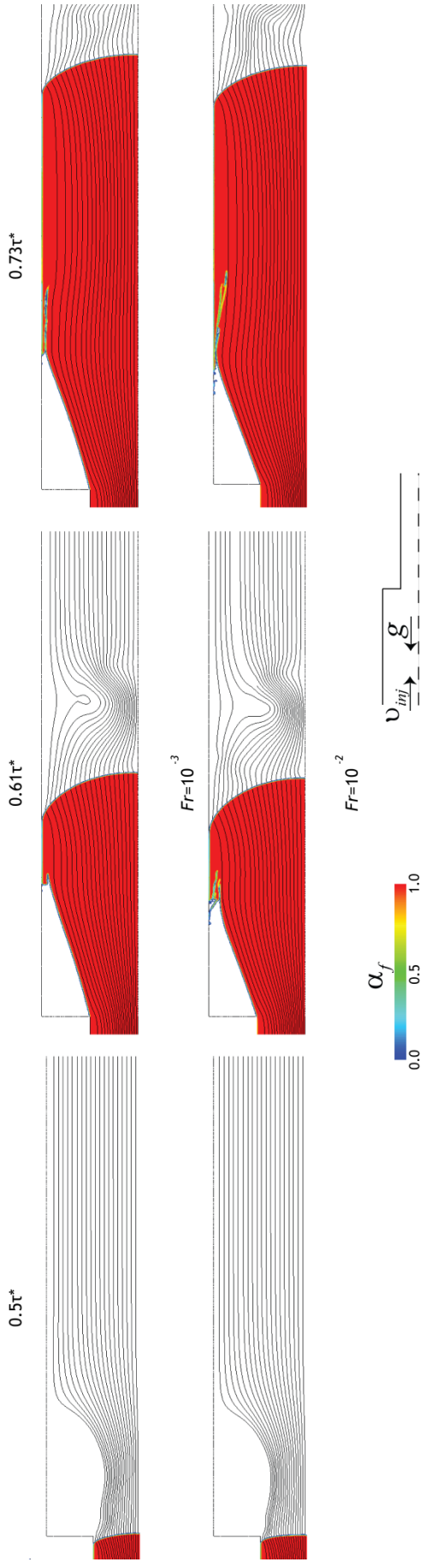

Figure 5-22 Flow front shape for flow expansion 1:2 for different *Fr*, above *Fr*<1 , at *Re*=1 and *We*=1000, taken at different filling times. The red colour corresponds to the fluid phase, and colourless to the air phase.

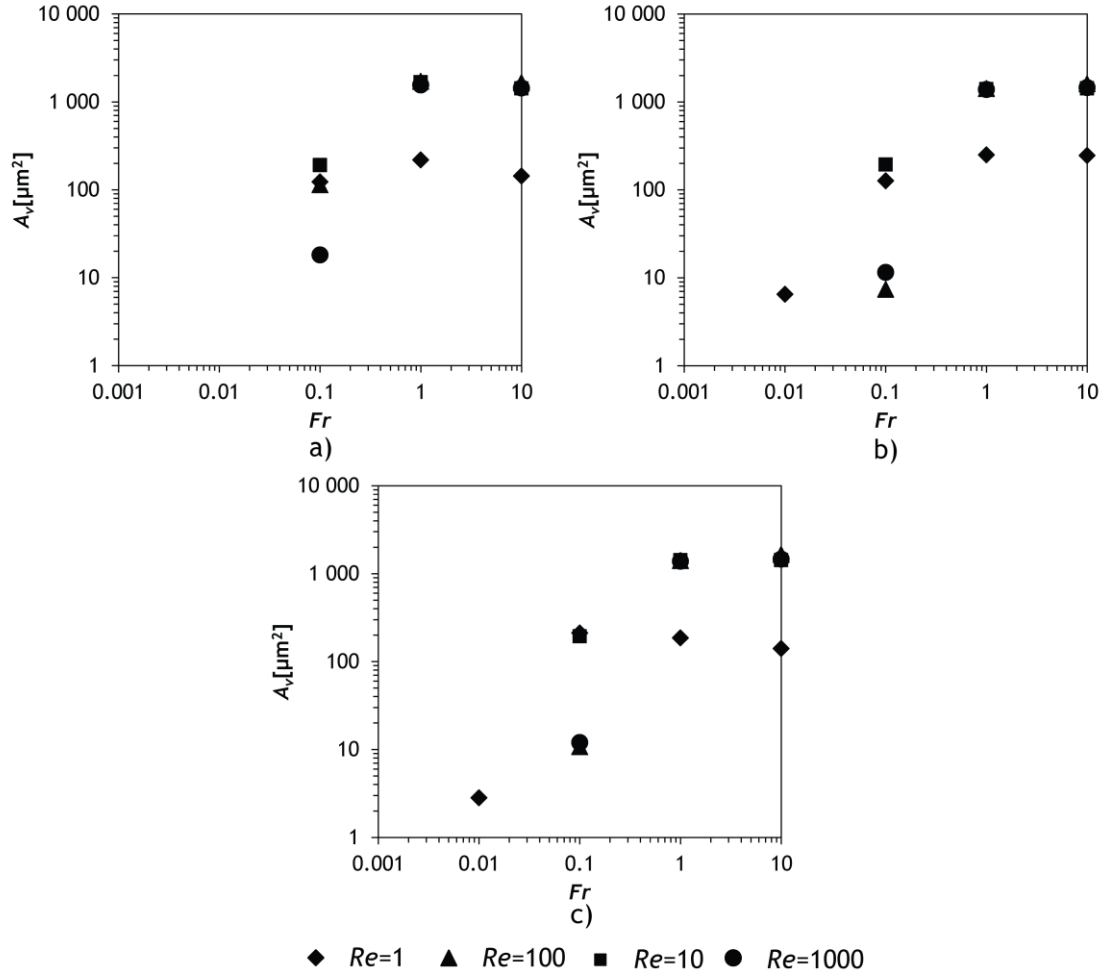

Figure 5-23 Effect of the Froude number on air entrapped area in salient corer at expansion flow 1:2, for different Reynolds number and Weber number: a) $We=10$ **b)** $We=100$ **and c)** $We=1000$

Regarding the air in the salient corner, Figure 5-24 shows that the area filled with air decreases with the rise of Re, since there is a lower resistance of the flow to shear deformation the fluid fills that zone more easily. These lower viscous forces influence, allows the air stuck in the salient corner to be drag by the liquid and flow along with the fluid. So, the area of the salient corner with air decreases when the Re number rises, as shown in Figure 5-25. Since it was also observed that the air area decreases whit the diminution of Fr number, the inertial terms of the filling front have opposite behaviours: they reduce air entrapment when increased in relation to the viscous forces, but have an opposite effect when increased in relation to the body force. The only exception is found for Fr number above 1, where the tendency is area vortex increase until $Re \approx 10$, and after the air area decreases, a tendency that was observed for all We number.

Two issues regarding the Reynolds number in addition to the air entrapment in the corner should also be addressed in the mould design: the filling front stability and the filling time. If the filling front gets too unstable it can engulf air rather than pushing it out of the

mould, and so a higher Reynolds number that could remove air stuck in cavities more easily is not always the best option. On the other hand lower Re number will have large mould filling times, and consequently there is a stronger effect of the viscosity build up due to reaction or of achieving the polymerization gel point which annuls the advantages of RIM that stem from the mould filling with low viscous fluids.

For the expansion, in the all Re number range studied, the flow exhibits a stable flow front as shown in Figure 5-26. The main effect of the Reynolds number, resides in the fact that during the flow front advancement the front becomes less resistant to deformation with increasing Re number. This resistance is related with pressure gradient along the flow front, as shown in Equation 5.22, where the pressure gradient depends on viscous forces variation, as given by Equation 5.26.

For lower Re number, there is air entrapment inside the flow, and increasing the Re, instabilities appear in the flow front and also in the air flow. However, when the inertial forces are increased in relation to the viscous forces the filling of the salient corner increases. From Figure 5-27, it is seen that air only gets stuck in the salient corner for $Fr > 10^{-1}$. The tendency of air entrapment with the Reynolds number for the lowest We number studied, is an increase in the area until a $Re \approx 10$, where after it, the air entrapment area decreases. For a $We = 100$ and $We = 1000$, it is observable an increasing until $Re \approx 10$, and after it, the vortex area has a asymptotic behaviour. For $We = 100$, a similar behaviour is found, but there is a decrease in the vortex area before the asymptotic performance.

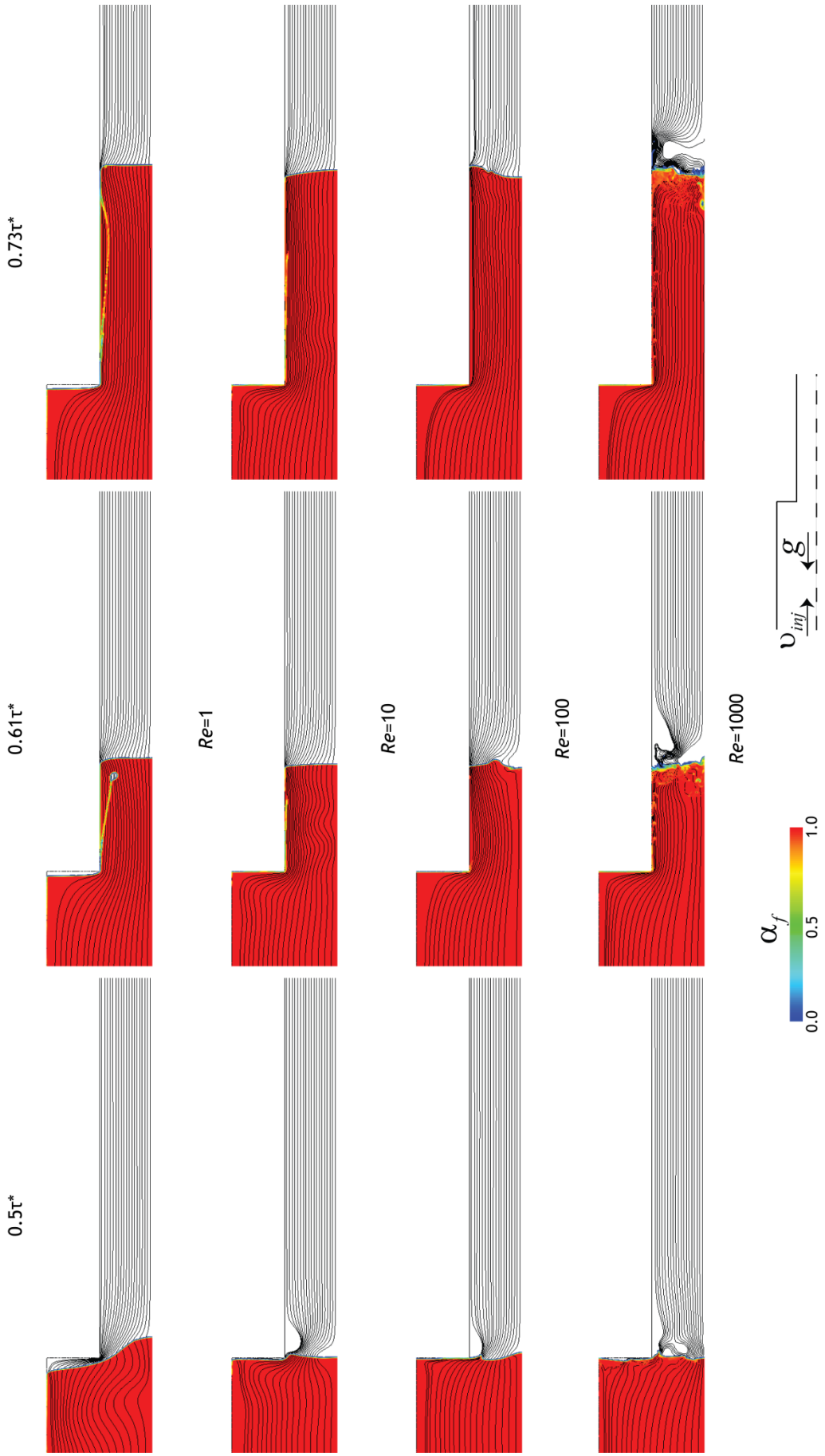

Figure 5-24 Flow front shape for contraction flow 2:1 for different *Re* at Fr=10^{-3} and We=1000, taken at different filling times. The red colour corresponds to the fluid phase, and colourless to the air phase.

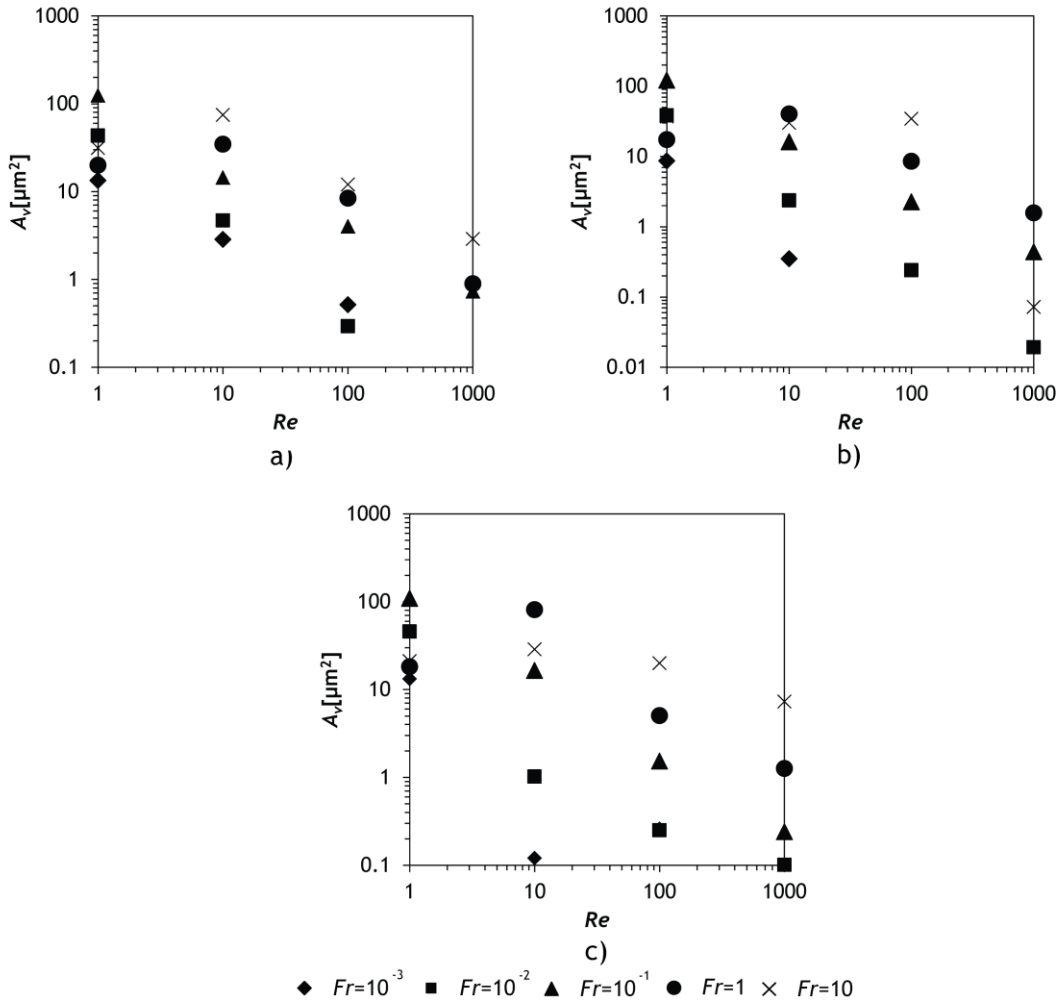

Figure 5-25 Effect of the Reynolds number on air entrapped area in salient corer at contraction flow 2:1, for different Froude number and Weber number: a) $We = 10$ **b)** $We = 100$ **and c)** $We = 1000$

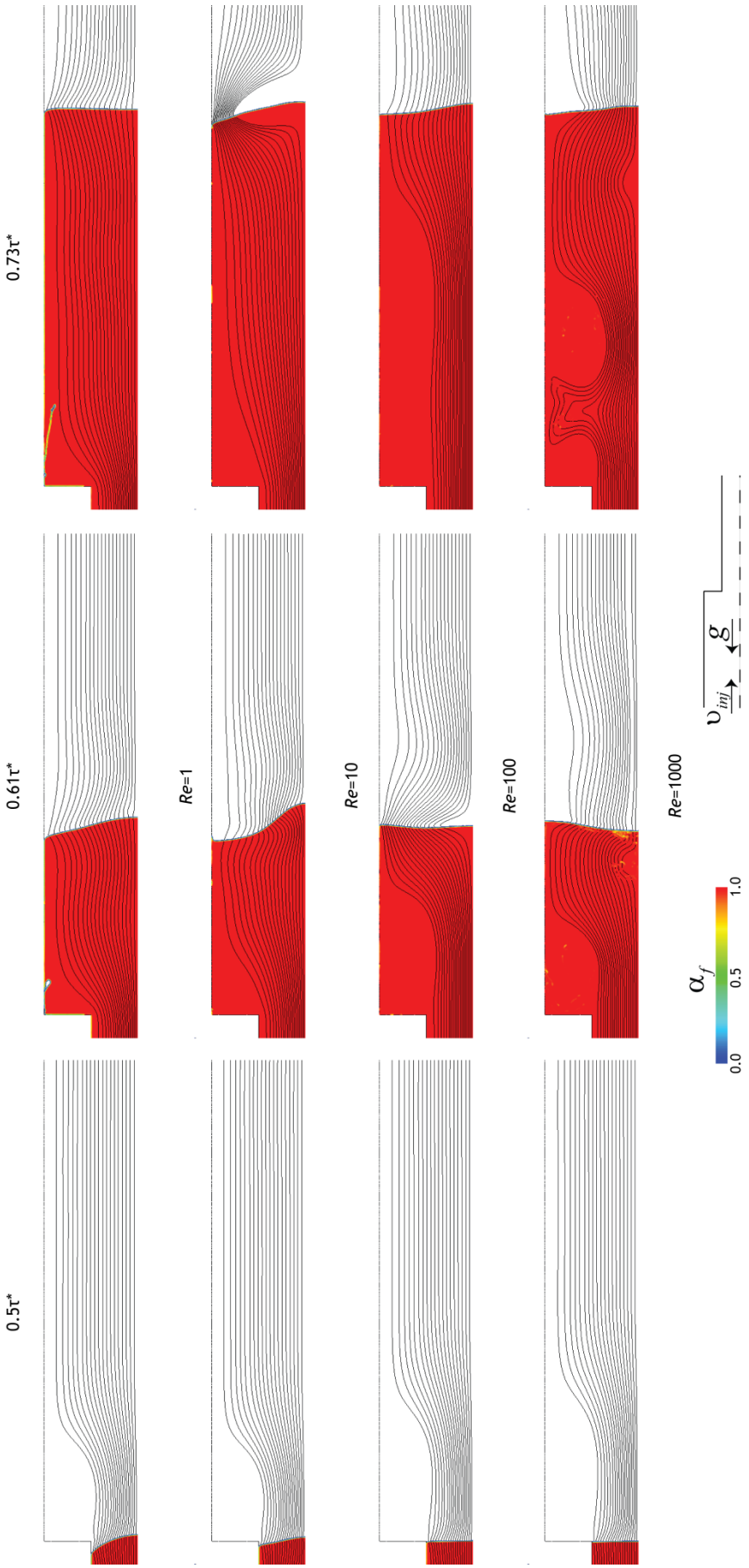

Figure 5-26 Flow front shape for flow expansion 1:2 for different *Re* at Fr=10^{-3} and We=1000, taken at different filling times. The red colour corresponds to the fluid phase, and colourless to the air phase.

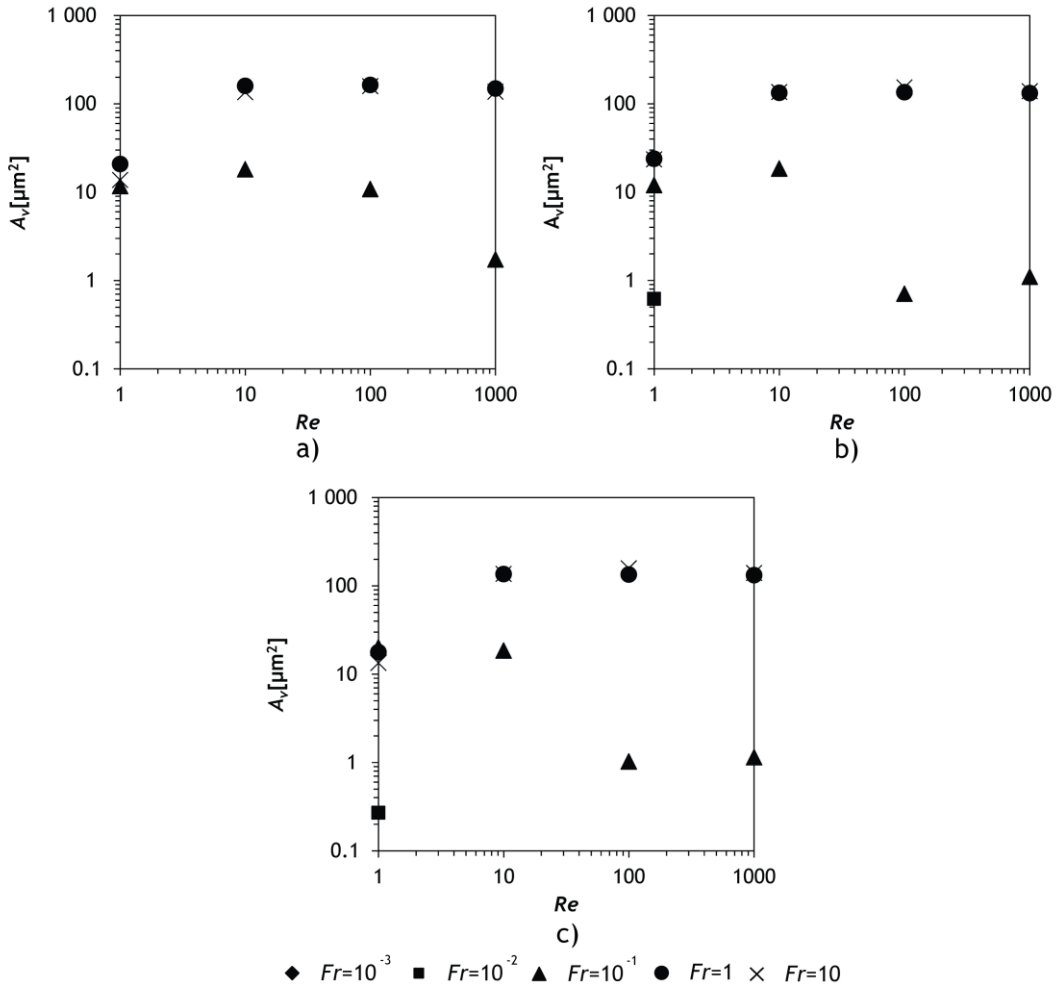

Figure 5-27 Effect of the Reynolds number on air entrapped area in salient corer at expansion flow 1:2, for different Froude number and Weber number: a) $We=10$ **b)** $We=100$ **and c)** $We=1000$

5.3.3.3 Surface forces during filling – effect of Weber

For TIM, the capillary effects can be neglected due the high viscosities evolved during the process (Cécile, 2005), however, since RIM materials have lower viscosities compared to the TIM, the surface tension plays an important role for the definition of the free flow front. The knowledge of how it could affect filling, is an important aspect in predicting the flow, and is the aim of the present sub-chapter.

For the above purposes, the influence of the ratio between the inertial forces to the surface tension, denominated Weber number, We, and defined by Equation 5.13 is studied. The We range for the present work are $We=10$, $We=100$ and $We=1000$. Besides the maps from Figure 5-28 that are obtained for lower Fr numbers, which flatten the flow front surface, it is possible to observe that the surface tension plays an important role in maintain the front shape, since for lower We number, the flow front shape is unstable. Mitsoulis (2010) showed, numerically, that for lower surface forces, the fluid is

accelerated towards the flow front increasing the stresses and reducing the flow curvature. Increasing the We number, i.e., decreasing the surface forces, the flow front shape remains along the flow, since the pressure gradient remains constant.

From the figure is possible to observe the presence of air entrapment on salient corner and in the fluid, however this behaviour is similar for all the We range studied and no difference in size or air quantity is noticed. Figure 5-29 shows and proves that the corner vortex exhibits a constant behaviour along the increase of We number.

For the expansion flow, the effect of the surface tension is slighter, since there is not a considerable difference between the studied We number values, as shown in Figure 5-30 However, it is possible to see that for the lowest We number of the range, the flow front shape is less flat than on the highest We. As for contraction, the flow front deformation depends on surface forces (Equation 5.22), being independent from pressure gradient, and mainly affected by viscous and gravitational force (Equation 5.26), that remains constant. Regarding the area of the air in the salient corner, shown in Figure 5-31, the We clearly shows no impact on it.

5.3.3.4 Effect of thickness ratio

The last dimensionless factor that characterizes the mould filling is the thickness ratio, defined by Equation 5.14. Using the same geometry, and for a contraction, four different geometries were studied with the following thickness ratios:

- $2{:}1$
- $5{:}1$
- $10{:}1$

A similar geometry used in the previous studies, from Figure 5-9, was studied for the thickness ratio, however just for the contraction. The values for the thickness ratio were chosen considering the hypothesis of a large variation between them. The influence of the thickness ratio was studied in order of the dimensionless numbers introduced before.

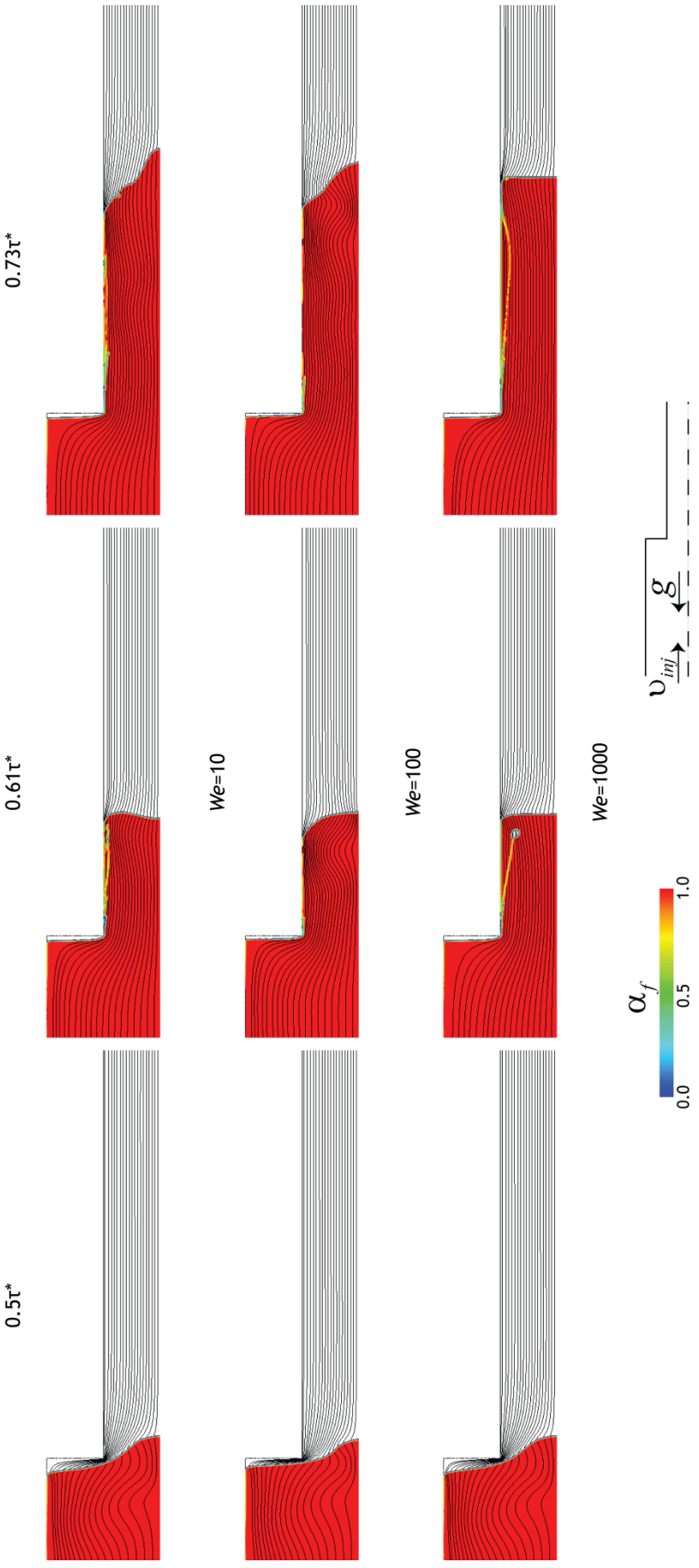

Figure 5-28 Flow front for contraction flow 2:1 for different *We* at $Fr=10^{-3}$ and $Re=1$, taken at different filling times. The red colour corresponds to the fluid phase, and colourless to the air phase.

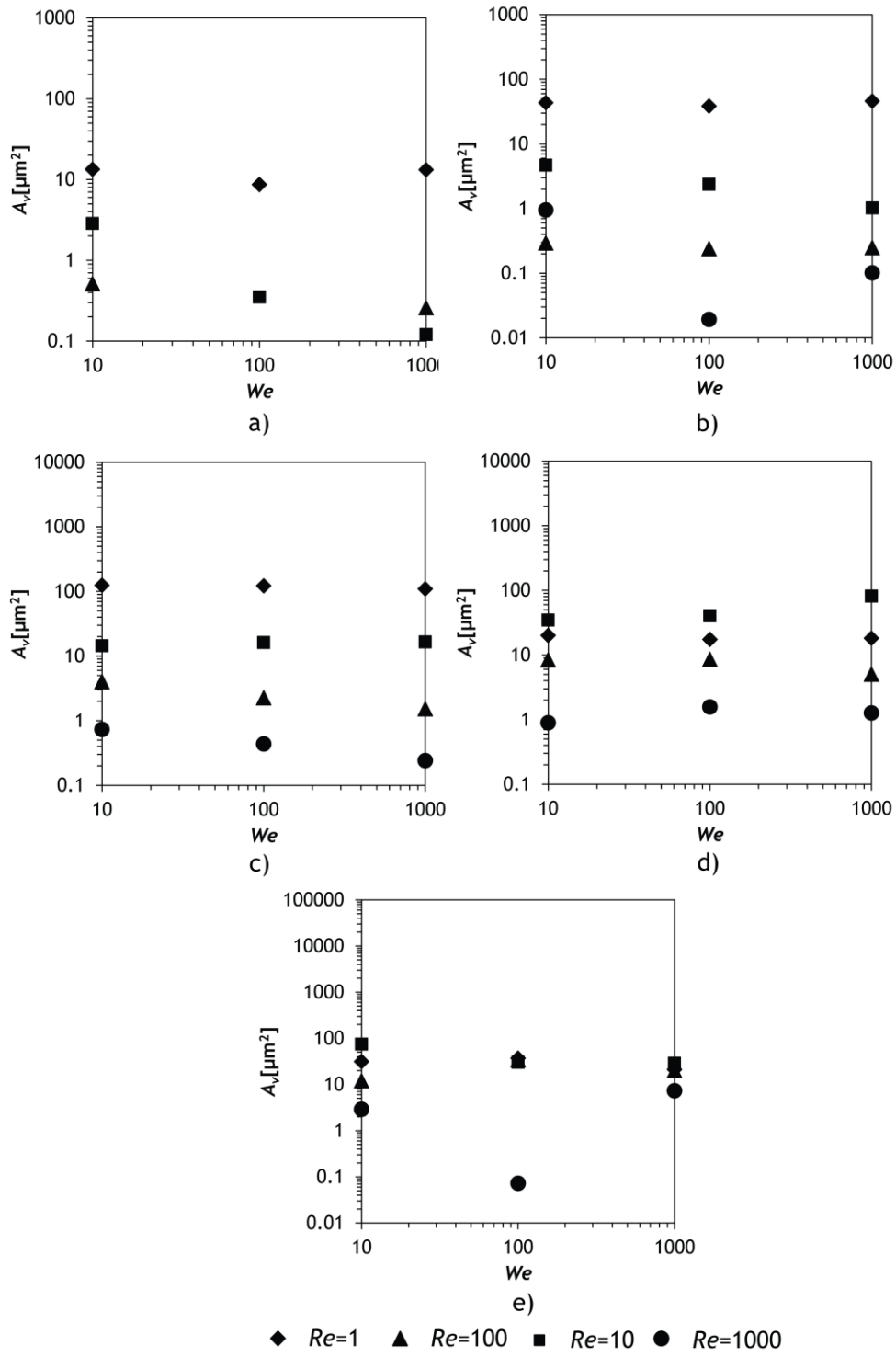

Figure 5-29 Effect of the Weber number on air entrapped area in salient corer at contraction flow 2:1, for different Reynolds number and Froude number: a) $Fr = 10^{-3}$ **b)** $Fr = 10^{-2}$ **c)** $Fr = 10^{-1}$ **d)** $Fr = 1$ **and e)** $Fr = 10$

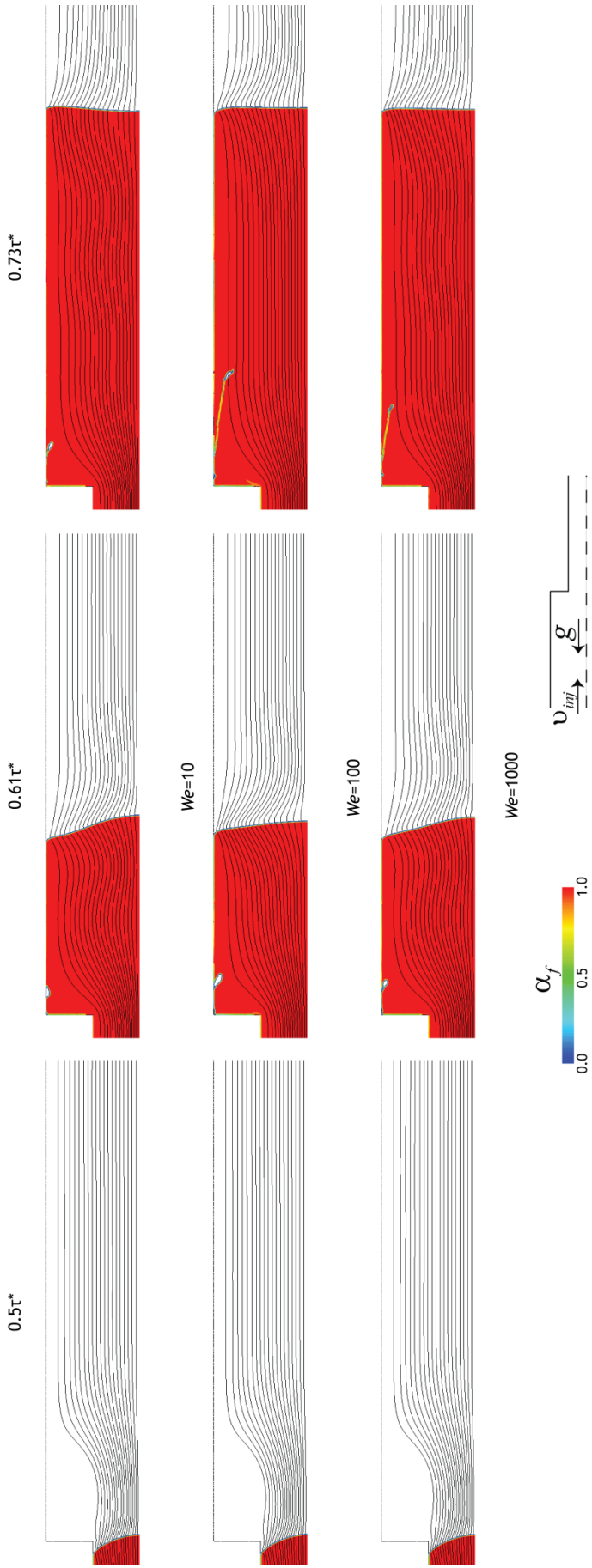

Figure 5-30 Flow front for flow expansion flow 1:2 for different *We* at $Fr=10^{-3}$ and *Re*=1, taken at different residence times. The red colour corresponds to the fluid phase, and colourless to the air phase.

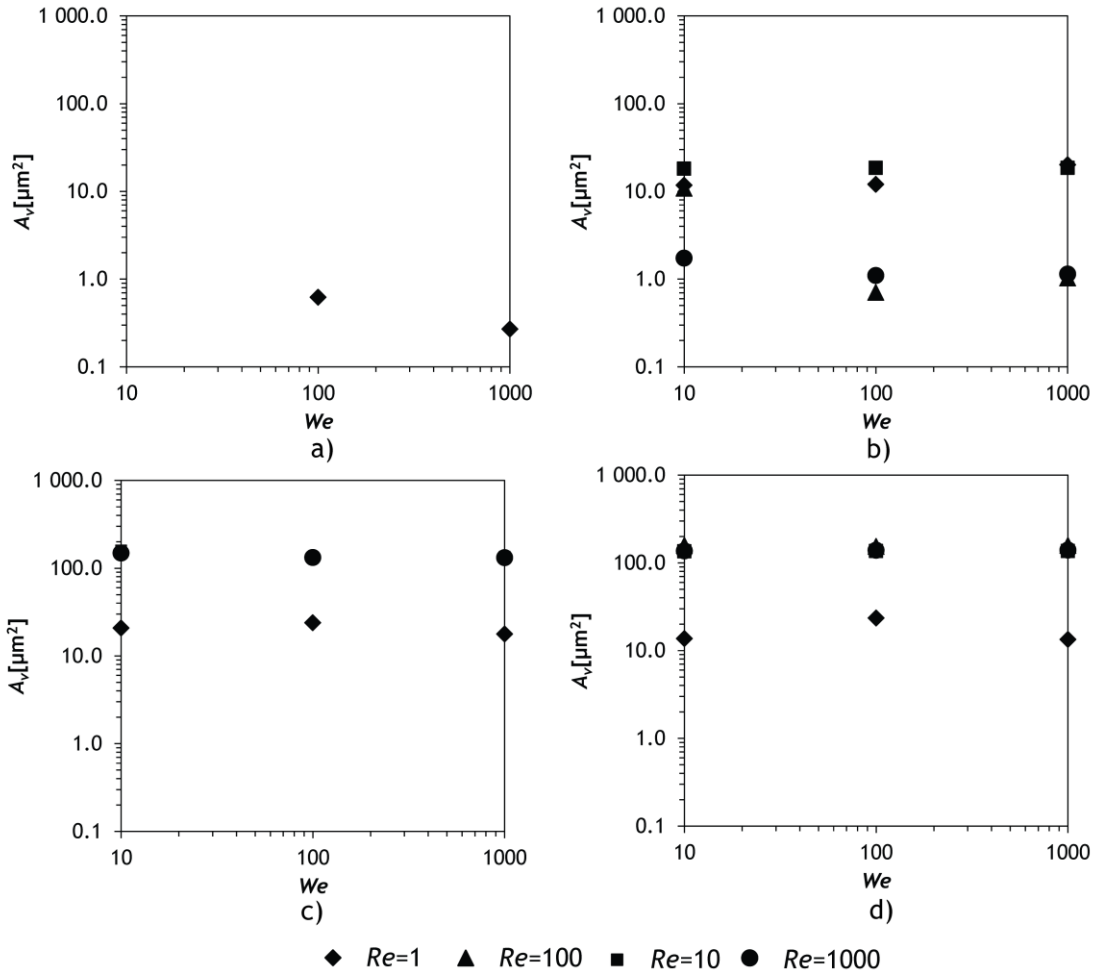

Figure 5-31 Effect of the Weber number on vortex area at expansion flow 1:2, for different Reynolds number and Froude number: a) $Fr = 10^{-2}$ **b)** $Fr = 10^{-1}$ **c)** $Fr = 1$ **and d)** $Fr = 10$

Considering the influence of gravitational forces for the different thickness ratios, it is noticed that the same flow front and the existence of air in salient corner are common phenomena along the increasing in the thickness ratio, as shown Figure 5-32. When the Fr number is increased, the air entrapment in the salient corner decreases, since the influence of the gravitational forces compared to the inertial forces is lower. An increase in air area in the salient corner with the rise of the thickness ratio was expected, due to the increasing difficulty to flow the same quantity of air through a narrow outlet; however, for the biggest thickness ratio, $10:1$, it is found that the air in the salient corner is less than in the $5:1$ thickness ratio. Here the increase of velocity of the flow towards the narrower channel may contribute to an increase on the dragging of air out of the channel.

Regarding the influence of the viscous forces, Figure 5-33 shows that for the range of Re studied, the flow front shape remains equal for all the thickness ratio values when $Re = 1$ and $Re = 10$. In addition there is always air stuck in the salient corner regardless of the

Reynolds number. When concerning to $Re = 100$, it is possible to observe that the flow front becomes very unstable, especially for the biggest thickness ratio studied. It is also observable that the area of air in the salient corner increases with the thickness ratio, but for the higher Re it decreases.

When looking at the surface forces, shown in Figure 5-34, it is possible to see that for $We = 10$ and $We = 100$ the flow front shape remains equal and also that the air area in the salient corner increases with the increase of the thickness ratio. The exception is for the $10:1$ where the air imprisonment is lower than the $5:1$. However, for the $10:1$ at $We = 1000$, the flow front becomes different from the other thickness ratio studied. As the figure shows the flow becomes unstable and there is more air in the corner than in the $5:1$ case, and in addition a gas boundary layer is formed.

For a laminar backward-facing step flow, Biswas et al. (2004) shows an increase in the air entrapment length with the increasing thickness ratio, similar to the observed in present work.

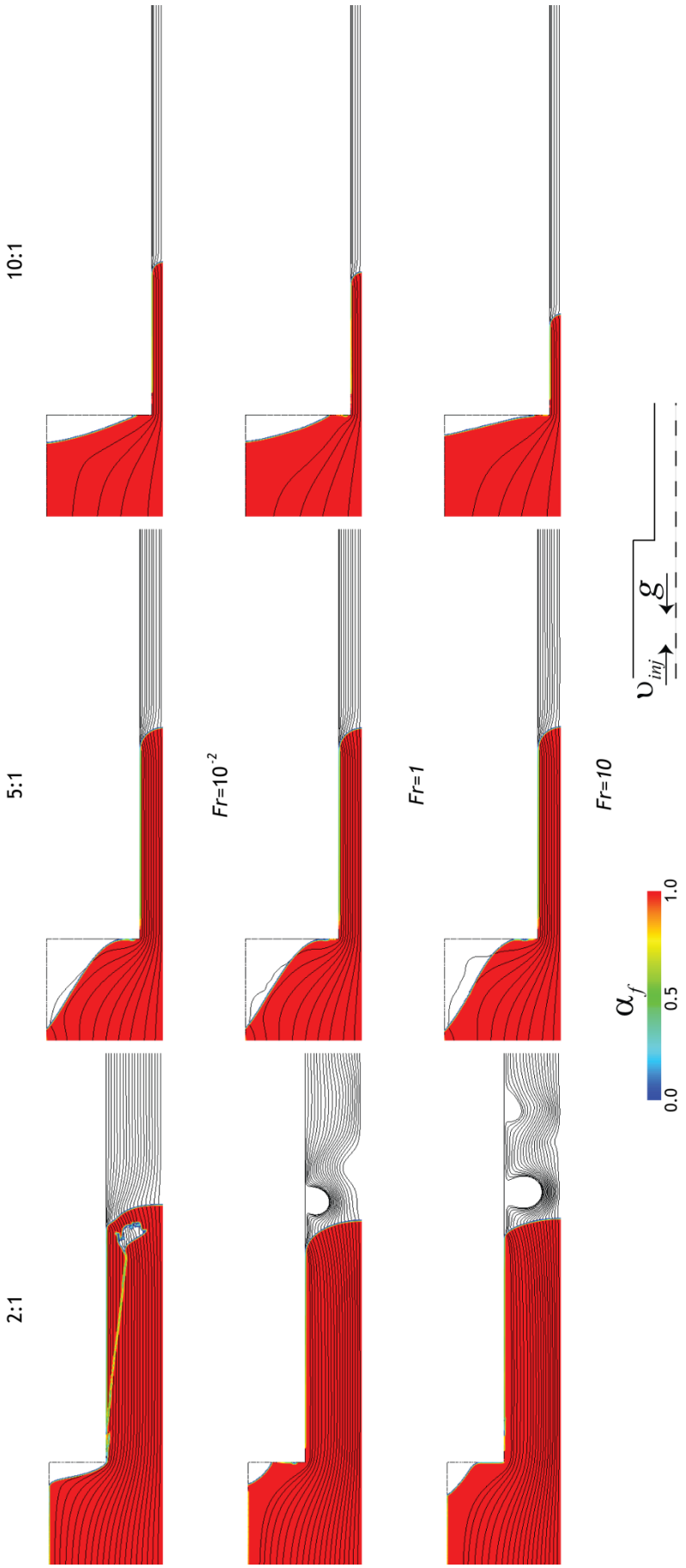

Figure 5-32 Flow front for flow contraction flow 2:1 for different *Fr* at *We*=10 and *Re*=1, taken at 0.73τ* and for different thickness ratio. The red colour corresponds to the fluid phase, and colourless to the air phase.

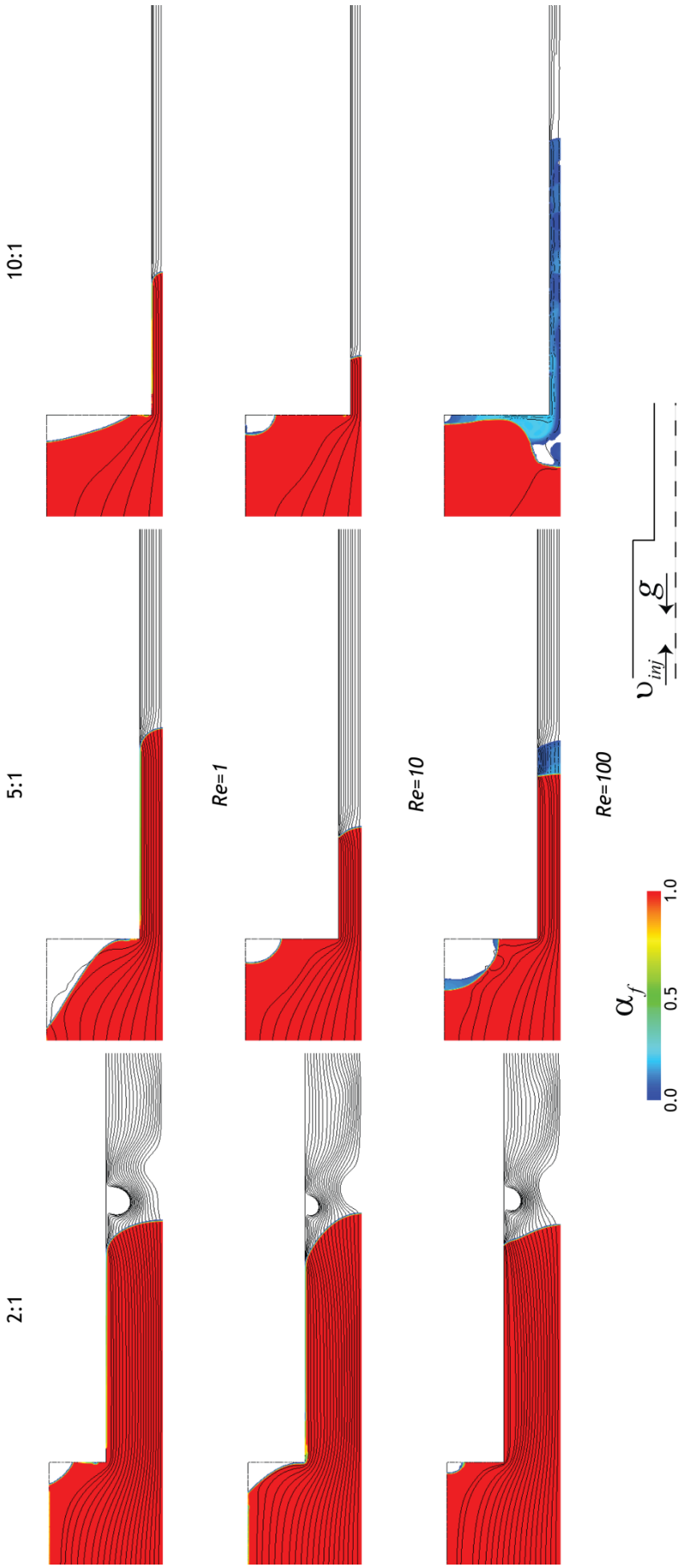

Figure 5-33 Flow front for flow contraction flow 2:1 for different *Re* at *We*=10 and *Fr*=1, taken at 0.73τ* and for different thickness ratio. The red colour corresponds to the fluid phase, and colourless to the air phase.

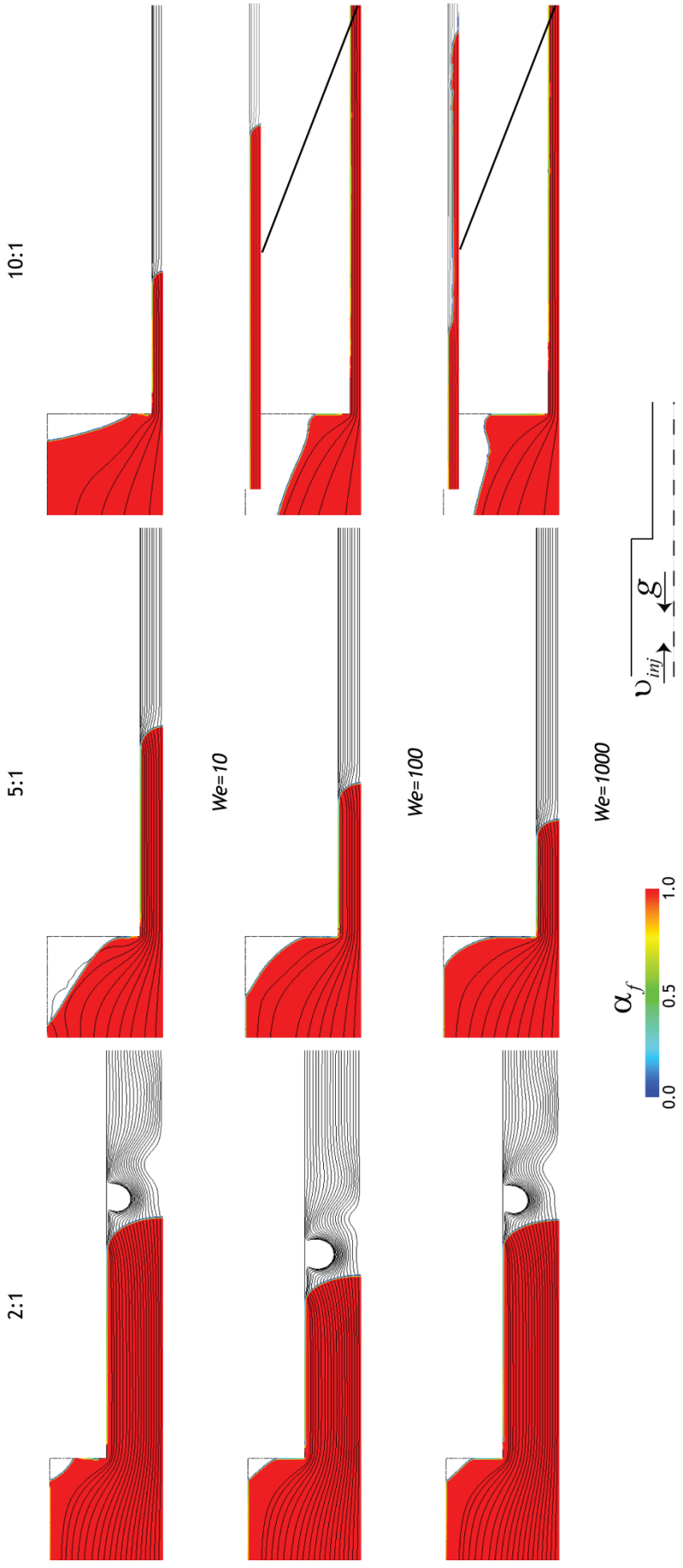

Figure 5-34 Flow front for flow contraction flow 2:1 for different *We* at *Re*=1 and *Fr*=1, taken at 0.73τ* and for different thickness ratio. The red colour corresponds to the fluid phase, and colourless to the air phase.

5.3.3.5 Velocity Field

The velocity profiles were taken at $0.73\tau^*$, along the symmetry axis of the contraction or expansion geometry. The velocity was normalized by υ_f. The abscissas axis from next figures are normalized by D_2 for contractions and D_1 for expansions, and the ranges are from two diameters before contraction or expansion until one diameter after. The contraction or expansion corresponds to $x/D_i = 0$. The upstream flow starts from $x/D_1 = -8.75$ for contractions and $x/D_2 = -4.375$ for expansions.

From Figure 5-35 it is clearly shown the expectable acceleration of the flow after the contraction. To avoid gas entrapment at the liquid/air interface it is of great interest to achieve a parallel streamline flow, i.e., a fully developed flow, however in the entrance of the contraction a boundary layer will be formed. The distance for the flow to evolve to a fully developed profile, denominated entrance length, is defined by (Langhaar, 1942) as

$$\frac{L}{D} = 0.058Re \qquad 5.27$$

where L is length and D is diameter. This relation sets the length of the influence of an obstacle as function of the Re, for lower Re the entrance length is smaller, e.g., for a $Re = 1$ $\frac{L}{D} = 0.058$, and for $Re = 1000$ is $\frac{L}{D} = 58$. Figure 5-35 shows the υ_x tends to a stable profile after a transient region where the flow is not fully developed, L'. Figure 5-35a and Figure 5-35b show that the upstream and downstream lengths for fully developed flow are smaller than the entrance length predicted from Equation 1.28, which thus probably have a security factor for the entrance length estimation. For higher Re, it is found that the length of the simulated channel is shorter than the minimal length to achieve a fully developed profile, and the velocity profiles show some instabilities, particularly for $Re = 1000$. However, it is not crucial to achieve a fully developed profile, since during the moulding, channel length could be shorter so the flow do not evolves until to a fully developed profile. The normalized velocity increases after the obstacle and later it decreases with the increase of the Re.

The Fr effect on L' it is not so clear as the Re effect. From Figure 5-35, it is possible to observe an increase in normalized x - velocity for a rise of Fr, however it is not possible to draw a tendency from the plots in Figure 5-35, since some normalized velocity curves

show some deviation from this trend, as for example the $Fr = 10^{-1}$ in Figure 5-35a and Figure 5-35d, and $Fr = 10$ in Figure 5-35a and Figure 5-35d.

Besides the importance on the part quality, the surface forces do not affect the velocity field, as shown in Figure 5-36, where within the range of We number studied no variation is noticed.

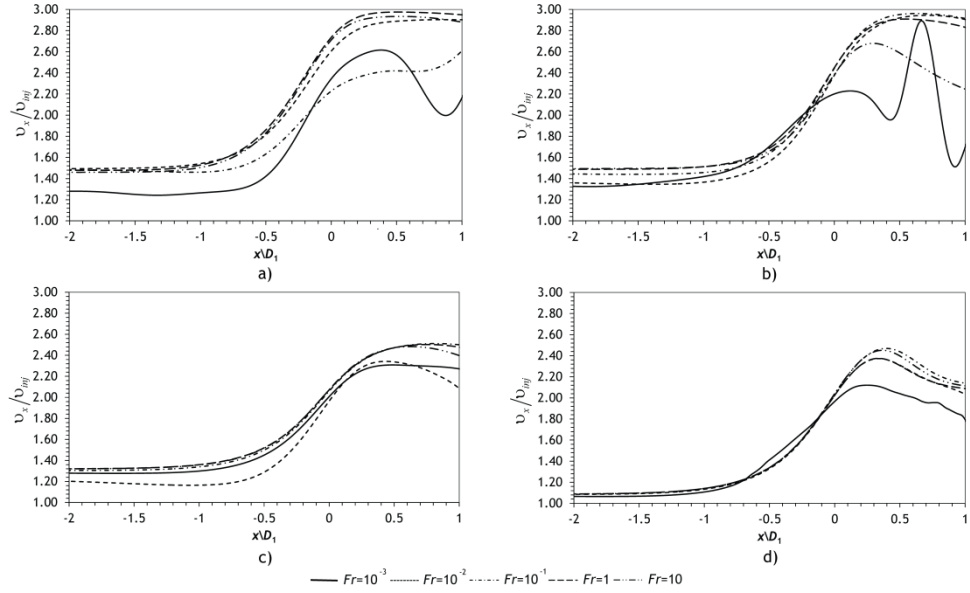

Figure 5-35 Normalized axial velocity along the symmetry line for contraction flow 2:1, for different Froude number for Weber $We = 10$ and Reynolds number: a) $Re = 1$ b) $Re = 10$ c) $Re = 100$ and d) $Re = 1000$

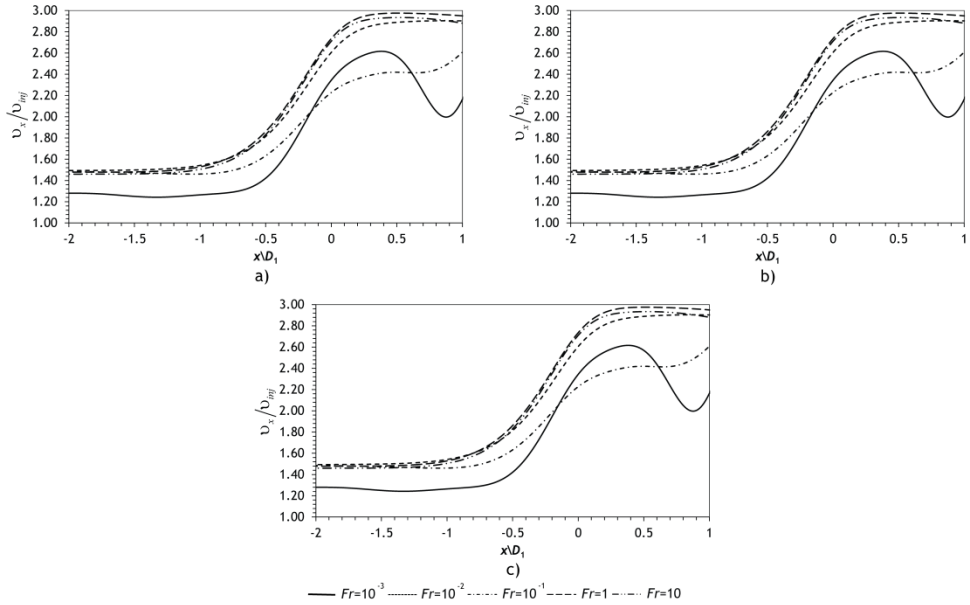

Figure 5-36 Normalized axial velocity along the symmetry line for contraction flow 2:1, for different Froude number, for Reynolds number $Re = 1$ and Weber number: a) $We = 10$ b) $We = 100$ and c) $We = 1000$

From Figure 5-37, it is shown the same entrance length phenomena for expansions. Contrarily to the contraction, for an expansion it is expected a deceleration, and for the lower Re, this is quite clear from Figure 5-36. As explained above, for the expansion there is a die swell of the flow, since it passes over a sheath of viscous flow. This sheath induces a recirculation flow region, and its length is proportional to the Re number (Acrivos and Schrader, 1982; Durst et al., 1974). As result, the flow velocity does not decrease with the expansion. This can cause bad parts with air being entrapped in the larger channel part that is not filled by the fluid.

The Fr decreases the normalized velocity, however, as for the contraction flow, this behaviour does not display a tendency since there are some exceptions.

Regarding the We number effect on the normalized velocity field, Figure 5-38, the flow shows only two cases where the Webber number clearly has an impact on υ_x profile: for $Fr=10^{-2}$ and $Fr=10$ from Figure 5-38a and Figure 5-38c, respectively.

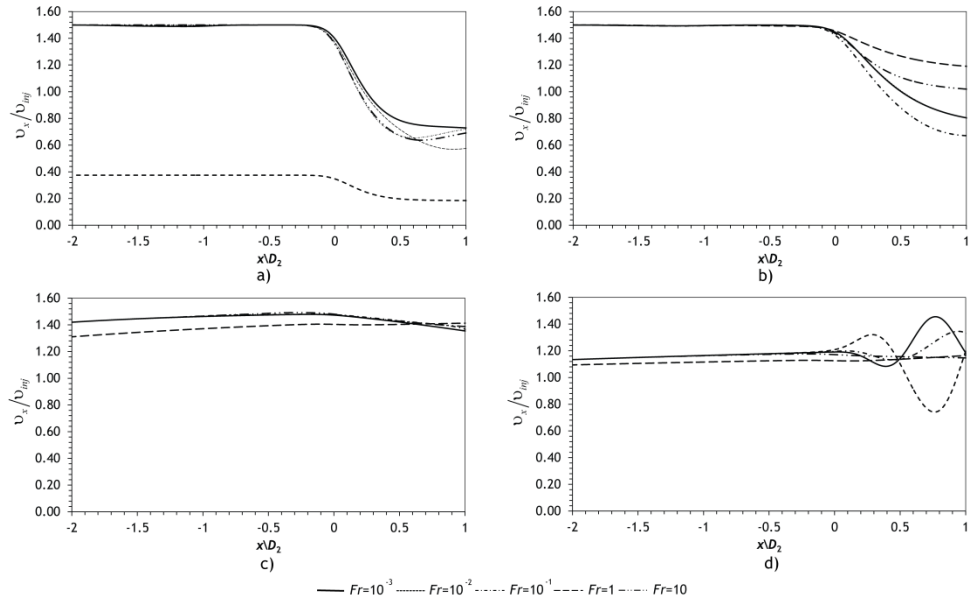

Figure 5-37 Normalized axial velocity along the symmetry line for expansion flow 1:2, for different Froude number for Weber $We=10$ and Reynolds number: a) $Re=1$ b) $Re=10$ c) $Re=100$ and d) $Re=1000$

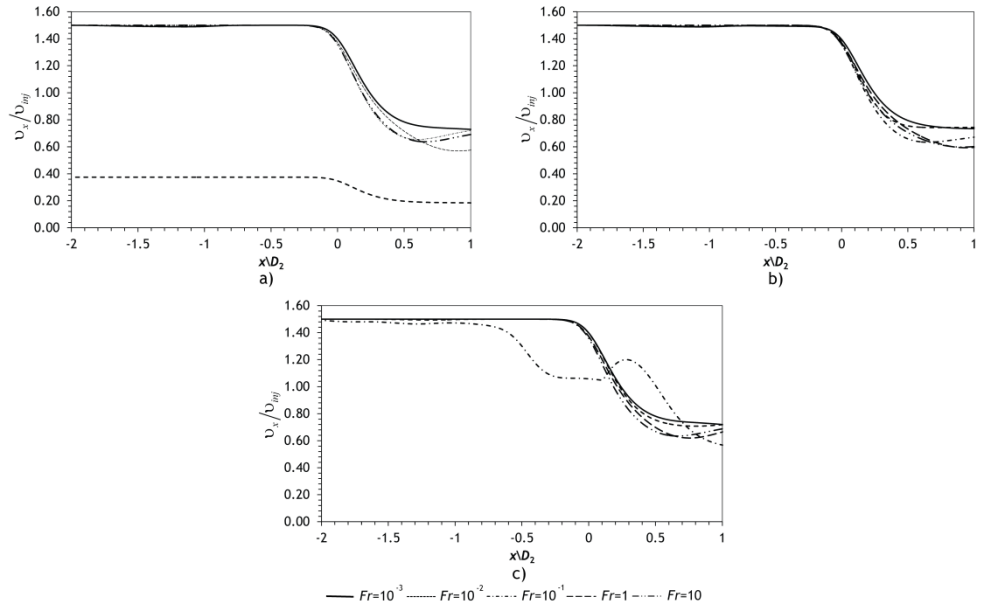

Figure 5-38 Normalized axial velocity along the symmetry line for expansion flow 1:2, for different Froude number for Reynolds number $Re=1$ and Weber number: a) $We=10$ b) $We=100$ and c) $We=1000$

5.3.3.6 Pressure drop

The effect of the previous fluid mechanics parameters on pressure drop along the contraction and expansion are studied in this section. This aims to help on the decision of the flow processing parameters, however the results present here cannot be used as universal guidelines, since each industrial part is unique. In this section, the pressure drop was considered between $\frac{x}{D_1}=-4.38$ to $\frac{x}{D_1}=0.50$, for the contraction and $\frac{x}{D_2}=-2.19$ to $\frac{x}{D_2}=0.25$ for the expansion, and is calculated as (Sousa et al., 2009)

$$\Delta p=\Delta p_{us}+\Delta p_{ds}+\Delta p_{e} \qquad 5.28$$

where the index us is upstream, ds is downstream and e is extra.

The upstream and downstream pressure losses are defined by Bernoulli Equation as (Shames, 1992)

$$\Delta p_i=\frac{\rho \upsilon_2^{\,2}}{2}\left(\frac{D_2}{D_1}-1\right)^2+\rho g\left(z_1-z_2\right)-\frac{32\mu\upsilon_i L}{D_i^2} \qquad 5.29$$

where the index i is substituted by u, for the upstream flow or by d for downstream flow, z is the *cota* of the section and L is the length of the section. For the present case the dynamic pressure and potential energy variation are null, since for upstream or downstream section the diameter remains constant.

The Δp_e arises from the *Bernoulli effect*, which corresponds to an effect in mean velocity due to the abrupt change of flow section, and is solely a function of expansion ratio (Biswas et al., 2004). The extra pressure drop due to acceleration of the flow, is a reversible loss of pressure, induced by the contraction and is usually associated with vortex enhancement. For a contraction, where this loss of static pressure cannot be neglected, the minor losses can be computed from the Borda-Carnot equation derived from Bernoulli equation for and defined as (Oertel, 2010)

$$\Delta p_e = \frac{\rho \upsilon_2^{\,2}}{2}\left(\frac{D_2}{\kappa D_1} - 1\right)^2 \qquad 5.30$$

where the υ_2 is taken downstream the contraction, and the κ is the contraction coefficient, which from Weisbach experiments is (Oertel, 2010)

$$\kappa = 0.63 + 0.37\left(\frac{A_2}{A_1}\right)^3 \qquad 5.31$$

Figure 5-39 shows the evolution of the pressure drop with the Fr number, where with Fr increase, there is an increase in Δp, with same tendency for all Re number. The influence of Fr on Δp can be expressed by

$$\Delta p = aFr^b \qquad 5.32$$

The values of leading coefficient and exponential for Equation 5.32 are in Table 5-8. For a Poiseuille flow, with a parallel and laminar flow, Δp would be proportional to Fr, however from Table 5-8 it is possible to observe that b coefficients are smaller than one. In the present case there is a secondary flow from the vortex trapped in the closed corner, and so the headloss is not varying directly with Fr. Since the Fr number was varied by increasing velocity, the Δp_i does not remain constant with velocity.

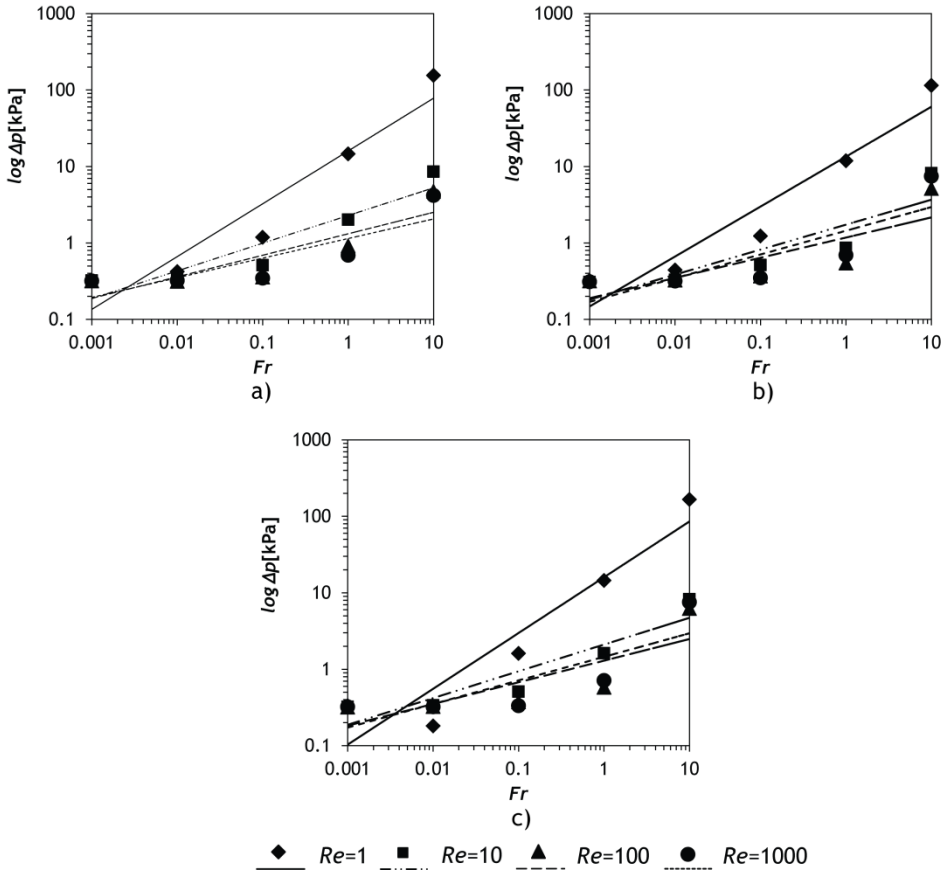

Figure 5-39 Pressure drop vs. Froude number for contraction flow 2:1, at different Reynolds number and Weber number: a) $We=10$ **b)** $We=100$ **and c)** $We=1000$

Table 5-8 Leading coefficient and exponential values for Fr **number dependency in** $2:1$ **contraction flow.**

We	*Re*	*a*	*b*
1	1	15969	0.690
	10	2288	0.362
	100	1319	0.281
	1000	1143	0.256
10	1	13465	0.653
	10	1736	0.327
	100	1177	0.264
	1000	1446	0.310
100	1	15996	0.730
	10	2108	0.350
	100	1296	0.283
	1000	1455	0.308

When the Re number increases, as can be observed from Figure 5-40, the pressure drop decreases, mainly the extra pressure drop. This decrease is more evident, i.e., has a steeper decay for the larger Fr number values studied. For different We number values, a similar behaviour is found. The dependency of Δp on Re number can be described by

$$\Delta p = aRe^{b} \qquad 5.33$$

The values for the leading coefficient and exponential for Equation 5.33 are present in Table 5-9. If one recalls Figure 5-25, the area of air also decreases as the extra pressure drop decreases, it is found that the pressure drop is affected by vortex enhancement, where the Re number plays a key role. The Re number was varied by lowering the viscosity, if the only effect of increasing Re was the decrease of viscous stress from the walls de Δp would be proportional to $1/Re$ and b coefficient in Table 5-9 would be around -1. This would be the case of Poiseuille flow, where flow is laminar, and parallel without secondary flow. In the present case there is a secondary flow from the vortex trapped in the closed corner, and so the headloss is not varying directly with $1/Re$. From Figure 5-40 it is seen that the major impact of Re on Δp is from $Re=1$ to $Re=10$, and then the impact of Re is diminished, probably due to the fact that the decrease on viscous forces is compensated by an increase in the corner vortex dissipation.

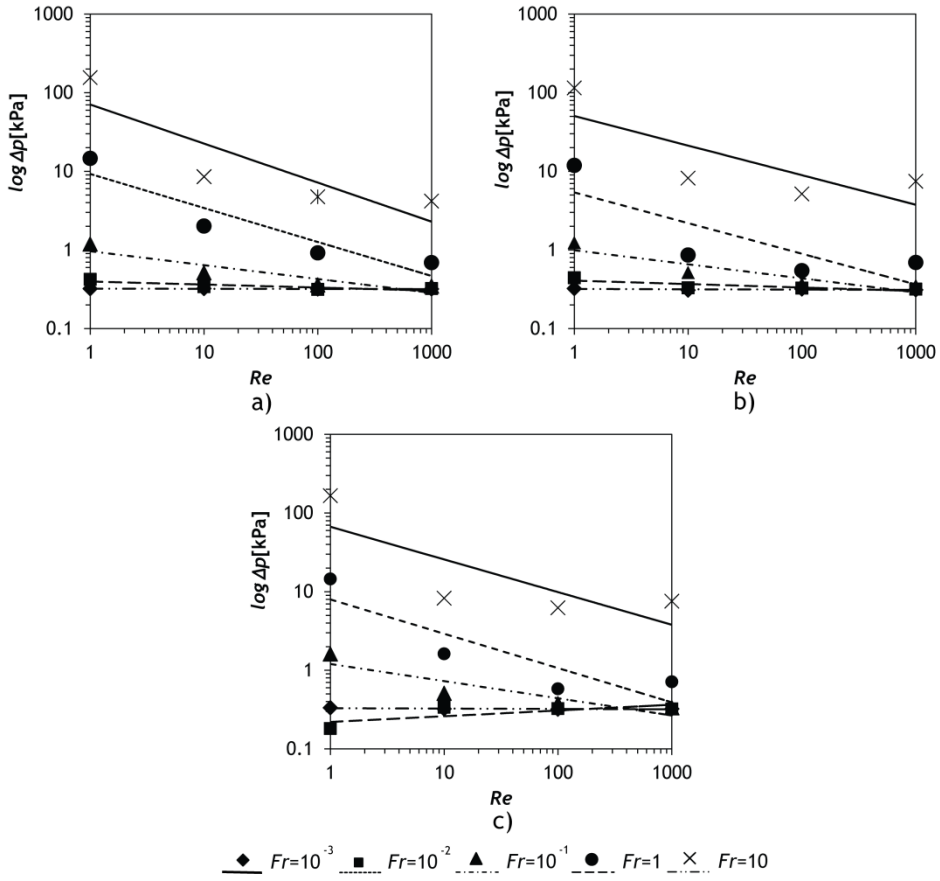

Figure 5-40 Pressure drop vs. Reynolds number for contraction flow 2:1, at different Froude number and Weber number: a) $We=10$ **b)** $We=100$ **and c)** $We=1000$

Table 5-9 Leading coefficient and exponential values for Re number dependency in $2:1$ contraction flow.

We	Fr	a	b
1	10^{-3}	322	–0.002
	10^{-2}	397	–0.039
	10^{-1}	961	–0.176
	1	9255	–0.432
	10	70785	–0.497
10	10^{-3}	319	–0.003
	10^{-2}	407	–0.044
	10^{-1}	990	–0.178
	1	5397	–0.390
	10	50563	–0.376
100	10^{-3}	220	0.0732
	10^{-2}	330	–0.005
	10^{-1}	1205	–0.219
	1	7966	–0.436
	10	66907	–0.415

From the previous figures, it is seen that We number does not have influence on Δp. However, Figure 5-41 shows a closer look to the influence of the surface tensions on Δp. For Fr number below the $Fr < 1$, it is shown that the variton on We number does not affect significatilly the Δp . These can be also shown from

$$\Delta p = aWe^{b} \qquad 5.34$$

The values of leading coefficients and exponential from the fitting of CFD data to Equation 5.34 are in Table 5-10. The coefficients are quite similar and the b values are significantly lower than those for the Re and Fr, due to the small slope along We number variation. So the We number, i.e. the surface tension plays a smaller role in the headloss when compared to viscous, intertial and body forces.

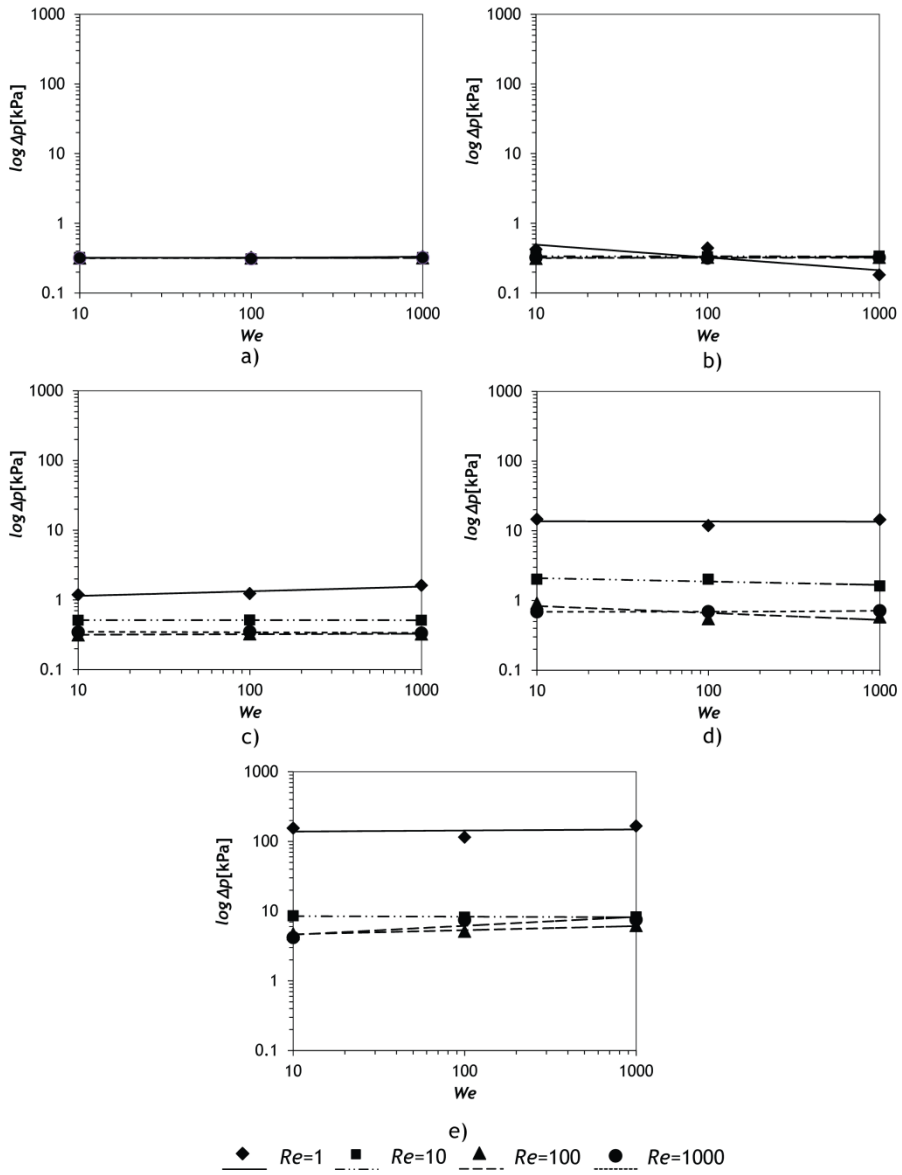

Figure 5-41 Pressure drop vs. Weber number for contraction flow 2:1, at different Reynolds number and Froude number: a) $Fr = 10^{-3}$ **b)** $Fr = 10^{-2}$ **c)** $Fr = 10^{-1}$ **d)** $Fr = 1$ **and e)** $Fr = 10$

Table 5-10 Leading coefficient and exponential values for We number dependency in $2:1$ contraction flow.

Fr	Re	a	b
10^{-3}	1	314	0.008
	10	317	5×10^{-5}
	100	318	4×10^{-4}
	1000	314	0.002
10^{-2}	1	753	–0.183
	10	338	–0.001
	100	312	0.0072
	1000	321	3×10^{-5}
10^{-1}	1	978	0.067
	10	512	-9×10^{-5}
	100	312	0.007
	1000	355	–0.008
1	1	13756	–0.002
	10	2339	–0.048
	100	1048	–0.099
	1000	673	0.008
10	1	133919	0.015
	10	8631	–0.008
	100	4074	0.059

For the expansion flow, the flow will also have an extra pressure drop. The Borda-Carnot equation for an abrupt expansion can be defined as (Oertel, 2010)

$$\Delta p_e = \frac{\rho v_1^2 \varsigma}{2}\left(1-\frac{D_1}{D_2}\right)^2 \qquad 5.35$$

here ς is the empirical loss coefficient and for sudden expansions is equal to 1.

Similarly to the contraction, the gravitational forces play an important role in Δp over an expansion, as shown in Figure 5-42. From this figure, it is observed that increasing the Fr number the Δp also increases, and this tendency is more pronounced for lower Re numbers. This is further seen from the leading coefficient and exponential values from Table 5-11, which were obtained by fitting CFD data in Figure 5-41 to Equation 5.32. Although it is not possible to isolate the Δp_e, from the Δp_t, since the Froude number is only varied by increasing the inertial forces. So the variation of Δp_e with Fr should be small, and the greater contribution to Δp should come from the increase in *cota*, gz, and thus the b coefficient in Equation 1.33 should be closer to 1, because $p \propto Fr$, which is the case at Re values close to 1.

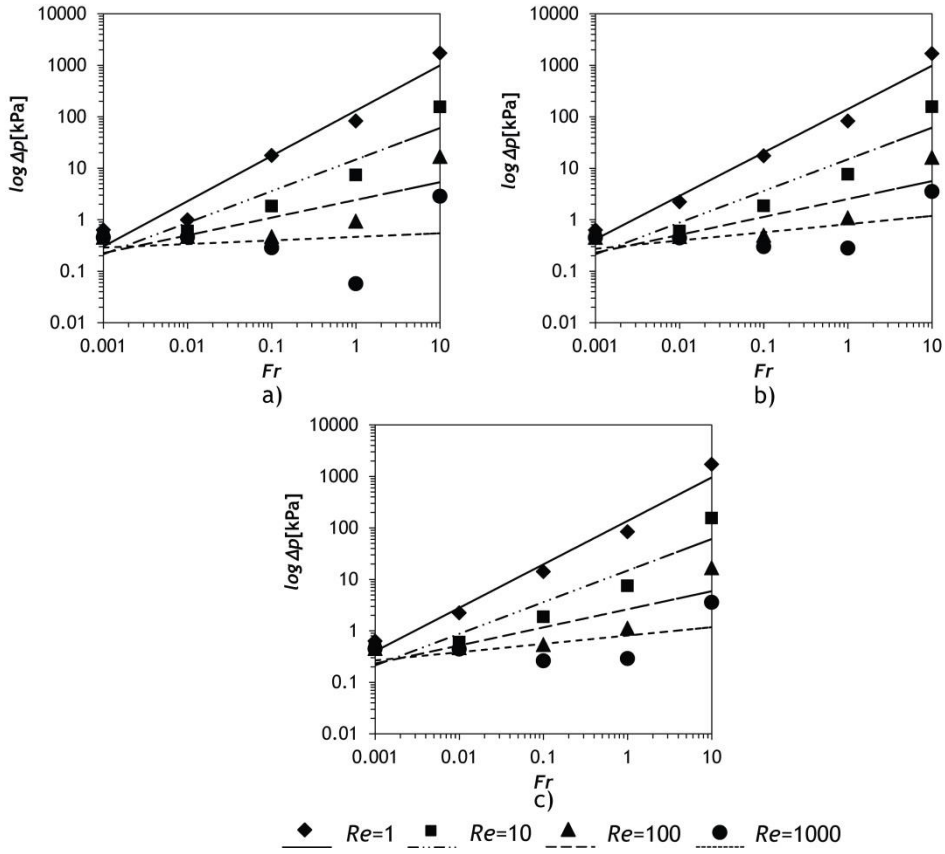

Figure 5-42 Pressure drop vs Froude number for expansion flow 1:2, at different Reynolds number and Weber number: a) $We=10$ b) $We=100$ and c) $We=1000$

Table 5-11 Leading coefficient and exponential values for Fr number dependency in $2:1$ expansion flow.

We	*Re*	*a*	*b*
1	1	131372	0.879
	10	14725	0.3613
	100	2424	0.342
	1000	465	0.070
10	1	141095	0.843
	10	14931	0.615
	100	2530	0.347
	1000	822	0.160
100	1	136943	0.844
	10	14836	0.613
	100	2628	0.351
	1000	812	0.161

Regarding the Re number influence shown in Figure 5-43, it is possible to observe a decrease in Δp for rising values of the Re number, a tendency that it is not affected by the We number. The effect of Re on Δp is also seen from the values of the leading and exponential coefficient obtained from CFD data fitting to Equation 5.33 that are shown Table 5-12. Similar to contraction, the Δp is not proportional to $1/Re$ and b coefficient in Table 5-12 are different than -1, indicating a secondary flow from salient corner vortex dissipation.

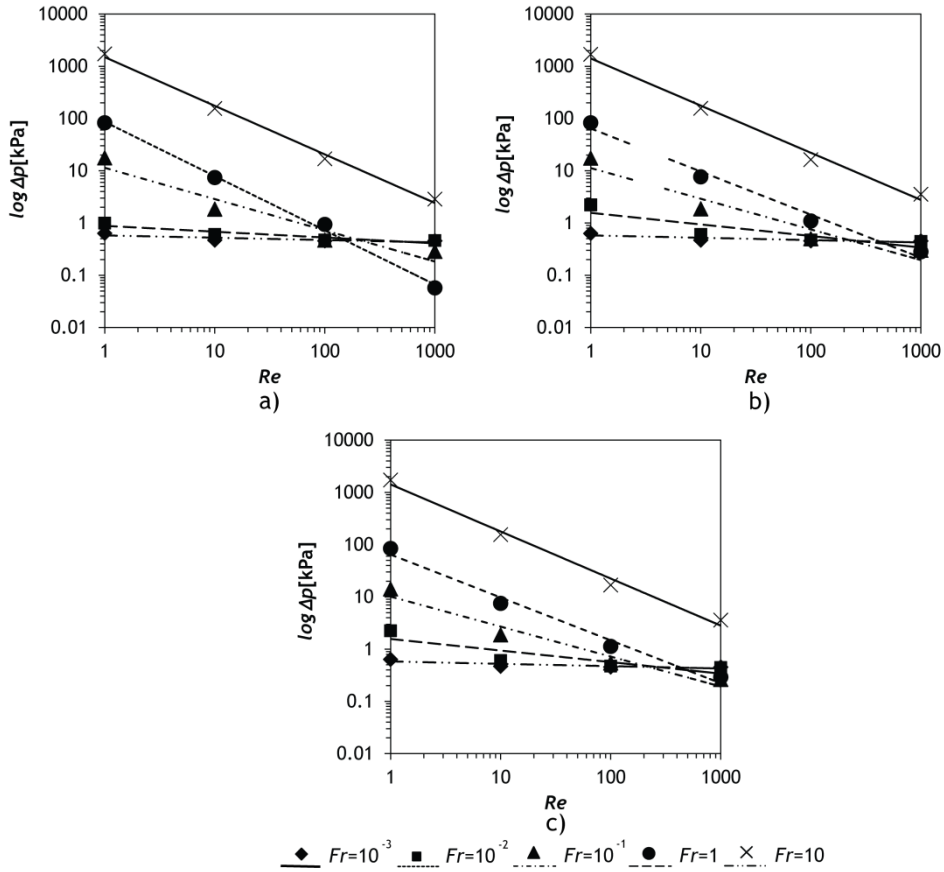

Figure 5-43 Pressure drop vs Reynolds number for expansion flow 1:2, at different Froude number and Weber number: a) $We=10$ b) $We=100$ and c) $We=1000$

Table 5-12 Leading coefficient and exponential values for Re number dependency in $2:1$ expansion flow.

We	Fr	a	b
1	10^{-3}	581	–0.045
	10^{-2}	881	–0.111
	10^{-1}	11378	–0.598
	1	86009	–1.037
	10	1×10^{6}	–0.930
10	10^{-3}	579	–0.045
	10^{-2}	1562	–0.221
	10^{-1}	11247	–0.587
	1	64404	–0.824
	10	1×10^{6}	–0.902
100	10^{-3}	581	–0.045
	10^{-2}	1570	–0.222
	10^{-1}	10093	–0.573
	1	64611	–0.821
	10	1×10^{6}	–0.900

When the fluid flow is passing through a contraction, or through an expansion, the surface forces (i.e., the We number) show very small influence over Δp. This can be observed from Figure 5-44, that shows a similar behaviour to the plots drawn from the contraction

case, Figure 5-41. However, for expansion case the Re number has a larger impact on Δp when $Fr > 10^{-2}$. The influence of We number can be assessed clearly by fitting the CFD data to Equation 5.34. The values of the exponential coefficient, see Table 5-13, are always much smaller than one and very close to zero, which is clear evidence that the We has very small impact on Δp.

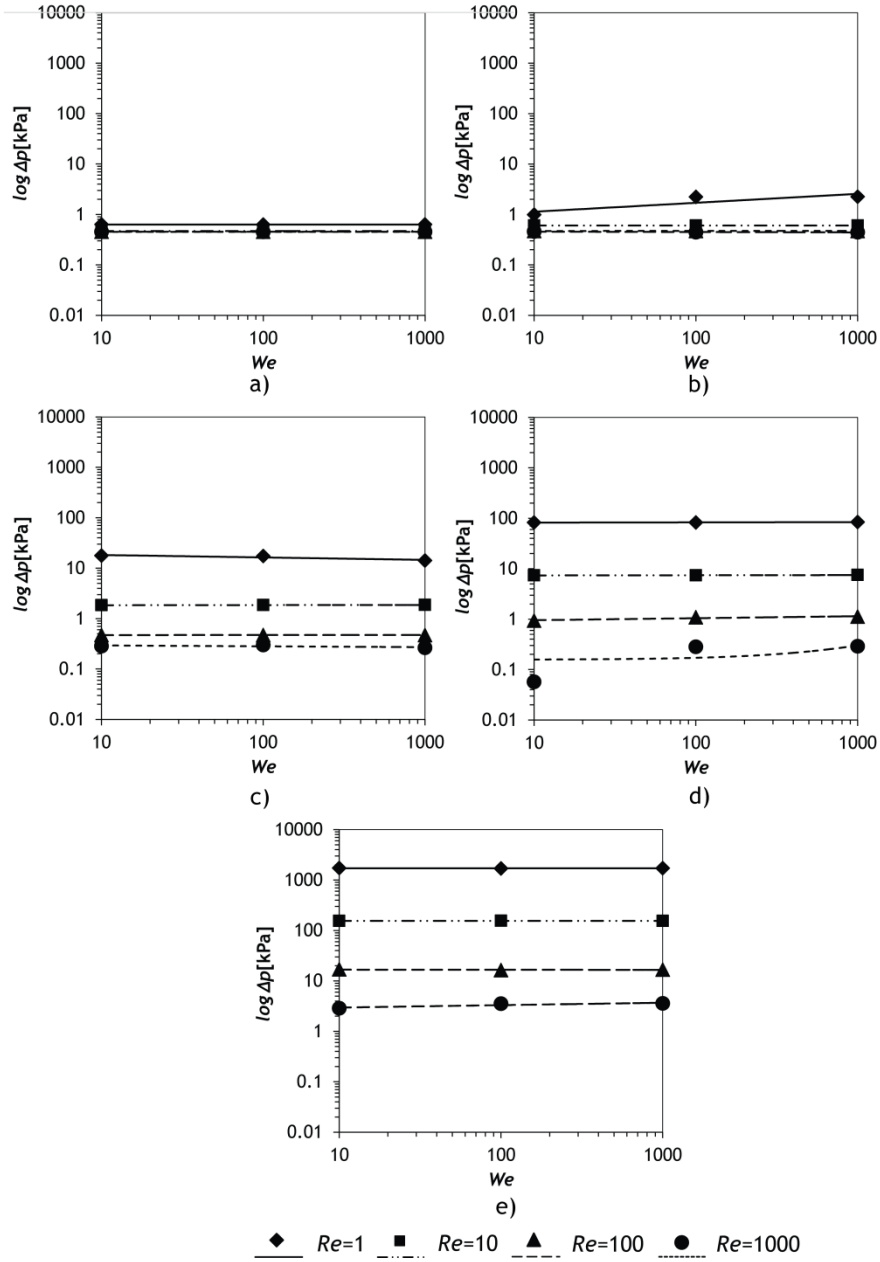

Figure 5-44 Pressure drop vs. Weber number for expansion flow 1:2, at different Reynolds number and Froude number: a) $Fr = 10^{-3}$ **b)** $Fr = 10^{-2}$ **c)** $Fr = 10^{-1}$ **d)** $Fr = 1$ **and e)** $Fr = 10$

Table 5-13 Leading coefficient and exponential values for We number dependency in $2:1$ expansion flow.

We	*Re*	*a*	*b*
10^{-3}	1	633	3×10^{-5}
	10	468	2×10^{-4}
	100	455	-2×10^{-5}
	1000	454	-6×10^{-4}
10^{-2}	1	755	0.177
	10	605	-6×10^{-5}
	100	471	2×10^{-4}
	1000	464	−0.007
10^{-1}	1	20411	−0.048
	10	1831	0.003
	100	471	2×10^{-4}
	1000	305	−0.017
1	1	81348	0.005
	10	7319	0.003
	100	871	0.040
	1000	33	0.353
10	1	2×10^{6}	-9×10^{-4}
	10	155226	-2×10^{-5}
	100	16819	−0.002
	1000	2650	0.048

5.3.4 Flow pattern maps

Previous sections studied the different phenomena that, due to the flow conditions occur in the flow during mould filling. Based on the obtained results, different phenomena can be associated with the quality of final parts. Also an assessment of the flow evolution during the mould filling can be done, which can aid mould designers on developing the best design solution. Based on the different dimensionless numbers studied, Re, Fr and We, several flow maps were constructed.

Four different flow phenomena are identified and each phenomenon is represented by a primary color, as shown in Table 5-14. Primary CMYK color model is used, the intersection of colors represents a flow field with two or more phenomena. Figure 5-45 shows the possible combinations and resulting colours. For example, if the flow conditions have a stable flow front and gas engulfment, the interception of these conditions originates an orange color, as shown in Figure 5-45a. Figure 5-45b shows all the combinations with the Air Entrapped at the Corner color combined with all the other colors and their respective combinations.

Table 5-14 Examples of flow pattern and corresponding color

Phenomena	Image	Corresponding color
Stable front	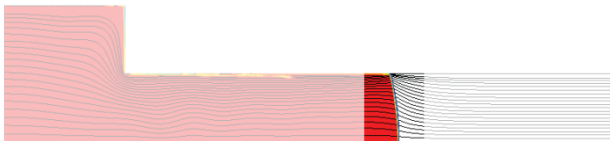	
Air entrapped at the salient corner	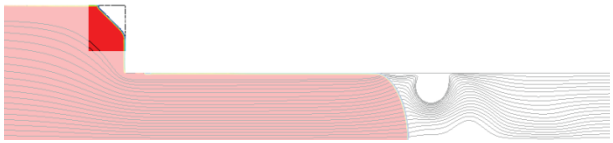	
Air entrapment and engulfment	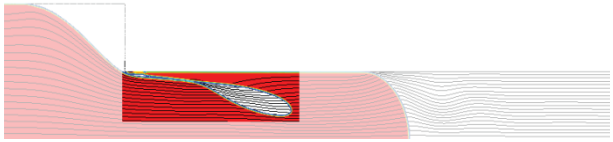	
Air boundary layer	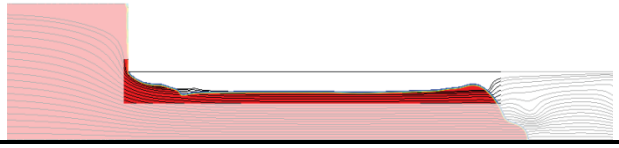	

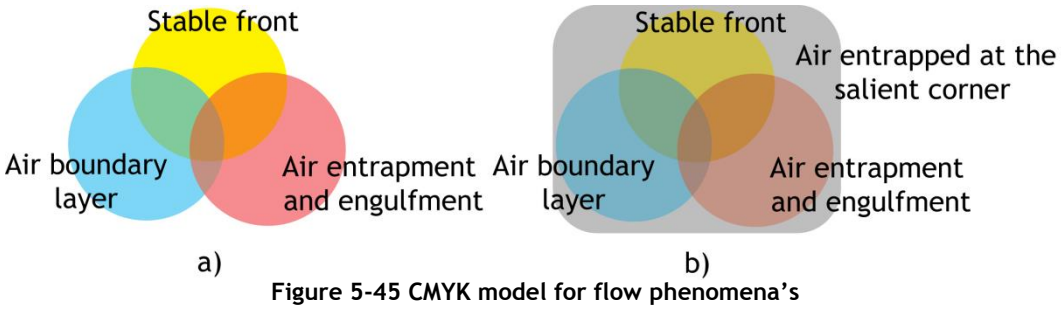

Figure 5-45 CMYK model for flow phenomena's

In Figure 5-46 to Figure 5-49 are shown the different flow phenomena colour maps for the studied Re range, for $Tr=2$. From the figures it is possible to see that only a small region, yellow colour strip in Figure 5-48, enables a perfect flawless injection, with a stable front and without flow front instabilities. However, depending on the polymer formulation and part application, this region could be bigger. For example, for foam formulations, the superficial quality is not a requirement, and presence of air and gas engulfment do not represent any considerable defect.

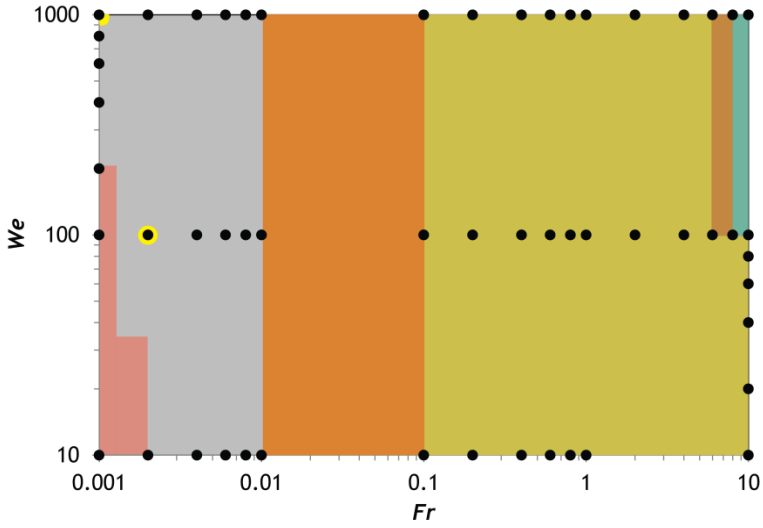

Figure 5-46 Flow pattern map for $Re=1$ and $Tr=2$

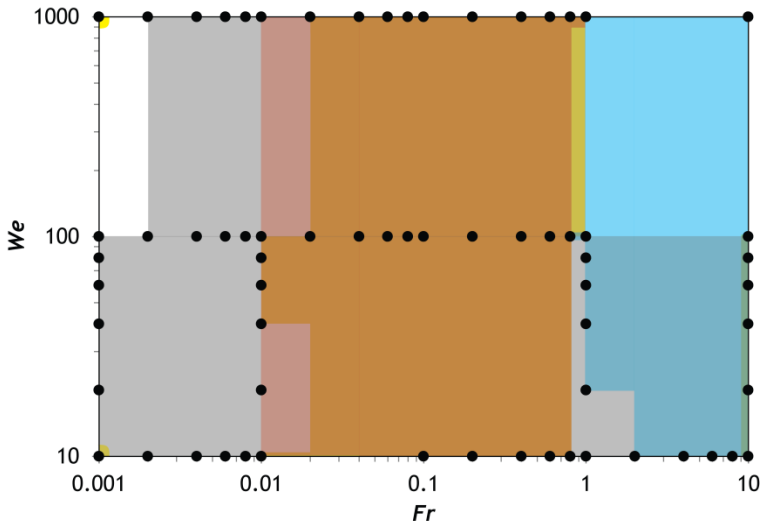

Figure 5-47 Flow pattern map for $Re=10$ and $Tr=2$

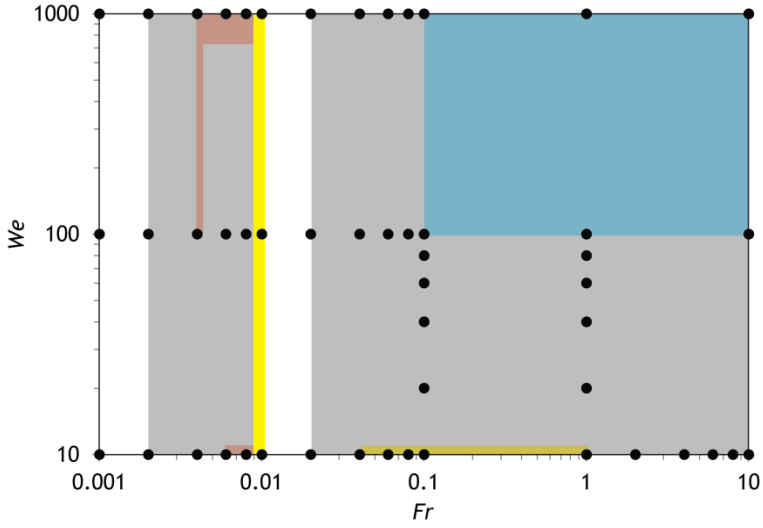

Figure 5-48 Flow pattern map for $Re=100$ and $Tr=2$

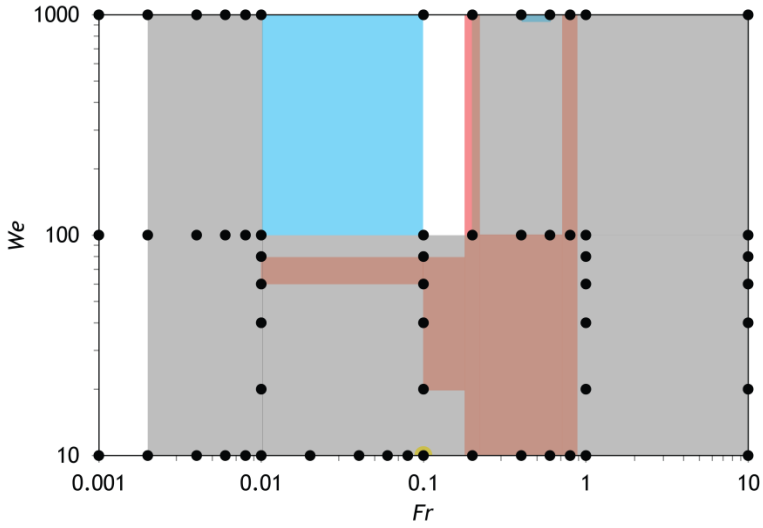

Figure 5-49 Flow pattern map for $Re=1000$ and $Tr=2$

5.4 Mould project recommendations

In the literature review in Section 2.4, are shown rules for the mould project. However, these rules are mainly based on empirical knowledge of RIM moulders or from raw materials producer's recommendations.

Nevertheless the importance of the rules present in the literature review, no scientific study was made concerning the mould cavity project itself, namely regarding the particularities of mould filling in RIM. The CFD results from the previous sections are the starting point for an insight into the mould cavity project, which was the basis for the set of rules that are introduced next, covering mould design, mould filling and heating system for curing.

5.4.1 Mould project

In RIM, the pressure values during the mould filling process are typically low, orders of magnitude below the Thermoplastics Injection Moulding, and so a wider range of mould materials can be used. It is also possible to set smaller thickness of the mould cavity and core when compared with TIM. A common procedure in RIM is to define the cavity and core thickness based on empirical knowledge, oversizing the thickness with all the material cost associated.

For a better design and reduction of material cost, the thickness of the cavity and core are designed according to the injection pressure during filling. For this it is important to know the complex set of forces that actuate over the mould.

During the injection in RIM the mould is exposed to mechanical loading, however it is allowed to deform in the elastic region, to avoid the permanent damage on the structure and dimensional deviations, that could originate plastic defects.

The complex configurations can make injection moulding statically indeterminated (Menges and Mohren, 1996). Since only elastic deformations can be allowed, the mould can be considered into separated elements and modeled as a set of springs. The whole system is computed as a set of springs that can be coupled in series or parallel.

The forces found during the injection are:

- Clamping forces
- Injection forces
- Ejection forces.

The clamping forces maintain the mould closed, and are compressive forces. During the injection, the compression is almost canceled by the clamp force, however a certain amount of compressive force should be maintained above the injection pressure, otherwise the mould could open and material could leak creating parts that need further post-operations or even part defects.

As the deformations are smaller, order of μm, a static analysis is sufficient, and a simpler model is proposed to determine the deformation (Menges and Mohren, 1996).

The forces acting in a mould plate are the sum of bending and shear forces, where the admissible displacement, f, can be calculated by

$$f = f_{bd} + f_{sh} \qquad 5.36$$

where the indices bd and sh are for bending and shear, respectively.

Considering that all deformations must occur in elastic regime and using the Hooke law applied to the bending,

$$\sigma_{bd} = E_i \varepsilon_{bd} \qquad 5.37$$

where σ_{bd} is the mould material strength, E_i is the Young modulus and ε_{bd} is the bending strain. According ISO 178 (ISO, 2003), bending strain, ε_{bd}, and strength, σ_{bd}, can be considered as

$$\varepsilon_{bd} = \frac{6 f_{bd} t_h}{L^2} \qquad 5.38$$

$$\sigma_{bd} = \frac{3F_{inj} L}{2bt_h{}^2} \qquad 5.39$$

where the plate thickness, length and width are t_h, L and b, respectively and F_{inj} is the injection force, defined by

$$F_{inj} = p_{inj} A_{inj} \qquad 5.40$$

where p_{inj} is the injection pressure and A_{inj} is the projected area of the injected part. The projected area can be defined by

$$A_{inj} = bL \qquad 5.41$$

Substituting Equation 5.41 into 5.40, and into 5.39, the bending strength becomes

$$\sigma_{bd} = \frac{3p_{inj} L^2}{2t_h{}^2} \qquad 5.42$$

Considering previous Equation 5.42 and Equation 5.38 and Hooke's law, the bending displacement becomes

$$f_{bd} = \frac{3p_{inj} L^4}{12Et_h{}^3} \qquad 5.43$$

For shear forces, the displacement can be considered as

$$f_{sh} = \varepsilon t_{h_0} \qquad 5.44$$

where t_{h_0} is the initial thickness.

From Hooke's law the strain can be defined as

$$\varepsilon = \frac{p}{AE} \qquad 5.45$$

where p is the pressure, A the cross-section area and E is young modulus.

Using Equations 5.44 and 5.45, the displacement from shear results

$$f_{sh} = \frac{p_{inj}}{A_s E} \qquad 5.46$$

where A_s is the section area of the plate and can be defined as

$$A_s = bt_h \qquad 5.47$$

Replacing Equations 5.40, 5.41 and 5.47 into 5.46, shear displacement becomes

$$f_{sh} = \frac{p_{inj} L^2}{Et_h} \qquad 5.48$$

Replacing Equation 5.43 and Equation 5.48 into Equation 5.36, the admissible displacement for each plate can be expressed as

$$f = \frac{3p_{inj} L^4}{12E_i t_h^{\,3}} + \frac{p_{inj} L^2}{Et_h} \qquad 5.49$$

Therefore, the admissible displacement can be defined as

$$f \geq S_w \qquad 5.50$$

where S_w is the thickness shrinkage. Depending on the raw material, the usual listed data shrinkage is related with length dimensions, S_L. The relation between S_L and S_w, should be

$$S_w \sim (3 \text{ to } 9) S_L \qquad 5.51$$

Considering the Rencast FC52, from the datasheet the linear shrinkage, S_L, is $S_L = 5\times10^{-2}\%$. The admissible displacement, f, can be calculated as $f = 1\times10^{-1}\%$. Considering the calculations for $L = 1\text{m}$ and a part thickness of 10^{-3}m the f_s is $f = 10^{-4}\text{m}$. Considering an injection pressure of $p_{inj} = 10\text{bar}$, which is a considerably high pressure for RIM injection, and a mould made of steel with $E = 210\text{GPa}$ and using the EXCEL Solver, the thickness is $t_h = 25\times10^{-3}\text{m}$. For example, considering an injection with same conditions but for a $p_{inj} = 100\text{bar}$, which are the typical values for TIM, the thickness gives $t_h = 55\times10^{-3}\text{m}$. Using the same material for moulds, a reduction of 65% is obtained considering RIM conditions.

5.4.2 Filling stage

Mould filling is a process where the flow is driven by the pressure gradients across the mould cavity. Pressure driven flow are generally named Poiseuille flow, and can be described by the following governing equations (White, 2006)

$$\frac{\partial \upsilon_x}{\partial x} = 0 \qquad 5.52$$

$$0 = -\frac{\partial p}{\partial x} + \mu\left(\frac{\partial^2 \upsilon_x}{\partial y^2} + \frac{\partial^2 \upsilon_x}{\partial z^2}\right) \qquad 5.53$$

Equation 5.53 indicates that the pressure drop only varies in the x direction and originates the Poisson equation defined by

$$\frac{\partial^2 \upsilon_x}{\partial y^2} + \frac{\partial^2 \upsilon_x}{\partial z^2} = -\frac{1}{\mu}\frac{\partial p}{\partial x} \qquad 5.54$$

During the mould filling, the flow passes over several different cross sections. Attending to the extraction phase of the RIM process, not all the cross section can be injected, since negative zones are impossible to extract, as shown in Figure 5-50. Based on these, the main feasible type of geometries for the mould cavity cross section are circular ducts, rectangles, ellipses, equilateral triangle. Considering the total volume rate of flow, Q, and solving Equation 5.54 base on geometrical parameters from figures present on Table 5-15, the solutions of pressure drop for the integration across the tube length can be found at Table 5-15.

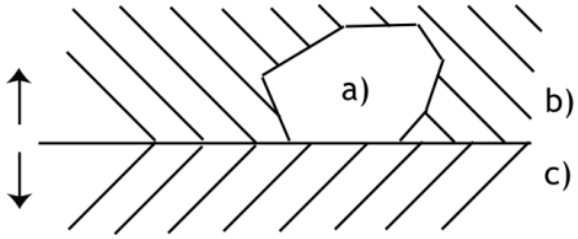

Figure 5-50 Part with negative angle of extraction, where the arrows represents the mould openning action: a) part b) cavity side c) core side

Table 5-15 Solutions for pressure drop over a length, L , for different cross sections (White, 2006)

Geometry	Cross Section	$\Delta p[\mathrm{Pa}]$	
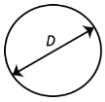	Circular $x^2+y^2=D/2$	$\Delta p=-\frac{128\mu QL}{\pi}D^{-1}$	5.55
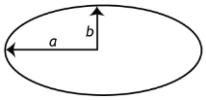	Ellipse $x^2/a^2+y^2/b^2\le 1$	$\Delta p=-\frac{4a\mu QL}{\pi}\left(\frac{a^3b^3}{a^2+b^2}\right)^{-1}$	5.56
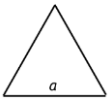	Equilateral triangle	$\Delta p=-\frac{320\mu QL}{\sqrt{3}}\left(a^4\right)^{-1}$	5.57
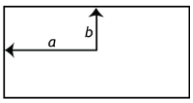	Rectangle $-a<x<a,-b<y<b$	$\Delta p=-\frac{3\mu QL}{4}\left(ba^3\right)^{-1}\left(1-\frac{192a}{\pi^5 b}\sum_{i=1,3,5,\ldots}^{\infty}\frac{\tanh\left(i\pi b/2a\right)}{i^5}\right)^{-1}$	5.58

It is also of the outmost importance to consider the position and the design of the gate. For the position of the gate, it should be considered the following (Shoemaker, 2006):

- Balanced filling;
- Thicker areas;
- Keep a minimum distance to thinner regions;
- Flow against the walls, to avoid jetting.

The balanced filling is achieved when the extremities of a part are filled at same time and same pressure. In some cases, more than one gate is needed to fill a part. The selection of the number of gates is, primarily, made according to the pressure requirements, and considering that the part should be filled with a smooth and uniform flow. When the pressure is higher than that, more gates should be placed according to (Shoemaker, 2006)

- Equal pressure drop in each sub-moulding zone
- Equal volume

- Careful selection of the gates position, in order to place the weld lines in less sensitive areas

Concerning the gate design, film gates (fan and sprue gates) and dam gates, which were already described in Section 2.4, are more used in RIM (BayerCorporation, 2008; Macosko, 1989). These gates are widely used, due to the normal procedure to fit the mixhead in the mould in the parting line (Sweeney, 1987). It is common use to place the mould in horizontal position, due to the configuration of the normal presses (Sweeney, 1987).

It is of great interest to understand the flow inside the gates, from a fluid mechanics point of view. For a gate design, Winter and Fritz (1986) set the following characteristics: a uniform distribution over the slip part, invariance of the flow rate across the width, invariance of the flow in polymer viscosities and uniform average RTD. Since the distribution of the flow in the gate occurs by pressure drop, it is vital for the flow front inside the mould, that the pressure drop should maintain a constant flow rate (Müller et al., 1985). In RIM, the invariance of viscosity across the gate is not difficult to be achieved, since the fluids are Newtonian, however at later stages in mould filling, if the reaction proceeds close to the gel point, careful attention should be paid because there is a critical point where the fluid changes from Newtonian to shear-thinning (Torres et al., 2012). Winter and Fritz (1986) suggest a rectangular manifold, ie., with a rectangular section to maintain a uniform RTD, specially for reactive processing

Using the flow maps from Section 5.3.4, the part can be divided into different parts and an association in series or parallel can be computed to estimate the flow problems that can occur inside the cavity.

As pointed in Section 2.4, for RIM mould project, the air trapping is a key aspect in order to avoid bad part qualities. Macosko (1989) noticed that temperature gradients and, consequently, wall and/or gate proximity can originate a gradient in bubble size and quantity. As shown in sub-Chapter 2.4, the common procedure to remove the air or gas trap is placing venting zones. Silva (2007) points out the following general dimensions for venting: 25mm length and 0.25mm thickness, and the particular dimensions of 10mm length and 0.05mm thickness for integral skin formulation. However, these values depend on the formulation used, and consequently the formulation viscosity, for example low viscosity materials will exit through the venting points, which causes the need for additional trimming operations, increasing the cycle time and the post-operation costs.

In order to avoid post-operations, CFD simulations can be made to predict air trapping zones and in addition predict the flow front position evolution, i.e. from CFD simulations it

is possible to map how the material and air flow inside the cavity, in order to place the best local for venting. To project the venting, it is assumed that the pressure drop along the venting is the difference between the injection pressure, p_{inj}, and atmospheric pressure, p_{atm}, according to

$$\Delta p = p_{inj} - p_{atm} \qquad 5.59$$

Using the Poisson equation from Equation 5.54, the pressure drop from Equation 5.59 and considering that the individual air or gas venting flow rate, q_v, is equal to the material flow rate, q_{inj}, divided by the number of ventings, n_v, as shown in

$$q_v = \frac{q_{inj}}{n_v} \qquad 5.60$$

the cross section dimensions can be calculated using Equation 5.55 to Equation 5.58 from

Table 5-15. The vents should have circular or rectangular cross-sections, since these are more feasible for machining.

5.4.3 Curing Stage

Another important stage in RIM cycle is the demoulding stage. On this stage, the part is released from the mould. After the filling step, the material keeps on curing until the necessary hardness for the extraction is achieved. Since the cure reaction is exothermic, the heat release will affects the part shrikange(Sekula et al., 2003) and consequently part quality. In order to prevent any defects, mould designers should improve moulds heating system project to avoid large temperature gradients in the part and, if possible, to promote a uniform cure reaction along the part. Also the cure cycle represents 60% of moulding cure cycle. Major issues stemming from curing are to know how to improve the part quality; to know when the part is ready for the extraction; and to know how to reduce the moulding cycle.

The answer for these issues lies in the cure reaction, which is schematically present in Figure 5-51 for the case of a polyurethane. A good knowledge of the cure phase has a vital importance for a proper optimization of the entire cycle. The cure reactions are typical of the thermoset polymers, and for the polyurethane formulations consist in highly exothermic and complex reactions of isocyanate groups with hydroxyl groups. After the

filling, the material is let curing inside the mould until the part achieves dimensional stability for the extraction. Besides the complex reactions that occur during the polyurethane polymerization, several authors (Castro and Macosko, 1982; Geier et al., 2009) consider that the complex process can be modeled considering just one simple reaction, represented by a single kinetic equation to model the cure reaction.

$$\underset{\textit{Isocyanate}}{R-NCO} + \underset{\textit{Polyol}}{R'-OH} \rightarrow \underset{\textit{Urethane}}{R-\overset{\overset{H}{|}}{N}-\overset{\overset{O}{||}}{C}-OR'}$$

Figure 5-51 Polyurethane reaction

Several authors have proposed different models for the cure reaction, and there are two types of models: mechanistic and phenomenological models. The mechanistic models enable a good interpretation of physic-chemical phenomena and prediction of the results, however they have a large number of experimentally determined parameters. The phenomenological models are simple models, based on the assumption that one reactional step represents all the polymer curing process and the general equation is defined by

$$\frac{d\alpha}{dt} = k(T)\, f(\alpha) \qquad 5.61$$

where $\frac{d\alpha}{dt}$ is the reaction rate, $k(T)$ is the chemical-controlled rate in function of temperature, T, and $f(\alpha)$ is function of conversion α. Some reviews on cure models can be found in Bártolo (2001), Halley and Mackay (1996) and Yousefi et al. (1997).

For the present study, it was considered a n^{th} order model, for the sake of simplicity, and the diffusion model (Mateus et al., 2006) to account for mass transfer phenomena during the cure, which are defined as,

$$\frac{d\alpha}{dt} = k_0 e^{-\left(E/RT_{abs}\right)} (1-\alpha)^n \qquad 5.62$$

$$\frac{d\alpha}{dt} = \frac{1}{1+e^{\left[\chi(\alpha-\alpha_d)\right]}} \varphi e^{-\left(E/RT_{abs}\right)} [NCO]^q \alpha^m (1-\alpha)^n \qquad 5.63$$

where k_0 is the pre-exponencial factor, E is the activation energy, R is the gas constant, T_{abs} is the absolute temperature, n is the reaction order, χ is the diffusion constant, α_d

is the critical value of the fractional conversion corresponding to the onset of diffusion-controlled effects over the curing reaction, φ is the pre-exponencial factor of the rate constant, $[NCO]$ is the NCO concentration, q is a constant, and m is the reaction order, being the sum $m+n$ the overall reaction order.

Both models were fitted to the experimental data obtained for $KE_r = 1$ experiments (cf. Section 4.3) using the Excel solver, and the values of the constants are shown in

Table 5-16. The experimental and numerical curves are shown in Figure 5-52, where the results are expressed in $d\alpha dt^{-1}$ as function of conversion rate. It is possible to observe that the *n*th order kinetic model gives a poorer adjustment, with $R^2 = 0.696$, than diffusion model, with $R^2 = 0.974$. The diffusion model is a relatively complex model due to the larger number of constants compared with *n*th model. This increases the difficulty in fitting the model to experimental data. For Rencast FC52 formulation, the model does not describe the phase separation, however very good results have been found for diffusion model with other formulations (Bártolo, 2001; Mateus et al., 2008; Mateus et al., 2006; Silva et al., 2006). The diffusion model, also, was implemented on CFD resulting in good agreement with experimental data (Dias et al., 2011).

From CFD results, the cure reaction evolution can be predicted (Foudrinier et al., 2008). Based on CFD results, the heating system could be placed to a more balanced cure reaction distribution along the part, improving the state-of-art (c.f. Sub-chapter 2.4) suggestions for heating channels size and distribution. The use of optimization processes as, for example, genetic algorithms (Muc and Saj, 2004) can be a strategy for faster results.

Beside the hot water as a heat source(Silva, 2007) other fluids can be employed, such as oil, and also heaters. Recently, microwaves have been employed in thermoset curing, promoting a faster and volumetric cure reaction, however non-uniform distribution of heat and poor control can be disadvantages.

Table 5-16 Constants for kinetic models

Model	k_0	χ	α_d	$\varphi[s^{-1}]$	q	m	n
*n*th order	1.02×10^{0}						7.00×10^{-1}
Diffusion		6	1	8.00×10^{-3}	2.50×10^{-1}	1.80×10^{-1}	5.20×10^{-1}

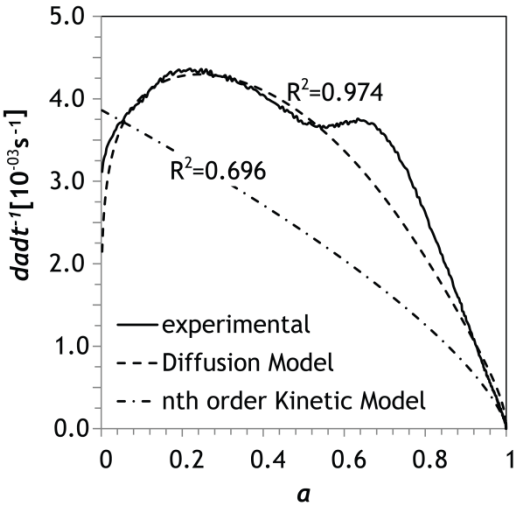

Figure 5-52 n^{th} order kinetic model and diffusion model fitted to experimental data obtained for $KE_r = 1$

5.5 Conclusions

A bidimensional model to simulate the filling of a RIM's mould was introduced. This model simulates the flow field and the air-reacting polymer interface using MVF and VOF. Several numerical schemes for the flow front calculation were studied. Due to the similar results obtained and computational times for the schemes, it was chosen the CICSAM model, which gives a good resolution for high viscosities ratio between phases, which in RIM can go up to orders of 10^4 to 10^5.

From the proposed model, there were not considerable differences between flow front definitions for the several contact angles used, and for this reason, it was considered the angle $90°$, corresponding to the flat plane which is the most used value over the literature. Comparing the model with experimental results it is possible to verify that the numerical results accurately describe the flow front and the fountain effect, since the numerical and experimental patterns are very similar.

The model was applied to a 3D case, with a similar flow front geometry and compared to the available literature. However, there is some divergence when the flow front is flowing around an obstacle between numerical and experimental data.

Using the model developed, several simulations were performed for contraction and expansion geometries. The model was able to describe physically and identify four different phenomena associated with the mould filling:

- Stable front
- Air entrapped at salient corner
- Air entrapment and engulfment

- Air boundary layer

The effect of inertial, gravitational, viscous and surface forces, was studied from three dimensionless numbers: Fr, Re and We. The gravitational forces tend to maintain the flow front flat, eliminating the gas entrapment and formation of gas boundary layer, and lowering the area of entrapped air, both in contraction and expansion geometries. Also decreases the pressure drop. Concerning the velocity field there is no tendency with Fr. Regarding the viscous forces, they tend to stabilize the flow front into a flat surface however, they allow gas entrapment at the corner. Viscous forces increase the pressure drop. The surface forces also help to stabilize the flow front and make it flat. The pressure drop and velocity field show not to depend on surface forces.

Also the thickness ratio, Tr, was studied for a contraction. It was observed that similar phenomena are observed for different Tr.

Regarding the flow pattern maps, it was possible to see that only a small region allows an injection without any defect, however, using these maps it is possible to predict potential problems and project a proper location for vents.

Despite Müller et al. (1985) suggest the injection in the direction of gravity, it was found that a more favorable flow pattern is achieved when injecting in the opposite direction to gravity. However, an accurate study must be performed to prevent any air or gas entrapment. This study should focus on flow front pattern and air/gas trap zones, in order to place the best location for the gate and venting.

Some mould design to RIM suggestions were proposed. Analyzing the forces during the RIM process, it was found some rules for mould thickness, and from Equation 5.49 it can be seen that the material reduction for the mould fabrication can be in order of 65%, when compared to the TIM.

The suggestions proposed for the mould filling were collected from the literature and adapted to RIM, and covered the gate selection, gate design principles and venting size. The results from the flow patterns maps are useful for mould design, since it allows to predict the possible problems that can be found inside the cavity during the filling. As already proposed, an association in serial or parallel of several mould zones can be performed to identify the problems during the mould filling. However, for each geometry some studies for obstacles to the flow front should be performed.

Diffusive models for cure provide better description of the physical phenomena, although due to their increased complexity they are thus better suited for application to mould design.

5.6 References

Acrivos, A., Schrader, M.L., 1982. Steady flow in a sudden expansion at high Reynolds numbers. Physics of Fluids 25, 923-930.

Armaly, B.F., Durst, F., Pereira, J.C.F., Schönung, B., 1983. Experimental and theoretical investigation of backward-facing step flow. Journal of Fluid Mechanics 127, 473-496.

Astarita, G., Greco, G., 1968. Excess Pressure Drop in Laminar Flow through Sudden Contraction. Newtonian Liquids. Industrial & Engineering Chemistry Fundamentals 7, 27-31.

Bártolo, P., 2001. Optical approuches to macroscopic and microscopic engineering, Ph.D. Thesis, Department of Physics, University of Reading, Reading, UK.

Batchelor, G.K., 2009. An Introduction to Fluid Dynamics. Cambridge Univeristy Press, New York.

BayerCorporation, 2008. Engineering Polyurethanes - RIM Part and Mold Design Guide. Bayer Material Science.

Behrens, R.A., Crochet, M.J., Denson, C.D., Metzner, A.B., 1987. Transient free-surface flows: Motion of a fluid advancing in a tube. AIChE Journal 33, 1178-1186.

Biswas, G., Breuer, M., Durst, F., 2004. Backward-Facing Step Flows for Various Expansion Ratios at Low and Moderate Reynolds Numbers. Journal of Fluids Engineering 126, 362-374.

Brackbill, J.U., Kothe, D.B., Zemach, C., 1992. A continuum method for modeling surface tension. Journal of Computational Physics 100, 335-354.

Castro, J.M., Lee, C.C., 1989. Model Simplification, in: III, C.L.T., Bernhardt, E.C. (Eds.), Fundamentals of computer modelling for polymer processing. Hanser Publishers, Munich.

Castro, J.M., Macosko, C.W., 1982. Studies of mold filling and curing in the reaction injection molding process. AIChE Journal 28, 250-260.

Cécile, J., 2005. Micro-Injection Moudling. Pu Louvain, Louvain.

Chang, R.-y., Yang, W.-h., 2001. Numerical simulation of mold filling in injection molding using a three-dimensional finite volume approach. International Journal for Numerical Methods in Fluids 37, 125-148.

Chen, S.C., Chen, N.T., Hsu, K.S., Hsu, K.F., 1996. Study of polymer melt flow in sequential injection molding process. AIChE Journal 42, 1706-1714.

Codina, R., Schafer, U., Onate, E., 1994. Mould Filling Simulation Using Finite Elements. International Journal of Numerical Methods for Heat & Fluid Flow 4, 291-310.

Cohnen, W., Osswald, T.A., 1992. Experimental Study of High Reynolds' Number Flows Between Narrow Gaps. International Polymer Processing 1992, 314-319.

Coyle, D.J., Blake, J.W., Macosko, C.W., 1987. The kinematics of fountain flow in mold-filling. AIChE Journal 33, 1168-1177.

Cuniot, A., Deur, L., Hansen, O., Dupret, F., 1989. A Finite Element Method for Simulating Injection Molding of Thermoplastics, in: Thompson, E.G. (Ed.), 3rd International Conference on Numerical Methods in Industrial Forming Processes, Fort Collins, Colorado.

Dean, W.R., 1936. Note on the slow motion of fluid. Mathematical Proceedings of the Cambridge Philosophical Society 32, 598-613.

Dean, W.R., Montagnon, P.E., 1949. On the steady motion of viscous liquid in a corner. Mathematical Proceedings of the Cambridge Philosophical Society 45, 389-394.

Dhatt, G., Gao, D.M., Cheikh, A.B., 1990. A finite element simulation of metal flow in moulds. International Journal for Numerical Methods in Engineering 30, 821-831.

Dias, R., Mateus, A., Mitchell, G., Bártolo, P., 2011. Computer modelling and simulation of reaction injection moulding, Innovative Developments in Virtual and Physical Prototyping. CRC Press, pp. 731-736.

Doormaal, J.P.V., Raithby, G.D., 1984. Enhancements of the SIMPLE Method for Predicting Incompressible Fluid Flows. Numerial Heat Transfer 7, 147-164.

Durst, F., Melling, A., Whitelaw, J.H., 1974. Low Reynolds number flow over a plane symmetric sudden expansion. Journal of Fluid Mechanics 64, 111-128.

Fauchon, D., Dannelongue, H.H., Tanguy, P.A., 1991. Numerical Simulation of the Advancing Front in Injection Moulding. International Polymer Processing 1991, 13-18.

Foudrinier, E., Venet, C., Silva, L., 2008. 3D Computation of reactive moulding processes. International Journal of Material Forming 33, 735-738.

Geier, S., Winkler, C., Piesche, M., 2009. Numerical Simulation of Mold Filling Processes with Polyurethane Foams. Chemical Engineering & Technology 32, 1438-1447.

Haagh, G.A.A.V., Van De Vosse, F.N., 1998. Simulation of three-dimensional polymer mould filling processes using a pseudo-concentration method. International Journal for Numerical Methods in Fluids 28, 1355-1369.

Halley, P.J., Mackay, M.E., 1996. Chemorheology of thermosets—an overview. Polymer Engineering & Science 36, 593-609.

Hetu, J.F., Garcia-Rejon, A., 1995. Numerical Simulation of the Flow and Fiber Orientation in Reinfor Thermoplastics Injection Molded Products, 5th International Conference on Numerical Methods in Industrial Forming Processes, New York, pp. 1135-1141.

Hieber, C.A., Shen, S.F., 1980. A finite-element/finite-difference simulation of the injection-molding filling process. Journal of Non-Newtonian Fluid Mechanics 7, 1-32.

Hirt, C.W., Nichols, B.D., 1981. Volume of fluid (VOF) method for the dynamics of free boundaries. Journal of Computational Physics 39, 201-225.

Huang, H., Usmani, A.S., 1994. Finite Element Analysis for Heat Transfer. Springer-Verlag, London.

ISO 178, 2003. Determination of flexural properties. ISO.

Kuei, S.C., Burton, T.E., 1987. Polyfill: A flow Simulation Code for Injection Molding. Computer in Engineering, 73-78.

Kundu, P.K., Cohen, I.M., 2004. Fluid Mechnics. Elsevier Academic Press, USA.

Langhaar, H.L., 1942. Steady Flow in the Transition Length of a Straight Tube. Journal of Applied Mechanics 9, A55-A58.

Lee, H.-S., 1997. Finite element analysis for the flow characteristics along the thickness direction in injection molding. Polymer Engineering & Science 37, 559-567.

Leonard, B.P., Mokhtari, S., 1990. ULTRA-SHARP Nonoscillatory Convection Schemes for High-Speed Steady Multidimensional Flow. NASA, Lewis Research Center.

Macosko, C., 1989. RIM Fundamentals of Reaction Injection Molding. Hanser Publishers, Munich, Germany.

Manas-Zloczower, I., Blake, J.W., Macosko, C.W., 1987. Space-time distribution in filling a mold. Polymer Engineering & Science 27, 1229-1235.

Martinho, P., Mateus, A., Bártolo, P., Bolrão, J., Gaspar, J., Ferreira, P., 2003. Utilização integrada de Técnicas Avançadas para Análise e Optimização do Processo RIM. O Molde 58, 43-49.

Mateus, A., Bártolo, P., Mitchell, G., Silva, M., Pouzada, A., Pontes, A., 2008. The effect of thermal conductivity of RIM moulds in kinetics cure, in: Bártolo, P. (Ed.), Virtual and rapid Manufacturing. Taylor & Francis Groud, Leiria.

Mateus, A., Martinho, P., Bártolo, P.J., 2006. Flow and cure modeling of RIM moulding - Thermal and flow validation, ANTEC 2006, Charleton, USA.

Mavridis, H., Hrymak, A.N., Vlachopoulos, J., 1988. Transient free-surface flows in injection mold filling. AIChE Journal 34, 403-410.

Menges, G., Mohren, P., 1996. How to make injection molds. Carl Hanser Verlag, Munchen, Germany.

Mitsoulis, E., 2010. Fountain flow revisited: The effect of various fluid mechanics parameters. AIChE Journal 56, 1147-1162.

Moffatt, H.K., 1964. Viscous and resistive eddies near a sharp corner. Journal of Fluid Mechanics 18, 1-18.

Mohammed, R.K., Osswald, T.A., Spiegelhoff, T.J., Sun, E.M., 1994. Modeling and Simulation of High Reynolds' Number Flows During Reaction Injection Mold Filling. International Polymer Processing 1994, 279-285.

Mori, K., Osakada, L., Takaoka, S., 1996. Simplified Three Dimensional Simulation of Non-Isothermal Filling in Metal Injection Moldoing. Engineering Computations 13, 111-121.

Muc, A., Saj, P., 2004. Optimization of the reactive injection moulding process. Structural and Multidisciplinary Optimization 27, 110-119.

Müller, H., Mrotzek, W., Menges, G., 1985. Mold Filling with Polyurethane, Reaction Injection Molding. American Chemical Society, pp. 237-258.

Muralidhar, K., Biswas, G., 2011. Advanced Engineering Fluid Mechanics. Narosa Publishing House.

Musarra, S., Keunings, R., 1989. Co-current axisymmetric flow in complex geometries: Numerical simulation. Journal of Non-Newtonian Fluid Mechanics 32, 253-268.

Muzaferija, S., Peric, M., Sames, P., Schellin, T., 1998. A Two-Fluid Navier-Stokes Solver to Simulate Water Entry, 22nd Symposium on Naval Hydrodynamics. NATIONAL ACADEMY PRESS, Washington DC.

Oertel, H., 2010. Prandtl-Essentials of Fluid Mechanics. Springer New York, New York.

Owens, R.G., Phillips, T.N., 2002. Computational Rheology. Imperial College Press, London.

Peyret, R., 1996. Handbook of Computational Fluid Mechanics. Academic Press.

Pichelin, E., Coupez, T., 1998. Finite element solution of the 3D mold filling problem for viscous incompressible fluid. Computer Methods in Applied Mechanics and Engineering 163, 359-371.

Richardson, S., 1970. The die swell phenomenon. Rheologica Acta 9, 193-199.

Schäfer, F., Breuer, M., Durst, F., 2009. The dynamics of the transitional flow over a backward-facing step. Journal of Fluid Mechanics 623, 85-119.

Schmidt, L.R., 1974. A special mold and tracer technique for studying shear and extensional flows in a mold cavity during injection molding. Polymer Engineering & Science 14, 797-800.

Sekula, R., Saj, P., Nowak, T., Kaczmarek, K., Forsman, K., Rautiainen, A., Grindling, J., 2003. 3-D modeling reactive molding processes: From tool development to industrial application. Advances in Polymer Technology 22, 42-55.

Shames, I., 1992. Mechanics of Fluids. MvGraw-Hill, Inc, New York.

Shen, S.-F., 1992. Grapplings with the simulation of non-Newtonian flows in polymer processing. International Journal for Numerical Methods in Engineering 34, 701-723.

Shiojima, T., Matsuhiro, T., Shimazaki, Y., Daihuji, H., 1989. Finite Element Analysis of Injection Process Using Marker Particles, in: Thompson, E.G. (Ed.), 3rd International Conference on Numerical Methods in Industrial Forming Processes, Fort Collins, Colorado, pp. 285-290.

Shoemaker, J., 2006. Moldflow Design Guide. Carl Hanser Verlag New York.

Silva, L., 2001. Modelação do Transporte de Fluídos Newtonianos e Newtonianos Generalizados, Master Thesis, Deparment of Mechanical Engineering, Universidade do Porto, Porto.

Silva, M., 2007. Moldes protótipos para a produção de peças em RIM, Master Thesis, Polymer Departament, University of Minho.

Silva, M., Mateus, A.J., Bartolo, P.J., Pouzada, A.S., Pontes, A.J., 2006. Assessment of the performance of products moulded by RIM, RPD 2006, Building the Future by Innovation, Marinha Grande, Portugal.

Sousa, P.C., Coelho, P.M., Oliveira, M.S.N., Alves, M.A., 2009. Three-dimensional flow of Newtonian and Boger fluids in square–square contractions. Journal of Non-Newtonian Fluid Mechanics 160, 122-139.

Stüer, H., Gyr, A., Kinzelbach, W., 1999. Laminar separation on a forward facing step. European Journal of Mechanics - B/Fluids 18, 675-692.

Sweeney, F., 1987. Reaction Injection Molding Machinery and Processes. Marcel Dekker, New York, USA.

Thompson, E., 1986. Transient Analysis of Metal Forming, Using Pseudoconcentrations, 2nd International Conference on Numerical Methods in Industrial Forming Processes, Gothenburg, Sweden.

Torres, M.V., Winter, U., Santos, R.J., Costa, M.R., Dias, M.M., Lopes, J.C., 2012. Rheology of a Reactive System of Polyurethanes for Production in RIMcop®, Polychar 20, Dubrovik.

Tucker, C.L., Dessenberger, R.B., 1994. Governing Equations for Flow and Heat Transfer in Stationary Fiber Beds, in: Advani, S.G. (Ed.), Flow and Rheology in Polymer Composites Manufacturing. Elsevier, Amsterdam, pp. 257-323.

Ubbink, O., Issa, R.I., 1999. A Method for Capturing Sharp Fluid Interfaces on Arbitrary Meshes. Journal of Computational Physics 153, 26-50.

van de Griend, R., Denn, M.M., 1989. Co-current axisymmetric flow in complex geometries: Experiments. Journal of Non-Newtonian Fluid Mechanics 32, 229-252.

Van Leer, B., 1977. Towards the ultimate conservative difference scheme. IV. A new approach to numerical convection. Journal of Computational Physics 23, 276-299.

Vrentas, J.S., Duda, J.L., 1973. Flow of a newtonian fluid through a sudden contraction. Applied Scientific Research 28, 241-260.

White, F.M., 2006. Viscous Fluid Flow, 3rd Edition ed. McGraw-Hill New York, USA.

Winter, H.H., Fritz, H.G., 1986. Design of dies for the extrusion of sheets and annular parisons: The distribution problem. Polymer Engineering & Science 26, 543-553.

Youngs, D.L., 1982. Time-Dependent Multi-Material Flow with Large Fluid Distortion, in: Morton, K.W., Baines, M.J. (Eds.), Numerical Methods for Fluid Dynamics. Academic Press, London.

Yousefi, A., Lafleur, P.G., Gauvin, R., 1997. Kinetic studies of thermoset cure reactions: A review. Polymer Composites 18, 157-168.

Zaidi, K., Abbes, B., Teodosiu, C., 1997. Finite element simulation of mold filling using marker particles and the k-ϵ model of turbulence. Computer Methods in Applied Mechanics and Engineering 144, 227-233.

6 Final remarks

6.1 General Conclusions

The main goals of the present work were to project a new industrial prototype equipment based on a patented novel technology, the RIMcop; assess the mixing quality in RIMcop technology for polyurethane processing and set rules for the mould design for RIM. CFD tools were used to compare commercial solutions for RIM mixing heads and to study the filling stage during RIM process. The mixing quality was assessed experimentally, measuring the mechanical properties and the kinetic parameters of curing reaction.

In Chapter 2, the mixing chamber design state of art is presented. Based on patent applications, different proposals for RIM mixing heads are introduced and studied. From this review it is clear that a common procedure to solve the mixing problems in RIM was the increase of the mixing chamber complexity to promote turbulence patterns and improve mixing quality. Later, some geometric studies introduced some scientific knowledge in mixing chamber designs. Also, from Chapter 2, were introduced some techniques to assess the quality of mixing in industrial mixing chambers for RIM. Mixing in RIM is mainly assessed from product distribution of micromixing test chemical reactions, tracer studies, physical characterization of the obtained polymer and adiabatic temperature rise.

Chapter 2 makes a very preliminary introduction of the studies on the numerical methods used for mould filling in RIM. Finally, the state of art rules for mould design were

collected. Beside some considerations from Knipp (1998); Müller et al. (1985a); Müller et al. (1985b), there were not found further works on RIM moulds, and most of rules collected are based on advices from material fabricants. This shows that the empirical knowledge is still prevalent in RIM companies (Torcato et al., 2011). The mould design should be done with care to avoid air entrapment during the mould filling, and some advices are introduced for the gate selection, venting zones project, flow distributor and cooling system project.

Different commercial mixing chambers designs were compared using 3D CFD simulations, in Chapter 3. The different mixing head designs were assessed from dimensionless maps of vorticity, pathlines and strain rate. The study includes an energy balance and the RTD from the analysed mixing chamber geometries. Chapter 3 also analyses the RIM equipment project that was proposed and built or adapted, with a mixing head based on the patent from RIMcop Technology, for this work.

Chapter 4 shows the experimental work performed with the RIM machines at CDRSP-IPL and LSRE-FEUP. The mechanical properties of polyurethane foam for different processing conditions were assessed. The mechanical properties showed a dependency of the material properties on the measured pressure difference at the mixing head, Δp^*, and it was also found that the pressure signal has typical frequencies. From the spectral analysis, some flow structures inside the mixing chamber were proposed as the underlying mechanism for the said typical frequencies. A model for the impingement point position was introduced and applied to the experimental results.

Previous work (Fonte, 2012), pointed that the ratio of kinetic energies of the opposed jets in the RIM mixing chamber, KE_r is the critical parameter for mixing quality, and this parameter was used as the set point condition for mixing, and was implemented in RIMcop technology. The kinetics of the polymerization was evaluated, and it was observed a clear influence of KE_r on the adiabatic temperature rise, and so on higher reaction rate. The KE_r also influences the final properties of the polymer produced. Physical properties such as the density, deflection temperature and glass temperature transition, were studied. The mechanical properties studied were tensile, compressive, flexural and dynamical mechanical analysis. From the referred properties, it is noticed the influence of KE_r. Using the optical microscopy and SEM, the morphology of processed polyurethane was studied as function of KE_r.

The flow front during the filling of the cavity of a RIM mould was studied using 2D and 3D CFD simulations with the VOF model for the simulation of the air/liquid interface. Phenomena such as the fountain flow that was previously described from experimental work of Coyle et al. (1987), were accurately predicted from the CFD simulations. The 3D model results were compared to the numerical results of Chang and Yang (2001), and only slight differences were found, particularly in the re-merging regions of the flow front.

Also in Chapter 5, it was studied the flow phenomena that occur during filling, over a contraction and an expansion of the flow. This type of phenomena are common during mould filling in RIM, and using the CFD simulations four main phenomena were identified, and described : stable front, air entrapment at salient corner, air entrapment and engulfment and air boundary layer. Also the gravitational, viscous, inertial and surface forces were analysed, and some results about their influence in pressure drop and velocity field were shown. With the results obtained were designed maps with the occurrence of each particular phenomena as function of some dimensionless numbers. This study aims to provide ranges of values for the injection parameters, according to the part geometry. The final part of Chapter 5 proposed some considerations for calculating the thickness of mould plates, gate location and venting zone dimension. A diffusion model that gave higher accuracy on the description of the curing reaction was used to model the cure reaction (Dias et al., 2011; Mateus, 2011).

The next sections highlight the main achievements from the present work.

6.1.1 RIMCop Technology Project

From the comparative study of commercial mixing chamber designs in Chapter 3, it is shown a critical Reynolds number, Re_{cr}, between 75 and 150, similar to the one obtained by Santos (2003) and Fonte (2012). The dimensionless vorticity and pathlines showed an increase of the mixing length with the Reynolds number. The different mixing chambers configurations have the following influence on flow patterns, mainly on the vortices inside the mixing chamber:

- In horizontal angled jets mixing chambers, different than $180°C$, the jets are impinged against each other laterally, and towards the walls, and the opposed tangential direction of the jets flow creates smaller vortices;
- In vertical angled jet mixing chambers, with the jets pointing to the chamber top, it is observed that the vortices upstream the jets are confined but vortices below the impingement point are also generated;

- Adding some restrictions or shortening the mixing chamber will break some of the flow patterns and symmetry, producing smaller vortices;

The energy dissipated in mixing was assessed from the strain rate values, and by a macroscopic energy balance. From the strain rate results, the energy used in mixing, as expectable, increases with Re and it is higher for horizontal angled jets, since

- In horizontal angled jets, most of the jet energy is dissipated in the mixing chamber walls;
- In vertical angled jets, the energy is mainly dissipated in the top wall of mixing chamber;
- The obstacles will increase the contact area between opposed fluids which is associated to the creation of larger regions with high energy dissipation;
- Shorter mixing chambers introduce more energy dissipation due to the walls.

Similar results were obtained using the macroscopic energy balance, where the fraction of energy dissipated by shear, $\varepsilon_{se}/\varepsilon_t$, is higher for opposed jets, when compared to the other geometries. The geometries with oppose jets favour shear, which is the main mechanism for the reduction of mixing scales in RIM. Larger values for shear can also be associated with some design changes, namely the insertion of obstacles in the mixing chamber, or angled jets. From the macroscopic energy balance, the power number was defined and applied to the different volume controls. The results were very similar to the ones reported by Leblebici (2011) for T-jets reactors, where all the energy is employed in mixing.

The RTDs of the different mixing chambers shown that opposed jets create flow short-circuits from inlet to outlet, being better described by piston like behaviours with axial and radial dispersion, where backmixing patterns do not play a major role.

The implementation of RIMCop technology in existent equipment was compared with RIMcop equipment made from scratch. Due to the specifications of the technology, the present work advices that is more suitable to build new dedicated equipment, than implementing in an existent one, since the technology requires a new control system, that controls directly the pumps, and also the mixing chamber should have a different design.

6.1.2 Physical Characteristics of Final Polymer

6.1.2.1 Assessment of RIM

From experimental work performed in CDRsp-IPL equipment, mixing in RIM was assessed from the mechanical properties of final parts and the results were shown in Chapter 4. Different stoichiometric ratios were tested, and the results showed that the better mechanical properties of the parts were obtained when the difference of the static pressure between the jets, $\overline{\Delta p^*}$, was closer to zero. For this situation it was possible to identify higher energy peaks from the frequency power spectra of $\overline{\Delta p^*}$ time history, which are related with oscillatory behaviour identified with strong convective mixing mechanisms by (Santos et al., 2005). The experimental frequency power spectra were compared with numerical results of a 3D dynamic simulation of the opposed jets mixing chamber. From the results of $\overline{\Delta p^*}$ the impingement point position was calculated from a model based on the opposed jets kinetic energy ratio, KE_r. It is possible to observe that for values close to $\overline{\Delta P^*} = 0$ the impingement point is closer to the center of the mixing chamber.

The results from this work have provided clear evidence that the pressure can be used as a control parameter for the assessment of mixing in RIM, as predicted by Erkoc et al. (2007) from CFD simulations.

6.1.2.2 Assessment of RIMcop

The opposed jets kinetic energy ratio, KE_r, was used as a control parameter in the RIMCop technology, and this was assessed from the polymerization kinetics and physical characteristics of final polymer. Using an adiabatic reactor, as proven in Chapter 4, the results of Adiabatic Temperature Raise, ATR, clearly showed that for unitary KE_r an higher adiabatic temperature was achieved. The results were compared for unitary momentum ratio M_r and flow rate ratio, F_r. The higher temperature raise values were achieved for the unitary KE_r, which proves this is the variable that should be used to set the better mixing conditions in RIM.

Regarding the physical characteristics of final polymer, several properties were measured: density, using an analytical balance, deflection temperature and glass temperature transition, both using a DMA; and mechanical properties such as tensile, compression and

flexural strengths and modulus, all using universal test machine, and viscoelastic properties using a DMA.

Although with opposite behaviour for different properties, it is clearly noticed that operating at unitary KE_r plays a major role in the physical properties, since it is found a peak for density and glass temperature transition and a local minimum for deflection temperature.

The same tendency was found on mechanical properties, where unitary KE_r reveals a clear influence on mixture. From Fonte (2012), it was shown that unitary KE_r promotes the growth of interfacial area between the fluids from the jets, and this is also clear from the results obtained with the DMA. These observations relate the mechanical properties with the growth of hard segments in the polyurethane network, and so the unitary KE_r increases the inter-domain between phases that will dilute the soft segments.

The cell size distribution was observed from optical microscopy and SEM analysis. Although the results suggest that cell size distributions are related with striation thickness, this is not clearly proven in this work; however, these results agree with the ones predicted numerically by Fonte (2012), with cell sizes smaller than $10\mu m$.

The present work shows the need for improvements in the control system of the RIMcop, since the mechanical properties of the parts injected with the controller on are lower than the ones obtained for unitary KE_r. Chapter 4 suggest some improvements on this regard.

6.1.3 RIM Mould Design

Using CFD commercial code Ansys Fluent, in Chapter 5 are introduced CFD simulations using FVM coupled with a VOF model, which is firstly used to calculate the fountain flow, and secondly to simulate the flow front in 3D. State of art computational applications for mould filling, as Moldflow or Moldex, are based in FEM, and have a significant number of black box features. The model developed was compared with experimental results from Coyle et al. (1987), and a good agreement was found.

The model was used to study the filling through geometrical changes, for the present work, contractions and expansions, taking into account gravitational, inertial, viscous and surface forces, was used to study the phenomena that occur during the filling. Four phenomena were identified:

- Stable front;
- Air entrapped at the salient corner;
- Air entrapment and engulfment;
- Air boundary layer.

Based on a dimensional analysis of the mould filling, three dimensionless parameters were used: Fr, Re and We. From the simulations, the results can be resumed as:

- For contractions:
  - Increasing the Fr, the flow front becomes more stable, and the tendency to air entrapment in salient corner decreases. The pressure drop increases and the velocity shows a strong dependence on the Fr number.
  - Increasing the Re, the flow front becomes instable, and air entrapment at salient corner decreases. The pressure drop decreases and the velocity depends on the Re number.
  - Increasing the We, the flow front becomes more stable, and the air entrapment in salient corner increases. The pressure drop and the velocity do not depend on We number.
- For expansions:
  - Increasing the Fr, the flow front becomes more stable, and the tendency for air entrapment in salient corner increases until the formation of a gas boundary layer for a critical Froude number, $Fr_{cr}=1$, above which the gas entrapment stops. The pressure drop increases and the velocity depends on Fr number.
  - Increasing the Re, the flow front becomes instable and air entrapment in salient corner decreases. The pressure drop decreases and the velocity field depends on Re number.
  - Increasing the We, the flow front becomes more stable, however a slight difference is noticed, and the air entrapment at salient corner increases. The pressure drop and the velocity do not depend on the We number.

For contractions, the thickness ratio, Tr was studied observing similar patterns for the studied range of Tr.

The results were aggregated in flow pattern maps, where the different phenomena shown the best region for mould filling without defects. The best regions are for $Fr=10^{-2}$ and for $Re=100$, being independent of We, both for contraction and expansion geometries.

Yet, other regions can permit the injection, depending on the physical properties of the filling material, or with the design of gas venting zones for gas purging.

Some suggestions were made for mould project. The forces during the injection were calculated, and some models were proposed to compute the thickness of a mould. When compared to the thickness of a TIM mould, it is possible to have a reduction of 65%.

With the flow patterns maps, some problems that will arise during mould filling can be predicted. The results can be used in parallel or in serial association to project the total pressure drop and all the phenomena during mould filling. Some suggestions from literature were collected and adopted to RIM, regarding the gate location, gate design and venting size calculation.

Torcato et al. (2011) showed that the industrial knowledge of RIM is based on empirical solutions based in long years of experience of a few industrial experts. Considering that the knowledge produced remains inside the company, the empirical knowledge faced several challenges as a demand of complex solutions in short time, or the replacement and training of project techniques. One of the main tasks of the present work was the introduction of science based knowledge that can be used by engineers during mould project. This study shows that mould filling is a complex multiphase flow of Newtonian fluids, and so it introduces innovative tools for mould design based on CFD results. Off course that working with these tools requires an experienced technician, but it is based, not in empirical and non-transmissible knowledge (considering that all the information available internally in the brain is not possible to transfer to another person), but on the scientific foundations. The author believes that these tools can expand the RIM horizons in the next years.

6.2 Future Work

This work was a transversal study about RIM, covering RIM technology project, RIM applications and the design of RIM and RIMcop machines and Mould design. Work that was not made in this thesis is suggested as future work.

Regarding the RIMCop technology, the implementation of a different control system is important to achieve the autonomous operation of the machine without a highly skilled technician that is needed for the industrial dissemination of the equipment. The suggestion relies on a fast response between the control system and equipment, and a new system to measure the pressure difference between the jets of monomers

Using the laboratorial facilities and knowledge developed, the work can be extended to new materials, other than polyurethanes. It should be an exciting task to embrace the study of the RIMcop process to new markets and products. Beside the materials suggestion done by Macosko (1989), as nylon, dicyclopentadiene, esters, acrylamate, epoxies, phenolics, some other as polycarbonate can be analysed for testing.

The present work revisited the effect of various fluid mechanics parameters on the flow of mould filling for a two-dimensional analysis. However, the state of art resides in three-dimensional work, although the quantity of simulations made and the computational resources available, did not allow the study of a three-dimensional model within the available time for this thesis. So, some further work can be made with a three-dimensional model, to refine the process maps. Beside the three-dimension model and map refination, other geometries and flow obstacles should be studied.

Using similar presses to those used in TIM, it is suggested to use a clamp force in horizontal direction, unlike the vertical traditional presses normally used in RIM. With this configuration, it is more confortable to inject in parting line against the gravity, position more favourable, according to results from present work.

Using CFD tools, some work on gates design can be done, and exploring new alternatives to the common ones, with focus on material losses and part defect minimization.

The final suggestion relies more on a personal desire than a scientific work, but for the author point of view, with enormous importance. The work and knowledge produced should be transferred to RIM companies, in order to improve the process dissemination and conquest new markets.

6.3 References

Chang, R.-y., Yang, W.-h., 2001. Numerical simulation of mold filling in injection molding using a three-dimensional finite volume approach. International Journal for Numerical Methods in Fluids 37, 125-148.

Coyle, D.J., Blake, J.W., Macosko, C.W., 1987. The kinematics of fountain flow in mold-filling. AIChE Journal 33, 1168-1177.

Dias, R., Mateus, A., Mitchell, G., Bártolo, P., 2011. Computer modelling and simulation of reaction injection moulding, Innovative Developments in Virtual and Physical Prototyping. CRC Press, pp. 731-736.

Erkoc, E., Santos, R.J., Nunes, M.I., Dias, M.M., Lopes, J.C.B., 2007. Mixing dynamics control in RIM machines. Chemical Engineering Science 62, 5276-5281.

Fonte, C., 2012. Mixing Studies with Impinging Jets - PIV/PLIF Experiments and CFD Simulation, Ph.D. Thesis, Deparment of Chemical Engineering, Universidade do Porto, Porto, Portugal.

Knipp, U., 1998. Molds for Polyurethanes Products, in: Stoeckhert, K., Menning, G. (Eds.), Mold-Making Handbook. Hanser Publishers, Munich, Germany.

Leblebici, E.N., 2011. Comparative Study of NETmix® and T-jets Reactors Based on Pressure Dynamics Master Thesis, Chemical Department, University of Porto, Porto, Portugal.

Macosko, C., 1989. RIM Fundamentals of Reaction Injection Molding. Hanser Publishers, Munich, Germany.

Mateus, A., 2011. Modelling and optimising of reaction injection moulding, Ph.D. Thesis, Departament of Physics, University of Reading, Reading, UK.

Müller, H., Küper, B., Maier, U., Pierkes, L., 1985a. The latest on molding of polyurethane. Advances in Polymer Technology 5, 257-304.

Müller, H., Mrotzek, W., Menges, G., 1985b. Mold Filling with Polyurethane, Reaction Injection Molding. American Chemical Society, pp. 237-258.

Santos, R.J., 2003. Mixing Mechanisms in Reaction Injection Moulding - RIM - An LDS/PIV Experimental Study and CFD Simulation, Ph.D. Thesis, Deparment of Chemical Engineering, Universidade do Porto, Porto.

Santos, R.J., Teixeira, A.M., Lopes, J.C.B., 2005. Study of mixing and chemical reaction in RIM. Chemical Engineering Science 60, 2381-2398.

Torcato, R., Santos, R., Dias, M., Olivetti, E., Roth, R., 2011. Concurrent Development of RIM Parts, in: Frey, D.D., Fakuda, S., Rock, G. (Eds.), 18th ISPE International Conference on Concurrent Engineering. Springer-Verlag, Boston.

A. Mixing head's material list

A complete material list for RIMCop mixing-head is detailed in Table B-1 to Table B-5.

Table A-1 – O-rings

$d_i \times d_s [10^{-3}\,\mathrm{m}]$	Quantity	Material
4×1.5	1	Viton
8×1.5	1	Viton
29×1.5	1	Viton
12×2	3	Viton
18×2	8	Viton
22×2	2	Viton
35×2	8	Viton
37×2	2	Viton
40×2	2	Viton

where d_i is the internal diameter of the o-ring, and d_s is the cross-sectional diameter of the o-ring.

Table A-2 – Cylinder Seals(from Kastas)

Seal	$d_e \times d_i [10^{-3}\,\mathrm{m}]$	Quantity	Material
Piston-rod guide strip KBT		4	NBR
Rod seal K38-010	18×10	1	NBR
Double wiper K10-010	18×10	1	Viton
Compact piston seal K18 040-030	40×30	1	NBR

where d_e is the external diameter of the seal.

Table A-3 – Screw

Size	Quantity
M6×25	8
M6×65	4
M8×20	8
M8×80	8

Table A-4 – Hydraulic material

name	Quantity
Tube S12	0.8m
Tube S12	0.8m
Hydraulic nuts S10	2
Hydraulic nuts S12	2
Hydraulic nuts S16	2

Table A-5 – Part Materials

Part name	Quantity	Material
Mixing-head body	1	Steel 1.2080
Injector	2	Steel 1.2080
Isolator	2	Nylon
Material inlet body		Steel 1.2080
Material inlet cover	2	Steel CK45
Material outlet cover	2	Steel 1.2080
Clean piston	1	Steel CK45
Clean piston head	1	Steel CK45
Clean piston flange	1	Steel CK45
Clean piston support	1	Steel CK45
Seal block	1	Steel CK45
Cylinder body	1	Steel CK45
Cylinder flange	1	Steel CK45

B. Detailed Experimental Procedure

B.1. Materials

The materials used in the present work are

- Materials:
  - Rencast FC52 Isocyanate (properties in Table B.1)
  - Rencast FC52 polyol (properties in Table B.1)
  - Carbon Black
  - Resealing agent VP12802
  - Dichloromethane
  - Water
  - Acetone
  - Nitrogen

Table B.1 – Reactants Properties

Proprierty	Material	
	Polyol	Isocyanate
Commercial name	Rencast FC52 polyol	Rencast FC52 isocyanate
$\rho[\mathrm{kgm^{-3}}]$	980	1120
$\mu[10^{-3}\mathrm{Pa.s}]$	18.88	18.25
$T_{inj}[°\mathrm{C}]$	55	25

- Equipment:
  - Prototype Equipment RIMCOP

        - Differential pressure transducer Valydine P55D, with an accuracy of $2.5\times10^{-1}\%$, and a range between $\pm2.2\times10^{-1}\text{bar}$
    - Closed conical mould
    - Tektronix TDS2002 oscilloscope, with a data rate of 1GHz, corresponding to frequencies of 200MHz.
    - Control and acquisition by computer
    - Polyurethane and silicon tubes
    - K Thermocouple
    - Scaltec sbc 31 balance
    - Ultrasonicss Dr Hielscher UP50H
    - FTIR
    - Individual protection equipment:
        - Individual mask with APX2 filters
        - Lab coat
        - EVAL gloves

B.2. Experimental Procedure

General marks:

- Collect raw materials samples for a FTIR analysis, in order to verify that raw material properties remain constant. The collect should occur when is considered important to analysis, namely:
    - Before fill the tanks with raw material (commercial samples)
    - After the nitrogen degasification
    - After the raw material heating
    - Before the injection
- Record photo and films during the different stages of the process
- The solvents are reused until the degradation

1. Glycerin clean from the tanks of the prototype equipment:
    1.1. Purge all from the tanks. For purge open the ball valves on pump's out, allowing all the material from tanks and mixing chamber to be purged. In order to, move the mixing head to injection position;
    1.2. Fill the tanks with water, until the maximum volume - 20L;
    1.3. Let, for one day, the compressed air bubbling the water in tanks, for a easily remove of glycerin rest in walls. The water is recirculated with a voltage of 4V and a flow rate of 4Lmin^{-1}. The recirculation is performed by mixing chamber in injection position and connected to the tanks;
    1.4. Purge the water from the mould outlet and after in identical method from 1.1;
    1.5. Repeat the 1.3 e 1.4 until a clean water without any glycerin tracer;
    1.6. Atomize around 5L of acetone, using a peristaltic pump Watson Marlow 323. Define a rotation of 360rpm and a flow rate of 1Lmin^{-1}. This quantity is enough for three complete recirculations between the

equipment tubes and mixing head. Recirculate the acetone with a voltage of $4V$.

1.7. Purge the acetone similarly to 1.1.

1.8. For a better drying, it is used dry air. The compressed air is dry in the tanks at $60°C$, and is recirculated, as shown Figure A.1, for $30min$. If there is an acetone smell, more recirculation passages should be performed until the dilution of acetone concentration in atmosphere.

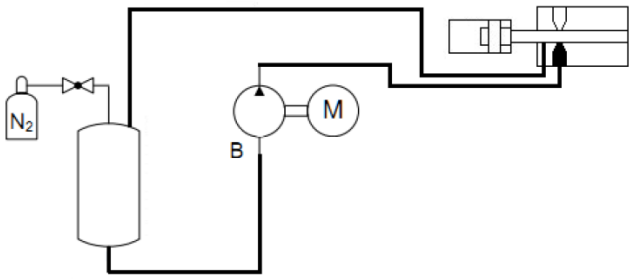

Figure B.1 Air dry recirculation, where the more thicker lines correspond to the recirculation circuit.

Note: The products used in the clean are compatible with all the materials used in the pumps, according to www.coleparmer.com/Chemical-Resistance(consulted at July of 2012)

2. Reactants preparation:

2.1. Polyol

2.1.1. Mixture 0.1% in mass of carbon black. For the present work, are $45g$, since the package as a raw materials mass of $4.5kg$, according to:

2.1.1.1. Out $0.25L$ of polyol;

2.1.1.2. Use the ultrasonic mixture to homogenize the mixing with polyol and carbon black. As operation parameters were used the lower cycle and 40% of amplitude;

2.1.1.3. Out another $0.25L$ of polyol;

2.1.1.4. Mix the polyol with the mixture of polyol and carbon black;

2.1.1.5. Use the rotative mixture to homogenize the mixture, during $1h$;

2.1.1.6. Mix all the mixture to the package content;

2.1.1.7. Manually mix the package;

2.1.1.8. Degasify with nitrogen;

2.2. Isocyanate

The isocyanate must be used as delivered, attending to the fact to reduce to minimal the contact time between isocyanate and air, due the toxicity and non-desired reactions due to the air humidity.

3. Tanks filling with raw materials:

3.1. Inertize the tanks with nitrogen, recirculating 10 times with a pressure of 0.125bar, corresponding to 20min with a flow rate of $1.1\times10^{1}\text{Lmin}^{-1}$.

3.2. Transfer the raw material from the packages to inside the tanks, using the peristaltic pump. The tube should be placed in the package depth and another tip in tank depth, as shown Figure A.2. Define a rotation of 360rpm for both reactants. Predicted filling time for one package is around 4.5min. The filling should be done with nitrogen recirculating under a pressure of 0.125bar. Be careful to do not entry air to tanks at the end of the process.

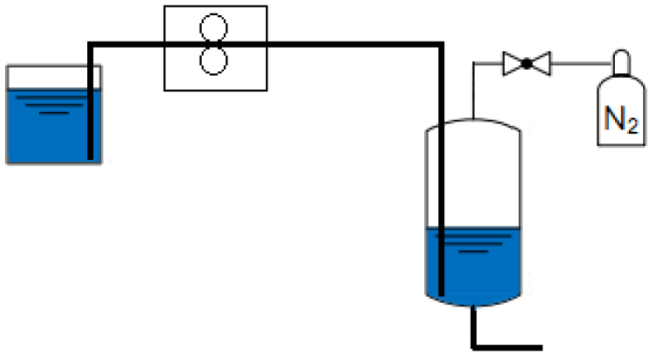

Figure B.2 Tanks filling and tubes position

3.3. Bubble the isocyanate and polyol in nitrogen under a pressure of 0.5bar, during 12h, to remove any humidity.

3.4. Remove the tube of reactants and close the tanks. When the tube is removed, fill the tanks atmosphere with nitrogen under a pressure of 0.5bar.

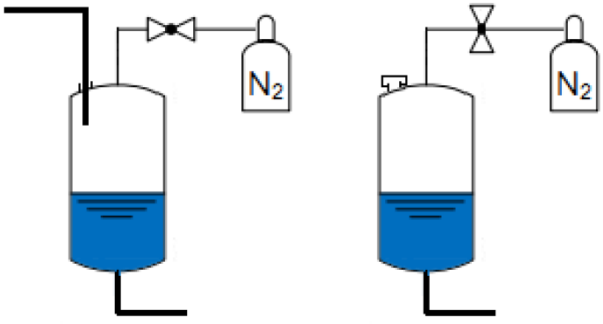

Figure B.3 Close of the tanks under inert atmosphere

4. Samples injection:

4.1. Stabilize the temperatures of the raw materials, according to the Table B.1;

4.2. Depressurize the tanks until a pressure of $0.125bar$.
4.3. Cover the mould and thermocouple surface with release agent, putting, at least, three layers. Putting the release agent in the mixing head, forward and downward the clean piston. Use an air dry to a faster application of the layers;
4.4. Close the mould without o-rings and neither a total grip, for a easily air release during the injection. Place the thermocouple in the mould. The thermocouple should be placed $85mm$, inside, being $15mm$ in contact with mixture inside the mould;
4.5. Assemble the oscilloscope, putting the cables of the sensor in channel one. Select a data rate of $2.5kHz$ to capture an enough samples for the wanted frequencies.
4.6. Acquire the temperature and pressure data in control software;
4.7. In control software set the injection time, for the present work is $7s$. Turn on the oscilloscope;
4.8. Inject the sample according to the processing parameters defined;
4.9. Record the oscilloscope data during the filling;
4.10. After the automatic stop of the injection, start the recirculation of raw materials.
4.11. Unmounts the mould and extract the part using the compressed air, after around $20min$.
4.12. Repeat 4.7 to 4.11, the enough times according to the samples number.

5. Clean of the raw materials from prototype equipment:

Note: the clean must be performed when the equipment is without any use more than one day, to prevent the isocyanate cristalization.

5.1. Cool the tanks at natural environment. The clean operation only can be done at room temperature. Mount the mould;
5.2. Purge all the content of the system, using the spherical valves, open the mixing chamber to the injection position, guaranteeing a purge from tanks and mixing chamber;
5.3. Despressurize the tanks;
5.4. Atomize the dichloromethane to tanks and system cleaning. Atomize a higher volume to the one used with raw materials;
5.5. Recirculate the dichloromethane during $30min$ with a voltage of $4V$, with a closed system, ie, clean piston in recirculation position;
5.6. Purge the dichloromethane similarity to 5.2.;
5.7. Fill the tanks with $3.2L$ of dichloromethane using the peristaltic pump, and recirculate two times by the system, one with closed system, ie., recirculation position of clean piston, and another one with an open system, ie., injection position of clean piston;
5.8. Purge the dichloromethane by the top of mixing chamber.

5.9. Use acetone to clean, adding $8\mathrm{L}$ to recirculate 5 times at $4\mathrm{V}$, being the recirculation time close to $2\mathrm{min}$. Purge the acetone identically to 5.2.;

5.10. For a better drying, use air dry during $30\mathrm{min}$. The air is dry in the tanks at $60°\mathrm{C}$. If there is some acetone smell in atmosphere, the air dry can be recirculated the needed times to a dilution of the acetone concentration, identical to 1.8.